Stoichiometric and substituted SBTi-layered ferroelectric system: Bulk and Thin films

A thesis submitted in partial fulfillment of the requirements for the award of the degree of

DOCTOR OF PHILOSOPHY

By

Rambabu Angalakurthi

School of Physics
University of Hyderabad
Hyderabad 500 046
India

December 2012

DECLARATION

I hereby declare that the work embodied in this thesis entitled "**Stoichiometric and substituted SBTi-layered ferroelectric system: Bulk and Thin films"** is carried out by me, under the supervision of **Prof. K. C. James Raju**, School of Physics, University of Hyderabad, Hyderabad, India.

Rambabu Angalakurthi

Place:

Date:

CERTIFICATE

This is to certify that the thesis entitled “**Stoichiometric and substituted SBTi-layered ferroelectric system: Bulk and Thin films**” submitted by **Rambabu Angalakurthi** to the University of Hyderabad is a bonafide work carried out by him under my supervision. The work embodied in this thesis has not been submitted to any other institute or university for the award of any degree or diploma.

Place: Hyderabad

Date:

(Prof. K. C. James Raju)

Thesis Supervisor

Dean

Prof. Surya P. Tewari,

School of Physics,

University of Hyderabad.

Acknowledgements

I have great pleasure to write this part of my thesis and express my gratitude to all those who have helped me. It's time to bring them to stage, since most of them was behind the screen. Many people have directly or indirectly contributed to the successful completion of this thesis.

I am deeply indebted to **Prof. K. C. James Raju**, for his guidance and support during the entire span of my doctoral research. The way he encouraged, advised and helped me in an academic, personal and spiritual life is unforgettable. I felt that it is my privilege to work with such a good person. I once again thank for his continuous guidance and motivation in all aspects during my research period.

I would like to extend thanks to **Prof. M. Ghanashyam Krishna** for suggestions and encouragement. I sincerely thank my doctoral committee member **DR. S. Srinath** for his constant encouragement and guidance throughout my research.

I gratefully acknowledge **Prof. R. Singh, Prof. G. Rajaram**, for their valuable remarks of my research work during every six months, being in the doctoral committee.

I thank **Prof. S. N. Kaul**, coordinator, Centre for nanotechnology, University of Hyderabad for allowed me to use TEM and RAMAN instruments.

I am also extremely thankful to our dean **Prof. S. P. Tewari** and former Deans **Prof. C. Bansal & Prof. Vipin Srivastava,** for their support and providing the necessary facilities. I would also like to thank other **faculty members** of school of physics.

I thank **Dr. Koteswarao** and **Dr. Srikanth**, SEST, University of Hyderabad, for allowed me to use instruments in their department.

It is my pleasure to acknowledge **Dr. A. R. James** of DMRL Hyderabad and **Dr. A. Srinivas,** DMRL Hyderabad for their timely help.

I thank **Mr. Abraham** and other office staff of the school for their timely help on every occasion. I am thankful to all the CIL staff members for technical support they provided.

I thank **Mr. Turumalaiah, Mr. Lakshmi Narayana, Mr. Ravi Shankar, Mr. Durga Prasad, Ms. Sunitha, Smt. Deepthi** for their timely help in providing technical data.

It is with enormous pleasure that I acknowledge the support and encouragements that I received from my seniors D**r. D. Pamu, Dr. Venkata Sarvanan, Dr. Sudheendran, Dr.**

Uma Mahendra Kumar, Dr. Kiran, Dr. Prashanth, Mr. G. Lakhminarayana Rao, Dr. Rajeeb Brhma. Their suggestions and encouragement in the lab made easy for analyzing the data.

I thank postdoctoral fellows in lab **Dr Ramesh, Dr Sachin, Dr.Ahamed** for their suggestions in academic issues.

I would like to thank all of my Ph.D batch mates **Bheema Lingam, Venkaiah, Shankaraiah, Vasu, Sadik Ali, Arun Kumar, Deva Raju, Balaji, Sita, Vijayan, Sendil Kumar, Parthasarathy, Yugander, Anil Kumar and Deepak** for encouraging and making the whole research period worthful.

I thank all **research scholars** from School of physics

I sincerely thank to all my **dearly juniors Anil. T, Bashaiah. S, Ramakanth K, Lakshun Naidu, Rama Obulesu K, Umar Pasha, Varma, Sivanagi Reddy, Santanu, Surya, Pavan, Srikanth, Santhosh, Shankar**, for their valuable help.

I thank **Mr Bansilal and Mr Subbirami Reddy** for their help during my research period.

I thank M.Sc friends from Andhra University **Mr. Balamurali Krishna, Mr. Anjaneyulu (Anji), Mr. K. Ramesh Babu, Dr. Srinivasa Rao, Ch. Rajasekhar, Rajesh, Babu B, Raja Babu. Anil**.

I gratefully thank from my bottom of heart to **CHILD CARE INDIA ORGANIZATION** which makes my dreams fulfill. I thank **Dr. MAX LAUNGE** (USA), **Sambaiah uncle, Thimothy sir, Sastry sir**, and my **sponsors** who helped me financially and prayer support from my childhood.

I am extremely grateful to my dearest friends from CCI for their prayer support, consistent concern and encouragement. Some of them are **Chinni, Sowja, Padma, Puspa, Sujatha akka & family, Ramana Reddy, Vinay, Anil, Jeevan, Arun, Suseela, Kotaiah, Pradeep, Srinu, Anusha, Ramanjaneyulu, Sarah, Subbarao,Venkata Reddy, Ratna Kumar, Babu anna, Rajendra, Veerendra, Salomi, Sudharson, Israel** and many more.

I also want to thank to my beloved ones **Kodanda Ram anna family, Thomas Anna family, Ratnakar family, Paul Kiran anna family, Adam anna family, Srinivas anna**

family, Jose anna family, Joshua anna family, Ramesh anna family, Franky Anna and Family, Andrew Anna and Family, Veeresh family, Ebinezar, Henry, Calvin, Philip, Rajesh Babu, Rajesh Gudipalli, Yellaswamy, Prasad Anna, Joseph Anna, M. Raju, Benhur, Prakash Elliot, Ravi Kiran, Vijay, Ganesh, M. V. Suresh, Vara Lakshmi, Sujatha, Anitha, Sudheer staff anna, Sudheer (KP), Sudheer (BHEL), Vijaya Prasad Anna, Neelima akka, , Sunil, Eswar, Johonson, RajKumar , and Anil for their kind loving nature and spiritual support during my stay in the CAMPUS.

My special thanks to EU believers, some of them are **Suresh P, Kishore, Ajay, Prabhu kumar, Nagarjuna, Manoj, Varma, Mani, Prathyusha, Ancy David, Prasanthi, Babu Rao** and all **EU believers** for their love and fellowship throughout my stay in campus. Joyful movements with them are unforgettable in my life.

I would like to thank to members of **New Jerusalem prayer house, Christian Brethren Church, Sinai Prayer house** for their continuous prayer support.

I am happy to express my gratitude for the financial support from University of Hyderabad **BBL** (Boarding/ Boarding–Cum-Lodging Allowance and Contingency) and **DST-ITPAR-II** made me to reach the goal of success in crucial time.

It is the endless sacrifice and support of my family members (**Father, Mother and Brother**) for their love, affection and moral support all the time and thanks to all my relatives for their support.

Above all, I thank to my Lord for His abundant grace and mercy on me though out life. I Praise and Worship Him, for all things that he has done for me.

Rambabu Angalakurthi

Dedicated to……

MY FAMILY

And

CHILD CARE INDIA ORG.

CONTENTS **Page no**

Preface

Recently, Bi based layered structure ferroelectrics received good attention because of their many applications in electronic devices as well as due to environmental concerns with Pb based materials. The SBTi ($SrBi_4Ti_4O_{15}$) ceramics have attracted the attention for high frequency and high-temperature applications due to their high Curie temperature (Tc $\cong$ 540^{o}C). Even the room temperature piezoelectric properties of SBTi samples are interesting compared to other layered structure ferroelectrics. It is well known that piezoelectric coefficients depend on the mechanical properties which are related to the mechanical state of such materials. Moreover, the mechanical behavior plays a crucial role in the delamination, cracking or fracture, and polarization fatigue of the multilayer thin-film structures. Consequently, the investigation on the mechanical properties of the bismuth layer-structured ferroelectric bulk and thin films are of practical importance in various situations and particularly for the design of piezoelectric devices. The importance of such samples has now increased with their potential for application in MEMS devices where they can be used not only for sensing and actuation but also for energy harvesting even at elevated temperatures. These applications require a closer study of the mechanical properties of the deposited thin films like the extent to which these material properties depend upon the substrate, crystallographic orientation, grain size, process conditions and the deposition procedure.

The potential applications of the dielectric thin films in microwave devices have accelerated the research for the development of new materials, thin film processing methods and optimization. The reliable and reproducible measurements on the dielectric properties of the bulk and thin films of ferroelectrics at microwave frequencies have become an essential requirement of these research activities. There are only few studies on the microwave dielectric properties of their thin films even though it is quite important in terms of application and from an academic point of view. There are reports on low frequency dielectric properties for layered structure ferroelectric thin films but there are no reports on the microwave dielectric properties, which again emphasize the relevance of the present study.

Hence a suitable bismuth layered structure ferroelectric composition ($SrBi_4Ti_4O_{15}$) was identified in this study to make both bulk and thin films. Mechanical and microwave dielectric properties along with other basic characterizations were done for both bulk and thin films to see whether same bulk characteristics are getting retained in thin film form for this composition. Most of the previous works are on the growth of poly crystalline SBTi films on Pt/Ti/Si/SiO_2. The growth of these films on a low-cost substrate such as fused silica is important in the microwave application of these thin films. However, growing crystalline thin films on amorphous substrates is challenging and requires serious process optimization, which is an important objective for this study.

This thesis consists of eight chapters and a brief overview of each chapter of the thesis is as follows.

Chapter I : This chapter discusses the electro ceramics and classification of electro ceramic materials. This chapter also presents the details about the drawbacks of Pb-based materials and application of layered structure ferroelectric materials to electronics devices. It also discusses the importance of the development of Bismuth layered structure ferroelectric materials. The importance of the $SrBi_4Ti_4O_{15}$ based ferroelectric ceramics is also described. A detailed review of the work being carried out on these material systems is given. Based on these understanding, the major objectives of the present study is identified and presented.

Chapter II : The second chapter describes the preparation and characterization techniques used in the study of SBTi ceramics and thin films. The Retsch make (RS-200-Germany) planetary ball mill was used for particle size reduction of SBTi ceramics. The parallel capacitance (C) and the dissipation factor D for all the bulk samples were measured using an Agilent 4294A impedance analyzer in the frequency range of 100Hz-1MHz in a temperature range of 50 to 600^oC with a Lab–Equip temperature control unit. Ferroelectric properties of all the bulk samples were measured using P-E loop tracer made by Marine India Pvt Ltd. We have used transmission/reflection method to measure complex permittivity in the X-band using a WR-90 wave guide connected to the PNA network analyzer (Agilent E8361C) at the frequency range of 8.2 GHz-12.4 GHz. An introduction to the rf magnetron sputtering technique employed during the preparation of SBTi thin films is also presented in this chapter. Characterization techniques such as XRD, FE-SEM and AFM are used for the structural, composition analysis and microstructural analysis respectively in this study. Envelope technique for optical properties and Raman studies for local structural analysis are discussed in detail. The details on Nanoindentation technique and its significance for mechanical properties are presented in this chapter. This chapter also contains the details of the split post dielectric resonator (SPDR) technique for measurement of microwave dielectric properties of these films. An Agilent 8722ES vector network analyzer was used for this measurement.

Chapter III : This chapter describes the results obtained during the optimization of the processing route of SBTi ceramic samples, realized to improve its reproducibility. This chapter contains two main parts. Part 1 deals with studies on SBTi ceramics. Single phase SBTi ceramic samples were prepared through conventional solid-state reaction technique by optimizing the calcination and sintering conditions systematically. Dielectric constant, remnant polarization and mechanical properties increased as the sintering temperature increases up to 1190^0C. With further increase of sintering temperature all the properties are degraded due to the presence of abnormal grain growth and bismuth loss at high temperatures. The influence of the Bi-loss and oxygen vacancies increases the pinning at the domain wall. The presence of the pinning centers at the domain walls can cause the decrease in observed dielectric and ferroelectric properties.

We have chosen alternate process routes such as reducing the particle size and microwave sintering in order to get a finer microstructure and smaller grain size. This part describes the effect of ball milling of SBTi ceramics on different sintering processes and resulting microstructure as well as on dielectric, ferroelectric, Raman modes and mechanical properties. The grain size of the sintered body is found to decrease for the samples with longer milling times for both microwave and conventional sintering except for 20 hours of milling. The microwave sintered samples exhibited smaller grain size than conventional sintered samples. The observed properties of SBTi ceramics strongly depended on grain size. The microwave sintering of SBTi ceramics milled for different time durations leads to higher densification and fine microstructure in much shorter time than conventional sintering. It is interesting to note that when the average grain size is minimum (for 15hours milling case), the density is maximum and the samples exhibited best dielectric, mechanical and ferroelectric properties for both conventional and microwave sintered samples. The results of microwave sintered samples are desirable for microelectronics industry such as capacitors and actuators.

Chapter IV : This chapter explains the effect of Sm-substitution on SBTi bulk ceramic samples for their structural, morphological, Raman modes, dielectric properties at low and high frequencies, ferroelectric and mechanical properties. The systematic comparison study for conventional and microwave sintered samples of SBTi ceramics with various amounts of

Sm-substitution have been studied and the dependence of their densification on sintering conditions are also studied. There was no observable change in structural properties as the substitution increases up to x=0.75. With the further increase of x, structural distortion changes are observed, and grain size decreased. The same samples when subjected to microwave sintering yielded good densities, fine microstructure and smaller grain size at lower temperatures with less socking time compared to conventional sintered samples. With the substitution of Samarium, the ferroelectric properties were degraded compared to pure SBTi ceramics due to relaxor behavior. The temperature dependent dielectric measurements exhibited a relaxor behavior in Sm-substituted SBTi ceramics. As the frequency increases, the Curie temperature increases for all Sm-substituted SBTi ceramic samples. The experimental data were fitted with an inhomogeneous micro region model which is well-established and suitable for relaxor materials. The measured standard deviation of the Curie temperature distribution was in good agreement with fitted values. Microwave dielectric measurements were carried out in X-band range frequencies by a waveguide based calibration comparison technique. From these results, the Sm-substituted SBTi ceramics can be seen not only as a good candidate for lead-free piezoelectric ceramics but also as a relaxor.

Chapter V : The fifth chapter deals with the results of the structural, microstructural, optical and Raman analysis of SBTi thin films deposited on fused silica substrates at room temperature. Two series of films were deposited as part of this work. They are designated as (i) the temperature variation series and (ii) the OMP series. All these films are post annealed with either the conventional or the microwave furnace. From the XRD analysis, it has seen that the as deposited films were amorphous in all cases. For films annealed at 600^{o}C or above, peaks of the orthorhombic structure could be detected. The microwave annealed films exhibited good Raman modes and reliable optical properties compared to conventional annealed films, though they are annealed rapidly with brief socking time (~20min). The investigation on the influence of oxygen mixing percentage (OMP - the ratio between oxygen and argon gases in the sputter chamber) on the microstructure of the rf sputtered SBTi thin films revealed that the oxygen pressure could significantly alter the surface morphology of the as grown SBTi thin films. The SBTi thin films are deposited at room temperature by varying the OMP in steps of 25%. The crystalline sizes of the films are found to be varying with the oxygen partial pressure during the deposition and annealing processes. The rms roughness was high for films deposited at 50% OMP in both microwave and conventional processes. The SBTi thin films exhibited refractive index within the range of 2.0-2.23 with an optical band gap value between 3.0-3.5eV. The refractive index and optical ban gap of the films deposited at 50% & 75% OMP are higher compared to other OMP percentages. Raman modes were observed at ~92,129, 154, 270, 489, 555, 788 and 865 cm^{-1} in SBTi thin films. There were no reports of Raman spectra on amorphous substrates. The observed Raman modes in thin films are relatively of same intensity and same frequency compared to bulk ceramic samples. These results suggest that there is no change in crystal structure and local symmetry between bulk and thin film versions of these compositions. As the OMP increases, the phonon modes are shifted towards higher-frequency side. The shift in the Raman modes to the higher-frequency side is an indication of the stiffening of the bonds, i.e. it indicates the shorter anion-cation distance which will result in vibration at higher frequencies. Shorter anion- cation distances also indicate that the films are under compressive stress.

Chapter VI : The sixth chapter describes the structural, morphological, optical, and Raman studies of SBTi thin films grown at different *in situ* substrate temperatures. Two sets of films are grown on fused silica substrates, and they are (i) unmodified SBTi thin films and (ii) Sm-substituted SBTi thin films deposited at various *in situ* substrate temperatures from 600 – 725^{o}C. The X-ray diffractograms of the SBTi thin films deposited at different substrate temperatures on amorphous fused silica substrates are crystallized into an obvious pervoskite phase with a standard orthorhombic structure. As the substrate temperature increases, orientation of the grains changes from (119) to (0010). The films were polycrystalline with a preferred non c-axis orientation at lower substrate temperatures, and the c-axis orientation is found to be increasing with the increase of substrate temperature. The degree of crystallinity of (119) peak decreases as the temperature increases with respect to (0010) peak. The films deposited at 700^{o}C exhibited lesser lattice distortion and values of the lattice parameters are well matched with standard JCPDS values compared to other films. The surface morphologies of the films are also found to depend on substrate temperature during the growth process. The grain size and surface roughness increased as the substrate temperature increases from 600-725^{o}C irrespective of orientation. This could be the result of an increase in the surface mobility available with increasing temperatures, thus allowing the film to lower its total energy by decreasing the grain boundary area resulting in larger grains. Thus, the films become more granular with the rise of temperature, which results in increased surface roughness. The Raman spectra for these samples were collected at room temperature. The Raman active modes for the films deposited at different temperatures are found to be slightly different. All films exhibited the modes between 90 and 160 cm^{-1} that are originated from the vibrations of the ions at the A site of the pseudo-perovskite blocks. But films deposited at 650 & 700^{o}C show their phonon mode at 270 cm^{-1} which arises from the torsional bending of TiO_6 octahedra, while it was absent for the films deposited at 600 & 725^{o}C. The possible reasons were mentioned throughout this chapter in detail. The optical band gap of the films deposited at 600 and 725^{o}C shows the highest value compared to the other two temperatures. Indications are that the films deposited at 600^{o}C shows higher band gap due to poor crystallinity and films deposited at 725^{o}C exhibited the high band gap due to non-stoichiometry of those films by losing Bi and oxygen which acts as defects. The refractive index also changes as the substrate temperature increases. The low values of refractive index for the as deposited films can be attributed to the rf sputtering deposition process that produces films with porous microstructure and consequently, with low packing density at the ambient temperatures. However, as the annealing temperature increases up to 700^{o}C, the refractive index increases. The relationship between the packing density and the refractive index has been discussed in detail by many researchers, and they have found that when the film achieves the bulk value of refractive index, its packing density will be the highest.

The Sm-substituted SBTi thin films are also deposited on fused silica substrates by varying the substrate temperature from 675 – 750^{o}C. The structural, morphological, optical and Raman studies of these films are also discussed throughout this chapter.

Chapter VII : This chapter describes the mechanical and microwave dielectric properties of the SBTi and Sm-substituted SBTi thin films deposited under different processing conditions with variations in (i) annealing, (ii) OMP and (iii) in-situ deposition temperature. The nanoindentation study allows us to estimate the capability of nanoindentation method in the determination of some mechanical characteristics of these thin films. More precisely, the elastic or Young’s modulus of film as well as its hardness (H) which is also an important mechanical parameter and coefficient of friction are obtained. The load-displacement curve can be used to extract mechanical properties of the materials. The presence of discontinuities in the load-displacement response reveals information about cracking, delamination, and plasticity in the film and substrate. The hardness of the amorphous films is less than that of the crystalline films. As the annealing temperature increases the values of the hardness and Young’s modulus also increases. These results follow the microstructure of the same films that are mentioned in Chapter 5. These results confirm that the mechanical properties of the films are improved after annealing due to grain growth. The increase in grain size leads to a hardening of the material. Scratch test was performed to identify the tribological properties of these thin films which supported the hardness and Young's modulus values measured. The microwave dielectric constant and loss tangents of the films were measured at spot frequencies of 10 & 20 GHz using SPDR (Split Post Dielectric Resonator) technique. Microwave dielectric properties have increased up to 700°C. With further increase of the temperature, dielectric properties are decreased due to bismuth loss and oxygen vacancies at higher temperatures. In case of OMP varying, films deposited at 50% OMP exhibited good mechanical properties than other values of OMP. It is observed that the microwave dielectric constant and loss tangent is strongly dependent on oxygen mixing percentage during deposition. The dielectric constant varied from 80-92 for 10GHz and 66-80 for 20GHz and loss tangent varied from 0.0052-0.0081 for 10GHz & 0.024-0.056 for 20 GHz for films deposited at 50% OMP.

Sm-substituted SBTi thin films were deposited by varying the substrate temperature from 675-750°C. The mechanical properties of these films improved compared to pure SBTi thin films as the substrate temperature increases. The addition of samarium seems to reduce the effects of Bi-volatization even at higher temperatures, which led to improvement of the mechanical properties. We have observed the same trend in bulk ceramics samples which are discussed in chapter 4. Though, the orientation of the films deposited at 750°C exhibited the (0010) direction which is different from the orientation (119) of films deposited at 700 &725°C, the mechanical properties of these films were not decreased as we observed in the previous section. One possible reason for this is that the samarium content suppresses porosity, which led to improve the grains in size without pores and cracks. Microwave dielectric properties also increased as the substrate temperature increases up to 725°C. With further increase in temperature, the dielectric constant is decreasing. Generation of oxygen vacancies at high temperature must be dominating the dielectric properties of these films even though they are mechanically strong. Finally Sm-substituted SBTi thin films deposited at 725°C exhibited good dielectric and mechanical properties compared to pure SBTi thin films. An interesting observation is that the trend exhibited by these films as well as their bulk counterparts in their mechanical and microwave dielectric properties with respect to the corresponding processing conditions are same. Both follow the same trend with only some deviations whose cause can easily be traced. This shows the inter relation between these two sets of properties even though in the first look they are unrelated.

Chapter VIII : The eighth chapter presents the major conclusions drawn from the present study, and it also gives some scope for future works on these systems.

Chapter 1

INTRODUCTION

Chapter 1

INTRODUCTION

1.1 Electroceramics:

The term ‘electroceramic’ is used to describe ceramic materials that have been specially designed for specific electrical, magnetic, or optical applications. Ceramic materials are mainly polycrystalline, non-metallic inorganic substances typically prepared by solid-state chemical reaction followed by a sintering process at elevated temperatures.

The field of electroceramics is application driven and technology oriented. Its foundations are the material sciences, the science of ceramic processing, chemistry, and solid-state physics. The tools in the hands of the electro ceramist include majority of elements of the periodic table, inorganic chemistry, solid state physics, crystallography and other structural, physical, chemical and electrical characterization tools, as well as modeling and device engineering [1]. The field is truly an inter-disciplinary one in both its fundamental and application aspects. The electroceramics today constitute about ninety percent of the value of the total ceramics manufactured. Although we hardly notice them, they are ubiquitous and touch our daily lives at every step. Essential, and often critical, components in devices ranging from the simple gas lighter to the sophisticated cellular phone make use of these electroceramics. The insulating, dielectric, piezoelectric, magnetic, optical, and lately, superconducting properties of these ceramics have led to their widespread use in electrical and electronic devices [2]. These include the piezoelectric lead zirconate titanate (PZT) elements in the gas lighter, telephones and autofocus cameras, capacitors made of barium titanate ceramic in televisions, radios and almost all the electronic equipment, the microwave dielectric ceramics used in highly selective filters for cellular base stations and satellite communication systems [3]. Soft ferrites are used in sensitive radio antennas and transformers; hard ferrites are used in many small electric motors as many as such motors are used in some models of automobiles for functions such as power seats and door locks. In the past decade, electroceramic materials have not only been introduced into microelectronic products like integrated capacitors, but also electroceramic memories have already reached the market, and researchers are at present developing ferroelectric transistors (Terabyte memories). In parallel, the vast areas of electroceramics sensors and actuators are expanding into the field of microelectro mechanical systems (MEMS). Micro sensors and micro actuators based on electroceramics are being fabricated, where in electroceramic materials and micro technologies are combined to form efficient micro devices for production control, environment monitoring and biomedical applications. To meet the increasing demand for the multifunctional materials, complexity of materials had to be increased by integrating different materials. This integration of functionality through materials leads to miniaturization of devices.

1.2 Classification of electroceramics

The electroceramic materials are widely used in many applications. Based on their applications, these electro ceramics are classified as follows.

Ceramics insulators:

The basic function of insulators is physical separation of conductors and regulation, mechanical support, heat dissipation and environmental protection for conductors. Ceramic insulators include glasses, porcelains, oxide and nitride materials. The advantage of ceramics as insulators is their capability for high temperature operation.

High-k ceramic dielectrics:

High–K dielectric ceramics play a key role in electronic industry for high voltage capacitors, used in color TV, computer monitors, and lasers and so on. The trend in the miniaturization of electronic devices and components is the driving force for high-K dielectric ceramics.

Piezoelectric ceramics:

Ceramics which generate electric potential on application of pressure across its surfaces and vice versa are known as piezoelectric ceramics. Piezoelectric ceramics are extensively used as transformers, piezoelectric vibrators, SAW devices, actuators and sensors. The well known piezoelectric ceramics are Barium titanate ($BaTiO_3$) and Lead Zirconate Titanate (PZT).

Ferroelectric ceramics:

Ceramics which show hysteresis loss and spontaneous polarization are known as ferroelectric ceramics. The spontaneous polarization arises due to dipole coupling with local field and impending ionic displacements. Ferroelectric ceramics have promising applications as high permittivity capacitors, ferroelectric memories, sensors, electro-caloric fridges, electro-optical devices and so on.

Magnetic ceramics (Ferrites):

Ceramics that contain iron oxide compounds and an additional metallic ion are known as magnetic ceramics. Magnetic ceramics has a key place in microwave applications due to its low cost and ability to minimize eddy currents at high frequency range. Ferrites are semiconductors or insulators and that give scope for potential applications in power electronics and telecommunication systems.

Superconductor ceramics:

Ceramics which show zero resistivity are known as superconducting ceramics. Since the introduction of superconducting ceramics by Bednorz and Muller in 1986, the research on high temperature superconductors has gained momentum. The superconducting ceramics can provide high magnetic field and high transition temperature. It provides scope for high potential applications in power systems, electronics and high magnetic field applications.

1.3 Crystallographic considerations of polar effects in Electroceramics

It is well known that crystals are divided into 32 point groups based on symmetry elements like center of symmetry, axes of rotation, mirror planes and combination of these three. Out of 32 crystal classes, 11 have a center of symmetry and hence cannot possess polar symmetry or spontaneous polarization. One of the remaining 21 crystal classes which lack a center of symmetry has a symmetry element which prevents polar characteristics. One or more polar axes are present in the remaining 20 point groups and hence these exhibit various polar effects such as piezoelectricity, pyroelectricity and ferroelectricity.

Piezoelectricity is the property of a crystalline material to exhibit electric polarity when brought under a stress, i.e when a compressive stress is applied, a charge flows in the opposite direction. On the other hand, if an electric field is applied, a piezoelectric crystal will stretch or compress depending on the orientation of the field with polarization in the crystal [4]. All of the 20 crystal classes which lack center of symmetry are piezoelectric. However, spontaneous polarization is not guaranteed in a material just because of its piezoelectric response. For example, in some cases as in quartz, which is a piezoelectric material, the polar directions are arranged in such a way that they self-compensate and cancel out spontaneous polarization and only exhibit a piezoelectric response. Out of the 20 piezoelectric crystal classes, 10 possess a unique polar axis i.e the properties measured along that axis is different from the others. As these types of crystals are spontaneously polarized, they are termed as polar crystals. The magnitude of polarization depends up on temperature and hence if there is a change in temperature it imposes an electric charge on the faces perpendicular to the polar axis of the crystal. This is called pyroelectric effect and each of the 10 classes of the polar crystals are pyroelectric [5].

All ferroelectric crystals are pyroelectric in nature and have the additional property than an external field can reverse their spontaneous polarization. Hence, ferroelectrics are spontaneously polarized materials with reversible polarization. This reversible polarization response manifests itself as a hysteresis loop in the presence of an external electric field which is similar to the hysteresis loop generally observed for ferromagnetic materials.

1.4 Ferroelectricity:

Sodium Potasium Tartrate Tetrahydrate ($NaKC_4H_4O_6.4H_2O$) was the first solid which was recognized to exhibit ferroelectric behavior and was observed by Joseph Valasek [6] in 1923. This crystal was discovered in La Rochelle, France in 1655 by Elie Seignette who was an apothecary. Joseph Valasek was the first to establish the analogy between the magnetic properties of ferromagnetism and the dielectric properties of Rochelle salt and hence the name ferroelectrics. He also demonstrated the hysteretic nature of the polarization and its marked dependence on temperature.

Ferroelectricity has also been called Seignette electricity, as Seignette or Rochelle Salt (RS) was the first material found to show ferroelectric properties such as a spontaneous polarization on cooling below the Curie point, ferroelectric domains and a ferroelectric hysteresis loop. In 1935 ferroelectricity in Potassium dihydrogen Phosphate (KH_2PO_4) (KHP) and its sister crystal (KD_2PO_4) (KDP), was observed by Busch and Scherrer [7]. A huge leap in the research on ferroelectric materials came in the 1950's after Wul and Goldman [8] discovered many anomalous dielectric properties in $BaTiO_3$, leading to the widespread use of barium titanate ($BaTiO_3$) based ceramics in capacitor applications and piezoelectric transducer devices. $BaTiO_3$ belongs to the family of materials called perovskite. $BaTiO_3$ is the prototype of many oxide based ferroelectric perovskites which are characterized by the chemical formula ABO_3. Since the discovery of ferroelectricity in $BaTiO_3$ ceramic, many other ferroelectric ceramics including lead titanate ($PbTiO_3$), lead zirconate titanate (PZT), lead lanthanum zirconate titanate (PLZT) and relaxor ferroelectrics like lead magnesium niobate (PMN) have been developed and utilized for a variety of applications [9]. The biggest use of ferroelectric ceramics have been in areas such as dielectric ceramics for capacitor applications, ferroelectric thin films for non-volatile memories, piezoelectric materials for medical ultrasound imaging and actuators, and electro-optic materials for data storage and displays. In the past few decades, many books and reviews have been written explaining the concepts of ferroelectricity in the materials [10-13].

1.5 General Properties of ferroelectric materials:

Ferroelectric materials are non-centrosymmetric, have a unique polar axis and therefore contain electric dipoles that are spontaneously polarized, which can be reversed by application of a field in the opposite direction. In these materials, there exists a particular temperature called the Curie temperature (T_c) where the materials undergo a transformation from a higher crystal symmetric paraelectric phase to a lower crystal symmetric ferroelectric phase. The ferroelectric phase shows hysteresis in polarization and is more useful in memory application whereas the paraelectric phase shows no hysteresis and the polarization changes with the applied field making it useful in DRAM application. This nature has been summarized in figure 1.1. Dielectric permittivity drastically increases in the vicinity of Curie temperature and above that it decreases according to the well-established Curie-Weiss law as given below [14].

$$\varepsilon = \varepsilon_o (1+ C/T-T_o) \qquad (1.1)$$

Where C is the Curie constant, T_o is the Curie-Weiss temperature ($T_o \leq T_c$)

In the ferroelectric state i.e below T_c, spontaneous polarization occurs. The structural transformation from a higher to lower symmetry causes a change in the cell volume leading to a strain in the system and hence the system exhibits domain structure in order to minimize this strain. Existence of domain structure is a hallmark of ferroelectric materials. Domains contain uniformly aligned electric dipoles and are separated by domain walls across which the spontaneous polarization is discontinuous. The thickness of the domain wall ranges typically from 1-10 lattice parameters across. The 180^o domains are considered to have an abrupt change in the polarization direction and the 90^o domain walls are thicker than that of the 180^o domain walls. The angle between the directions of polarization on either side of the wall is a characteristic of domain walls. A schematic of diagram of ferroelectric material at different length scales is shown in figure 1.1. These domain walls are generally formed to reduce the energy of the system. The grain size, crystal symmetry, magnitude of spontaneous polarization, defect structure, as well as the sample geometry and the method of preparation contribute to the size and structure of these domains [15].

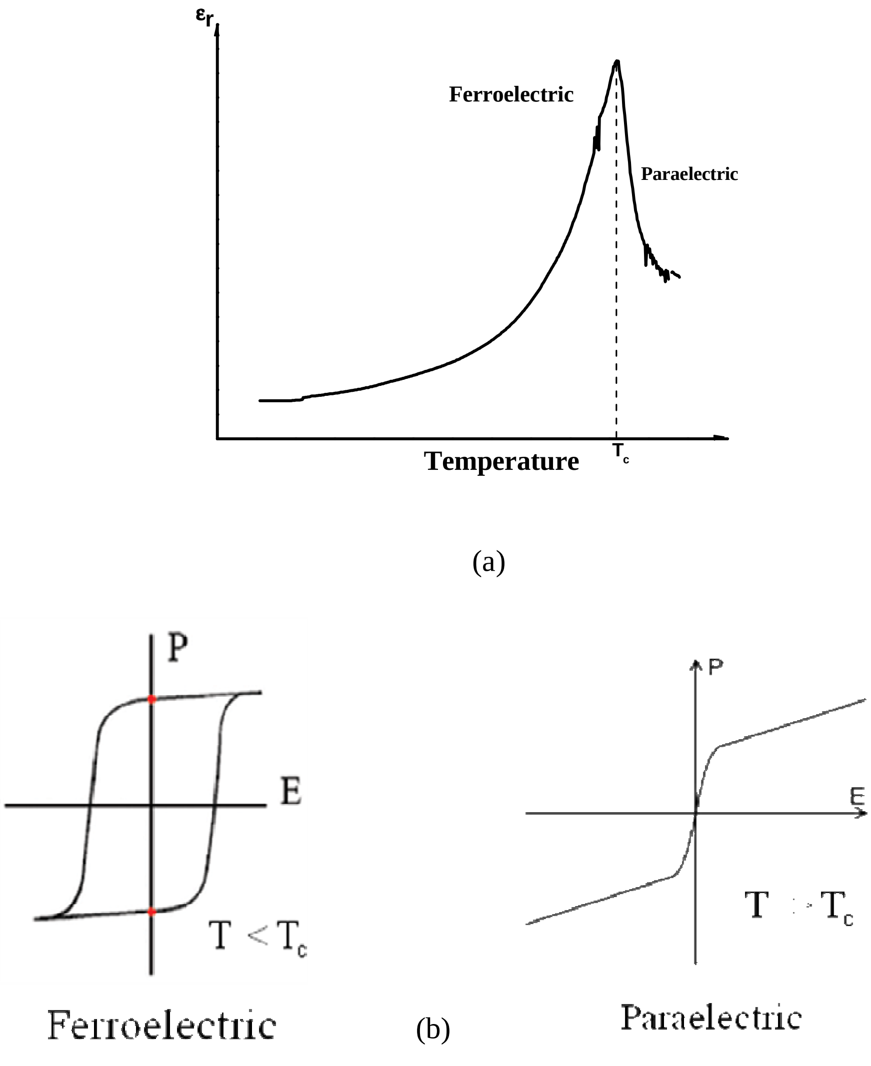

(a)

(b)

Figure 1.1: (a) Permittivity verses temperature and (b) the corresponding polarization characteristics of phase transition.

1.6 Lead-free ferroelectric materials:

A major breakthrough came with the discovery of PZT and $BaTiO_3$ in the 1950s [16-17] and the family of these materials exhibited very high dielectric and piezoelectric properties. To date, PZT is one of the most widely exploited and extensively used piezoelectric materials, having secured permanent place in the field of material science and engineering. They are widely used as sensor and actuator devices [18–21], in multilayered capacitors, as hydrophones, etc. with an estimated market of tens of billions of dollars worldwide. However, lead oxide, which is a component of PZT, is highly toxic and its toxicity is further enhanced due to its volatilization at high temperatures particularly during calcination and sintering causing environmental pollution [22]. According to the recent developments, European Union (EU) is planning to restrict the use of hazardous substances such as lead as well as other heavy metals [23, 24]. However, there is no equivalent substitute for PZT. Therefore, its use is still continued. This may be a temporary respite, but the legislation certainly impressed the researchers to develop alternative lead-free ferroelectric materials in order to replace lead-based materials [25, 26]. There had been many attempts by researchers in the past to develop alternative lead-free materials but the properties are nowhere near to the PZT system. Basically, the lead-free systems are (i) perovskite type, i.e., BNT, $BaTiO_3$ (BT), $KNbO_3$, $NaTaO_3$, etc., (ii) tungsten-bronze type ferroelectrics (iii) bismuth layered structure ferroelectrics (BLSF).

Perovskite type materials: The perovskite-type (ABO_3) ferroelectrics such as $BaTiO_3$ (BT), $(Bi_{0.5}Na_{0.5})TiO_3$ (BNT), $KNbO_3$, $NaTaO_3$, etc. are well-known lead-free ferroelectric materials. These ceramics show relatively large piezoelectric constant. However, the main drawbacks generally are low Curie temperatures (T_c), difficulties in poling treatments and/or low relative densities [25].

Tungsten-bronze type ferroelectrics: The tungsten bronze type ferroelectric crystals have a structure similar to tetragonal tungsten bronze K_xWO_3 (x<l). $BaNb_2O_6$ ($BaNb_2O_6$) was one of the first crystals of the tungsten bronze type structure to show useful ferroelectric properties. For barium niobate the B_1 and B_2 sites are occupied by Nb^{5+} ions. The open nature of the structure as compared to the perovskite allows a wide range of cation and anion substitutions without loss of ferroelectricity. The ferroelectric crystals grown from solid solutions of alkali and alkaline earth niobates have shown great potential for being used as a material for laser modulation, pyroelectric detectors, hydrophones and ultrasonic applications. The high Curie point (T_c = 460°C for barium

niobate) of their compounds makes them suitable for high temperature applications. A problem associated with this type of materials is the large volume change due to phase transformation on cooling below the Curie point, leading to cracking of the ceramic [27-28].

Bismuth layered structure ferroelectrics: Bismuth layered structure ferroelectrics (BLSFs) are materials of interest as they exhibit ferroelectricity, pyroelectricity and piezoelectricity. Lead based ferroelectrics have been extensively studied, but recent issues with fatigue, environmental safety, and health concerns have prompted interest in layered perovskite family. Pb based compounds present contamination and hazardous problems during fabrication. The bulk bismuth layer-type ferroelectric compounds are discovered in 1959 [29-32]. The family of bismuth layered oxides has the formula

$$(Bi_2O_2)^{2+}\ (Me_{m-1}R_mO_{3m+1})^{2-} \qquad (1.2)$$

Where

Me = Mono-, di-, or trivalent ions,
R = Ti^{4+}, Nb^{5+}, Ta^{5+} etc.., single or in combination
m = 2,3,4,5 etc.

The structure for m= 3 layered compound system [33-35] is shown in figure 2.

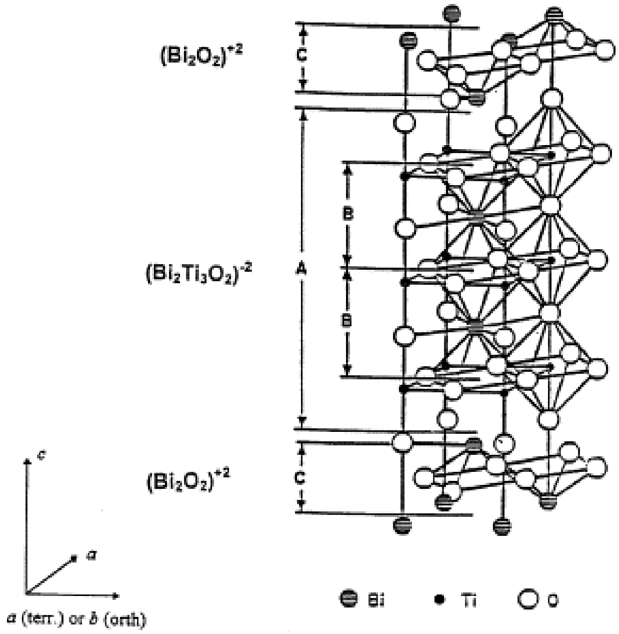

Fig.2. Schematic drawing showing the crystal structure of BLSF (*m* = 3).

These compounds have a structure comprised of a stacking of *m* perovskite-like units of O-R-O chains between Bi_2O_2 layers along the pseudo-tetrahedral c-axis. The perovskite like units continue only in the planes perpendicular to the c-axis. Along c-axis, the continuous extension of O-R-O chains is interrupted not only by the presence of Bi_2O_2 layers but also by the translation of the perovskite-like units in the planes perpendicular to the c-axis. Because of the presence of RO_6 octahedrons in perovskite layers, spontaneous polarization can occur in the planes of these layers. The layered perovskite materials are attractive because of their good fatigue, retention, and electrical characteristics [36-39]. The ceramics fabricated from the Bi_2O_2 top layer compounds do not have good piezoelectric properties because of very low poling efficiency. The bismuth oxide layer compounds may become important piezoelectric ceramics because of their high stability, higher operating temperature (because of high T_c) and higher operating frequency. These ceramic samples are mainly useful for piezoelectric resonators, which need to exhibit a very stable resonance frequency.

BLSF compounds with different '*m*' values form a large group of ferroelectric materials and the properties of these materials vary depending upon the number of perovskite layers that exist between the two bismuth oxide layers along the pseudo tetragonal c-axis. On the other hand, unbroken chains of O-R-O are present in the plane perpendicular to the c-axis. The presence of Bi in these compounds enhances the transition temperature and hence most of these compounds have high Curie temperatures. The c-axis is generally found to be the polar axis in these compounds. Hence, the spontaneous polarization observed along the c-axis suggests that Bi_2O_2 layers also take part in the co-operative phenomenon responsible for the occurrence of ferroelectricity in the mixed bismuth oxides. It is also observed in general that the Curie temperature decreases with increasing the separation between the Bi_2O_2 layers, other things being the same. According to Newnham R.E [40], odd layer compounds belonging to orthorhombic space group B2cv show a single first order transition, where as even layer compounds with space group $A2_1am$ show two phase transitions above 200^oC apart. The lower transition is generally found to be first order with large thermal hysteresis. The upper transition in the even layer is considered to be the Curie point and appears as a second order transition.

1.7 Literature survey on Bismuth layered structure ferroelectrics:

During last 40 years, a tremendous increase in the investigation of piezoelectric and ferroelectric materials has taken place. The cross-fertilization between research in piezoelectric/ferroelectric films and semiconductor materials and technology proved to be the key for the takeoff of integrated ferroelectrics. During the last 20 years, advances in this field are made at an ever increasing pace.

Jae-Sun Kim reported [41] the low temperature processing of SBT films by a modified RF magnetron sputtering process. The metallic bismuth existing in SBT films had a bad influence on the ferroelectric properties as it is easily evaporated by the second annealing at 650°C. The $Sr_{0.7}Bi_{2.7}Ta_{2.0}O_9$ films prepared by the second annealing at 650°C shows a well-saturated hysteresis loop and remanent polarization P_r of $12\mu C/cm^2$, a coercive field (E_c) of 45 kV/cm at an applied voltage of 5V. The leakage current density of the second annealed SBT films was about $4.0x10^{-8}A/cm^2$ at 100kV/cm. The films showed fatigue-free characteristics up to $2.0x10^{10}$ switching cycles under 5V bipolar pulses.

The effects of concentration and distribution of defects controlled by quenching and doping of higher valence cations on the ferroelectric properties of dense $Bi_4Ti_4O_{12}$ ceramics are investigated by Yuji Noguchi et.al [42]. $SrBi_4Ti_4O_{15}$ single crystals are grown, and their dielectric and ferroelectric properties are investigated along the a(b) axis and c-axis, separately [43]. The dielectric permittivity at 1 MHz is 1900 along the a(b) axis at the Curie temperature of 520°C. This is ten times higher than that along the c- axis. With respect to the ferroelectricity, the saturated remanent polarization is $29\mu C/cm^2$ and the saturated coercive field is 26kV/cm along the a(b) axis under an electric field of 59kV/cm, and ferroelectricity is not observed along the c-axis.

Kazumi Kato et.al [44] reported that $Ca_2Bi_4Ti_5O_{18}$ (CBTi) thin films crystallized on $Pt(111)/TiO_x/SiO_2/Si(100)$ substrates showed random orientation, a columnar structure, and P-E hysteresis loops. The remanent polarization and coercive field of CBTi thin films annealed at 650°C at 12V are $4.7\mu C/cm^2$ and 111kV/cm respectively. The dielectric constant and loss factor at 100 kHz are 330 and 0.028 respectively.

Masaru Yokosuka [45] synthesized solid solution ceramics of the $Bi_4Sr_xMn_yCa_{1-(x+y)}Ti_4O_{15}$ system by the conventional ceramic process. Piezoelectric properties are greatly improved as the appropriate amount of Mn ion is introduced into the Ca ion-site.

Electromechanical coupling factor $k_p = 0.064$, piezoelectric constant $d_{33} = 21$pC/N for the composition with x = 0.5 and y =0.1 and mechanical quality factor Qm = 3250 for the composition with x = 0.5 and y = 0.05.

Two site substitutions in $Sr_{1-x}Bi_{4-x}Ti_{4-x}Ta_xO_{15}$, where Sr^{2+} and Ta $^{5+}$ are substituted for Bi^{3+} and Ti^{4+} respectively, is done by Minglei Zhao et.at [46]. This two site substituted system showed the largest piezoelectric coefficient, electromechanical coupling factor and excellent pyroelectric response compared to the single site substituted Bi-layered structure materials.

A strong low frequency dielectric dispersion associated with an impedance relaxation has been found to exist in $SrBi_2Nb_2O_9$ ceramics in the temperature range 573-823K by Harihar et.al [47]. The Z" of the AC complex impedance showed two distinct slopes in the frequency range 100Hz -1MHz suggesting the existence of two dispersion mechanisms.

Ho Jung Chang et.al [48] compared $Bi_{4-x}La_xTi_3O_{12}$ (BLT, x= 0.67- 0.7) ferroelectric thin films coated on c-Al_2O_3/Si and a-Al_2O_3/Si substrates by sol-gel method annealed at 650 and 700^{o}C for 30min under an air ambient. The BLT film coated on c-Al_2O_3/Si substrate showed better crystallization and electrical properties and also denser microstructure with granular grain shapes when compared with the one coated on a-Al_2O_3/Si substrate (which gave island grain shapes) under the same process conditions.

Xue J.M et.al [49] reported the formation and ferroelectric properties of $0.6SrBi_2Nb_2O_9 - 0.4BiFeO_3$ thin films with layered perovskite structure on Pt/Si substrate, which are prepared via sol-gel route. When measured at an applied field of 225kV/cm, this system showed remanent polarization ($2P_r$) of 5.5µC/cm^2 and coercive field of 65.6kV/cm respectively, together with a leakage current density of 5x10^{-8}A/cm^2 at 125kV/cm. Its dielectric constant and dielectric loss factor measured at the frequency of 1MHz and at room temperature are ~130 and ~2% respectively.

Won-Jeong Kim et.al [50] prepared $Bi_{3.4}Eu_{0.6}Ti_3O_{12}$ thin films by sol-gel spin coating process. The $2P_r$ and $2E_c$ values at an electric field of 400kV/cm are 38 µC/cm^2 and 309kV/cm respectively. This $2P_r$ value is larger than that of lanthanum-substituted thin films and comparable with $2P_r$ values of the niobium substituted thin films.

Thin films and dense ceramic samples of $Pr_{0.14}Sr_{0.8}Bi_{2.1}Ta_2O_9$ are prepared by Atsushi Kitamura et.al [51]. The Rietveld analysis of powder X-ray diffraction and X-ray photoelectron spectroscopy revealed that praseodymium ions are substituted at the Sr site as Pr^{3+} with Sr vacancies. The thin film with the thickness of 280nm showed smaller $2P_r$

of 15µC/cm^2 than dense ceramics (its $2P_r$ = 21µC/cm^2). On other hand, the $2E_c$ for the films is about 52kV/cm at E_m of 185 kV/cm and the $2P_r$ is 5.4µC/cm^2 at E_m of 37kV/cm.

S T Zhang [52] reported that the Bi-layered SBTi films were deposited on (001) $SrTiO_3$ (STO) single-crystal substrates and $Pt/TiO_2/SiO_2/Si$ substrates by PLD. XRD and HRTEM measurements confirmed that the SBTi is really a single-phase material. The epitaxial relation of the SBTi film on STO was established to be (001) SBTi‖(001)STO, [110]SBTi‖[010]STO, by SEAD and XRD φ-scans. A special kind of atomic shift along the c-axis and a local slight tilting of TiO_6 octahedra, which is intrinsic to Bi-layered oxides, were observed and discussed. The dielectric constant of the epitaxial SBTi films was measured to be 211 ± 20 by evanescent microwave probe (EMP) at 100KHz. Based on the existence of single-phase SBTi, electrical properties of polycrystalline SBTi films with Pt bottom and top electrodes were examined. The measured P_r and E_c were 4.1 μC/cm^2 and 75 kV/cm respectively. Excellent fatigue-free property up to 2.2×10^9 switching cycles was experimentally shown. The dielectric constant and loss tangent of the polycrystalline films were 363 and 0.04 at 100 kHz.

The dielectric and electrical property study together with the microstructure of $SrBi_2Nb_2O_9$ modified by substituting Ca for Sr and La for Bi is done by Rizwana et.al [53]. There is a decrease in the lattice parameters because of this cationic substitution. Also reduction in conduction is found with La doping.

Tomer M.S et.al [54] synthesized $Bi_{4-x}M_xTi_3O_{12}$ (M= Nd, Sm) for different compositions by sol-gel process and thin films are deposited by spin coating on Pt substrate. Nd and Sm substituted thin films showed ferroelectric polarization >50 µC/cm^2 and 18µC/cm^2 respectively, and leakage current densities about 10^{-7}A/cm^2. Large polarization in rare earth substituted $Bi_4Ti_3O_{12}$ layered perovskites is attributed to the dipole formation, which tilts TiO_6 octahedra to Bi_2O_2 interlayer of the unit cell.

Sang Su Kim et.al [55] successfully deposited Lead-free bismuth layered perovskite ferroelectric $Bi_{3.4}Gd_{0.6}Ti_3O_{12}$ (BGT) thin films on $Pt(111)/Ti/SiO_2/Si$ and P-type Si(100) substrates by sol-gel spin coating process followed by annealing. The remanent polarization ($2P_r$) and coercive field ($2E_c$) of metal-ferroelectric-metal capacitor using a BGT film deposited on $Pt(111)/Ti/SiO_2/Si$ by annealing at 700°C are 49.6µC/cm^2 and 249kV/cm respectively. The BGT film exhibits a good fatigue resistance up to 1.45×10^{10} switching cycles at a frequency of 1MHz.

Rizwana et.al [56] has done the detailed impedance studies on $Sr_{0.2}Na_{0.4}Bi_4Ti_4O_{15}$ sample prepared by sol-gel method using Pechini process. Grain and grain boundary effects are separated in the frequency domain of the impedance spectrum. Analysis of AC conductivity data on this sample shows that high conduction occurs because of hopping of charge carriers between the trap sites.

Hong Cheng Liu and Biao Wang et.al reported [57] the Gadolinium-substituted bismuth titanate ($Bi_{4-x}Gd_xTi_3O_{12}$, BGT) thin films fabricated on the (111)Pt/Ti/SiO_2/(100)Si. The appropriate Gd-substitution content x value was 0.75 to realize the largest remanent polarization. The P–E hysteresis loop of the films revealed the remanent polarization $2P_r$ value was 15.4 μC/cm^2 and the coercive field E_c value was 54.17 kV/cm.

A.Z. Simoes et.al [58] reported strontium bismuth titanate ($SrBi_4Ti_4O_{15}$) thin films deposited on (111) Pt/Ti/SiO_2/Si substrates by spin coating from the polymeric precursor method. SBTi films annealed in static air possess a higher dielectric permittivity and lower leakage current than the films annealed in oxygen atmosphere due to differences in grain size, crystallinity and structural defects. The hysteresis loop for the films annealed in static air was not saturated even at 350 kV/cm, the remnant polarization (P_r) was only 5.4μC/cm^{2}and the coercive field (E_c) was as high as 80 kV/cm. The leakage current density at 1.0 V for the film annealed in oxygen atmosphere is 9.0 x 10^{-8} A/cm^2 while for the films annealed in static air is 3.0x 10^{-9} A/cm^2.

Chia-Erh Liu et.al [59] reported the $Bi_4Ti_3O_{12}$ thin films deposited using rf sputtering on dip-coated (110) - oriented $La_2Ti_2O_7$ buffer layers. A preferred orientation (001) of $Bi_4Ti_3O_{12}$ thin films are obtained after annealing at a temperature lower than 650^{o}C. Such a buffer layer exhibiting crystallographic features equivalent to a (110) perovskite plane was used to favor the preferential growth of $Bi_{3.25}La_{0.75}Ti_3O_{12}$ layers along *a* axis.

Suhua Fan et.al [60] reported that the predominantly (100)-oriented $Ca_{0.4}Sr_{0.6}Bi_4Ti_4O_{15}$ ($C_{0.4}S_{0.6}$BTi) thin films were prepared on Pt(111)/Ti/SiO_2/Si substrates by a sol-gel method at annealing temperatures ranging from 650 to 850°C. The growth mode of the predominantly (100)-oriented $C_{0.4}S_{0.6}$BTi thin films fabricated by the sequential layer annealing was discussed based on the structure evolution with the annealing temperature. The remnant polarization and coercive field of the $C_{0.4}S_{0.6}$BTi film annealed at 800°C are 16.1μC/cm^2 and 85 kV/cm, respectively. No evident fatigue can be observed after 10^9 switching cycles.

P. Sarah [61] reported that the Ho^{3+} doped SBT ceramics (SBHT) were prepared by solid state reaction method. The Curie point increased gradually from 535^{o}C for SBT to 630^{o}C for SBHT-0.06. Dielectric constants were found to gradually increase with an increasing concentration of holmium, reaching maxima at 4% Ho^{3+}. These samples maybe suitable for piezoelectric applications at higher temperatures. In addition, SBHT-x (x = 0, 0.02, 0.04 and 0.06) ceramics exhibited good electromechanical coupling coefficients (0.61) and piezoelectric constants (17pC/N), which have considerable potential for use in piezoelectric applications at high temperatures.

Sugandha et.al [62] reported that the nanocrystalline $Sr_{0.8}Bi_{2.2}Ta_2O_9$ has been successfully synthesized by the mechanical activation process. The synthesized samples exhibit single phase layered perovskite structure. Transmission electron microscope image and electron diffraction patterns reveal that the particle size in the specimen milled for 20 h reduces to nano range. As the milling duration has increased dielectric constant increases considerably whereas the Curie temperature decreases slightly. $Sr_{0.8}Bi_{2.2}Ta_2O_9$ compound prepared by above technique for 20 h milling exhibited highest dielectric constant (860), dc resistivity and lowest dielectric loss.

1.8 Introduction to SBTi ($SrBi_4Ti_4O_{15}$) material:

Bismuth layered structure ferroelectric (BLSF) compounds of Aurivillius family are found to be interesting because of their crystallographic nature. The structure of these compounds consists of bismuth oxide layers, interleaved with pseudo perovskite blocks of $[A_{m-1}B_mO_{3m+1}]^{2-}$ along the crystallographic c axis [63-64]. The 12-coordinated A site can be occupied by cations such as La^{3+}, Bi^{3+}, Ba^{2+}, Sr^{2+}, Pb^{2+}, Ca^{2+} etc. while the octahedra-coordinated B site can be occupied by W^{6+}, Nb^{5+}, Ti^{4+}, Fe^{3+} etc. The number of octahedra along the c axis between two neighbouring $(Bi_2O_2)^{2+}$ layers is indicated by *m*. For most of these compounds, the unit cell is orthorhombic below the Curie temperature and tetragonal otherwise. Polar axis of BLSFs compounds lies in the a-b plane in which octahedra extend continuously. The two-dimensional configuration leads to electrical anisotropies in single crystals and textured ceramics. The value of *m* in BLSFs is closely related to its ferroelectric properties and structure instabilities. An increase in *m* in certain compound systems led to an increase in the lattice parameters in a-b plane and an increase in strain energy originating from the size mismatch between the bismuth oxide layers and perovskite layers which will make the structure unstable [65]. The reason may be the existence of maximum number if *m* in BLSFs. Some of the layered ferroelectric materials and their properties are listed in table 1.

Compound	T_c (^oC)	Piezoelectric Coefficient (pC/N)	Dielectric constant	Reference No.
Bi_3TiNbO_9	940	5	100	101
$SrBi_2Nb_2O_9$	440	10	190	70
$BaBi_4Ti_4O_{15}$	395	12	150	71
$CaBi_4Ti_4O_{15}$	787	14	90	71
$SrBi_4Ti_4O_{15}$	530	20	180	74-75
$PbBi_4Ti_4O_{15}$	570	26	240	102

Table 1: Properties of some layered bismuth titanate materials at room temperature

According to table 1, Bi_3TiNbO_9 would be suitable for very high temperature piezoelectric applications, however its piezoelectric sensitivity is quite low. $Bi_4Ti_3O_{12}$ has also a quite elevated ferroelectric phase transition with higher piezoelectric sensitivity, but due to elevated electrical conductivity [66], it should be doped in order to be used. $SrBi_4Ti_4O_{15}$ can have ferroelectricity only up to 530^{o}C and its piezoelectric sensitivity is slightly smaller compared to $Bi_4Ti_3O_{12}$. However, its room temperature piezoelectric properties are very interesting as reported by Damjanovic [67].

Among bismuth layer structured ferroelectrics, $SrBi_2Ta_2O_9$ (SBTa) (n = 2) and lanthanide doped $Bi_4Ti_3O_{12}$ (BTO) (n = 3) have been extensively studied so far [68-69]. Recently, much attention has been paid on four-layer perovskite BLSFs (n = 4) such as $SrBi_4Ti_4O_{15}$ (SBTi), $CaBi_4Ti_4O_{15}$ (CBTi) and $BaBi_4Ti_4O_{15}$ (BBTi) due to their good ferroelectric and fatigue properties [70-71].

Bismuth-layer-structured ferroelectrics are considered to be candidate materials for lead-free ferroelectrics [72]. The higher order structures such as $SrBi_4Ti_4O_{15}$ (SBTi) films may have larger remanent polarization, due to the increased number of perovskite units generating ferroelectric properties. SBTi, which has a crystalline structure similar to BIT, is another typical layer-structured ferroelectric (m=4) [73]. It's high Curie temperature (T_c = 520°C) makes it useful over a wide temperature range [74-75]. However, the $2P_r$ of SBTi thin films is lower (6.2 μC/cm^2, compared to bulk ceramic 13 μC/cm^2) [76-77], and the fatigue endurance property deteriorates with the increase of switching pulse width.

$SrBi_4Ti_4O_{15}$ is a four layered compound of BLSFs. The pseudo-perovskite block $(SrBi_2Ti_4O_{13})^{2-}$ is sandwiched between $(Bi_2O_2)^{2+}$ layers. One Sr ion and two Bi ions compose the A-site of SBTi blocks. The distance between the two bismuth ions is along the a-axis and is half the lattice parameter *a* [78]. The structure of $SrBi_4Ti_4O_{15}$ is shown in figure 3. The BO_6 octahedra in SBTi are TiO_6. The chains of O-Ti-O in the TiO_6 octahedra are connected with each other in the plane perpendicular to c-axis, but those along the c-axis are interrupted by the presence of $(Bi_2O_2)^{2+}$ layers. For $SrBi_4Ti_4O_{15}$ system, the molecular formula can be written in the form $Bi_2O_3.4\ [(Bi_{2/4}Sr_{1/4}O_{1/4})\ TiO_3]$. It obviously belongs to the perovskite structure of ABO_3 type. The properties of these materials basically depend upon the TiO_6 octahedra. In case of compounds, Ti is at the centre of these compounds. It is well known that the octahedra in these compounds are not perfect octahedra but shows a rotation or tilt about c-axis [79].

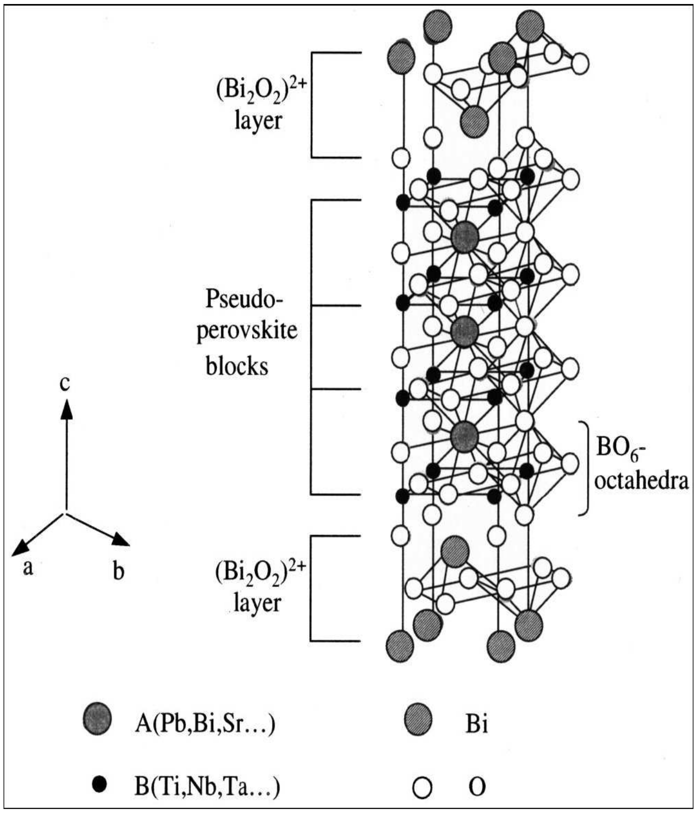

Fig.3. Schematic drawing showing the crystal structure of $SrBi_4Ti_4O_{15}$

The polar axis in these materials is a-axis and the polar components are confined within pseudo blocks along the crystallographic a-b planes. The number of Bi^{3+} ions in the pseudo perovskite layer is two times as much as that of Sr^{2+} ions, in addition to its much large polarizability. These factors probably make Bi^{3+} ions to have large influence on the ferroelectricity in this system. From the principle of minimum strain energy in phase transitions, the oxygen octahedra within the crystals with Bi-layer structure consisting of even perovskite layer, such as $SrBi_4Ti_4O_{15}$, will exhibit a zig-zag orientation along the c-axis with mirror symmetry. As the cation with small ionic radius is used to replace the cation Sr^{2+} at A-site, the angle of zig-zag would become small, that is the ratio of a polarization axis to non-polarization axis would be large. This fact has been proved by the measurements of crystal lattice parameters [80].

1.9 Motivation and objective of present work

Among the bismuth layered structure ferroelectrics, $SrBi_4Ti_4O_{15}$ (SBTi) attracted much attention due to their potential use in high-temperature piezoelectric devices and ferroelectric random access memories because of their relatively high Curie temperature (T_c), lead free composition and excellent fatigue endurance property [81-83]. Above literature tells that the composition ($SrBi_4Ti_4O_{15}$) of bulk ceramic materials is extensively studied in case of dielectric properties at low frequency range, ferroelectric and piezoelectric properties [41, 43, 55, 56, and 58]. For industrial use of SBTi ceramics, it is essential to develop and characterize a tailored microstructure. Grain size, density and development of domain structure are extremely sensitive on even small variations in the processing techniques. The interest on the mechanical properties of Pb-based ceramics has increased in recent times compared to electrical properties [84-85]. Until recently very less focus was on the mechanical properties of layered structure ferroelectric ceramics. The investigation on the mechanical properties of the bismuth layered-structure ferroelectric ceramics is of practical importance in various situations and particularly for the design of piezoelectric devices. On the other hand, these ceramic samples faces problem with bismuth volatization at higher temperatures which lead to non-stoichiometry in the ceramic samples [86-87]. Alternative approach is required to control the grain growth and Bi-volatization. The microwave heating presents a potential economical sintering process with shortened processing time for the materials. This method is expected to overcome many of the shortcomings of the conventional sintering process [88]. Thus, there has been considerable interest in microwave heating for the synthesis and processing of materials. Microwave processing has gained worldwide acceptance as a novel method for heating and sintering a variety of materials, as it offers many advantages in terms of enhanced diffusion processes, reduced energy consumption and processing cost, very rapid heating rates and significantly reduced processing times, decreased sintering temperatures, improved physical and mechanical properties, simplicity, unique properties, new materials and products and lower environmental hazards, which are not observed in conventional processes [89-92]. Another important observation is that rare-earth ion substitution in various bismuth layered structures such as strontium bismuth titanate (SBTi), bismuth titanate (BiT), etc. has been studied to improve its dielectric, ferroelectric, and mechanical properties [93-95].

Among published results, fatigue free and good ferroelectric properties of SBTi films have been successfully deposited on platinized substrates Pt/TiO2/SiO2/Si by various methods, such as sol–gel techniques (CSD) [48, 49, 54], MOCVD [51,57] and recently by PLD [52]. PLD is known as a technique of choice for congruent deposition of complex materials like SBTi, BLT and BST etc. However, until now, PLD suffers from weak uniformity control on large areas, leading to intrinsic difficulties to extrapolate towards industrial applications [96]. Among deposition methods, sputtering enables to reach good uniformity over large areas and is thus widely used for industrial and large scale applications. Published results on reactive sputtering of complex oxides revealed that, after optimization of experimental conditions, thin films of complex oxides can be obtained with a well-controlled stoichiometry [96-98] and even improved dielectric properties, while controlling energy of involved species. To our knowledge, few literature are available on rf sputtering of layered structure ferroelectric thin films. This indicates that obtaining stoichiometric layered structure (where m = 3, 4, 5) thin films using rf sputtering is a challenging task. In sputtering process, the desired film property can be achieved by carefully controlling the processing parameters, which include power density, working/sputtering gas pressure, sputter gas mixture i.e the Ar:O_2 ratio (oxygen mixing percentage), substrate to target distance and deposition/post deposition annealing temperature. The exact OMP i.e Ar:O_2 ratio used in sputtering atmosphere during deposition of oxides is always the subject of detailed optimization in any oxide system. There is a tradeoff between the ideal level of energetic impingement in oxygen containing plasma and the risk of anion deficiency that can occur under low OMP. Another important observation is that most of the previous works are on SBTi thin films deposited on Pt/Ti/SiO_2/Si substrates and single crystal substrates such as Lanthanum aluminate, Si and MgO [99-100]. However, for non-military applications, the high cost of conventional processed ferroelectric thin films and devices are a limiting factor. Alternatively, SBTi thin films deposited directly on fused silica substrates can prove to be cost effective. There are no reports of SBTi thin films grown directly on fused silica substrates. If the films are grown on fused silica substrates, it opens the possibility for integrating SBTi with existing Si technology by using thick insulating layer of SiO_2. Hence a study on the growth of SBTi films on SiO_2 as the substrates and the impact of thermal treatments on them is an important prelude to develop process technologies for SBTi thin films with Si technology. Consequently in this study the effect of thermal treatment on the growth of SBTi thin films on fused silica substrates and their properties are key objectives. But obtaining crystalline SBTi thin films on amorphous substrates pose a great challenge. To achieve this objective, it is important to study the influence of processing and post processing conditions on the structural and microstructural features using various tools like, optical, dielectric and Raman spectra for successful implementation.

On the other hand, the investigation on the mechanical properties of the bismuth layered-structure ferroelectric thin films is of practical importance in various situations and particularly for the design of piezoelectric devices. The importance of thin films have now increased with their potential for application in MEMS devices where they can be used not only for sensing and actuation but also for energy harvesting even at elevated temperatures. The reliable and reproducible measurements of the dielectric properties of these thin films at microwave frequencies have become an essential requirement of these research objectives because of the unique insight that this data can provide. Microwave characterization techniques for bulk materials are a well developed field but for thin films it is still challenging. There are few studies on the microwave dielectric properties of thin films even though it is quite important both in terms of application and academic point of view. There are reports on low frequency dielectric properties for layered structure ferroelectric thin films but there are no reports about the microwave dielectric properties which emphasize the relevance of the present thesis work.

The major objectives of the present thesis work are:

1. Synthesize of $SrBi_4Ti_4O_{15}$ single phase ceramic samples and study their properties such as microstructural, dielectic, ferroelectric and mechanical properties.
2. Study the effect of ball milling of SBTi ceramic powders in order to reduce the grain size and control the grain growth. Comparison study was made for conventional and microwave sintered ceramic samples.

3. Preparation of Sm-substituted (rare-earth) SBTi ceramic samples and to study their structural and microstructural characteristics, dielectic properties at low frequency and microwave frequency range, Raman spectra, relaxor behavior, ferroelectric properties and mechanical properties.
4. Fabrication of 2” dia ceramic targets of SBTi ($SrBi_4Ti_4O_{15}$) and Sm-substituted SBTi ($SrBi_{3.25}Sm_{0.75}Ti_4O_{15}$) suitable for sputter deposition process.
5. Preparation of stoichiometric SBTi thin films using rf sputtering by optimizing the deposition parameters.
6. Study the effect of crystallization of films on amorphous substrates using conventional and microwave annealing processes.
7. Study the effect of deposition/post deposition annealing on the structural, microstructural, optical, mechanical, microwave dielectric properties and Raman spectra of films.
8. Establish the influence of OMP on stoichiometry of the deposited films and their properties.
9. Study the effect of in-situ deposition of SBTi and Sm-substituted SBTi films and their properties such as structural, microstructural, Raman spectra, Optical, mechanical and microwave dielectric properties.

References:

1. Nava Setter, J.Eur.Cer.Soc., **21**, 1279-1293 (2001).
2. N. SETTER and R. WASER, J.Act.Mater., 48, 151-178 (2000).
3. Malti Goel, J.Cer.International., **30**, 1147-1154 (2004).
4. B.Jaffe, W.R Cook, and H.Jaffe, “Piezoelectric ceramics”, John Wiley and Sons, New York, USA (1960).
5. J.C.Burfoot and G.W.Taylor, “Polar dielectrics and their applications” University of California Press, Los Angeles, CA (1979).
6. J.Valasek, J.Phys.Rev., **15,** 537 (1920).
7. G.Busch and P.Scherrer, Naturwissenschaften., **23**, 737 (1935).
8. B.M.Wul, I.M.Goldman, Dokl.Akad.Nauk SSSR, **46**, 154 (1945).
9. A.J.Moulson and J.M. Herbet, Electroceramics: Materials, Properties, applications” Chapman and hall, New York, USA (1997).
10. W.G.Cady, Piezoelectricity, Dover Publications, New York (1962).
11. M.Deri, Ferroelectric ceramics, Gordon and Breach, New York (1969).
12. M.E.Lines and A.M Glass, Principles and applications of ferroelectric and related materials, Clarendon Press, Oxford (1977).
13. T.Mitsiu, I.Tatsuzaki and E.Nakamura “An introduction to the physics of ferroelectrics”, Gorden and Breach Science Publishers, Ltd., London (1976).
14. D.Damjanovic, “Ferroelectric, dielectric and piezoelectric properties of ferroelectric thin films and ceramics”, J. Rep.Prog.Phy., **61**, 1267-1324 (1998).
15. Jaffe B, Jaffe H, Cook WR, Piezoelectric ceramics, 1st edn. Academic Press, London (1971).
16. Haertling GH,Buchanan RC, Piezoelectric and electro-optic ceramics in ceramic materials for electronics, 2nd edn. Marcel Dekkar, Newyork (1991).
17. Uchino K, mater.Res.Bull, **18**, 42 (1993).
18. Newnhan RE, Functional composites for sensors and actuators, Pennsylvania Academy of Science,PA, USA (1998).
19. Sahoo B, Jaleel VA, Panda PK, J.Mat Sci and Engg B., **126**, 80 (2006).
20. Sahoo B, Panda PK, J.Mat Sci., **42**, 4270 (2007).
21. Yugong W, Zhang H, Zhang Y, Jinyi M, Daohua X, J.Mat Sci., **38**, 987 (2003).
22. Ringgaard E, Wuritzer T, J.Eur. Cer. Soc., **25,** 2701 (2005).
23. Takenaka T, Nagata H, J.Eur. Cer. Soc., **25**, 2693 (2005).
24. Yi L, Moon K, Wong CP, J. Science., **308**, 1419 (2005).

25. Shimamura K, Takeda H, Kohno T, Fakuda T, J. Cryt. Growth., **163**, 388 (1996).
26. G.Goodman, J.Ame.Cer.Soc., **36**, 368 (1958).
27. M.H.Francombe and B.Lewis, J.Acta.Cryst., **11,** 696 (1958).
28. Somolenskii G.A, Isupov V.A and Agranovskaya, Soviet. Phy.Solid. State., **3**, 651 (1959).
29. Somolenskii G.A, Isupov V.A and Agranovskaya, J.Soviet. Phy.Solid. State., **3**, 149 (1961).
30. Subbarao E.C, J.Chem.Phy., **34**, 695 (1961).
31. Subbarao E.C, J.Ame.Cer.Soc., **45**, 166 (1962).
32. Ikegami S and Ueda E., Jap.J.Appl.Phy., **13**, 1572 (1974).
33. Tadashi Takenka and koichiro Sakata, Jpn.J.Appl.Phy., **19**, 31-39 (1980).
34. Kaoru Miura and Masahiro Tanaka, Jpn.J.Appl.Phy., **37,** 2554-2558, (1998).
35. In-Sook Yi, and Masaru Miyayama, Jpn.J.Appl.Phy., **36**, 1321-1324 (1997).
36. Scott J.F and Paz de Araujo C.A., Science., **246**, 1400 (1989).
37. Paz de Araujo C.A, Cuchiaro J.D, McMillan L.D, Scott M.C et.al, Nature (London) **374**, 627 (1995).
38. Desu S.B and Vijay D.P., J.Mat.Scie and Engg. B., **99**, 75 (1995).
39. Sang-Ouk Ryu, PhD thesis,Virginia University, (1999).
40. Newnham R.E, Wolfe R.W and Dorrian J.F, J.Mat.Res.Bull., **6**, 1029 (1971).
41. Jae-Sun Kim, Cheol-Hoon Yang, Soon-Gil Yoon, et.al., J.Appl.Surf.Sci., **140**, 150-155 (1999).
42. Yuji Noguchi, Ichiro Miwa, Yu Goshima and Masaru Miyayama, Jpn.J.Appl.Phy., **39**, 1259-1262 (2000).
43. Hiroshi Irie and Masaru Miyayama, J.Appl.Letts., **79**, 251-253 (2001).
44. Kazumi Kato, Kazuyuki Suzuki, Desheng Fu et.al., Jpn.J.Appl.Phy., **41**, 2110-2114 (2002).
45. Masaru Yokosuka., Jon.J.Appl.Phy., **41**, 7123-7126 (2002).
46. Minglei Zhao, Chunlei Wang, Weilie Zhong, et.al., Jpn.J.Appl.Phy., **41**, 1455-1458 (2002).
47. Harihar B, Venkataramana and Varma K.B.R., J.Phys & Chem of Solids., **64,** 2105-2115 (2003).
48. Ho Jung Chang, Sun Hwan, Hyeongtag Jeon, et.al., J.Thin. Solid Films., **443**, 136-143 (2003).

49. Xue J.M, Sim M.H, Ezhilvalavan, Zhou Z.H et.al., J.Thin Solid films., **460**, 1-6 (2004).
50. Won-Jeong Kim, Sang Su Kim, Kiwan Jang, et.al., J.Crys.Growth., **262**, 327-333 (2004).
51. Atsushi Kitmura, Yuji Noguchi and Masaru Miyayama, J.Matt.Letts., **58**, 1815-1818 (2004).
52. S.T.Zhang, Y.F Chen. H.P Sun et.al., J.Phys:Conds.Matter., **15,** 1223 (2003).
53. Rizwana, Sarah P and Kumar G.S., Indian.J.Phy., **79**, 267-272 (2005).
54. Tomer MS, Melgarejo R.E and Singh S.P., J.Microelectronics., **36**, 574-577 (2005).
55. Sang Su Kim, Ji Cheul Bae and Won-Jeong Kim, J.Cryst.Growth., **274**, 394-401(2005).
56. Rizwana, Radhakrishna T, James A.R and Sarah P, J.Cryst.Res.Tech., **42,** 699-706 (2007).
57. HongCheng Liu, Biao Wang, Rui Wang, et.al., J.Matt.Letts., 61, 2457-2459 (2007).
58. A.Z.Simoes, M.A.Ramirez, C.S.Riccardi, et.al., J.Solid State Sciences., **10**, 1951-1957 (2008).
59. Chia-Erth Liu, Mireille Richard-Plout, Marie-Paule, et.al., J.Eur.Cer.Soc., **29**, 1977-1985 (2009).
60. Sahua Fan, Jing Xu, Guangda Hu,et.al., J.Key Engineering Materials., **368**, 100-102 (2008).
61. P.Sarah. J.Proce.Engg., **10**, 2684-2689 (2011).
62. Sugandha and A.K Jha, J.Mater.Characterization., **65**, 126-132 (2012).
63. Aurivillius B, Ark.Kemi., **1**, 499 (1949).
64. Aurivillius B, Ark Kemi., **2**, 519 (1950).
65. Kikuchi T, J.Mater.Res.Bull., **14**, 1561 (1979).
66. H.S.Shulman, Piezoelectric Bismuth Titanate Ceramics for high temperature applications, EPFL (1997).
67. D.Damjanovic, M.Demartin, H.S.Shulman and N.Setter., Int.Con.Solid-State Sensors and Actuators IX, Stockholm (1995).
68. H.Tabata, H.Tanaka, T.Kawai, Jpn.J.Appl.Phy.Lett., **34**, 5146 (1995).
69. T.Li, Y.Zhu,S.B.Desu, C.H.Peng, Appl.Phy.Lett., **68**, 616 (1996).

70. Haoshuang Gu, Kaihong Zheng, Kansong Chen, Wanqiang Cao, et.al., J.Matt.Letts., **59**, 912-915 (2005).
71. Xi Wang, Pilong Wang, Guangda Hu, Jing Yan, et.al., J.Mat.Sci.Electron, **19**, 1031-1034 (2008).
72. D.Wu, A.Li, T.Zhu, Z.Liu, N.Ming, J.Appl.Phy., **88**, 5941 (2000).
73. M.Hirose, T.Suzuki, H.Oka,K.Itakura., Jpn.J.Appl.Phys., **38**, 5561 (1999).
74. H.Lrie, M.Miyayama, J.Appl.Phy.Lett., **77**, 251 (2001).
75. Hui Sun, Hong Fang, Wei-Dong Zhou et.al., J.Int.Ferro., **79**, 203-210 (2006).
76. A.Z Simoes, E.C.Aguiar, C.S.Riccardi et.al., J.Alloys.Comps., **447**, 85-89 (2009).
77. K.Kato,K.Suzuki, K.Nishizawa, T.Miki, J.Appl.Phys., **89**, 5088 (2001).
78. Yuji Noguchi, Hiroyuki Ahimizu, Masaru Miyayama, Kenichi Oilawa et.al., Jpn.J.Appl.Phys., **40**, 5812-5815 (2001).
79. Kim S.K, Miyayama M. and Yanagida H., J.Mater.Res.Bull., **31**, 121 (1996).
80. Subbarao E.C., J.Ame.Cer.Soc., **45**, 166 (1962).
81. P.Sarah, J.Procedia Engineering., **10**, 2684-2689 (2011).
82. Hong Fang, HuiSun, JunZhu et.al, J.Appl.Phy.D. **39**, 5300-5304 (2006).
83. A.Z.Simoes, M.A.Ramirez,C.S Riccardi et.al., J.Mat.Chararization., **59**, 675-680 (2008).
84. R.A Pferner, G.THurn and F.Aldinger, J.Mat.Chem and Phys., **61**, 24-30 (1999).
85. K.Uchino,R.W Cahn, P.Haasen et.al., A compressive Treatment, Vol **11**, 637-677 (1994).
86. Chung-Hsin Lu, Chung-Han Wu, J.Eur.Cer.Soc., **22**, 707-714 (2002).
87. S.O Brien, G.M Crean, L.Cakare, M.Kosec, J.Appl.Surf.Sci., **252**, 4497-4501 (2006).
88. R.R.Menezes, P.M.Souto, R.H.G.A. Kiminami, J.Mat.Proce.Tech., **190**, 223 – 229 (2007).
89. P.Yadoji, R.Peelamedu, D.Agarwal, R.Roy, J.Mat Sci and Engg B., 269-278 (2003).
90. D.Agarwal, Jour.Mats Edu., **19**, 49-58 (1999).
91. D.E Clark, D.C Folz, J.K.West, J.Mat.Sci and Engg A., **287**, 153-158 (2000).
92. C.Leonelli, P.Veronrsi, L.Denti, A.Gatto, et.al., J.Mat Proce.Tech., **190,** 489-496 (2007).
93. S. Ezhilvalavan, J.M. Xue, John Wang, J.Mater. Chem. and Phys.,**75,** 50 (2002).

94. Y. Wu, Mike J. Forbess, S. Seraji, S.J. Limmer, T.P. Chou, G. Cao, J. Appl. Phys. **89**, 5647 (2001).
95. K.Stanly Jacob, R.Satheesh and R.Ratheesh, J.Mat.Res.Bull., **44**, 2022-2026 (2009).
96. TAKESHI MASUDA, Yusuke Miyaguchi,KouKnou Chu, et.al., J.Int.Ferro. **31**, 23-34 (2000).
97. Huei-Mei Tsai, Pang Lin and Tseung-Yuen et.al., J.Appl.Phy., **85**, 1095 (1999).
98. Shi-Jian Liu, Xiang-Bin Zeng and Jun-Hao, J.Microelectronic., **35**, 601 (2004).
99. A.Z Simoes, M.A Ramirez, C.S Riccardi et.al., J.Solid state Sciences., 1-7 (2008).
100. W.Chang, J.Horwitz, A.Carter, J.Pond et.al., J.Appl.Phys.Lett., **74,** 1033 (1999).
101. D. Damjanovic. J.Solid State Mater. Sci., **3**(5):469–473 (1998).
102. Takenaka, T and K.Sakata, J.Appl.Phy., **55**, (4) 1092 (1984).

Chapter 2

Material processing and characterization techniques used for bulk ceramics and thin films of SBTi system

Chapter 2

Material processing and characterization techniques used for bulk ceramics and thin films of SBTi system

This chapter describes the preparation and characterization techniques used for both bulk ceramic samples and thin films of SBTi and Sm-substituted SBTi system.

2.1 Preparation and characterization techniques for bulk ceramic samples

This section deals with the preparation and characterization techniques used for bulk ceramic samples. Since this material has to be characterized for its dielectric, ferroelectric and mechanical properties, it has to be prepared in a regular geometry with the highest possible densification. This being a ceramic oxide material, the available methods for its preparation are (a) Solid-state reaction method (or ceramic method) (b) Chemical methods and (c) Mechanical methods [1-3]. Of these, the method used for bulk SBTi preparation in this study is the solid-state reaction method.

2.1.1 Solid-state reaction method

Ceramics are polycrystalline materials having fine crystalline grains and imperfections like grain boundaries, impurities segregated in the grains and grain boundaries, pores etc. Since they are, in general, brittle refractories, shaping them and densifying them without cracks and deformation is a challenge. The solid-state reaction method is used for forming SBTi and Sm-substituted SBTi compositions from the reagents. The shaping and densification are separate processes, which are described in subsequent sections.

The conventional solid state reaction method involves the following steps: (a) Uniform mixing of the initial reagents (b) Phase formation of the required compound at a high temperature, which is called the calcination stage. The main disadvantage of this method is it needs high processing temperatures in order to achieve the best properties and this process increases the particle size. But cost effectiveness and simplicity are the major advantages of this process.

2.1.2 Stoichiometric weighing of reagents

Raw materials Bi_2O_3, Sm_2O_3, $SrCO_3$ and TiO_2, of purity >99.9% from Aldrich Chemicals were used as the initial reagents to achieve control over impurities in the product and to maintain reproducibility in properties. An electronic balance (Adair & Dutt technologies, Model GR-120) is used to weigh the reagents, which has an accuracy of up to 0.001mg.

2.1.3 Uniform mixing of reagents

The individual reagents are to be mixed uniformly in order to increase the point of contact between the reagents, which will act as product layer formation centers. Therefore, the initial stoichiometric reagents must be mixed uniformly with a suitable mixing medium. The powders were mixed at150rpm for about 2 hours using a planetary ball mill (Retsch PM 100) in a zirconia jar with different diameters of zirconia balls (5 and 20mm). Deionized water was used as the mixing medium.

2.1.4 Calcination stage

The solid-state, diffusion controlled chemical reaction between the initial reactants resulting in the desired phase formation is called calcination. It is the intermediate heat treatment at lower temperatures prior to sintering. Calcination could involve chemical decomposition reactions in which solid reactants are heated to produce a new solid phase and remove the gases which are commonly associated with the initial metal oxide compounds such as carbonates, hydroxides, nitrides, sulphates, acetates and other metal salts. The parameters of the calcination stage such as temperature, duration of heating and atmosphere are important factors influencing shrinkage during sintering. In the present case, the reagents being oxides, they do not undergo any decomposition. All the mixed reagents used in the present study were calcined at 750°C to form the required composition and the phase formation is confirmed by XRD.

2.1.5 Particle size reduction:

The particle size reduction (milling) of the complex oxides after the calcination stage is important to homogenize the formed phase. It is well known that the smaller initial particle size reduces the sintering temperature and enhances the density of the ceramics. Planetary ball mills are generally used for milling the powders to achieve particle size reduction.

There are several processing variables that determine the finite size of the particles after milling process, such as type of mill, vial, milling speed, milling time; type, shape and size of milling medium and ball to powder ratio [4]. In the present study, Retsch PM 100 planetary ball mill was employed to achieve the initial stoichiometric mixing before the calcination and to reduce the particle size of the calcined powders (300rpm for 5, 10, 15 & 20 hours). Zirconia vials and different diameters of spherical (5 & 20mm) zirconia balls are used. All the processing conditions were optimized to achieve finite particle sizes. In the milling process, the particle experiences the mechanical stresses at their contact points due to compression, shear with the milling medium or with other particles. The mechanical stresses lead elastic and inelastic deformation. If the stress is exceeding the ultimate strength of the particle, it will result in fracture of the particles. The mechanical energy supplied to the particle is used not only to create new surfaces but also to produce physical changes in the particle.

2.1.6 Uniaxial pressing

After reducing the particle size of the calcined powder, the fine powder is compacted into cylindrical specimens (green pellets) by uniaxial pressing. The compaction of the powder should be done slowly to facilitate the escape of the entrapped air. To make the green pellets of the ceramic powder, a rigid die, which is rust free, is needed. To make the inner walls of the die smooth, stearic acid is used as an internal lubricant. The pressure gradient on the die as a function of the distance from the upper punch is given by the equation

$$P_x = P_a e^{\frac{-4\mu KL}{D}} \tag{2.1}$$

where, μ is the coefficient of friction, P_a is the applied pressure, L is the length and D is the diameter of the die and K is a constant [5].

2.1.7 Solid-state sintering

In ceramics, porosity is an important parameter which governs many of its properties. For maximizing properties such as the dielectric constant, mechanical strength, translucency and thermal conductivity, it is desirable to eliminate as much of porosity as possible. The purpose of sintering is the reduction of porosity in the compact. The development of microstructure and densification during sintering is a direct consequence of mass transport through several possible paths and one of these paths is usually predominant at any given stage of sintering [5]. In the present study all the samples were sintered at a temperature range of 1180°C-1250°C for 2 hrs.

2.1.8 Microwave sintering

The particular requirements of sintering phenomena make this process one of the most challenging applications for microwave processing. These requirements often include the following parameters: high temperature, high heating rates, uniform temperature, and equivalent thermal history throughout the specimen. The process of sintering materials in the conventional method involves mixing of material powder with additives, milling, and pressing into green parts followed by sintering with direct heating of green pellets in a refractory type electrical resistance furnace, induction furnace or fossil fuel furnace. These furnaces use a large number of expensive heating elements, fuel and refractory materials to achieve and maintain the high temperature for a long time. Moreover, it consumes much electrical energy, much fuel, and longer time. These kinds of furnaces with indirect heating are called conventional sintering furnace and the heating mechanism is called conventional heating. Microwave heating however provide direct heating of the green body. The fundamental difference between microwave sintering and conventional sintering is in the heating mechanism. For conventional sintering, heat is generated by heating elements and transferred to samples via radiation, conduction, and convection. In microwave sintering, however, the materials themselves absorb microwave energy, and then transform it into heat within their bodies [6, 7]. The microwave heating presents a potential economical sintering process with shortened processing time for the materials. This method is expected to overcome many of the shortcomings of the conventional sintering process [8]. Thus, there has been considerable interest in microwave heating for the synthesis and processing of materials. Microwave processing has gained worldwide acceptance as a novel method for heating and sintering of a variety of materials, as it offers many advantages in terms of enhanced diffusion processes, reduced energy consumption and processing cost, very rapid heating rates and significantly reduced processing times, decreased sintering temperatures, improved physical and mechanical properties, simplicity, unique properties, new materials and products as well as lower environmental hazards, which are not observed in conventional processes [9-12].

In the present study, microwave sintering was conducted using a 1.3 KW, 2.45 GHz multimode microwave furnace. For the runs in the multimode microwave furnace, the samples were loaded in the cavity in an insulating package, with appropriate amount of silicon carbide used as a microwave susceptor around the sample to preheat the sample and to compensate the heat loss from the sample. This configuration makes the microwave heating more uniform. The temperature of the sample was monitored with IR pyrometer. In the present study all the samples were sintered at a temperature range of 1100°C-1150°C for 45min with ramping rate 40°C/min. Photograph of microwave system is shown in figure 2.1.

Figure 2.1: Photograph of microwave sintering system

2.2 Characterization techniques used for the bulk compositions

a. Powder X-Ray Diffraction
b. Scanning Electron Microscopy
c. Low frequency dielectric characterization
d. P-E loop hysteresis studies
e. Mechanical characterization
d. Microwave characterization

2.2.1 X-ray diffraction

Powder X-Ray Diffraction is a powerful non-destructive method for determining a range of physical and chemical characteristics of materials. The applications include the type and quantities of phases present in the sample (phase analysis), the crystallographic unit cell and crystal structure, crystallographic texture, crystallite size, macro-stress and micro-strain and also electron radial distribution functions [13].

In the present work, an X-ray diffractometer was used to characterize the samples with Cu Kα (1.5406 Å) radiation, using a Philips PW 1830 diffractometer. Calibration using a Si standard was done to account for the instrumental line broadening and the value was approximately 0.15^{o}.

2.2.2 Scanning Electron Microscopy

In Scanning Electron Microscope (SEM), electrons are thermionically emitted from a tungsten cathode and are accelerated towards an anode. Alternatively, electrons can be emitted via field emission (FE). The electron beam, which typically has an energy ranging from a few hundred eV to 50 keV, is focused by one or two condenser lenses into a beam with a very fine focal spot size of 1 nm to 5 nm. The beam passes through pairs of scanning coils in the objective lens, which deflect the beam in a raster fashion over a rectangular area of the sample surface. Through these scattering events, the primary electron beam effectively spreads and fills a teardrop-shaped volume, known as the interaction volume, extending from less than 100 nm to around 5 µm into the surface. Interactions in this region lead to the subsequent emission of electrons, which are then detected to produce an image. X-rays, which are also produced by the interaction of electrons with the sample, may also be detected in an SEM equipped for energy-dispersive X-ray spectroscopy or wavelength dispersive X-ray spectroscopy. The most common imaging mode monitors low energy (<50 eV) secondary electrons. Due to their low energy, these electrons originate within a few nanometers from the surface. The electrons are detected by a scintillator-photomultiplier device and the resulting signal is rendered into a two-dimensional intensity distribution that can be viewed and saved as a digital image. This process relies on a raster-scanned primary beam.

The brightness of the signal depends on the number of secondary electrons reaching the detector. If the beam enters the sample perpendicular to the surface, then the activated region is uniform about the axis of the beam and a certain number of electrons "escape" from within the sample. As the angle of incidence increases, the "escape" distance of one side of the beam will decrease, and more secondary electrons will be emitted. Thus, steep surfaces and edges tend to be brighter than flat surfaces, which result in images with a well-defined, three-dimensional appearance. Using this technique, resolutions less than 1 nm is possible [14]. In addition to the secondary electrons, backscattered electrons can also be detected. Backscattered electrons may be used to detect contrast between areas with different chemical compositions.

2.2.3 Low frequency dielectric measurements

The low frequency dielectric spectroscopy is emerging as an important material characterization tool [15]. The low frequency dielectric measurements are unequaled in their ability to dynamically monitor the many chemical and physical processes important in the investigation of new materials such as polymerization, phase transition and diffusion. The conventional way for making the low frequency measurement (below<10MHz) of the dielectric properties of solids is to place a sample between closely spaced parallel conducting plates and monitor the AC equivalent capacitance $C_{(\omega)}$ and the dissipation factor (also known as the loss tangent) $D_{(\omega)}$ of the resulting capacitor [16]. Normally one has to design the plate spacing to be much less than the plate size as this serves to minimize the effect of the fringing field. The material under test in the parallel plate configuration can be modeled as a frequency dependent capacitance $C_{(\omega)}$ in parallel with a frequency independent resistor $R_{0.}$ The DC resistance R_0 takes into account processes such as tunneling of thermally activated hopping and ionic conduction. The capacitance $C_{(\omega)}$ is proportional to the complex dielectric function of the material under test which can be represented as follows,

$$\varepsilon_{(\omega)} = \varepsilon_{r(\omega)} - j\varepsilon''_{(\omega)} \tag{2.2}$$

The capacitance $C_{(\omega)}$ can be measured by a typical capacitance bridge which can be used to calculate the real part of the complex dielectric function $\varepsilon'_{(\omega).}$

$$C_{(\omega)} = \frac{\varepsilon_{r(\omega)}\varepsilon_0 A}{d} \tag{2.3}$$

Here, A is the cross section area of the capacitor, d is the separation between the plates and ε_0 =8.85 x10^{-12}F/m is the absolute permittivity of free space. The other measured quantity, the dissipation factor (the loss tangent) given by

$$D_{(\omega)} = \frac{\varepsilon''_{(\omega)}}{\varepsilon_{r(\omega)}} + \frac{d}{\omega \cdot \varepsilon_0 \cdot \varepsilon'_{(\omega)} \cdot A \cdot R_0} \tag{2.4}$$

and can be used to extract the imaginary part of the dielectric function $\varepsilon''_{(\omega)}$.


2006 9 29

Figure 2.2 Photograph of the temperature dependent dielectric measurement set up.

For the dielectric measurement, silver paint was applied on both sides of the pressed pellets and cured. The samples were fixed in the spring loaded sample holder attached to a heating and cooling chamber. The parallel capacitance (C) and the dissipation factor (D) for all the samples were measured using an Agilent 4294A impedance analyzer in the frequency range of 100Hz-1MHz in a temperature range of 50 to 600°C with a Lab –Equip temperature control unit. The temperature and measurement process were controlled electronically by a lab made programme using lab view software. The temperature was maintained with an accuracy of ±1°C. A photograph of this measurement set up is shown in figure 2.2.

2.2.4 P-E hysteresis loop studies:

The ferroelectric behavior in a given material can be identified by polarization reversal, i.e. ferroelectric switching. The polarization reversal can be studied by recording the hysteresis loop (P Vs E loop) using Sawyer-Tower circuit (Lines and Glass -1977).

The hysteresis loop shown in figure 2.3 gives information about the remanent polarization which a material possesses when the applied field is zero. The length OA represents the remanent polarization (P_r) and OB represents the minimum filed required to reverse the direction of polarization i.e coercive field (E_c). The shape of the loop is affected by number of factors such as dimensions of the sample, thermal and electrical treatment of the sample, humidity, and temperature and crystal symmetry.

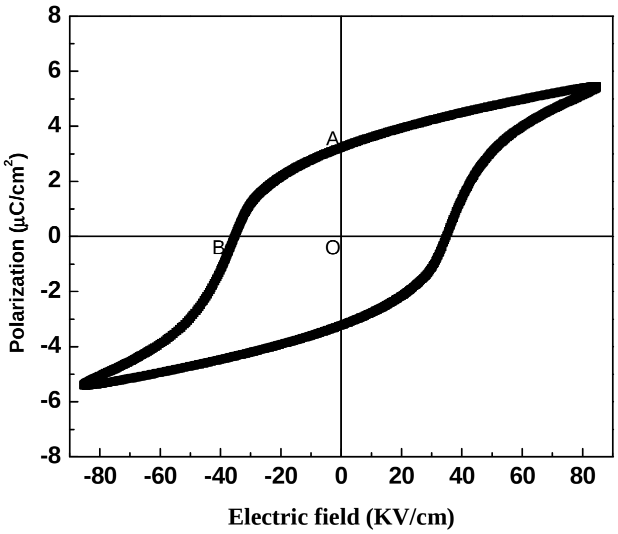

Figure 2.3: Schematic diagram of P-E hysteresis loop

In the present study, the polarization Vs electric field loop is traced by using a computer controlled standardized ferroelectric test system with maximum operating voltage limit of 4KV built using the Sawyer-Tower circuit.

2.2.5 Mechanical properties:

Nanoindentation is a simple method that consists essentially of touching the materials of interest whose mechanical properties such as elastic modulus and hardness are unknown with another material whose properties are known. Nanoindentation is a simple indentation test in which the length scale of the penetration is measured in nanometers rather than in microns or millimeters, the later is common in conventional hardness tests. To measure the mechanical properties of our bulk ceramics samples, we have used Hysitron Triboindenter, USA. Schematic diagram of an intrumented indentation system is shown in figure 2.4.

The Hysitron Triboindenter is a multi load range indentation/scratch test system designed for measuring hardness, elastic modulus and dynamic viscoelastic properties of thin films, bulk materials and MEMS/NEMS type fabricated structures. This indenter provides quantitative testing capabilities with both normal and lateral force loading configurations. The transducer used in the indenter is based on a three-plate capacitor technology providing simultaneous actuation and measurement of force and displacement with a range of 1nN to 10mN. Due to the compact size of the sensor /actuator, it can be interfaced with piezo electric scanner that provides very precise X,Y and Z controlled indenter tip positioning. Piezoelectric scanner is able to raster the tip over a specimen, while a feedback loop controls the Z axis height of the scanner to maintain a constant force between the indenter tip and specimen. The Z-axis movement of the scanner is then calibrated to a height to obtain a three dimensional topographical image. Using in-situ imaging, it is possible to place indentations on a surface with a precision of ±10nm. This allows us to make repeatable penetration below 10nm depth. Photograph of the nanoindenter is shown in figure 2.4.

Figure 2.4: Photograph of nanoindentation system

2.2.6 Microwave dielectric measurements

The microwave dielectric properties of the bulk ceramic samples were characterized using PNA network analyzer (Agilent E8361C) at the frequency range of

8.2 GHz-12.4 GHz. We have used transmission/reflection method to measure complex permittivity. For microwave measurements the samples were prepared in rectangular disks (10.2 mm x 22.9 mm) to fit in the X- band wave-guide (WR-90). The measurements were carried out by inserting the samples inside the X-band waveguide. In order to determine the complex permittivity at X-band frequencies (8.2-12.4 GHz), the complex scattering parameters were measured using the PNA network analyzer. The real and imaginary parts of complex permittivity ($\varepsilon_r = \varepsilon' - j\varepsilon''$) were calculated from the measured scattering parameters.

Scattering parameters were measured for the waveguide partially filled with the dielectric samples of two different lengths. The complex propagation constant γ can be expressed as

$$\gamma = \alpha + j\beta \tag{2.5}$$

Where α is the attenuation factor and β is the phase factor. For a TE_{10} mode rectangular waveguide, we can relate the real part of the sample permittivity ε_s' to the phase constant β [17, 18] by

$$\varepsilon_s' = \frac{\beta^2 + \left(\frac{\pi}{a}\right)^2}{\omega^2 \mu_0 \varepsilon_0} \tag{2.6}$$

Where a is the longer width of the wave guide, ω is the angular frequency, μ_0 and ε_0 are the free space permeability and permittivity.

In the same manner, the imaginary part of the permittivity ε_s'' can be related to the attenuation α by [17, 18]

$$\varepsilon_s'' = \frac{2\alpha\varepsilon_s'}{k}\sqrt{1 - \left(\frac{\lambda}{2a}\right)^2} \tag{2.7}$$

Where

$$\lambda = \frac{2\pi}{k}$$

$$k = \omega\sqrt{\mu_0 \varepsilon_0 \varepsilon_s'}$$

2.3 Processing of SBTi thin films

2.3.1 Target preparation

Highly dense targets of SBTi and Sm-SBTi ceramics were prepared by the conventional solid state reactions. Starting powders of $SrCO_{3,}$ $Sm_2O_{3,}$ Bi_2O_3 and TiO_2 (99.9% purity, Aldrich chemicals) were used for the solid state reactions. The details of the solid state reaction process are given in section 2.1.1. The calcined powders were then pressed into pellets in a hydraulic press using a 57mm die. The pressed pellets were placed on a platinum foil in a furnace for the final sintering process. The targets were sintered at 1150°C for two hours. Finally both the surface of the pellets were ground, cleaned and polished to ensure a proper surface finish. Polishing the surface was necessary to improve the sputtering properties. The crystallographic structure of the targets was determined from the X-ray diffraction (XRD) pattern.

2.3.2 Preparation of thin films:

RF magnetron sputtering has been widely accepted as one of the versatile technique for the deposition of high quality ferroelectric thin films by many research groups [19-22]. It has been employed for the following reasons: any solid material (metals, insulators and semiconductors) can be sputtered, complex compounds can be sputtered stoichiometrically, use of low gas pressure during processing possible, appreciable rates of deposition and uniform deposition over large area is possible. The parameters such as the RF power density, substrate temperature, sputter gas mixture i.e the Ar/O_2 ratio, working/sputtering gas pressure and target to substrate distance can be controlled to influence the material properties of the sputtered films. It is important to note that the control over parameters that influence the physical properties of the growing film in general are greater during the deposition process (in-situ) than after deposition (ex-situ). Therefore, in-situ treatment of thin films is always preferred over ex-situ treatments. However, some of the thermal processes in the device fabrication procedure could amount to an ex-situ annealing treatment as far as the film is concerned. Hence, it is important to study the influence of each type of processing (in-situ as well as ex-situ) and optimize for the ideal device behavior.

The RF magnetron sputtering system used in this work is shown in figure 2.5. It consists of a 30 liter stainless steel vacuum chamber which houses 3 cathodes and a substrate holder. Out of the 3 cathodes, 2 are RF powered while the third one is dc powered. One of the RF powered cathodes was used for the deposition of SBTi thin films. During deposition of thin films, the vacuum chamber is continuously cooled by flow of water.

Figure 2.5: RF sputtering system used in the present study to deposit the thin films

As mentioned earlier, parameters such as RF power density, substrate temperature, OMP, working gas pressure, substrate to target distance, type of substrate used and post deposition annealing treatments influence the properties of the sputtered films. Optimization of all the sputtering conditions for the best material properties in the deposited film can be cumbersome and time consuming. Initial studies indicated that the power densities <2.5 W/cm^2 resulted in very low rates of sputtering where as power density > 3.5 W/cm^2 resulted in target damage. Hence, the power density was fixed at 3 W/cm^2. The substrate to target distance was fixed at 5cms because higher distances led to lower deposition rates and lower distances led to damage of the vacuum seals near the cathode due to heat from the substrate heater at higher temperatures. The working pressure was fixed at 20mTorr.

2.4 Physical characterization of thin films

Several analytical techniques were used to determine the material properties of the rf sputtered SBTi thin films. The deposited films were characterized for its thickness, structure, composition and microstructure using the techniques such as surface profilometer, X-ray diffraction (XRD), Energy dispersive analysis of X-rays (EDAX) from FE-SEM, and atomic force microscopy (AFM). A brief introduction about each of these experimental techniques is given below.

2.4.1 Thickness measurement

Profilometry is a fast and simple method to measure film thickness. It works by gently dragging a mechanical stylus across the sample surface. The stylus is placed in contact with the substrate, and then gently dragged along the surface over the film. The vertical deflection over the step measures the change in height and the trace is recorded. To measure the thickness of thin films used in this work, a part of the substrate was covered with a piece of scotch tape during film deposition. After the thin film deposition, the tape was removed and the film thickness was then measured over the step. For the experiments in this work, an Ambios XP-1 stylus profiler was used and the instrument was calibrated using standard substrates.

2.4.2 Composition analysis

The composition analysis of the films was carried out using the energy dispersive analysis of X-rays (EDAX) method in a field emission scanning electron microscope. EDAX uses the technique in which emitted X-rays from the target sample are resolved in energy electronically by pulse height analysis instead of resolving them in wavelength by a diffraction crystal. In FE-SEM, the incident electron beam on the sample generates X-rays due to the interaction between the high-energy electron beam and the sample [23]. The generated X-rays consist of the characteristic wavelengths of the elements constituting the sample. Each emitted x-ray photon adds a count to the appropriate channel of a multi-channel analyzer (MCA), which reproduces the x-ray spectrum. Intensity of each peak is related to the concentration of that element in the sample. The intensity of the x-ray signal depends on the beam current, accelerating voltage, geometry of the system and concentration of the constituent elements. Analysis of an acquired spectrum comprises accounting for spurious peaks and identifying the elements present in the sample. The energy of the characteristic X-rays is given by Mosley's law

$$E \cong C_1(Z - C_2) \tag{2.8}$$

where, Z is the atomic number, C_1 and C_2 are constants. Thus, from the energy location of the peaks in the spectrum, software routines sort out the elements present by comparison with the tabulated characteristic energy values. For EDAX measurements the sample was prepared by coating a thin conducting layer of gold by sputtering to avoid charge buildup.

2.4.3 Structural analysis

The crystallographic structures of the films were determined from the obtained X-Ray Diffraction (XRD) patterns. In the present work, two types of X-ray diffractometer were used to characterize the samples. One was with Co Kα (λ=1.7889Å) radiation in a wide angled powder X-ray diffractometer (INEL Model CPS120) equipped with a position sensitive detector and the other one is Bruker D8 X-ray diffractometer with CuKα radiation of 1.5046 Å wavelength. Calibration using a Si standard was done to account for the instrumental line broadening and the value was approximately 0.15^o. The patterns were compared with standard patterns (JCPDS) and the phases and degree of crystallinity were determined. A slow scanning rate of 1°/min was used to extract data for the measurement of grain size from peak full width at half maxima (FWHM). These results gave important information regarding the film microstructure and changes in the grain size with thermal treatment. The crystallite size was determined from the Scherrer equation [24] given by

$$C_{size} = (k \times \lambda)/(\beta \times \cos\theta) \tag{2.9}$$

where, k is a constant (normally 0.94 for Scherrer method, λ is the wavelength, β is the FWHM of the peak and θ is the angular position of the peak. The determined grain sizes were compared for films grown under various processing conditions.

2.4.4 Atomic force microscope

The schematic diagram of atomic force microscope is shown in figure 2.6. The microstructures of the deposited films were obtained using an AFM. The AFM consists of a microscale cantilever with a sharp tip (probe) at its end that is used to scan the specimen surface. The cantilever is typically made of silicon or silicon nitride with a tip radius of curvature of the order of nanometers. When the tip is brought into the proximity of a sample surface, forces between the tip and the sample lead to a deflection of the cantilever according to Hooke's law. Depending on the situation, forces that are measured in the AFM include mechanical contact force, Vander Waals forces, capillary forces, chemical bonding, electrostatic forces, magnetic forces etc. Typically, the deflection is measured using a laser spot reflected from the top of the cantilever into an array of photodiodes. The AFM can be operated in a number of modes, depending on the application. The primary modes of operation are static (contact) mode and dynamic mode [25].

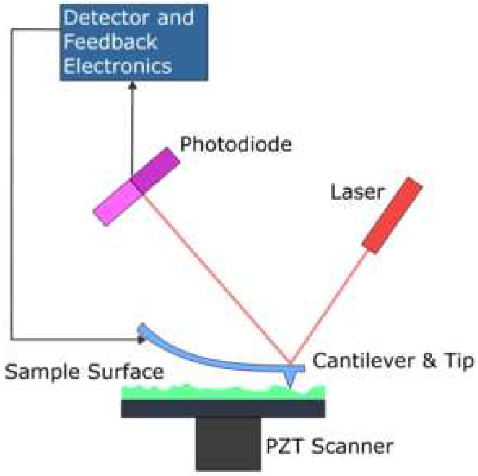

Figure 2.6 Schematic diagram of an atomic force microscope.

In the static mode of operation, the static tip deflection is used as the feedback signal. Since the measurement of a static signal is prone to noise and drift, low stiffness cantilevers are used to boost the deflection signal. However, close to the surface of the sample, attractive forces can be quite strong, causing the tip to 'snap-in' to the surface. Thus static mode AFM is almost always done in contact where the overall force is repulsive. Consequently, this technique is typically called 'contact mode'. In the contact mode, the force between the tip and the surface is kept constant during scanning by maintaining a constant deflection through feedback circuitry. In the dynamic mode, the cantilever is externally oscillated at or close to its resonance frequency. The oscillation amplitude, phase and resonance frequency are modified by tip-sample interaction forces. These changes in oscillation with respect to the external reference oscillation provide information about the sample's characteristics. Schemes for dynamic mode operation include frequency modulation and the more common amplitude modulation. In frequency modulation, changes in the oscillation frequency provide information about tip-sample interactions. Frequency can be measured with very high sensitivity and thus the frequency modulation mode allows for the use of very stiff cantilevers. In this work, the microstructure of the oxide films was imaged in an atomic force microscope in the dynamic force mode [Model SPA400 of SII Inc, Japan).

2.5 Optical properties

The spectral transmission and Raman scattering studies of these thin films were carried out to have an understanding about the optical and local structural characteristics. The optical characteristics such as transmission, refractive index, and the lattice dynamics for the thin films were estimated. The details of these measurement techniques are given below.

2.5.1 Spectral transmittance studies

The optical constants of the thin films were calculated using the envelope technique [26]. The spectral transmission characteristics in the wavelength range 190-1500 nm were measured using a JASCO V570 UV-VIS-NIR spectrophotometer. A typical optical transmittance spectrum of a thin film is shown in figure 2.7.

If light is incident on a film of refractive index n, coated onto a substrate of refractive index s, then at the air-film, film-substrate and substrate-air interfaces part of the incident light is reflected and part of it is transmitted. Since the reflected and transmitted beams originate from a single source, the beams exhibit interference effects. The condition for constructive interference in such a case is given as

$$2nd = m\lambda \tag{2.10}$$

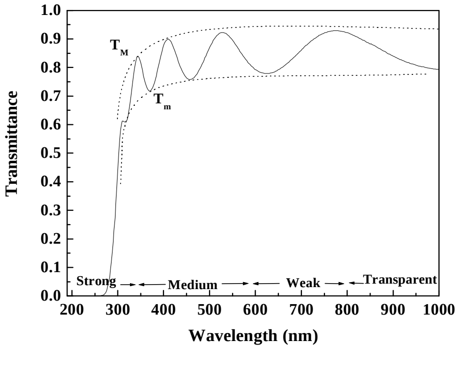

Figure 2.7 Typical transmittance spectrum of the film.

where, n is the refractive index of the film at a wavelength λ and m is the order of interference, d is the thickness of the film that can be calculated from the derived values of refractive indices.

In general, the transmission T, is given by the expression

$$T = \frac{Ax}{B - Cx\cos\phi + Dx^2} \tag{2.11}$$

where, $A=16n^2s$, $B=(n+1)^3 (n+s)^2$, $C=2(n^2-1) (n^2-s^2)$, $D= (n-1)^3 (n-s^2)$

$\phi=4\pi nd/ \lambda$

For such a system, at the points of constructive and destructive interference, the transmittance T_M and T_m, respectively are given as

$$T_M = \frac{Ax}{B - Cx + Dx^2} \tag{2.12}$$

and $$T_m = \frac{Ax}{B + Cx + Dx^2} \tag{2.13}$$

For simplicity, it can be assumed that the transmission is a continuously varying function of the wavelength which can be approximated by drawing the envelope across the spectrum, connecting all the maximas and minimas as shown in figure 2.6.

$$n = \left[N + \left(N^2 - n_s^2\right)^{1/2}\right]^{1/2} \tag{2.14}$$

Here, N is a constant, n_s is the refractive index of the substrate used and n_s is the refractive index of the film at that particular wavelength.

$$N = 2S\frac{T_M - T_m}{T_M T_m} + \frac{S^2 + 1}{2} \tag{2.15}$$

Adding the reciprocals of equations 2.13 and 2.14 yields

$$\frac{2T_M T_m}{T_M + T_m} = \frac{Ax}{B + Dx^2} \tag{2.16}$$

and, solving for x we get,

$$x = \frac{F - F\left[F^2 - \left(n^2 - 1\right)\left(n^2 - s^4\right)\right]^{1/2}}{\left(n-1\right)^3 \left(n - s^2\right)} \tag{2.17}$$

where,

$$F = \frac{8n^2 s}{T_i} \tag{2.18}$$

and

$$\mathrm{T_i} = \frac{2T_M T_m}{T_M + T_m} \tag{2.19}$$

where, T_M is the maximum of the transmission on the envelope at a wavelength λ and T_m is the minimum of the transmission on the envelope at the same wavelength. The T_M and T_m at each wavelength can therefore be read off from the envelope and the refractive index can be derived at each wavelength.

From the equation of constructive interference, it can be seen that for two successive maxima occurring at λ_1 and λ_2, the equation becomes

$$2n_1 d = m_1 \lambda \tag{2.20}$$

and

$$2n_2 d = m_2 \lambda \tag{2.21}$$

Also $\left|m_1 - m_2\right| = 1$

Therefore,

$$d = \frac{\lambda_1 \lambda_2}{2\left(n_1 \lambda_2 - n_2 \lambda_1\right)} \tag{2.22}$$

In the strong absorption region, from Beer-Lambert’s law given by

$$I = I_o \exp(-\alpha, d) \tag{2.23}$$

where, I_o is the incident intensity =1, I is the intensity at a given wavelength λ, d is the thickness of the film and α is the absorption coefficient in cm^{-1}.

Since d is known from previous calculations and I is a measured quantity (i.e. transmission at a wavelength λ), the absorption coefficient α can be calculated. Knowing α from the expression for the so-called “Tauc gap”, the fundamental absorption edge of the material can be determined. The expression for the Tauc gap is given as

$$\alpha h\upsilon = Const.(h\upsilon - E_g)^2 \tag{2.24}$$

The X- Intercept of the extrapolation of the linear region in a plot of $(\alpha h\nu)^{1/2}$ vs. hν will give the value of band gap E_g. The error associated with the measurement of k, n and d is ±0.005, ±0.02 and ±10nm respectively.

2.5.2 Raman spectroscopy

This is a versatile non-destructive technique to monitor short-range structural properties of materials. In this characterization method, a monochromatic light beam is directed at the sample, and the reflected light is measured in the frequency domain. To this end, lasers of different wavelengths may be employed. This technique is based on the physical principle of inelastic scattering by molecular vibrations. Two kinds of light scattering are possible when a photon with $h\nu_0$ energy collides with a molecule. Rayleigh scattering occurs when the photon frequency remains constant after the collision. It corresponds to an elastic collision. On the other hand, Raman scattering is a process generated by inelastic collisions. The molecule is initially in the fundamental state of vibration and it is then promoted to an excited state due to the absorption of the photon energy. The emitted radiation has an energy of $h(\nu_0 - \nu_\nu)$ which defines the radiation detected in a Raman spectrum.

Raman measurements were performed at room temperature with a Lab-Ram spectrometer with a magnification of 50 and resolution of 2cm^{-1}, using the 514.5nm line of argon ion laser as the excitation source.

2.5.3 Microwave dielectric properties:

The microwave dielectric properties of thin films were determined using an Agilent 8722ES vector network analyzer by employing the Split Post Dielectric Resonator (SPDR) based measurement technique. This is a non-destructive and accurate technique for measuring the complex permittivity of dielectric substrates and thin films at a spot frequency [27]. For thin films deposited on a substrate, the frequency shift due to the film has to be separated from the overall frequency shift of the film substrate combine. For this purpose one has to measure the resonance frequency and quality factor (f_{01},Q_{01}) of the empty resonator and do the same (f_s,Q_s) with the substrate. After the film deposition, the resonance frequency and quality factor of the ($f_{sf,}Q_{sf}$) substrate coated with the film have to be measured again. Picture of the SPDR measurement set up with the schematic diagram is shown in figure 2.8

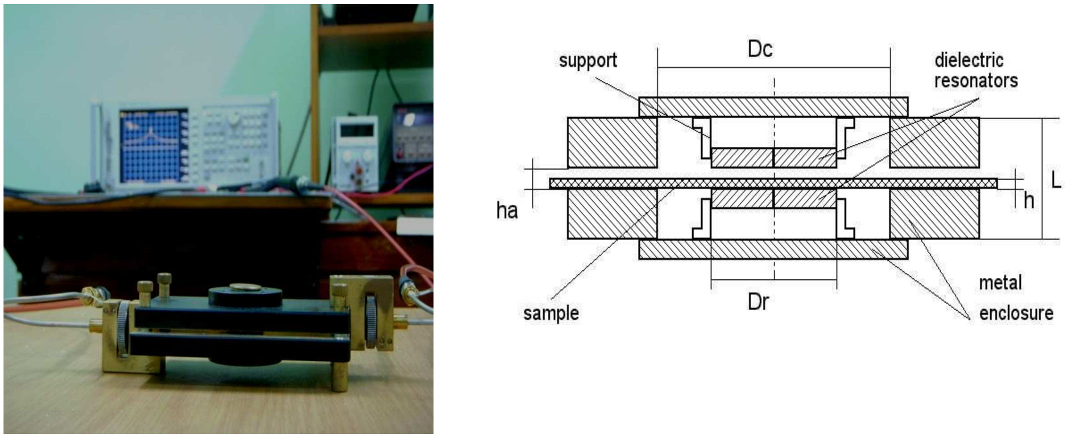

Figure 2.8 Picture of the SPDR measurement set up with the schematic diagram of an SPDR.

The SPDR typically operates in the $TE_{01\delta}$ mode that has only an azimuthal electric field component, so that the electric field remains continuous on the dielectric interfaces [28]. This makes the system insensitive to the presence of air gaps perpendicular to the z-axis of the fixture. The real part of permittivity ε_r of the sample is found on the basis of the measurements of the resonant frequencies and thickness of the sample as an iterative solution to equation 2.25.

$$\varepsilon' = \frac{1+(f_0 - f_s)}{hf_0 K_s(\varepsilon', h)} \tag{2.25}$$

Here, h is the sample thickness, f_0 is the resonance frequency of the SPDR with the substrate, and f_s is the resonance frequency of the SPDR with the film coated substrate. K_s is a function of the sample's dielectric constant, ε_r and thickness h. Since K_s is a slowly varying function of ε_r and h, the iterations using the formula (2.25) converge rapidly.
The loss tangent is computed using the equation (2.25)

$$\tan\delta = \frac{Q^{-1} - Q_{DR}^{-1} - Q_c^{-1}}{p_{es}} \tag{2.26}$$

where, Q is the unloaded Q factor of the SPDR containing the dielectric sample and p_{es} is the electrical energy-filling factor of the sample. Qc is the Q factor depending on the metallic conduction losses of the SPDR containing the dielectric sample and Q_{DR} is the Q-factor depending on the dielectric losses in the dielectric resonators.

References:

1. M.N.Rahaman, (Marcel Dekker, Inc, New York) 2003.
2. D.Seagal, (Cambridge University Press, Cambridge) 1991.
3. R.E.Carter, J.Chem.Phys., **34**, 2010 (1961).
4. C.Suryanarayana, Progress in Mater. Sci., **46**, 1 (2001).
5. S-J. Kang (Elsevier, Amesterdam) 2002.
6. O.P Thakur, Chandra Prakash, D.K Agrawal., J. Mat Lett., **56,** 970-973 (2002).
7. D.E.Clark, W.H.Sutton, Annu.Rev.Mat Sci., **26**, 299-331 (1996).
8. R.R.Menezes, P.M.Souto, R.H.G.A. Kiminami, J.Mat.Proce.Tech., **190**, 223 – 229 (2007).
9. P.Yadoji, R.Peelamedu, D.Agarwal, R.Roy, J.Mat Sci and Engg B., 269-278 (2003).
10. D.Agarwal, Jour.Mats Edu., **19**, 49-58 (1999).
11. D.E Clark, D.C Folz, J.K.West, J.Mat.Sci and Engg A., **287**, 153-158 (2000).
12. C.Leonelli, P.Veronrsi, L.Denti, A.Gatto, et.al., J.Mat Proce.Tech., **190**, 489-496 (2007).
13. D.Cullity, (Addision-Wesley, Reading, MA) 1956.
14. K.D.Vernon,-Parry, III-Vs Review., **13**,40 (2000).
15. Helene Hagerstrom, Katarina Edgman, Maria Stromme, J.Pharma.Sci., **92**, 1869 (2003).
16. J.F.Johnson and R.H.Cole, J.Ame.Che.Soc., **73**, 4536 (1951).
17. R.Marks, IEEE Trans.Microwave Theory Tech., **39,** 1205 (1991).
18. S.Ramo, etc “Fields and waves in communication electronics” *New York:Wiley* (1984).
19. P.Padmini, T.R.Taylor, M.J Leferve, A.S.Nagra, J.Appl.Phy.Lett., 75 (1999) 3186.
20. J.Im, O.Auciello and S.K Streiffer, J.Thin Solid films., **413**, 243 (2002).
21. A. Roy, A. Dhar, and S. K. Ray, J.Appl.Phy., **104**, 064103 (2008).
22. K. Sugibuchi. Y. Kurogi. and N. Endo, J.Appl.Phy., **46**, 2877 (1975).
23. www.Edax.com
24. A.L.Patterson, Phy.Rev, **56,** 978 (1939).
25. www.nanoscience.com/education/AFM
26. R.Swanpoel, J.Phy.E: Sci.Instru., **16,** 1214 (1983).

27. J.Krupa, R.N. Clarke O, C.Rochard and A.P Gregory, XIII Int.Conf.MIKON. 2000, Wroclaw, Poland, **305** (2000).
28. J.Krupa, A.P.Gregory, O, C.Rochard and R.N. Clarke, J.Eur.Cer.Soc., **10** 2673 (2001).

Chapter 3

Preparation and characterization of bulk SBTi ($SrBi_4Ti_4O_{15}$) Ceramic samples

Chapter 3

Preparation and characterization of bulk SBTi ($SrBi_4Ti_4O_{15}$) Ceramic samples

3.1 Introduction

Bismuth layered structure ferroelectric (BLSF) compounds of Aurivillius family are interesting because of their crystallographic anisotropic nature. The structure of these compounds consists of bismuth oxide layers, interleaved with pseudo pervoskite blocks of $[A_{m-1}B_mO_{3m+1}]^{2-}$ along the crystallographic c axis [1]. The 12-coordinated A site can be occupied by cations such as La^{3+},Bi^{3+}, Ba^{2+}, Sr^{2+}, Pb^{2+}, Ca^{2+}, Na^{2+} etc. While the octahedral-coordinated B site can be occupied by W^{6+}, Nb^{5+}, Ti^{4+}, Fe^{3+} etc. The number of octahedra along the c-axis between two neighboring $(Bi_2O_2)^{2+}$ layers is indicated by *m*. The value of *m* in BLSFs is closely related to the ferroelectric properties and structure instabilities. An increase in *m* in certain compound systems led to an increase in the lattice parameters in the a-b plane as well as an increase in strain energy originating from the size mismatch between the bismuth layers and pervoskite layers, which will make the structure unstable [2]. For most of these compounds, the unit cell is orthorhombic below Curie temperature.

This chapter describes the results obtained during the optimization of the processing of SBTi ceramic samples, directed to improve its reproducibility. This chapter contains two main parts. Part 1 is about studies on SBTi ceramics and part 2 describes the effect of milling on SBTi ceramics. The bulk ceramic samples were prepared by the conventional solid-state method throughout the work. The structural, microstructural, ferroelectric, dielectric and mechanical properties were studied. Same properties were studied in the second part along with Raman studies and compared conventional sintered samples with microwave sintered samples. Details of the characterization procedures have been described in chapter 2.

3.2 Preparation of SBTi ceramics

The weights of initial reagents are calculated according to the stoichiometry ratio of SBTi. The reagents used are $SrCO_3$, Bi_2O_3 and TiO_2 powders of purity (99.9%) of Sigma-Aldrich, USA.

$$SrCO_3 + 2\,(Bi_2O_3) + 4\,(TiO_2) \text{ ---------- } SrBi_4Ti_4O_{15} + CO_2 \qquad (3.1)$$

Steps involved in the processing of SBTi ceramic samples are:

(a) Weighing
(b) Mixing using ball mill
(c) Drying
(d) Calcination at 750°C
(e) Phase analysis (XRD)
(f) Particle size reduction using ball mill
(g) Pelletization
(h) Sintering via conventional and microwave routes
(i) Characterization

The stoichiometric amounts of these oxides are weighed using as electronic balance (accuracy 0.001mgm) and mixed in a zirconia jar with zirconia balls. Distilled water is used as a mixing medium. To mix these powders a planetary ball mill (Retsch PM-100, Germany) is used as shown in figure 3.1. For mixing of reagents the stoichiometric powders are mixed at the speed of 150rpm (rotations per minute) for an hour. The mixed powders were dried in a hot oven at 150°C for 1hour. The calcination temperature of SBTi ceramics is optimized, and phase purity is checked in each case from the XRD patterns. The optimum calcination temperature was found to be 750°C for duration of 5h.

Figure 3.1: Photograph of the ball mill used in this study.

3.3 Characterization of SBTi bulk ceramics:

3.3.1 Structural properties:

Figures 3.2 show the XRD diffractograms of SBTi ceramics recorded using CuK$_\alpha$ radiation. The mixed reagents for SBTi ceramics were calcinated at different temperatures in order to produce a new solid phase and to remove the gas which is commonly associated with carbonates, nitrides, and acetates. The reflection in the diffractogram shows the formation of the orthorhombic structure with all the major peaks well matched with standard JCPDS file [43-0973]. As shown in figure 3.2, calcination at lower temperature results in some secondary phases. As the calcination temperature increases, the intensity of the secondary phases comes down and finally disappeared. By optimizing the temperature and socking time, single phase SBTi ceramics is successfully prepared. The calcined powders were milled at 300rpm for 5hours with distilled water as a mixing medium. Pellets of 10mm diameter were made with the milled powder. These pellets were sintered at 1170 -1230^{o}C for about 2hours to get densified ceramic samples having fine microstructure and using a high-temperature furnace (MHI, – USA make).

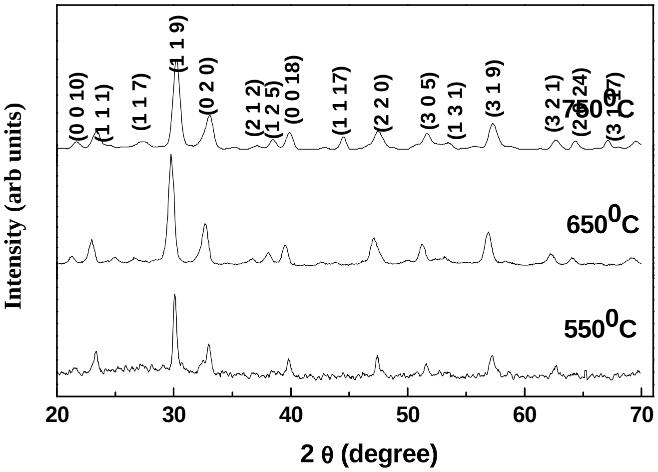

Figure 3.2: XRD pattern of the SBTi calcined powders at different temperatures.

3.3.2 Microstructural characteristics:

The microstructure images of the SBTi samples sintered by conventional route are shown in figure 3.3(a-d). The grain shapes of SBTi samples are in the form of platelets. This orientation is typical of Aurivillius phases and is due to the polycrystalline nature of the samples. SEM micrographs show that the grains are non-uniform, which leads to less densification as the temperature increases. Same trend was observed by O.P Thakur, Chandra Prakash et al [3]. The densities of the sintered SBTi ceramics were measured by water displacement method (Archimedes principle). The percentages of relative densities were 86, 90, 83, 79 for samples sintered at 1170^{o}C, 1190^{o}C, 1210^{o}C and 1230^{o}C respectively. The relative density of SBTi ceramic samples sintered at different temperatures is shown in table 3.1. At higher temperatures, the relative densities are very less due to evaporation of Bi, which led to inhomogeneous stoichometry. The Bi-loss and oxygen vacancies were confirmed from the EDAX data taken from FE-SEM. The atomic percentage of each element is shown in table 3.2. At higher temperatures, these losses are increasing gradually. This is due to sintering at higher temperatures and long socking time in a conventional furnace. From SEM micrographs it could be noticed that, as the sintering temperature increases the grain size increases gradually. This indicates that at higher temperatures, there is no control in grain growth of conventional sintered samples. The average grain size of the conventional sintered samples was found to range from 15-20µm.

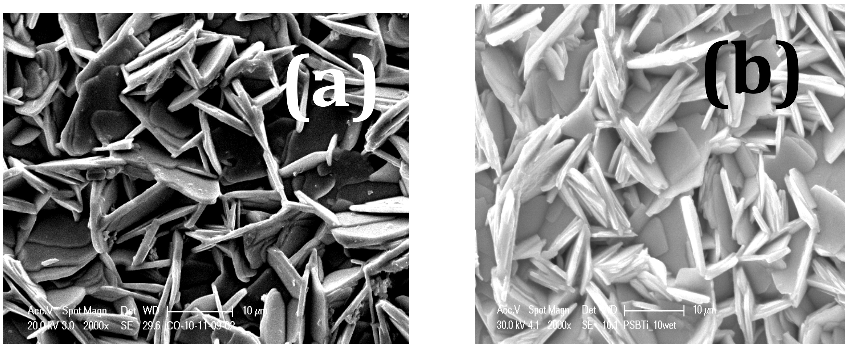

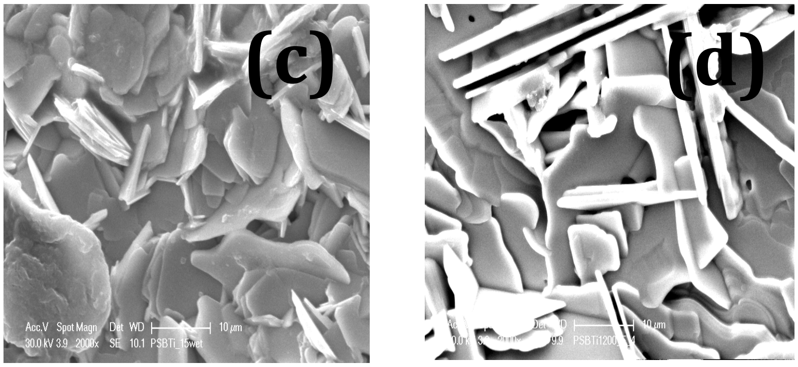

Figure 3.3 (a-d): SEM micrographs of SBTi ceramics sintered at different temperatures (a) 1170^{o}C (b) 1190^{o}C (c) 1210^{o}C (d) 1230^{0}C

Sintering Temperature (^{o}C)	**1170**	**1190**	**1210**	**1230**
Relative density (%)	86	90	83	79

Table3.1. Relative density of SBTi ceramics sintered at different temperatures

	Element – Atomic %			
Sintering Temp (^{o}C)	**Bi**	**Sr**	**Ti**	**O**
1170	**17.1**	**4.2**	**16.04**	**61.1**
1190	**16.7**	**4**	**16.1**	**61.71**
1210	**13.4**	**4.01**	**15.8**	**58.8**
1230	**13.01**	**3.9**	**16**	**56.89**
Green sample	**16.66**	**4.16**	**16.11**	**62.49**

Table3.2. Atomic percentage of each element of SBTi ceramic samples sintered at different temperatures (1170-1230^{o}C) derived by EDAX spectrum.

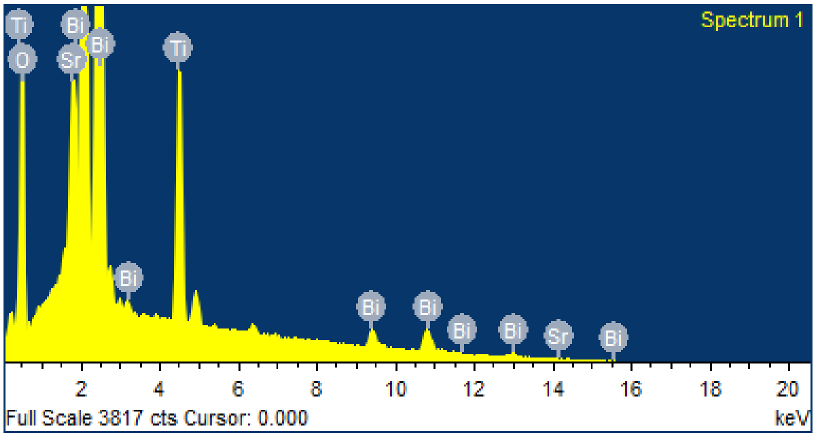

Figure 3.4: EDAX spectrum of SBTi ceramic samples sintered at 1190°C/2h

3.3.3 Low frequency dielectric properties:

The low frequency dielectric properties of SBTi ceramics measured at room temperature from 100 Hz to 1MHz are shown in figure 3.5. Dielectric properties of conventional sintered samples of SBTi ceramics are measured as a function of frequency. Observed dielectric constant decreased with increasing frequency. This phenomenon of appreciable decrease of dielectric constant with increasing frequency characterizes a dispersion character in the material and is usually attributed to the grain-to-grain interfacial effects and defects arising at the grain boundaries. The dielectric constant was increased up to samples sintered at 1190°C. Further increase in temperature (above 1190°C), the dielectric constant was decreased gradually. The oxygen vacancies and Bi-losses in samples sintered at higher temperatures plays a crucial role in decreasing the dielectric properties. The observed dielectric losses are quite high compared to other classes of ferroelectrics. The similar values are reported by Shujun Zhang et.al [4]. The dielectric losses in ceramic samples are generally caused by extended dislocations, grain boundaries and secondary phases. SEM micrographs clearly show abnormal grain growth and high porosity for samples sintered at higher temperatures, which could be a cause for higher losses.

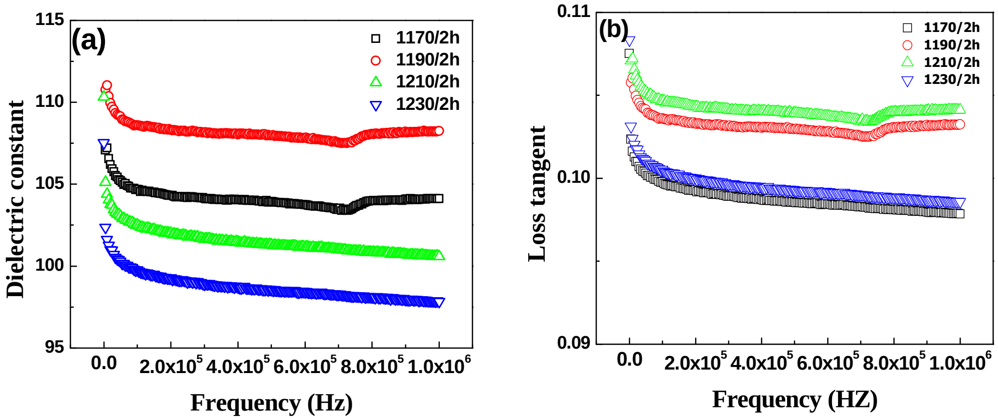

Figure 3.5 (a-b): (a) Dielectric constant (b) Loss tangent as a function of frequency of SBTi ceramics sintered at different temperatures.

3.3.4 Ferroelectric properties:

The most outstanding feature of ferroelectric ceramics is its hysteresis loop. It describes the nonlinear polarization switching behavior as a function of electric field. Presence of permanent dipoles in the crystallites and their switching with an electric field is characteristic of ferroelectric materials. The remanent polarization and coercive field at room temperature is obtained from the polarization vs. electric field measurement on unpoled ceramic samples of diameter 10mm and 0.65mm thickness using a ferroelectric hysteresis measurement system built based on the Sawyer-Tower circuit by Marine India Ltd.

Figure 3.6 (a-d) shows the polarization vs. electric field loop for different sintered samples. The ferroelectric properties of the materials depend not only upon the crystal structure, but also on the microstructure like grain size and orientation [5]. The hysteresis characterizations were carried out to explore how these properties vary due to different sintering temperatures for a material of the same composition, which in turn could reveal the possible applications in memory and actuators. The ferroelectric hysteresis loops (P-E) were recorded for an applied pulse voltage with a maximum electric field of 80KV/cm. The range of the 2Pr (Pr- remnant polarization) values of conventional sintered samples are 3.1-1.8μC/cm^2 respectively. The remnant polarization increased for samples sintered up to a temperature of 1190^{o}C. With further increase in temperature, the remnant polarization is decreased gradually. The values of remnant polarization and coercive filed is shown in table 3.3. The reduction of remnant polarization for high temperature sintered samples could be due to the presence of oxygen and metal ion vacancies which causes strong domain pinning [6]. For bismuth layer structured ferroelectric, the contribution of pseudo-perovskite blocks to 2Pr is dominant [7]. Ferroelectric properties are subjected to the influence of oxygen and metal ion vacancies, which cause strong domain pinning [8-9]. Here, Oxygen vacancies (V_o) within the perovskite structure are known to be generated along with bismuth vacancies (V_{Bi}), which are associated with Bi_2O_3 volatization occurring during the sintering process at elevated temperatures. The lack of saturation of P-E loops in all the samples indicates that the system is highly conductive; one possible reason for high conductivity can be the presence of oxygen vacancies and dipole complexes in the system.

Sintering temperature	**$2P_r$ (μC/cm^2)**	**E_c (KV/cm)**
1170^{o}C	**1.56**	**58.8**
1190^{o}C	**1.82**	**53.52**
1210^{o}C	**1.72**	**55.12**
1230^{o}C	**1.1**	**50.81**

Table 3.3: P_r and E_c values of SBTi ceramics sintered at different temperatures

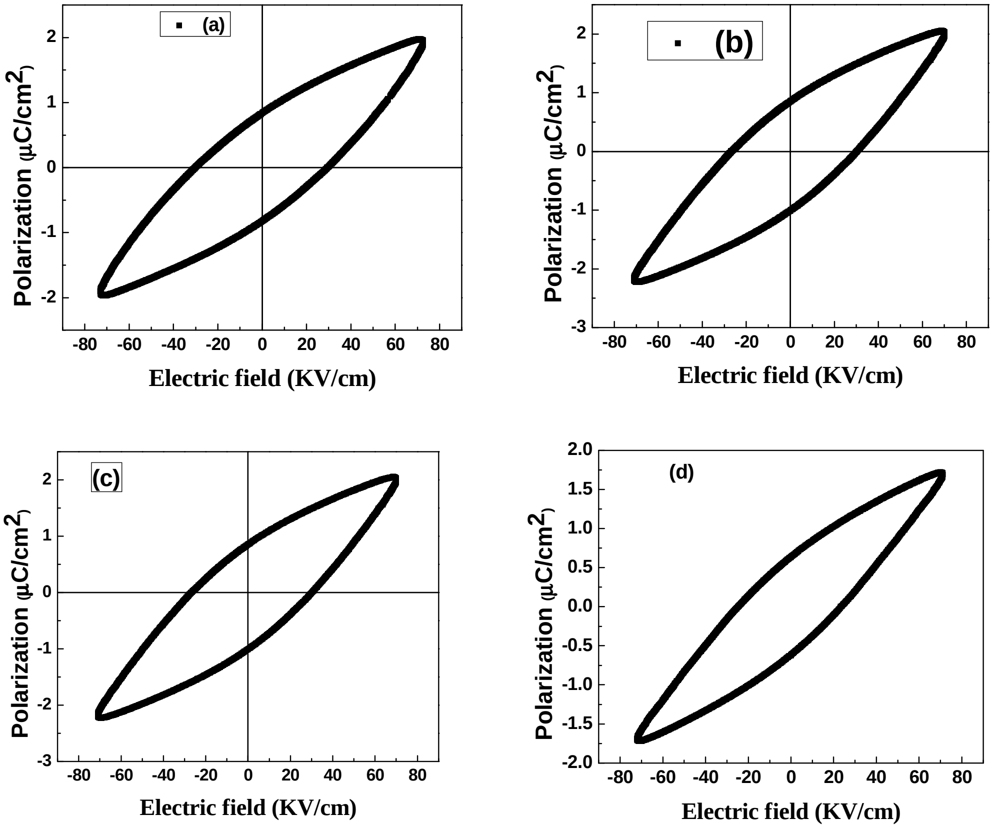

Figure 3.6(a-d): P-E hysteresis loops of SBTi ceramics sintered at different temperatures (a) 1170^{o}C (b) 1190^{o}C (c) 1210^{o}C (d) 1230^{o}C.

3.3.5 Mechanical properties:

It is well known that piezoelectric coefficients depend on the mechanical coefficients which are related to the mechanical states of materials [10]. Moreover, the mechanical behavior plays a crucial role in the delamination, cracking or fracture, and polarization fatigue of the multilayer thin-film structures [11-12]. Mechanical properties of ceramics such as hardness (H), Young’s modulus, yield stress and ultimate tensile stress are derived from the response of the applied force. In the present study, mechanical properties such as hardness and Young’s modulus were determined using nanoindentation. During the instrumented indentation process, a record of the depth of penetration is made, and then the area of the indent is determined using the known geometry of the indentation tip. While indenting, various parameters such as load and depth of penetration can be measured. A record of these values can be plotted on a graph to create a load-displacement curve as shown figure 3.7. These curves can be used to extract mechanical properties of the material.

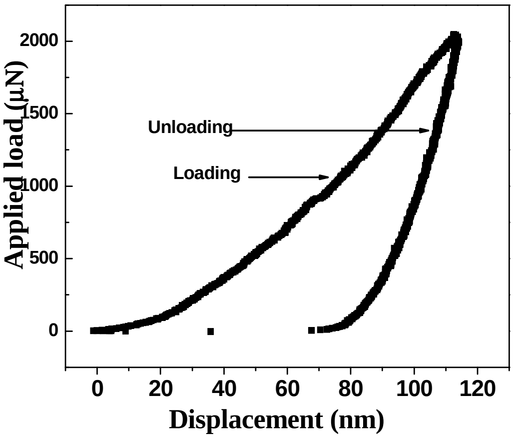

Figure 3.7: Load-displacement curve of SBTi ceramic samples.

Prior to indentation test, samples were highly polished without any surface roughness and pores. SBTi ceramics are indented by Berkovich-type pyramidal diamond tip with a maximum load of 2000μN. The trapezoid load was used to measure the hardness and Young's modulus. The hardness and Young's modulus of the SBTi ceramics as a function of contact depth are shown in figure 3.8(a-b). It was observed that the hardness and Young's modulus have increased for samples prepared at sintering temperatures up to 1190^{o}C. With further increase in temperature, the hardness and Young's modulus has decreased. These results are well matched with SEM images as shown in the previous section. It can be concluded that the mechanical properties are mainly depending on the microstructural properties like grain size, density and orientation. In the present case, densities of these samples are supporting the mechanical properties. The samples having higher density have exhibited higher hardness and Young's modulus values. The average hardness and Young's modulus of the SBTi ceramics are 10- 12.5 GPa and 120 – 140 GPa respectively.

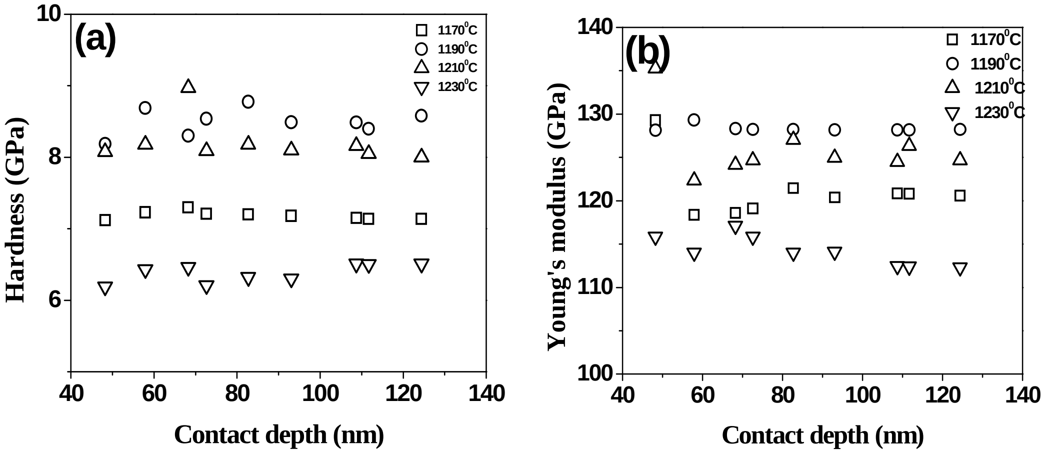

Figure 3.8 (a-b): (a) Hardness & (b) Young's modulus as a function of contact depth for SBTi ceramic samples sintered at different temperatures.

3.4 Effect of milling on SBTi ceramics:

3.4.1 Introduction:

Miniaturization of ferroelectric components is of current interest in the microelectronics industry. Recent advances in solid state science have enabled the fabrication of ferroelectric materials and devices with nanostructures. The influence of size effects on their ferroelectric properties may limit their future applications [13-14]. Therefore, it is important to understand the ferroelectric material behavior as the particle size reduces. Most of the reported results on the size effects in ferroelectric ceramics have focused on pervoskite structured $BaTiO_3$ [15-16]. There is only limited reported data on Bi-layered structured materials due to the difficulty of obtaining fully dense bulk ceramics. However, recent advances in ceramic sintering have opened up the possibility of extending these studies to BLSFs. For example, microwave sintering has been successfully used to fabricate nanostructured ferroelectric ceramics because it can achieve rapid heating rates [17-18]. The high temperatures used during the sintering can cause problems in the stoichometry of the final product owing to the volatility of Bi, and hence an alternative process is often needed. Some methods used to obtain bismuth-layered pervoskite ceramic precursors are hydrothermal, sol-gel and co- precipitation synthesis. But even after preparing precursors with these chemical methods, the sintering in general is done with the conventional heating. An attractive alternative for these problems is microwave sintering technique, which often eliminates the stoichiometry problems by accomplishing the process at much lower sintering temperatures over a short period of time.

The synthesis of the material was carried out with a powder mixture containing an equimolar amount of 99.9+ % pure Bi_2O_3, $SrCO_3$, and TiO_2 (Sigma-Aldrich make). The powder mixture was ball milled in deionized water and then calcined at 750^0C for 5 hours. Calcined powder was ball milled for about 5-20h to reduce the particle size. Here the grain size effect on microstructure, dielectric, ferroelectric and mechanical properties of SBTi ceramics processed by microwave sintering as well as by conventional sintering are discussed and a comparative study is made.

3.4.2 Structural properties:

Figures 3.9 (a-d) and 3.10 (a-d) show the X-ray diffraction patterns of microwave and conventional sintered SBTi ceramics respectively. They indicate that even at higher milling time the structure of SBTi ceramics does not change or generate new phases. The positions of the diffraction peaks are in good agreement with the standard orthorhombic pattern. The crystallite size of the conventional and microwave sintered samples were calculated by Debye-Scherrer formula. The crystallite size decreases as the milling time increases. The crystallite sizes of the conventional sintered samples are ranged between 60-75nm, which is more than that for microwave sintered samples, which is 39-45nm. It is evident from the XRD pattern as each peak broadens more in microwave sintered samples than in conventional sintered samples.

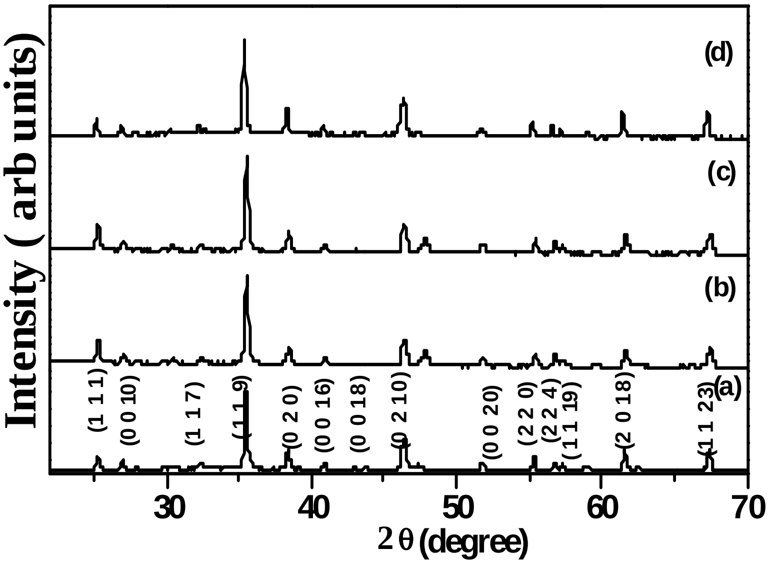

Figure 3.9 (a-d): X-ray diffraction patterns of microwave sintered SBTi ceramics ball milled for different durations (a) 5h (b) 10h (c) 15h (d) 20h.

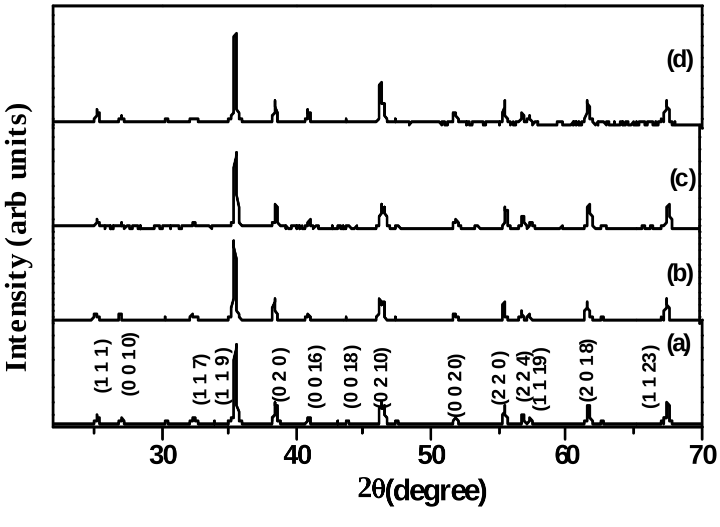

Figure 3.10 (a-d): X-ray diffraction patterns of conventional sintered SBTi ceramic samples ball milled for different durations(a) 5h (b) 10h (c) 15h (d) 20h.

3.4.3 Microstructural:

The microstructure of the SBTi samples ball milled for about 5-20 hours and sintered by conventional and microwave routes are as shown in figure 3.11 (a-d) and figure 3.13(a-d). SEM images of SBTi samples show grains in the form of platelets. This orientation is typical of Aurivillius phases. SEM micrographs, shows that conventionally sintered samples got grains that are non-uniform and of platelet like shape, whereas microwave sintered samples are highly densified and got uniform grain size. It was found that there is obvious densification in the microwave field at 1050^{o}C for 40min. It is observed that the samples sintered at lower temperatures exhibit a reduction in the grain size. The density of the samples increased as the milling time increases up to 15h.In case of 20h milling time, the average grain size of the conventional and microwave sintered samples is slightly increased compared to 10 & 15h milling time samples. The increase in grain sizes for 20h milling time samples is due to agglomeration of the grains [19]. The relative density of the microwave sintered samples is higher than the conventional sintered samples. The relative density of the microwave and conventional sintered samples as a function of milling time is shown in figures 3.14 and 3.12. Maximum relative density of 97.5% is obtained at 1050^{0}C for 40min of microwave sintering. By contrast, conventional sintering of SBTi is slow**.** For example, 4h sintering at 1050^{0}C led to 70.5% of relative density. To get high densification conventionally, samples are to be sintered at high temperatures and for a longer period [20]. The grain size is decreasing with an increase in the milling time, and that is clearly observed in micrographs for both microwave and conventional sintering. The grain size observed in the microwave processed samples is smaller and denser than conventional one. The average grain size of the conventional and microwave sintered samples at different milling time is as shown in table 3.4. The rapidity of microwave sintering method could be a reason for suppression of grain growth resulting in a finer and uniform microstructure. The same phenomenon was observed by Chris Y Fang et.al also [21]. The substantially enhanced densification in the microwave sintered samples can be considered as the cause for their fairly high dielectric and mechanical property enhancement.

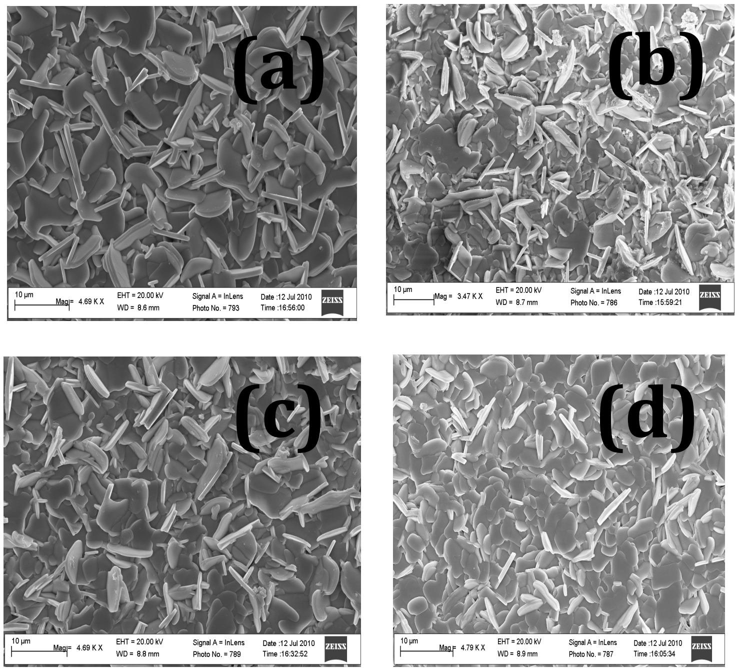

Figure 3.11 (a-d): SEM images of conventional sintered SBTi ceramic samples ball milled for different durations (a) 5h (b) 10h (c) 15h (d) 20h.

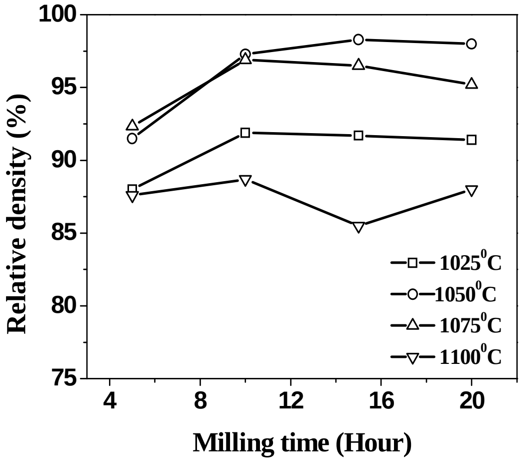

Figure 3.12 Relative density as a function of milling time for different sintering temperatures. Sintering by microwave heating.

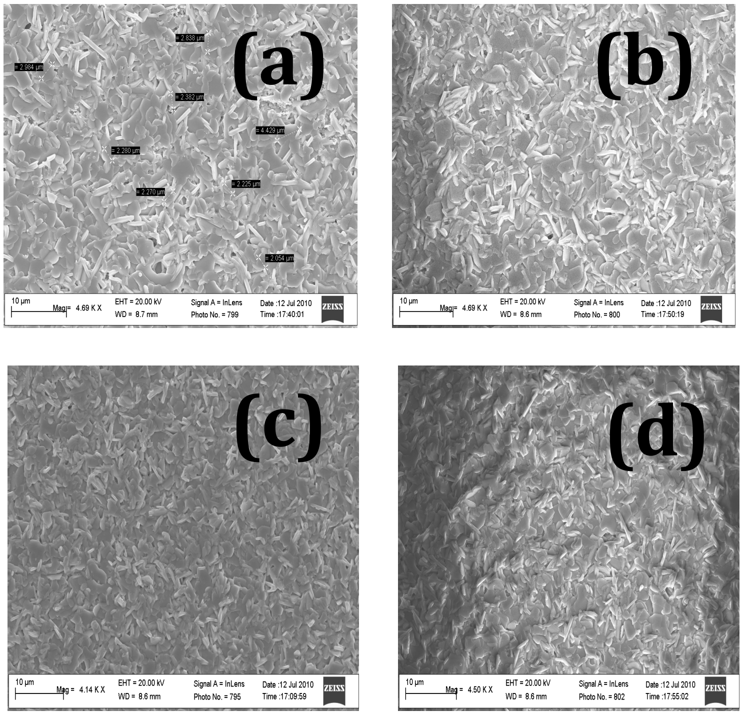

Figure 3.13: (a-d): SEM images of microwave sintered SBTi ceramic samples ball milled for different durations (a) 5h (b) 10h (c) 15h (d) 20h.

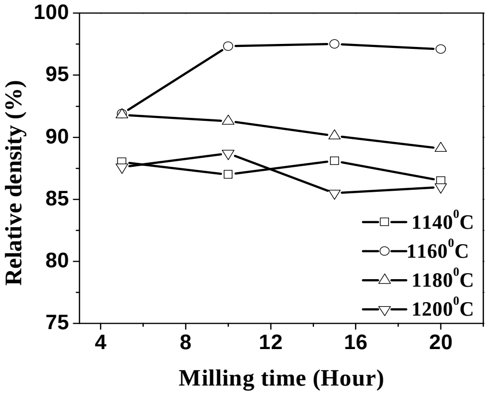

Figure 3.14: Relative density as a function of milling time for different sintering temperatures. Sintering by conventional heating.

Milling time (Hour)	Conventional sintered/ Average grain size (μm)	Microwave sintered/ Average grain size(μm)
5	9-10	4-5
10	6-8	3-4
15	4-6	1-2
20	5-6	2-3

Table 3.4: Average grain size for different milling time for both microwave and conventional sintered samples.

3.4.4 Dielectric Properties:

Dielectric properties of microwave and conventional sintered samples of SBTi ceramics milled for different durations are measured as a function of frequency at room temperature and are shown in figures 3.15 (a-b) and 3.16 (a-b) respectively. As the milling time increases, the dielectric constant also increases up to 15 hours of milling along with the dielectric loss (generally loss goes with the dielectric constant). For 20 hours of milling, the grain size is higher and the dielectric properties are quite dissimilar to the rest of the cases. This indicates that as the grain size decreases, the dielectric constant is increasing. This is understandable as the grain size decreases the stress state in the grains changes, and the dielectric properties in ferroelectrics are heavily dependent on the stress values and their direction in each grain. The enhancement of dielectric constant can also be attributed to the increase in domain wall density with decreasing domain size [22]. The dielectric constant of the microwave sintered samples is little higher than that of conventional sintered samples. In both microwave and conventional sintered process, the dielectric constant is more for 15h milled samples compared to other cases. The enhanced dielectric behavior can be directly related to the higher density, more uniform and finer microstructure, which is characteristic of microwave sintering and also to possible reduction in defects induced dielectric relaxation, which could directly be related to the concentration of defects at the grain boundaries. The reduction in defects and the associated possible dielectric relaxation in microwave sintered samples are evident in that the dielectric constant of these samples (fig.3.15a) are less frequency dependent compared to that for the conventional samples (fig.3.16a) and the losses for the former case is lower and less frequency dependent compared to the latter case (figures 3.15b and 3.16b).

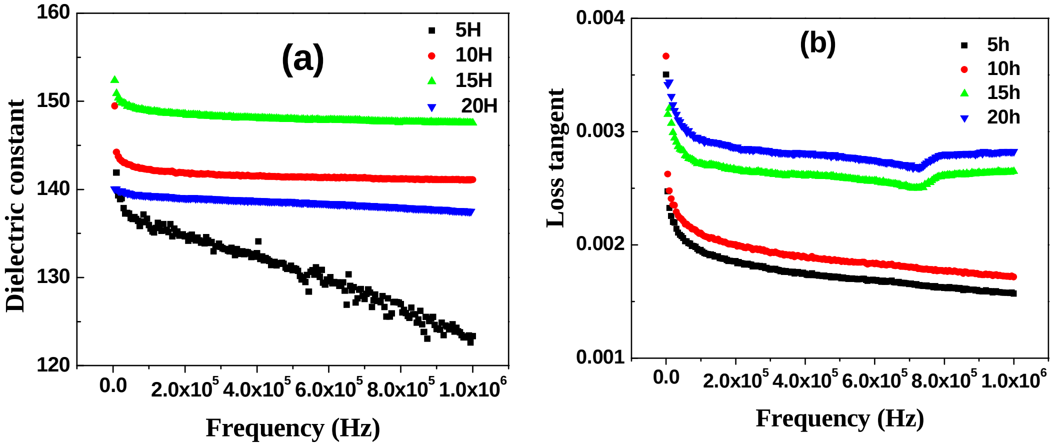

Figure 3.15 (a-b): (a) Dielectric constant and (b) loss tangent of the microwave sintered SBTi ceramic samples as a function of frequency.

SEM micrographs clearly shows grain growth and high porosity in conventional sintered samples than in microwave sintered samples, which could be a cause for higher losses. These losses in ceramics are generally caused by extended dislocations, grain boundaries and secondary phases. Observed dielectric constant marginally decreased with increasing frequency for both the set of samples. This reduction in dielectric constant with increasing frequency at the lower frequencies characterizes a dispersion character in the material and is usually attributed to the grain-to-grain interfacial polarization effects arising from the defects at the grain boundaries and to the oscillation of ferroelectric domain walls.

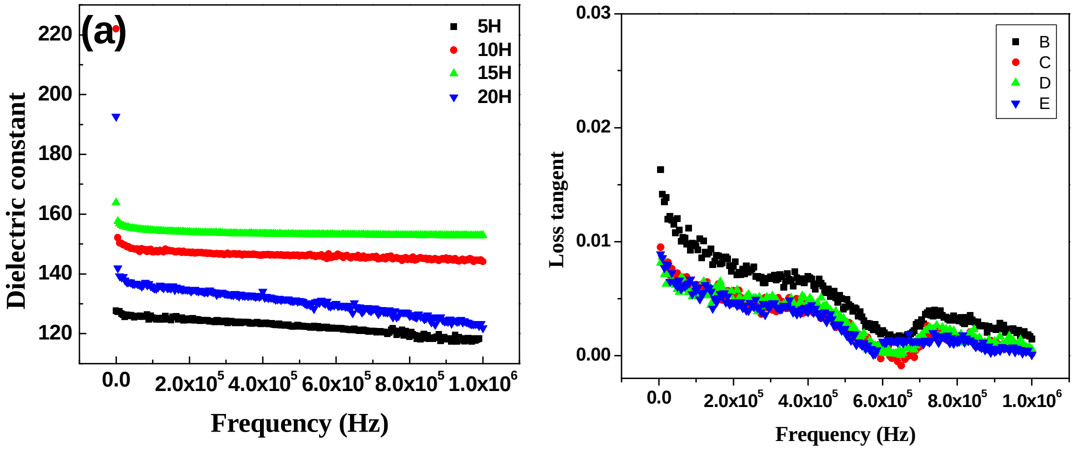

Figure 3.16 (a-b): (a) Dielectric constant and (b) loss tangent of the conventional sintered SBTi ceramic samples as a function of frequency.

3.4.5 Mechanical properties:

During the instrumented indentation process, a record of the depth of penetration is made, and then the area of the indent is determined using the known geometry of the indentation tip. While indenting, various parameters, such as load and depth of penetration can be measured. A record of these values can be plotted on a graph to create a load-displacement curve as shown in figure 3.17. These curves can be used to extract mechanical properties of the material.

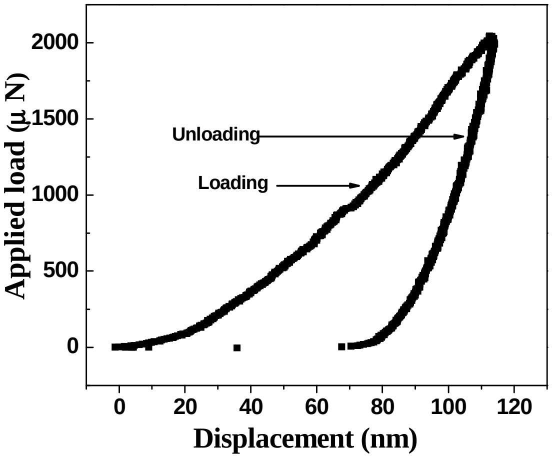

Figure 3.17: Load-displacement curve of SBTi ceramic samples

Figure 3.18 (a-b) & 3.19 (a-b) shows the mechanical properties of the microwave and conventional sintered SBTi ceramics samples of different milling time, measured by nanoindentation technique. Each point of the hardness and Young's modulus values are the average of five indentations at different places to avoid microstructural effect on mechanical properties. It should be mentioned that the mechanical properties of SBTi ceramics were previously not reported. As the milling time increases, the hardness and Young's modulus of microwave and conventional sintered samples also increases up to 15hours of milling time. This implies that the microstructure particularly the grain size is affecting more the mechanical properties of the SBTi ceramics. Materials can be strengthened by changing their average grain size. It is based on the observation that grain boundaries impede dislocation movement and that the number of dislocations within a grain has an effect on how easily dislocations can traverse grain boundaries and travel from grain to grain. So, by changing grain size one can influence dislocation movement and hardness. In the present study, as the grain size decreases the dislocation movement could have decreased, which can lead to enhancement of the mechanical properties of the samples. Same trend was observed by Weimin Wang et.al [23]. As the grain size decreases the density increases, and the hardness and Young's modulus is increasing for both microwave and conventional sintered samples up to 15hours of milling time. The same phenomenon was observed by Tetsu Miyoshi and Hiroshi Funakubo [24]. In case of 20hours of milling time, the hardness and Young's modulus of the microwave sintered samples are less than that for the cases of 10 and 15hours of milling time. But in conventional sintered samples, the hardness and Young's modulus of the 20hours of milling time sample is less than the rest of the cases. This could be the result of lower density exhibited by microwave and conventional sintered samples when milled for 20 hours.

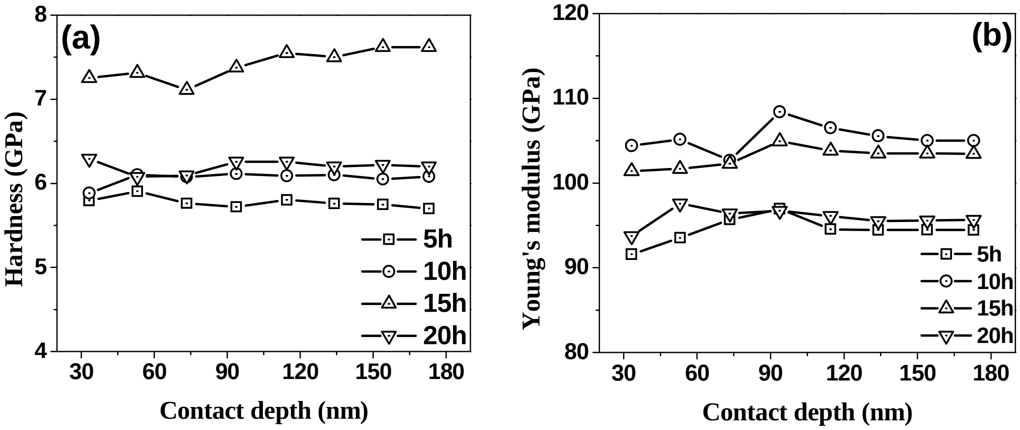

Figure 3.18(a-b): (a) Hardness and (b) Young's modulus as a function of contact depth of the SBTi ceramic samples sintered with a conventional furnace.

Higher density exhibited by the microwave sintered samples could be the reason for the higher hardness and Young's modulus exhibited by them over the conventional sintered samples. The improved mechanical strength in microwave processing could also be attributed to small grain size and uniform microstructure where crack centers like large pores and defects are few. The high Young's modulus value reflects the lower defect density and finer grains of the samples. Same trend was observed by Szuecs and Werner

[25]. In addition, rapid microwave processing can reduce Bi ion volatilization and reduce impurity/solute segregation at grain boundaries. Previous work [26] has shown that microwave sintered samples are effective for increasing mechanical strength.

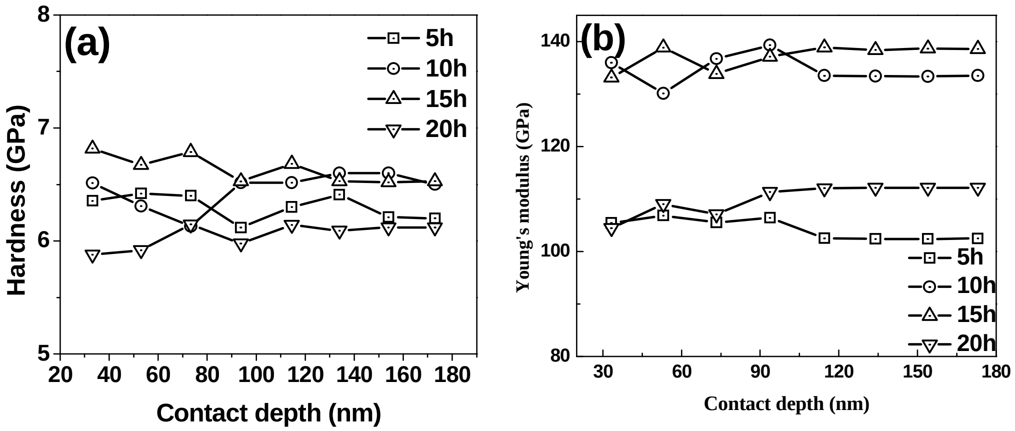

Figure 3.19(a-b): (a) Hardness and (b) Young's modulus as a function of contact depth of the microwave sintered SBTi ceramic samples.

3.4.6 Ferroelectric properties:

Figure 3.20 (a-d) and 3.21 (a-d) displays the ferroelectric hysteresis loops of conventional and microwave sintered SBTi ceramics milled for different-durations. The ferroelectric property of the materials depends not only upon the crystal structure, but also on the microstructure, like grain size and orientation. The hysteresis characterizations were carried out to explore how these properties vary due to different sintering techniques and different milling time for a material of the same composition, which in turn are relevant for the possible applications in memory and actuators. The ferroelectric hysteresis loop (P-E) is recorded for an applied pulse voltage with a maximum electric field of 80KV/cm. In both conventional and microwave sintering process, as the grain size decreases, the ferroelectric properties were enhanced up to 15hours of milling time.

From graphs (3.20) & (3.21), the remnant polarization (P_r) can be seen to be increasing as the grain size decreases with milling time increasing up to 15hours. In both microwave and conventional sintering process, the remnant polarization is more for 10hours and 15hours of milled samples compared to other cases. In case of 20hours of milling time, the P_r value of the microwave sintered samples is less than that for the 10 and 15hours of milling time cases. But in conventional sintered samples the P_r value for 20 hour milled samples is the least. The $2P_r$ values of the microwave sintered samples are higher than the corresponding values for the conventional sintered samples in each case. This may be due to low evaporation of Bi during the preparation process such as low sintering temperature and lesser soaking time.

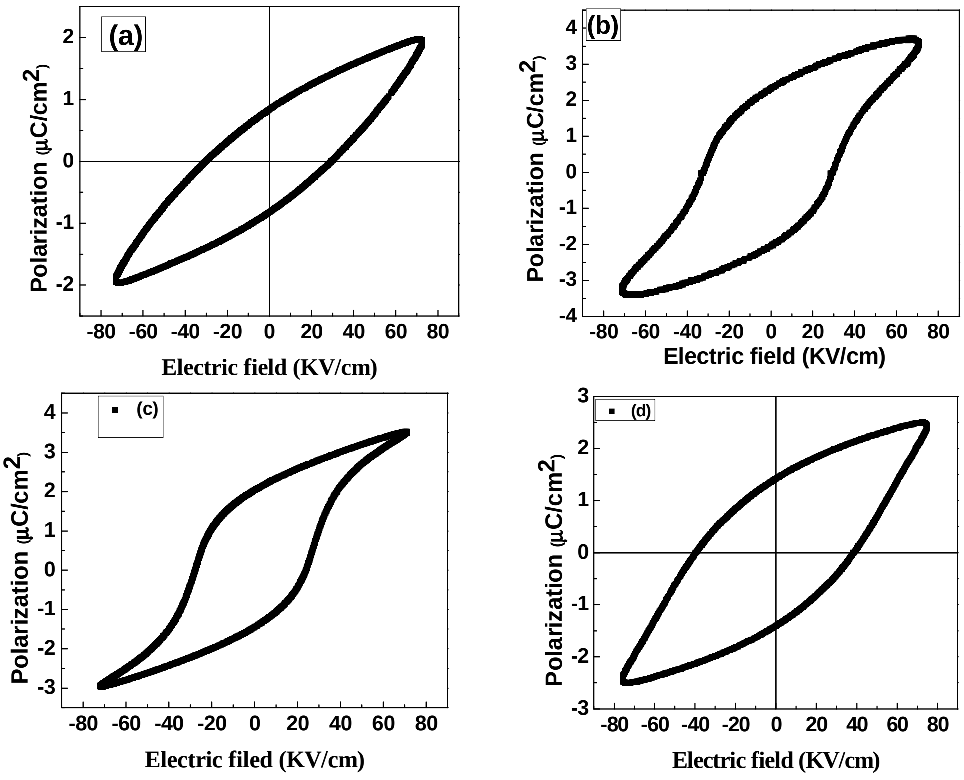

Figure 3.20 (a-d): P-E hysteresis loops for microwave sintered SBTi ceramic samples, ball milled for different durations: (a) 5h (b) 10h (c) 15h (d) 20h.

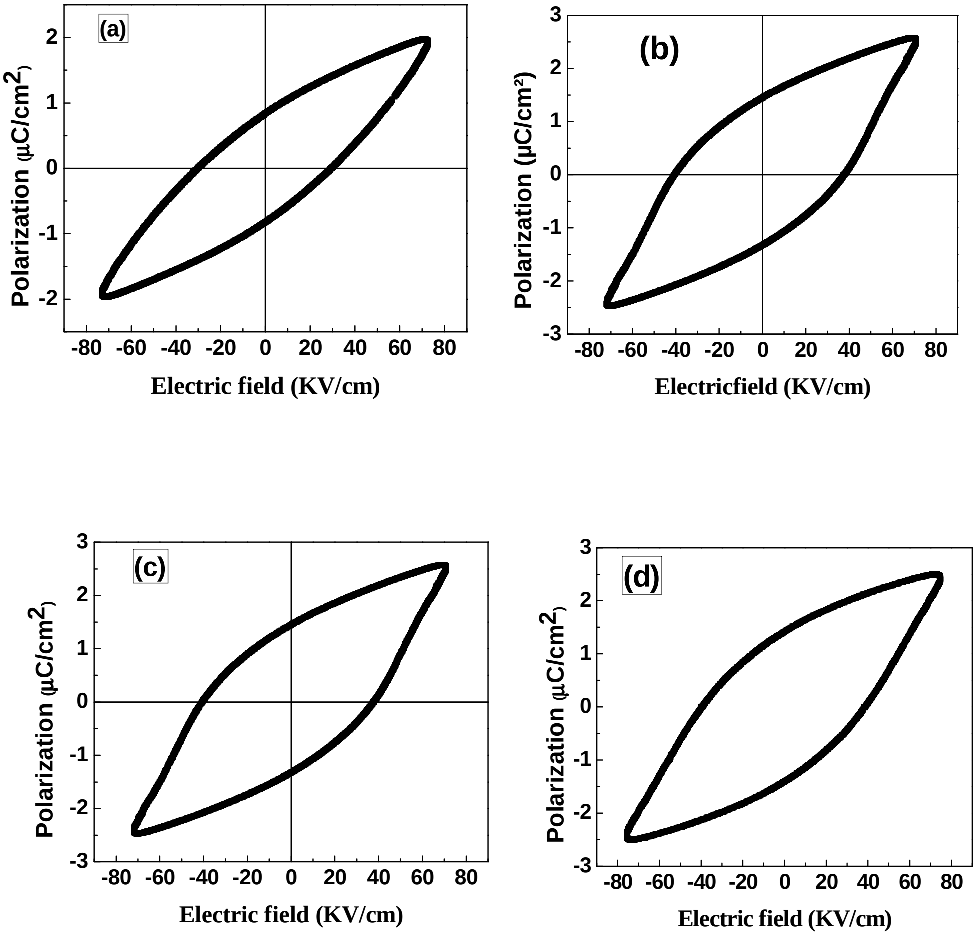

Figure 3.21(a-d): P-E hysteresis loops for conventional sintered SBTi ceramic samples ball milled for different durations: (a) 5h (b) 10h (c) 15h (d) 20h.

The range of the $2P_r$ values of conventional and microwave sintered samples are 1.33-2.32 and 1.6-3.06μC/cm^2 respectively. The smaller grain size samples exhibited the better ferroelectric properties in both conventional and microwave sintered samples. This indicates that the ferroelectric properties are strongly depending on grain size. In case of larger grains, the domain walls are quite free to move and their movement is inhibited as the grain size decreases, since the grain boundaries will contribute additional pinning points for the moving walls. If the walls become less mobile, their ability to hinder the ferroelectric properties will also decrease. As a result, ferroelectric properties were improved. The reduction of remnant polarization in conventional sintered samples could be due to the presence of Bi and oxygen vacancies and lesser polarization pinning centers in them. This results in the loss of polarization due to leakage in the material. The uniform microstructure with smaller grain sizes offered by the microwave sintering process could be the consequence of microwave energy being deposited instantaneously and volumetrically within the bulk of the material, wherein thermal gradients are avoided. It is quite interesting that as the grain size decreases, the ferroelectric properties are getting enhanced, which is quite good for applications and it is worth exploring whether the same trend could continue into the nano size grains in thin films also by manipulating the thin film microstructure by similar processing techniques.

3.4.7 Raman studies:

Figure 3.22 and 3.23 shows the Raman spectra of SBTi ceramics sintered in conventional and microwave furnaces respectively. At room temperature, the Raman spectra exhibited intense phonon modes at 55,~90,~126,~151,~268,~476,~561,~726,and ~ 865 cm^{-1} in addition to some weak peaks. The spectrum of SBTi is similar to that reported by Kojima et al. [27, 28]. The vibrational modes of the bismuth layered structure ferroelectrics can be classified as internal modes of TiO_6 octahedra and the lattice translation modes related to the motion of the cations in the pseudo-pervoskite slabs and the Bi_2O_2 layers [29]. The modes with Raman shift lower than $200cm^{-1}$ are related to the motion of heavier ions. For the BLSFs, the mode between 50 and 60 cm^{-1} is reported to rise from the displacement of Bi^{3+} ions in Bi_2O_2 layers. Those between 90 and $160cm^{-1}$ originate from the vibrations of the ions at the A sites of the pseudo-pervoskite blocks. Although Sr^{2+} ion is much lighter than Bi^{3+}, the radius of Sr^{2+} (0.132nm) is larger than that of Bi^{3+} (0.117nm) and the Sr^{2+} ion has a lower chemical valance than that of Bi^{3+} ion. Thus, the mode related to Sr^{2+} ion is expected to be located in the same region as that of Bi^{3+} ions [30]. The modes with the Raman shift above 200cm^{-1} are associated with the TiO_6 octahedra due to large intra group binding energy in the octahedra and much smaller mass of Ti^{4+} ions [31]. The mode at ~268cm$_{-1}$ arises from the torsional bending of TiO_6 octahedra and those at ~ 550 cm^{-1} and 850 cm^{-1} correspond to the stretching of TiO_6 octahedra.

The Raman spectra for samples sintered in a microwave furnace is slightly different from the Raman spectra for the samples sintered conventionally. In conventional sintered samples, the observed phonon modes above the ~450cm^{-1} are shifted to the lower frequency side. This indicates that the stretching modes of the TiO_6 are affected by the lattice parameters. In conventional sintering, generation of oxygen vacancies at high temperatures results in non-stoichiometry which can distort the TiO_6 bond causing changes to lattice parameters [32]. Raman studies are well supporting with XRD patterns which are given on section 3.4.2

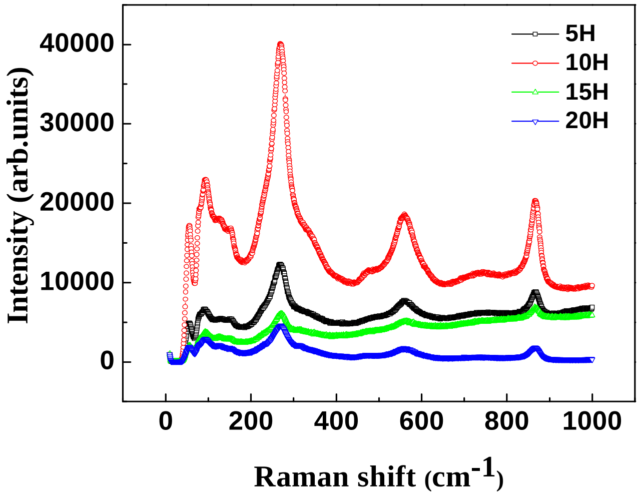

Figure 3.22: Raman spectra of conventional sintered SBTi ceramics.

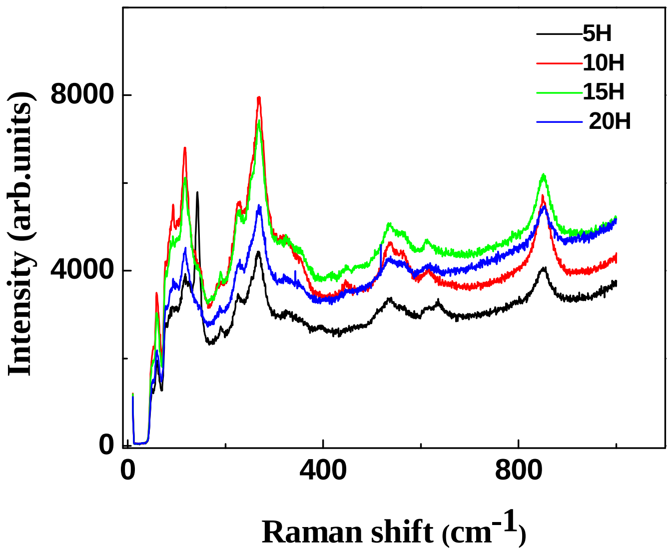

Figure 3.23: Raman spectra of microwave sintered SBTi ceramics

3.5 Summary

- **S**ingle phase SBTi ceramic samples were prepared through conventional solid-state reaction technique by optimizing the calcination and sintering conditions systematically.
- Structural, microstructural, mechanical properties, dielectric, ferroelectric, and Raman studies are studied.
- Samples sintered at 1190^{0}C exhibited high density and uniform microstructure. Above that temperature, the observed density decreased and grain growth is non-uniform due to pores in the samples and volatization of Bi at higher temperatures.
- Dielectric constant, remnant polarization and mechanical properties increased as the sintering temperature increases up to 1190^{0}C. With further increase of sintering temperature, these properties are degraded due to the presence of abnormal grain growth, which can lead to a reduction in pinning of domain walls within the grains.

- The effect of ball milling on different sintering processes, microstructure as well as on dielectric, ferroelectric, Raman spectra and mechanical properties of SBTi ceramics are identified.

- The grain size of the sintered body is found to decrease for the samples with longer milling times for both microwave and conventional sintering except for 20 hours of milling. In the case of 20 hours of milling all the data are not in trend with the rest of the cases, and that could be due to possible re-agglomeration of the milled powders.
- It was observed that as the grain size decreases, the dielectric, ferroelectric and mechanical properties of the SBTi ceramics are enhanced. From this we can conclude that the properties of SBTi ceramics strongly depend on grain size.
- The microwave sintering of SBTi ceramics leads to higher densification and fine microstructure in much shorter time duration than conventional sintering. They gave better dielectric, mechanical and ferroelectric properties also. The results of microwave sintered samples are desirable for microelectronics industry such as capacitors and actuators. It is interesting to note that when the grain size is minimum (for 15hours milling case), the density is maximum and the samples exhibits best dielectric, mechanical and ferroelectric properties for both conventional and microwave sintered samples.

References.

1. Aurivillius B., Ark Kemi., **2,** 519 (1950).
2. Hiroshi Irie and Masaru Miyayama, J App Phy Lett., **79,** 251-253 (2001).
3. O.P Thakur, Chandra Prakash, D K Agrawal. J Matt Sci and Engg B., **96**, 221-225 (2002).
4. Shujun Zhang, Namchul Kim, Thomos R et al, J.Sol. State. Coomu., **140,** 154-158 (2006).
5. Chung-Hsin Lu, Chung-Han Wu, J.Eur. Cer.Soc., **22,** 707-714 (2002).
6. Shimakawa I.M, Kubo Y, Tauchi Y, Kamiyama T et al, J. Appl, Phy, Lett., **77**, 2749 (2000).
7. Park B.H, Kang B.S, Bu S.D, Noh T.W, Lee, J. Nature., **401,** 682 (1999).
8. Watanabe T, Funakubo, Osada M, Noguchi Y, J. Appl. Phy. Lett., **80,** 100 (2002).
9. R.C. Budhani et al, J.Phys. Rev. Lett., **72**, 566 (1992).
10. Wang Da-Wei, Jin Hai-Bo, Yuan Jie et al, J.Chin.Phy.Lett., **27,** 047701 (2010).
11. Roy S, Chandra Rao, B S S and Subramanyam, J. Scripta. Matt., **57**, 1024 (2007).
12. Zhou Z G, Wang B, and Cao M S, J. Mech. Res. Commu., **30**, 395 (2003).
13. Setter N and Waser R, J. Acta. Matter., **48**, 151 (2000).
14. Shaw T M, Trolier-McKinstry S and McIntyre P C, J. Rev.Mater Sci., **30,** 263 (2000).
15. Frey M H and Payne D A, J. Phys. Rev. B., **58**, 1619 (1996).
16. Frey M H, Xu Z, Han P and Payne D A, J. Ferroelectrics., **206/207**, 337 (1998).
17. Hongtao Zhang, Haixue Yen, Huanpo Ning et al, J. Nanotechnology., **20**, 385708 (2009).
18. D Ravichandran, R Mayer, Jr R Roy, J Mat Res Bell., **31,** 817 (1996).
19. E. Brzozowski∗, M.S. Castro, J.Thermo.Chimica. Acta., **398**, 123-129 (2003).
20. P.K. Patro, Trans. Ind. Inst. Metals., **59**, 229 (2006).
21. Chris Y Fang, Clive A Randal, Michael T Lanagan, J.Electro.Cer., **22,** 125-130 (2009).
22. Youn-Kyu Choi, Takuya Hoshina, Hiroaki Takeda et.al, Appl Phy Lett., **97,** 212907 (2010).

23. Weimin Wang, Zhengyi Fu, Hao Wang, Runzhang Yuan, J.Eur.Cer.Soc., **22,** 1045-1049 (2002).
24. Tetsu Miyoshi and Hiroshi Funakubo, Jpn. J. Appl Phys., **49**, 09 MD131 (2010).
25. F. Szuecs, M Werner, R S Sussmann, C S J Pickles, H J Fecht, J. App. Phy., **86,** 6010-6017 (1999).
26. Dj. Veljovic, E. Palcevskis, A. Dindune, S. Putic, J. MAT, SCI., **45,** 3175- 3183 (2010).
27. S Kojima, R.Imaizumi, S.Hamazaki, M.Takashige, Jpn,J,Appl,Phy., part1 **33,** 5559 (1994).
28. S Kojima, R.Imaizumi, S.Hamazaki, M.Takashige, J.Mol. Struc ., **384,** 37(1995).
29. M. Osada, M Tada, E Kakithana, T.Watanabe, Jpn.Jour Appl Phy., (part1) **40,** 5572 (2001).
30. R.D Shannon, J.Acta. Crys A., **32,** 751(1976).
31. J Zhu, X.B Chen, Z.P Zhang, J.C Shen, Acta Matt., **53**, 3155 (2005).
32. Guo Zhen Liu, Can Wang, Hao Shuang Gu and Hui Bin Lu, J.Phy.D:Appl.Phys., **40** 7817-7820 (2007).

Chapter 4

Effect of Sm-substitution on SBTi ceramics

Chapter 4

Effect of Sm-substitution on SBTi ceramics:

4.1 Introduction:

Recent studies revealed that, ionic substitution in perovskite BLSF materials is an efficient technique to reduce their drawbacks of ferroelectric ceramics [1-3]. It is reported that fatigue free films with excellent ferroelectric properties are obtained by substitution of La^{3+} ions at Bi-site in $Bi_4Ti_4O_{15}$ films using pulsed laser deposition [4]. In this aspect, the properties of $SrBi_{4-x}Pr_xTi_4O_{15}$ system synthesized by soft combustion method [5] are interesting. Piezoelectric properties of this system got greatly improved when appropriate amount of Pr ions are introduced into the Bi ion-site. This result shows that the substitution of Bi^{3+} by rare earth ions of smaller ionic radius is effective in improving the dielectric and ferroelectric properties.

In this study, SBSmTi ceramic samples are prepared by solid-state reaction. However, the high temperatures are used during the sintering stage can cause problems in the stoichiometry of the final product owing to the volatization of Bi, and hence an alternative process to be explored. Some methods used to obtain bismuth-layered pervoskite ceramic precursors are hydrothermal, sol-gel and co- precipitation synthesis. But even after preparing precursors with these chemical methods, the sintering in general is done with the conventional heating. An attractive alternative for these problems is microwave sintering technique which often eliminates the stoichiometry problems by accomplishing the process at much lower temperatures over a short period of time, greatly diminishing the chances for Bi volatization.

4.2 Literature survey on rare-earth doped SBTi ceramics:

$Bi_4Ti_4O_{15}$ (BTO) is an attractive material that has low processing temperature (700-750^oC) than other BLSF (e.g. $SrBi_2Ta_2O_9$) and it exhibits strong anisotropy of the spontaneous polarization (P_s) along the *a*-axis (~50μC/cm^2) and *c*-axis (~ 4μC/cm^2) [6-7]. However, the low remanent polarization (P_r = 5μC/cm^2), low fatigue resistance and high dielectric loss of BTO would limit its application. The reduction in remanent polarization and fatigue with high dielectric losses become more serious issues due to defects in perovskite structure. It gets aggravated with the Bi ion volatization during sintering process, which creates the Bi vacancies accompanied by oxygen vacancies.

Two-site substitution in $Sr_{1+x}Bi_{4-x}Ti_{4-y}Ta_yO_{15}$, where Sr^{2+} and Ta^{5+} are substituted by Bi^{3+} and Ti^{4+} respectively, is done by Minglei et al [8]. This system showed the largest piezoelectric coefficients, electromechanical coupling factor and excellent pyroelectric responses. The piezoelectric, ferroelectric and dielectric properties of Nd-modified Bi_3TiTaO_9 (BNTT) and La-modified $Bi_{3-x}La_xTaO_9$ (BLTT) dense ceramics are compared by Muneyasu et al [9]. The BNTT and BLTT ceramics showed the highest coercive field (E_c) of 150KV/cm and highest mechanical quality factor of 11,000 respectively. Zheng Liaoying et al [10] investigated the structural and piezoelectric properties of $Ca_{1-x}Sr_xBi_4Ti_4O_{15}$ ceramics (x=0-1.0). The dependence on x is determined. The results showed that excellent properties are found in the composition of x=0.4. Rizwana et al observed that the Pr-doped SBTi ceramics exhibited the enhanced dielectric, ferroelectric and impedance properties than the un-doped SBTi ceramics [11].

The current study describes the results obtained during the optimization of Sm-substituted SBTi ceramics samples prepared by solid-state method. The structural, microstructural, Raman, dielectric, ferroelectric, mechanical and microwave dielectric properties were studied for both conventional and microwave sintered samples.

4.3 Preparation of Sm-substituted SBTi ceramics:

Synthesis of the material was carried out with a powder mixture containing equimolar amount of 99.9+ % pure Bi_2O_3, $SrCO_3$, Sm_2O_3 and TiO_2 (Aldrich make). The powder mixture was ball milled in deionized water for 1 hour at 150rpm. Zirconia vials and different diameter of spherical (5 and 20mm) zirconia balls are used for this study. These powders are dried in hot oven and then calcinated at 750^0C for 5 hours. Calcined powders are ball milled again for particle size reduction for about 15h at 300rpm with deionized water as mixing media. These powders were uniaxially pressed into circular pellets. Green pellets were sintered at 1190^oC for 2h in ambient atmosphere in a conventional furnace and 1150^oC for 40min in a microwave furnace. These sintering temperatures and duration are arrived at after optimizing for maximum density.

4.4 Characterization of Sm-substituted SBTi (SBSmTi) ceramics

4.4.1 Structural properties:

X-ray diffraction patterns of microwave and conventional sintered $SrBi_{4-x}Sm_xTi_4O_{15}$ (where x = 0.25, 0.5, 0.75 and 1) ceramics are shown in fig.4.1 and 4.2 respectively. It indicates that samarium substitution does not change the structure of SBTi or generate new phases. No significant difference in the lattice parameters was observed in samples with various contents of Sm as shown in table 4.1. The position of the diffraction peaks are in good agreement with the standard orthorhombic pattern. The similarity of XRD patterns are indicative of the similarity of chemical valance involved and close values of the ionic radii between Bi^{3+} and Sm^{3+} ions. The crystallite size of the conventional and microwave sintered samples were calculated by Debye-Scherrer formula. The crystallite size of the conventional sintered samples ranged from 60 to 80nm which is more than that of microwave sintered samples is around 40-50nm. As expected, the crystallite sizes of the microwave sintered samples are less than conventional sintered samples. It is evident from the XRD pattern that each peak broadening is more in microwave sintered samples than conventional sintered samples.

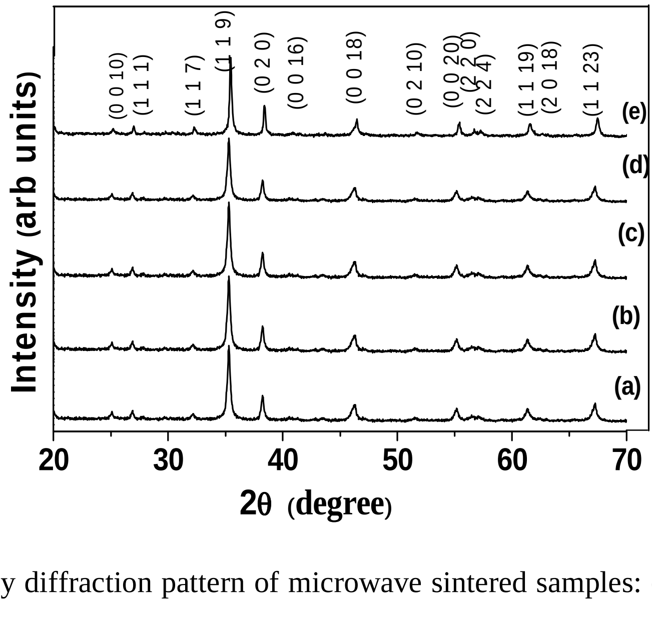

Figure 4.1: X-Ray diffraction pattern of microwave sintered samples: (a) $SrBi_4Ti_4O_{15}$ (b) $SrBi_{3.75}Sm_{0.25}Ti_4O_{15}$ (c) $SrBi_{3.5}Sm_{0.5}Ti_4O_{15}$ (d) $SrBi_{3.25}Sm_{0.75}Ti_4O_{15}$ (e) $SrBi_3Sm_1Ti_4O_{15}$.

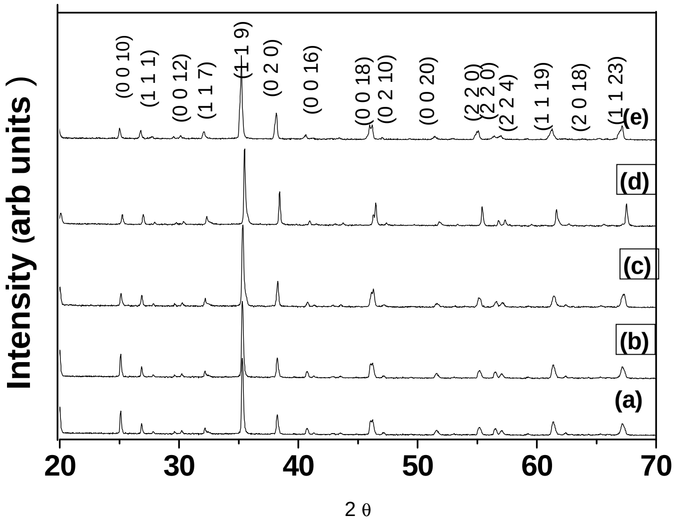

Figure 4.2: X-Ray diffraction pattern of conventional sintered samples: (a) $SrBi_4Ti_4O_{15}$ (b) $SrBi_{3.75}Sm_{0.25}Ti_4O_{15}$ (c) $SrBi_{3.5}Sm_{0.5}Ti_4O_{15}(d)SrBi_{3.25}Sm_{0.75}Ti_4O_{15}$ (e) $SrBi_3\,Sm_1Ti_4O_{15}$.

Sm content in sample	Lattice parameters (Å)			Volume (Å)^3
	a	**b**	**c**	
Sm 0	5.425	5.436	40.95	1207.62
Sm 0.25	5.424	5.439	40.932	1207.51
Sm 0.5	5.42	5.431	40.928	1204.75
Sm 0.75	5.423	5.434	40.921	1205.88
Sm 1	5.416	5.417	40.90	1998.81
Standard	5.428	5.438	40.94	1208.88

Table 4.1: Lattice parameter values of Sm-substituted SBTi ceramic samples.

4.4.2 Microstructural properties:

The microstructure of the Sm-substituted SBTi samples sintered by microwave and conventional routes are shown in figure 4.3 (a-d) and figure 4.4 (a-d) respectively. SEM images of Sm-substituted SBTi samples show grains in the form of platelets. This orientation is typical of Aurivillius phases and is due to the polycrystalline nature of the samples. SEM micrographs, shows that conventionally sintered samples got grains that are non-uniform and of platelet like shape. The microstructure of conventional sintered SBTi ceramics exhibits grains of different size ranges as well as micro cracks as reported by P.K Patro [12]. Whereas microwave sintered samples are highly densified and got uniform grain size. Uniaxially pressed circular samples of Sm-substituted SBTi pellets of 0.4 gm mass and 10mm diameter, were conventionally sintered in air at 1190^{o}C for about 2h to achieve above 90% of relative density. Similar samples were sintered in a microwave furnace at different temperatures and different time durations. It was found that there is obvious densification in the microwave field even at 1150^{o}C for 40min heating. The relative density of conventional and microwave sintered samples are shown in table 4.2. Maximum relative density of 97.5% is obtained at 1150^{o}C for 40min of microwave sintering. By contrast, conventional sintering of SBSmTi is slow. For example, 4 hour sintering at 1150^{o}C led to 80.5% of relative density. To get high densification conventionally, samples are to be sintered at high temperatures and for long period of time. The average grain size of the conventional and microwave sintered samples was found to range from 8-10µm and 4-6µm respectively. The increase in grain size for conventional sintered samples is not fully understood and needs further investigation but could be due to a phase with greater wettability resulting in a liquid phase that is clearly visible in the micrograph of figure 4.4. The grain size observed in microwave processed samples is smaller and denser than the conventional one. It was noticed that the average grain size relatively decrease with increasing Sm^{3+} contents, indicating a strong influence of substitution concentration which resulted in lesser amount of the Bi^{3+} in SBTi. The longer soaking time is required in conventional sintering as well as, its slow heating rate also could accelerates the grain growth at the cost of nucleation [13]. The density of the SBSmTi with x= 0.5 and 0.75 is higher than that of original SBTi ceramics in both conventional and microwave sintered processed samples. On the contrary, SBSmTi with x=1.0 is having lower density and this is due to structural distortion. Structural distortion in this composition is indeed evident through the shifts in both XRD pattern and Raman spectra. The rapidity of microwave sintering method could be a reason for suppression of grain growth resulting in a finer and uniform microstructure. The same phenomenon was observed by Chris Y Fang et. al also [14]. The substantially enhanced densification in the microwave sintered samples can be considered as the cause for their fairly enhanced mechanical properties. The atomic percentage of each element of the composition sintered by conventional and microwave process is shown in table 4.3.

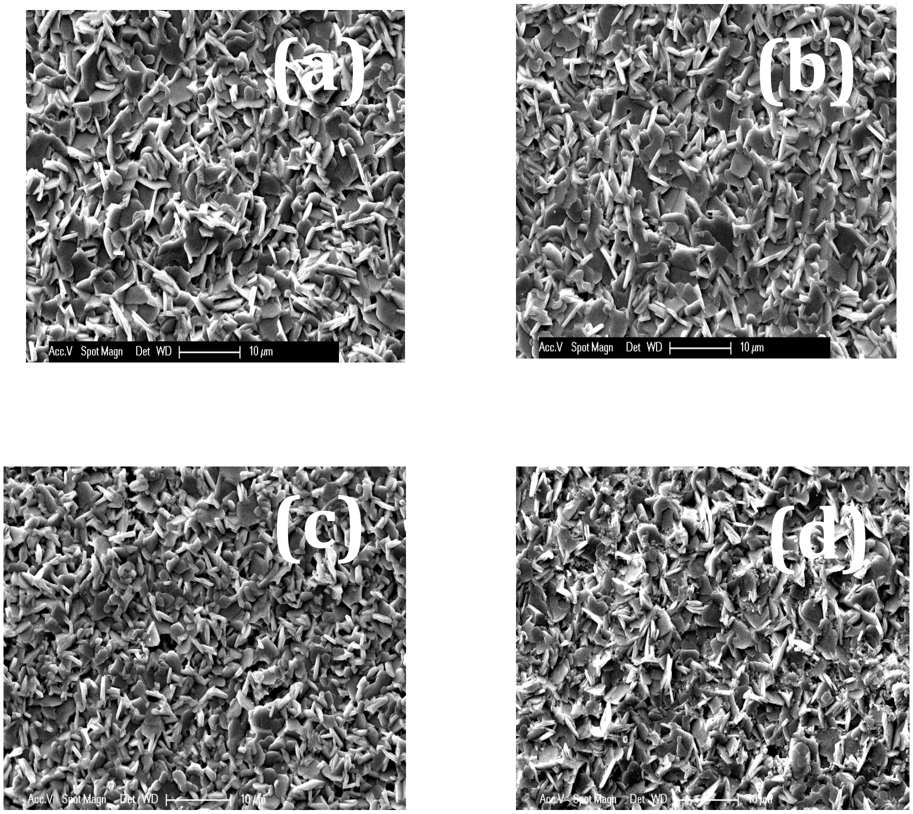

Figure 4.3(a-d): SEM micrographs of microwave sintered samples: (a) $SrBi_{3.75}Sm_{0.25}Ti_4O_{15}$ (b) $SrBi_{3.5}Sm_{0.5}Ti_4O_{15}$ (c) $SrBi_{3.25}Sm_{0.75}Ti_4O_{15}$ (e) $SrBi_3 Sm_1Ti_4O_{15}$.

Samples	**Relative density of samples with varying Sm content (x)**					**Sintering temperature (^{0}C)**
	Sm 0	**Sm 0.25**	**Sm 0.5**	**Sm 0.75**	**Sm 1.0**	
Microwave sintered	**92.7**	**92.5**	**95.5**	**97.5**	**88.4**	**1150**
Conventional Sintered	**90.6**	**91.6**	**93.8**	**94.1**	**88.1**	**1190**

Table 4.2: Relative density of microwave and conventional sintered SBTi and Sm-substituted SBTi ceramic samples

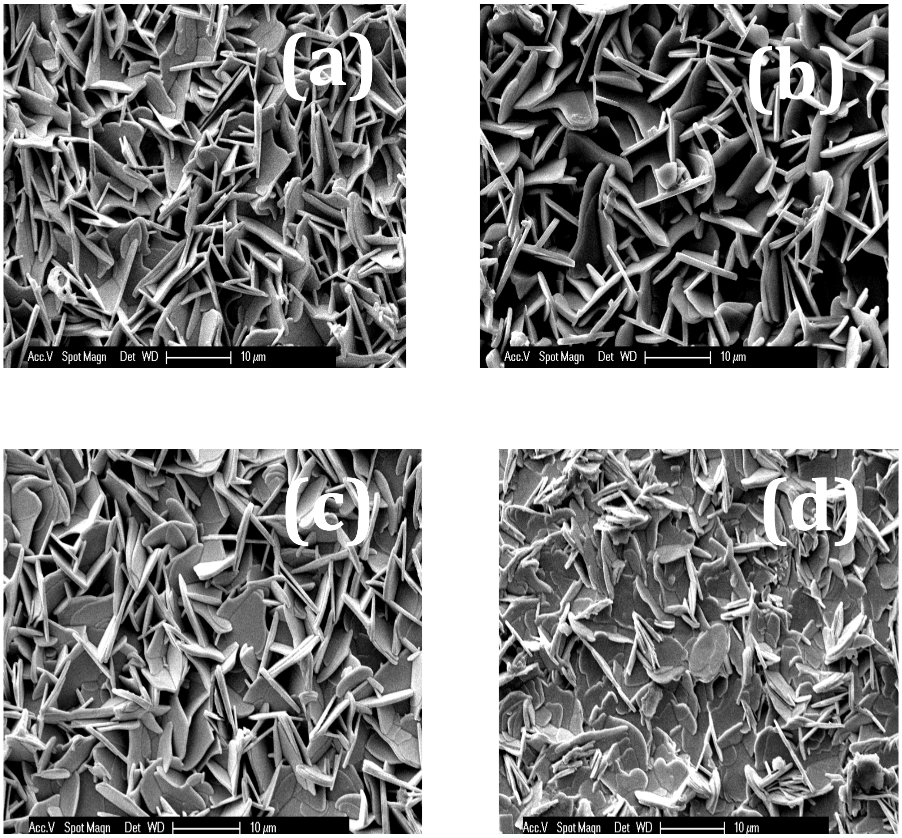

Figure 4.4(a-d): SEM micrographs of conventional sintered (a) $SrBi_{3.75}Sm_{0.25}Ti_4O_{15}$ (b) $SrBi_{3.5}Sm_{0.5}Ti_4O_{15}$ (c) $SrBi_{3.25}Sm_{0.75}Ti_4O_{15}$ (e) $SrBi_3Sm_1Ti_4O_{15}$.

	Element – Atomic %				
Conventional Sintering	**Bi**	**Sr**	**Ti**	**Sm**	**O**
Sm 0.25	**14.58**	**4.02**	**16.04**	**0.98**	**62.31**
Sm 0.5	**13.74**	**4.0**	**16.1**	**2.01**	**61.71**
Microwave sintering					
Sm 0.25	**15.55**	**4.11**	**16.44**	**1.12**	**62.89**
Sm 0.5	**14.51**	**3.91**	**16.32**	**2.08**	**62.49**

Table 4.3: Atomic percentage of each element in the samples sintered in conventional and microwave furnace obtained by EDX Technique

4.4.3 Raman spectroscopic studies:

Sm^{3+} ions can substitute for Bi^{3+} ions in $(Bi_2O_2)^{2+}$ layers and in pseudo-pervoskite blocks, since the chemical valance of Sm^{3+} is same as that of Bi^{3+} and their ionic radii are almost identical (Sm^{3+}:1.08 Å, Bi^{3+}:1.170 Å). Figure 4.5 and 4.6 showed the Raman spectra of microwave and conventional sintered $SrBi_{4-x}Sm_xTi_4O_{15}$ ceramic samples at room temperature. At x=0, the Raman spectra exhibits intense phonon modes at ~90,~133,~156,~268,~485,~561,~749, and ~ 866 cm^{-1} in addition to some weak peaks. The spectrum of SBSmTi is similar to that reported by Kojima et al. [15, 16]. The vibrational modes of BLSFs are classified as internal modes related to the motion of TiO_6 octahedra and the lattice translational modes related to the motion of the cations in the pseudo-pervoskite slabs and the Bi_2O_2 layers [17]. The modes with Raman shift lower than 200 cm^{-1} are related to the motion of heavier ions. For the BLSFs, the mode between 50 and 60 cm^{-1} is reported to arise from the displacement of Bi^{3+} ions in Bi_2O_2 layers, while those between 90 and 160 cm^{-1} originate from the vibrations of the ions at the A sites of the pseudo-pervoskite blocks[18]. The mode at ~268 cm^{-1} arises from the torsional bending of TiO_6 octahedra and those are at ~ 561, 726 and 866 cm^{-1} corresponds to the stretching of TiO_6 octahedra [19, 20]. Since Sm^{3+} ions substitute for the Bi^{3+} ions in Bi_2O_2 layers or pseudo pervoskite blocks, investigations on the modes with Raman shift at 55, ~90, ~126 and ~151cm^{-1} can explain the Sm substitution sites of SBTi. These Raman shifts exhibit the extent of changes with lattice modes on varying Sm content. For example, in the case of x <0.5, the Raman shift of the mode is at ~ 90 cm^{-1} corresponding to the vibration of Bi^{3+} ions in the Bi_2O_2 layers does not change with Sm- substitution while at x >0.5, the Raman shift decreases from 90 to 84 cm^{-1}, which is possible due to the Sm^{3+} substitution at Bi^{3+} site in Bi_2O_2 slabs. This implies that Sm^{3+} starts getting into the Bi^{3+} site of Bi_2O_2 layers only at x> 0.5. This feature remains same for both the sintering routes followed. On the other hand, Sm^{3+} ionic substitution may lower the corresponding binding strength and decrease the Raman shift due to the lower binding energy of Sm in comparison to that of Bi [21]. The mode at ~268 cm^{-1} from the torsional bending of TiO_6 octahedra does not shift with substitution. The modes that are at ~561, ~726 and ~ 866 cm^{-1} relate to the TiO_6 stretching mode. There is no observable difference in the peak positions and peak width between conventional and microwave sintered samples for all the modes, even with increasing Sm-content up to x= 0.75. It can be concluded that, the differences in sintering procedure is not affecting the intrinsic properties of the samples significantly. That means the microwave sintering influences only the extrinsic factors like density, grain size, grain morphology and crystallite size which are also important for determining the dielectric, mechanical and ferroelectric properties of a ceramic. In case of x=1.0, all the observable modes shifted towards higher frequencies in both conventional and microwave sintered samples. This could be attributed to the structural distortion at higher values of substitution in SBSmT system [22]. Same phenomena observed in XRD pattern also figure no.4.1. In addition, the Raman peak widths for this composition are different for the samples that are given different sintering treatments, with conventional sintering yielding a larger peak width compared to microwave sintering. One possible reason for the difference in peak widths could be the difference in Bi volatilization. Table 4.3 showed the atomic percentage of each element in the samples sintered in conventional and microwave processes.

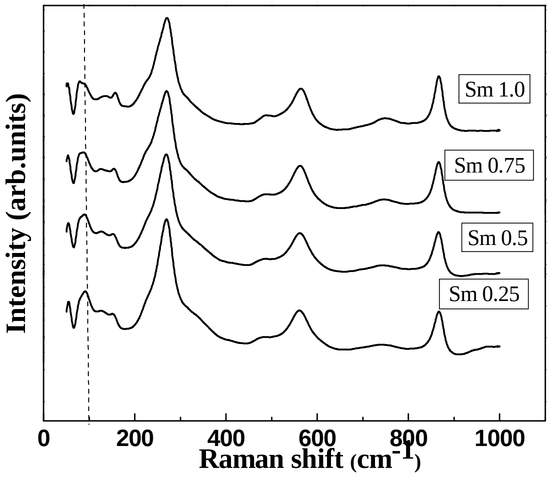

Figure 4.5: Raman spectra of microwave sintered Sm-substituted SBTi ceramic samples.

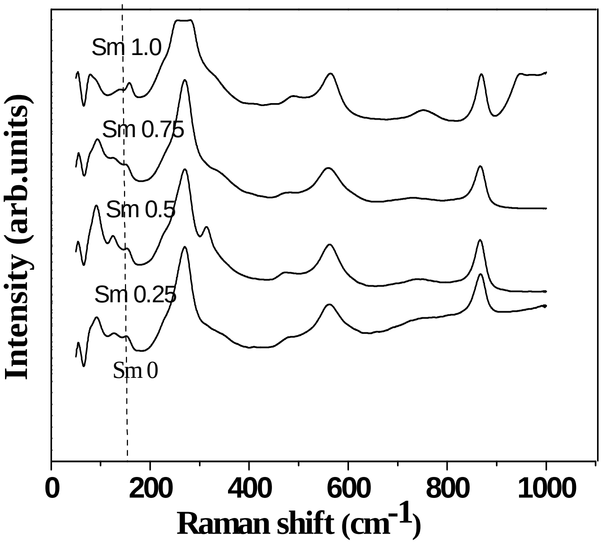

Figure 4.6: Raman spectra of conventional sintered Sm-substituted SBTi ceramic samples.

4.4.4 Dielectric properties:

Dielectric properties of SBTi with various Sm contents are investigated. Figure 4.7 (a-b) shows the frequency dependence of dielectric properties of microwave sintered Sm substituted SBTi ceramic samples while Figure 4.8 (a-b) shows that of conventional sintered Sm substituted SBTi ceramic samples. The measurements were performed at the frequency range from 40 Hz to 1 MHz. These results showed that the Sm-substituted SBTi ceramic samples exhibited better dielectric properties than the pure SBTi ceramics. Also, Sm-substituted samples sintered in microwave furnace exhibited higher dielectric constant than samples sintered in conventional furnace. As the Sm content increases, the dielectric constant increases except for x=1 case. This may be due to changes in structural and bonding characteristics at x=1 composition. This can be seen as a shift in the XRD pattern. In microwave and conventional sintering process, x = 0.5 and 0.75 shows the enhancement in properties. The differences in dielectric behavior between the conventional and microwave sintered samples are directly related to the higher density as well as more uniform and finer microstructure of the microwave sintered samples. The observed dielectric constant decreased slightly with increasing frequency. It is more pronounced in conventional samples except for x=0.5 and 0.75 cases. The phenomenon of appreciable decrease of dielectric constant with increasing frequency characterizes dispersion in the material and is usually attributed to the grain-to-grain interfacial effects, defects within the grains as well as interactions between the ferroelectric domains and charge carriers. But on contrary, the dielectric loss is increasing with increasing frequency for all the cases. The dielectric losses of microwave sintered samples are relatively less than conventional sintered samples. In case of microwave sintered samples, the samples which shows more dielectric constant (x=0.5 and 0.75) are having less dielectric loss indicating a highly ordered scenario**.** It is also noticed that the tan δ abruptly decreased for x = 0.5 and 0.75. The decrement in the tan δ can be attributed to a reduction in grain imperfections. It was also supported by an increase in relative density, in which the same ceramic samples appeared to be more dense. Above x= 0.5, the tan δ is almost consistent with the reduction of defects such as bismuth and oxygen vacancies. The rapidity of the microwave method also avoids the undesirable grain growth and provides a finer and uniform microstructure which led to high dielectric constant and lower dielectric loss values. In both cases the highest value of dielectic constant was observed for x=0.75 followed by x=0.5, x=1.0, x=0.25 and x=0. For microwave sintered samples, a reverse order could be observed in the case of the values of loss tangent. That means barring the case of x=1, higher Sm substitution is making the material more polarizable but with lesser losses for microwave sintered ceramic samples. With x=1, obviously the material changes its characteristics.

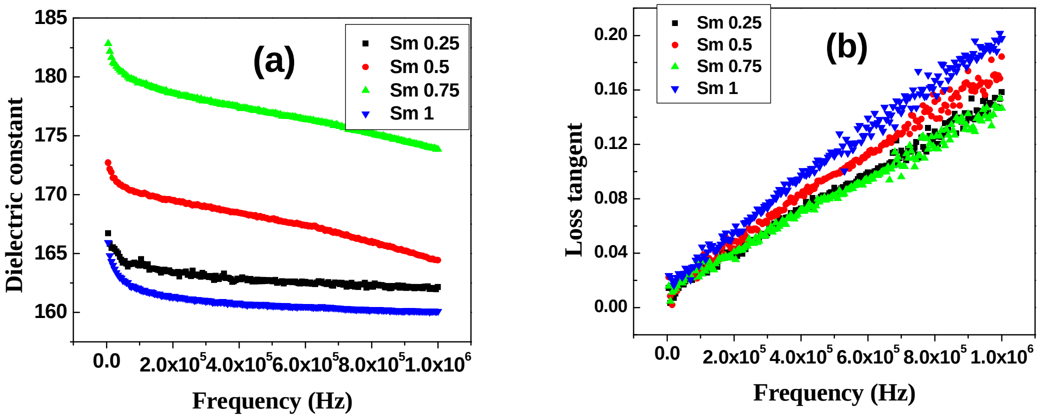

Figure 4.7: (a) Dielectric constant and (b) Loss tangent of microwave sintered SBSmTi ceramic samples as a function of frequency.

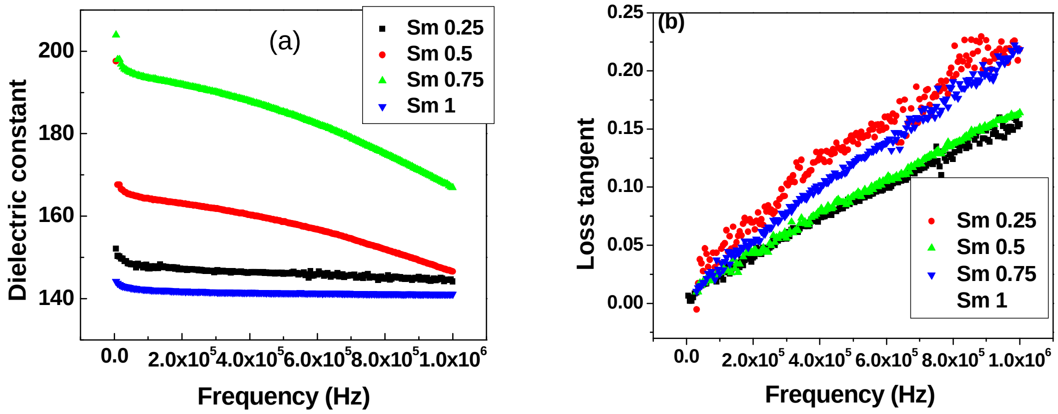

Figure 4.8: (a) Dielectric constant and (b) Loss tangent of conventional sintered SBSmTi ceramic samples as a function of frequency.

4.4.5 Temperature dependant dielectric properties:

Introduction to Relaxor Ferroelectrics:

The ferroelectric materials, which exhibit diffuse phase transition and dielectric dispersion, are usually named as Relaxor Ferroelectrics (RFEs). Dielectric dispersion generally explains the shifting of T_m towards higher temperature with increasing frequency. In order to understand the behavior of relaxor ferroelectrics, it is essential to contrast their characteristic properties from that of normal ferroelectrics [23]. A normal ferroelectric generally possesses a square hysteresis loop with large coercive field, spontaneous polarization and remnant polarization where as the relaxor possess slim loop. The P_r or P_s vanishes at T_c in normal ferroelectrics but they remains even above T_m in a relaxor. This indicates that the relaxors possess nano sized polar domains compared to the macro-size ferroelectric domains in normal ferroelectrics. For sufficiently high electric fields the nano domains of the relaxor can be oriented with the applied field leading to large polarization and on removing the field most of these domains reacquire their random orientations resulting in a small P_r. The small P_r is evidence for the presence of some degree of cooperative freezing of dipolar orientation. In ferroelectrics, the transition can be thermodynamically first or second order and involves a macroscopic symmetry change at T_c. Above T_c, the dielectric constant obeys Curie-Weiss law. In contrast, relaxor ferroelectrics exhibits diffuse phase transition with strong dielectric dispersion without undergoing any structural phase transition across T_m. The peak in the dielectric response is simply a manifestation of the slowing down of the dipolar motion below T_m [24]. The above discussion makes it clear that the properties and physics of relaxor ferroelectrics are different from those of normal ferroelectrics.

4.4.6 Theoretical models to explain relaxor behavior:

The relaxor behavior in the normal ferroelectric materials results from compositionally induced disorder or frustration. In the ABO_3 oxides, substitution of ions of different sizes, valences, electronegativities and polarizabilities at the A and B lattice sites produces dipolar defects and induces a sufficiently high degree of disorder so as to break transitional symmetry and prevent the formation of long range ordered state [25-26]. In reflecting on the occurrence of relaxor behavior in pervoskites, there appear to be three essential ingredients: the existence of lattice disorder [27-28], evidence for the existence of polar nanodomains at temperatures much higher than T_m and these domains existing as islands in a highly polarizable host lattice [29]. The existence of nano polar regions has also been evidenced by several other experimental techniques such as transmission electron microscopy [30], diffuse x-ray scattering and neutron diffraction studies [31-33]. Various physical models such as superparaelectric model, order-disorder transition model, microdomain switching model, dipolar glass model and random field model have been proposed to explain the behavior of relaxor ferroelectrics. However, none of these models has been successful in explaining it completely. Among them, the microdomain switching model is suggested to be the preferable one to study the diffused phase transition (DPT) phenomenon. Several researchers still adopt this model to discuss the DPT characteristics of the relaxors [34-37].

Study of dielectric properties over a wide range of frequency, electric filed and temperature is the principal tool for uncovering ferroelectricity. A strong temperature dependence of dielectric constant is associated with crystallographic phase transitions. In the present work, dielectric data is obtained at different frequencies from the low frequency impedance analyzer. Measurements are done as a function of frequency (100Hz-1MHz) from room temperature to 600^oC. Dielectric data is presented at four frequencies 10 KHz, 100 KHz, 500 KHz and 1 MHz in the temperature range from RT to 600^oC.

Figure 4.9 (a-e) shows the thermal variation of dielectric constant at different frequencies for microwave sintered samples. The dielectric constant of the sample didn’t vary considerably with increase of temperature from RT to 300^{o}C. With further increase of temperature from 300^{o}C, the magnitude of dielectric constant increases showing a peak around 520^{o}C. This temperature corresponds to Curie temperature at which ferroelectric phase transition to paraelectric phase takes place. The value of dielectric constant at T_c is found to be 510 for x =0. The values of the ε_{Tc} for x=0 at frequencies 10 KHz, 100 KHz, 500 KHz and 1 MHz are found to be 334, 321, 300 and 285 respectively. There is a decrease in dielectric constant with increase in frequency. For temperatures above T_c, dielectric constant decreases with increasing temperature.

Figure 4.10 (a-d) shows the temperature dependent dielectric constant at different frequencies for conventional sintered samples of Sm substituted SBTi. The dielectric constant of the samples didn't vary considerably with increase of temperature from RT to 300^{o}C. With further increase of temperature from 300^{o}C, the magnitude of dielectric constant increases showing a peak around 520^{o}C. This temperature corresponds to Curie temperature at which ferroelectric phase transition to paraelectric phase takes place. There is a decrease in dielectric constant with increase in frequency. For temperatures above Tc, dielectric constant decreases with increasing temperature.

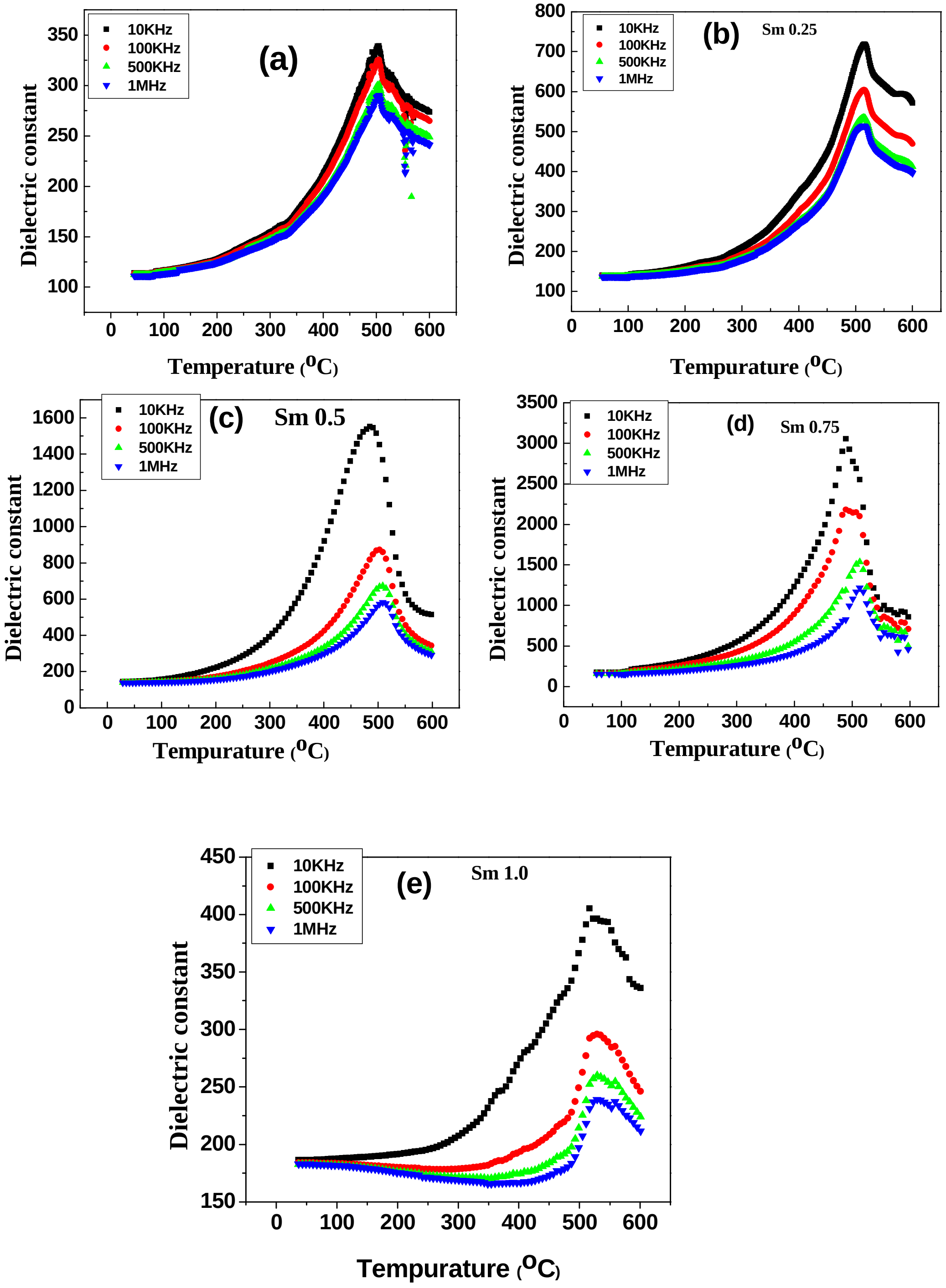

Figure 4.9(a-e): Temperature dependence of dielectric constant for different Sm-content SBTi ceramic sintered by microwave heating (a) Sm 0 (b) Sm 0.25 (c) Sm 0.5 (d) Sm 0.75 and (e) Sm 1.

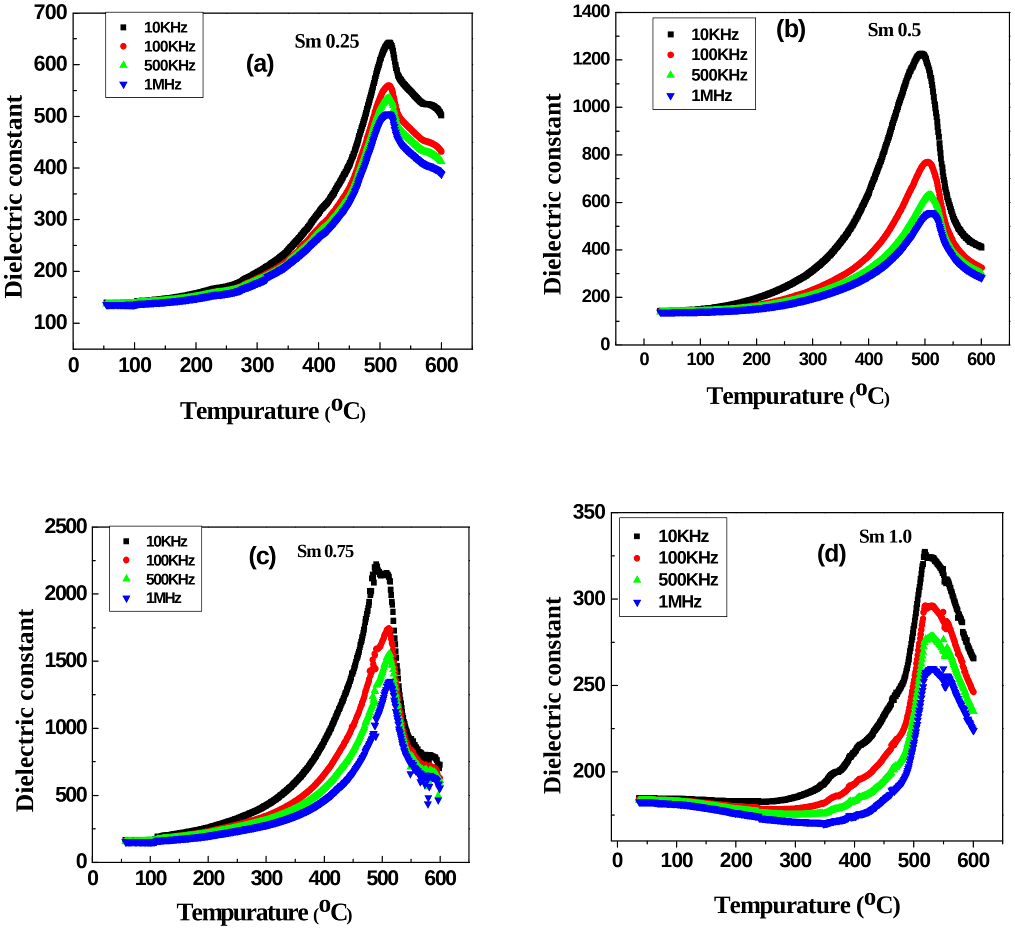

Figure 4.10 (a-d): Temperature dependence of dielectric constant for different Sm-content SBTi ceramic sintered by conventional heating (a) Sm 0.25 (b) Sm 0.5 (c) Sm 0.75 and (d) Sm 1.

The temperature dependence of permittivity for x=0 samples, follows the Curie-Weiss law and there is no dielectric permittivity shift at higher temperatures. For substituted samples, obvious deviations from the Curie-Weiss behavior on the high temperature side of the permittivity peaks were observed. It is interesting to observe that the dielectric constant of Sm-substituted SBTi is significantly increasing with increasing substitution concentration up to Sm 0.75. Another interesting observation is that substitution of samarium exhibited the relaxor behavior in the system. It is seen that as the substitution content increases, the peak is broadening in the dielectric permittivity curve except for x= 0.75, which corresponds to the ferro-paraelectric phase transition. There is a clear dielectric permittivity shift towards higher temperature side as the frequency increases. These are the typical behavior of relaxor ferroelectrics as observed by many researchers [38-40]. This indicates that Sm substitution brings about a strong diffusion of the ferro-paraelectric phase transition. The shift of T_m with measuring frequency suggests the existence of polar regions in Sm-$SrBi_4Ti_4O_{15}$ [41]. Typical relaxor ferroelectrics usually exhibit a high dielectric constant around T_m due to the rapid slipping of polar clusters [42]. The observed dielectric data has followed the same trend and moreover, improved its properties by substituting the samarium compared to reported values [43]. The observed dielectric permittivity as a function of temperature was fitted using Gaussian distribution. According to Gauss's law, the phase transition temperature T_c, tends to be the normal distribution when it is near T_m and the dielectric constant ε can be described as

$$\varepsilon = \varepsilon_m \exp\left[-\frac{(T-T_m)^2}{2\delta^2}\right] \tag{4.1}$$

Where ε_m is the maximal dielectric constant, ε is the dielectric constant, Tm is the temperature where ε_m occurs and δ is the standard deviation of the Tc distribution. The higher the δ value is, the broader the Tc distribution and diffusion characteristic is more obvious. Kirlov and Isupov derived the following equation by using Taylor's series expansion by ignoring the higher-order terms [44].

$$\varepsilon = \frac{\varepsilon_m}{\left[1+\frac{(T-T_m)^2}{2\delta^2}\right]} \tag{4.2}$$

Where the physical meaning and mathematical meaning of the ε_m, T_m and δ are the same as mentioned above. Researchers used equation 2 to describe the diffusion characteristics in relaxor materials [45]. The experimental and fitted graphs are shown in figure 4.11. The observed standard deviations of the fitted values are exactly matched with standard deviation of the experimental values as shown in table 4.4. From these results we can conclude that the samarium substituted SBTi ceramics exhibited the relaxor behavior. As observed in dielectric data, the dielectric constant increased as the samarium substitution increases up to 0.75 in both microwave and conventional sintered samples. For x=1.0, the dielectric constant is decreased due to structural distortion with higher content of samarium.

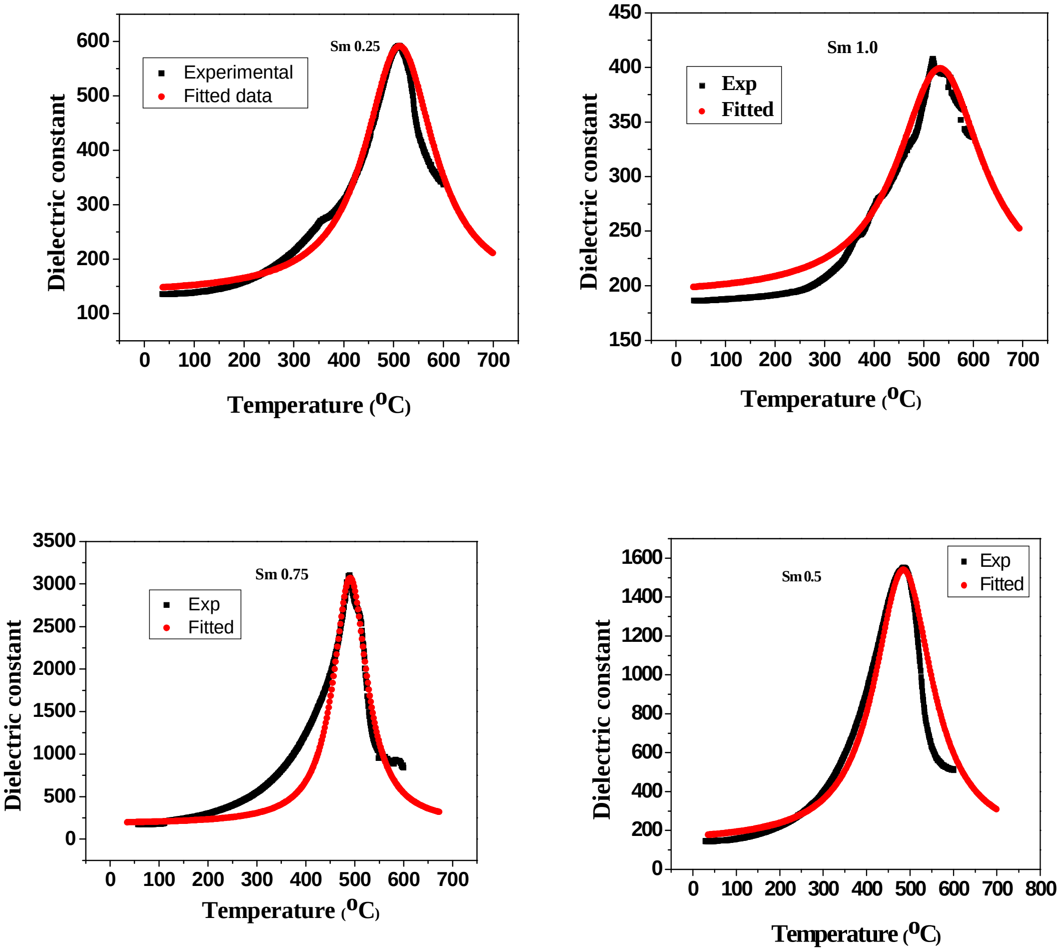

Figure 4.11: The experimental and fitted graphs of the dielectric constant vs. temperature data for Sm-substituted SBTi ceramic samples sintered in microwave furnace.

	10KHz				**1MHz**			
	Tc (^{o}C)	**e_m**	**δ (exp)**	**δ (fit)**	**Tc (^{o}C)**	**e_m**	**δ (exp)**	**δ (fit)**
Sm 0.25	511	717	31	28	516	505	29	28
Sm 0.5	485	1409	57	58	510	543	54	54.1
Sm 0.75	492	2875	27	24	514	1072	30	29
Sm 1.0	531	393	73	69	544	235	68	67.07

Table 4.4: Experimental and fitted values of the standard deviation of T_c distribution of Sm-substituted SBTi ceramic samples

Variation of dielectric loss with temperature and frequency

When alternating fields are applied, the charge stored on a dielectric has both real and imaginary components, which is caused by either resistive leakage or dielectric absorption. This is nothing but dielectric loss or loss tangent (tan δ). This loss is expressed by the ratio of the out-of-phase component to the in-phase component. Dielectric loss is calculated as tan δ = ε”/ ε’ where ε” is the imaginary and ε’ is the real part of the complex permittivity.

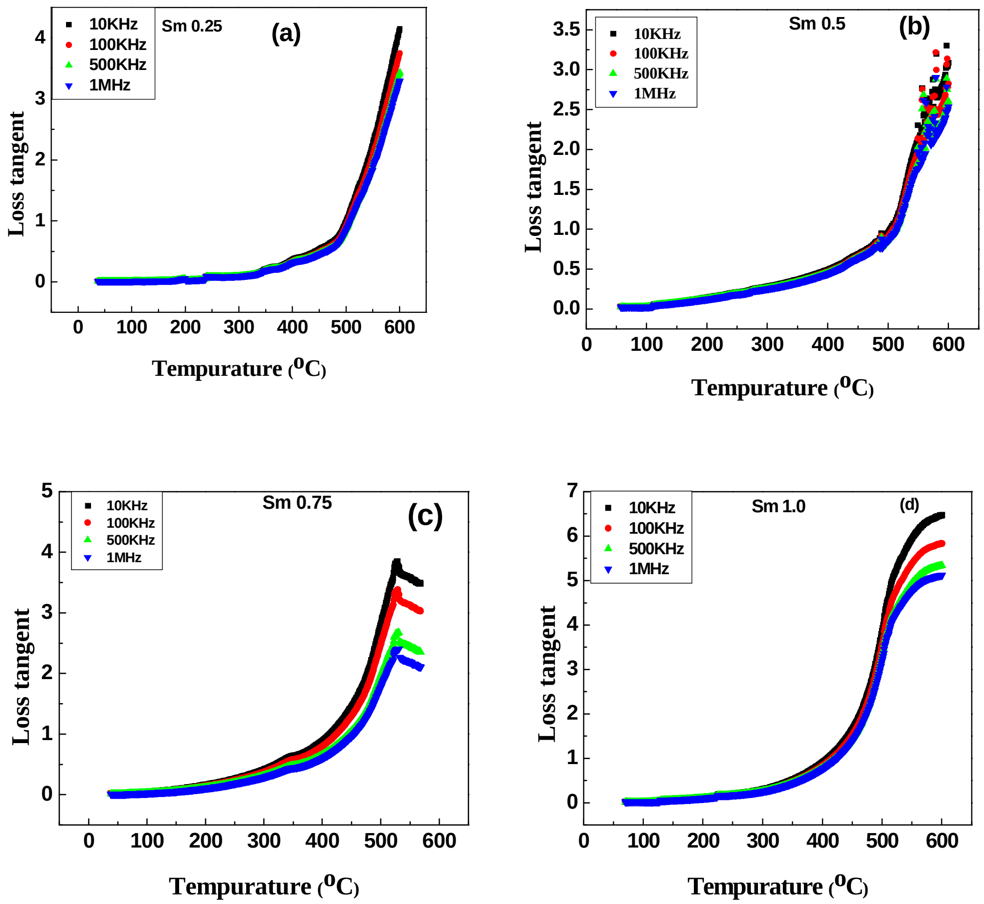

Figure 4.12 (a-d): Temperature dependence of loss tangent of SBTi ceramics with different Sm-content, sintered by microwave heating (a) Sm 0.25 (b) Sm 0.5 (c) Sm 0.75 and (d) Sm 1.

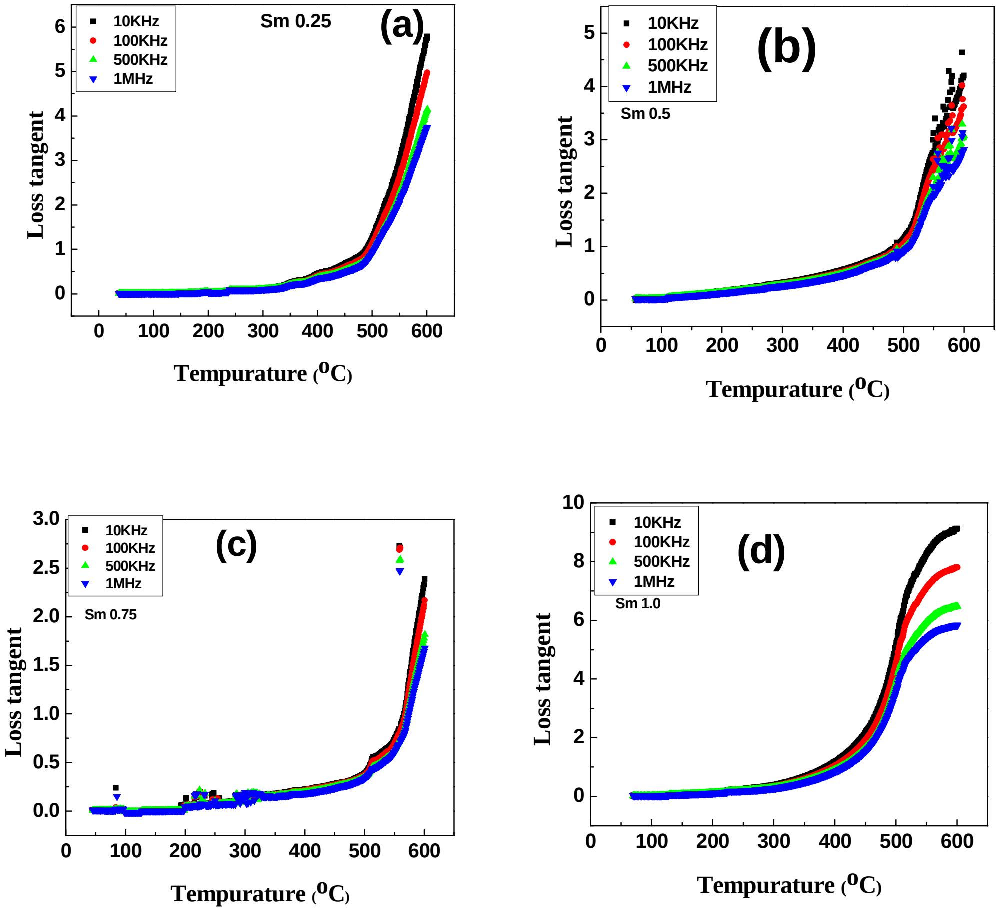

Figure 4.13 (a-d): Temperature dependence of loss tangent of SBTi ceramics with different Sm-content, sintered by conventional heating (a) Sm 0.25 (b) Sm 0.5 (c) Sm 0.75 and (d) Sm 1.

Figure 4.12 (a-d) shows the variation of dielectric loss as a function of temperature (RT-600^{0}C) at four different frequencies 10 KHz, 100 KHz, 500 KHz and 1 MHz for microwave sintered samples. As seen in the graph, dielectric loss increases slowly with increase in temperature. But once temperature is above Curie temperature, there is an abrupt increase in the dielectric loss due to conductivity of the samples at high temperature. Interestingly, dielectric loss is decreased as the frequency is increased which indicates that these samples are of high purity and confirms the ferroelectric phase transition [46]. In all cases we have observed the same trend. Figure 4.13 (a-d) shows the variation of dielectric loss as a function of temperature at different frequencies for conventional sintered samples. These samples also follow the same trend. The observed dielectric loss of the conventional sintered samples is more than the microwave sintered samples. X = 0.75 samples exhibited low dielectric loss compared to other compositions in both conventional and microwave sintered samples which is supported by the microstructure and density of the same samples.

4.4.7 Ferroelectric properties:

Figure 4.14(a-d) and 4.15(a-d) displays the ferroelectric hysteresis loops of conventional and microwave sintered Sm-substituted SBTi ceramic samples. The observed ferroelectric properties got reduced compared to pure SBTi ceramics. It is well known that the occurrence of the ferroelectric micro domains gives birth to properties typical for the ferroelectric relaxor [47]. In case of observed relaxor behavior in Sm-substituted SBTi ceramics; the Sm content plays an important role in this property. As the relaxor behavior increases, the ferroelectric properties are degraded. There is no observable changes in ferroelectric properties of Sm-substituted SBTi ceramics for x = 0.25 and 0.5. At x = 0.75, the ferroelectric properties are enhanced. These results are supporting the relaxor properties of Sm-substituted SBTi samples which are discussed in 4.4.6. Substitution of Samarium ion into A-site of SBTi leads to the decrease of point defects such as oxygen vacancies so that relatively ferroelectric properties are enhanced up to x = 0.75. For x = 1.0, the relaxation of lattice distortion of SBTi become prominent and exerted a negative influence on the increase of $2P_r$ though Sm ions at A-site still contribute to increase in $2P_r$. The overall Sm-substitution in SBTi becomes weak which leads to decrease of 2Pr value at higher Sm content [48]. In these compositions, bismuth oxide planes got a net electrical charge, their positioning in the lattice is self-regulated to compensate for the space charges [49]. The defects, such as oxygen vacancies can easily migrate and accumulate at the domain walls, thereby pinning the domains [50]. However, this kind of migration and accumulation may be restrained by the Bi_2O_2 layers due to their effect on the space charge compensation and the insulation layers, thereby weakening the pinning of the domains. The substitution of Sm ions into Bi_2O_2 layers may destroy the original effects of the insulation layers as well as the space-charge compensation. Consequently, it weakens the role of Bi_2O_2 layers as refraining from the accumulation of oxygen vacancies in the pseudo-pervoskite slabs. Thus, the defects can easily migrate toward and concentrate at the domains walls, which may increase local strain fields. The interactions among the ferroelectric domains are blocked and the micro domains are induced [51]. Hence, the appearance of the ferroelectric relaxor transition can be generated from the competition of the micro domains induced by the interactions among the ferroelectric domains and micro domains induced by the random strain fields. In other hand, Samarium substitution enhances the chemical and structural inhomogeneity, and leads to a break in the translational symmetry, which is unfavorable for the coupling of the concentration and coupling of the dipole moments [52]. With samarium substitution, both the concentration and coupling of the dipoles are decreased. Consequently, the ferroelectric properties are decreased.

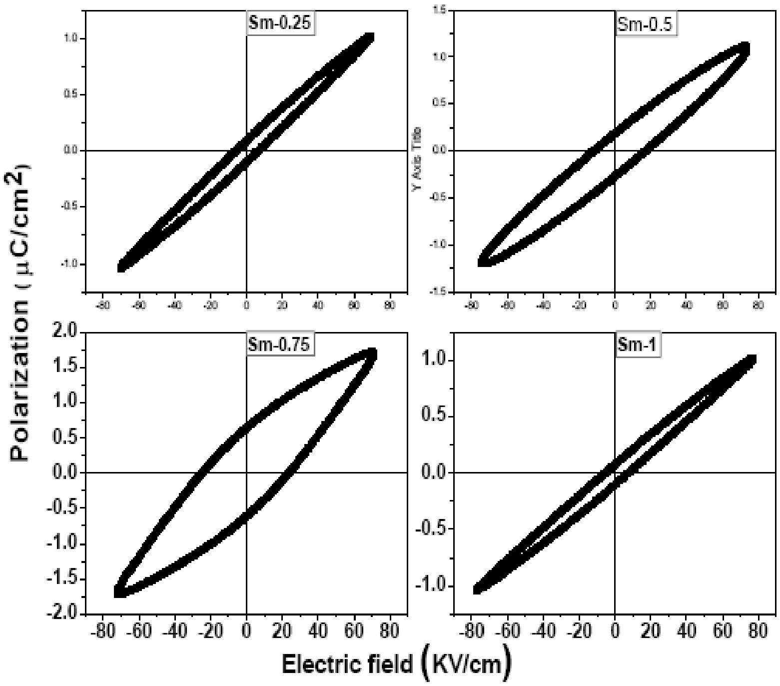

Figure 4.14: P-E loops of microwave sintered Sm-substituted SBTi ceramic samples.

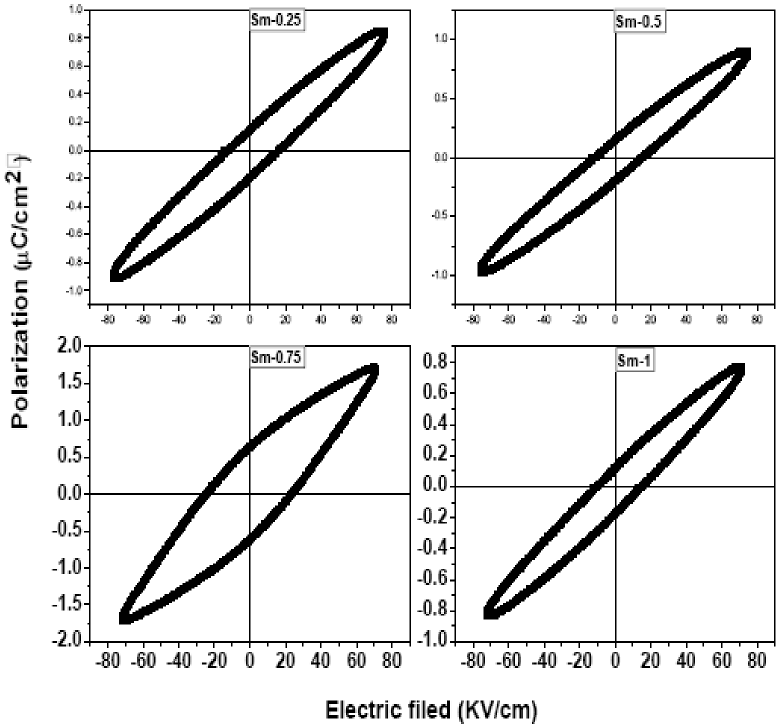

Figure 4.15: P-E loops of microwave sintered Sm - substituted SBTi ceramic samples.

4.4.8 Mechanical properties:

Figure 4.16 showed the typical measured Load-Displacement curve of SBSTi ceramics. Figure 4.17 (a-b) & 4.18 (a-b) shows the mechanical properties of the conventional and microwave sintered samples of Sm substituted SBTi ceramics measured by nanoindentation technique. The hardness and Young's modulus values are the average of the five indentations at different places to avoid microstructural effect on mechanical properties. It should be mentioned that mechanical properties of SBTi ceramics are previously not reported. The hardness of the microwave sintered samples ranged from 8.8 to 11.5 GPa and that for the conventional sintered samples is 8–11 GPa. It could be noted from figures 4.17 (a) and 4.18(a) that, as the Sm content increases the hardness also increases in both conventional and microwave sintered processes. Sm ~ 0.75 samples showed good mechanical properties for both microwave and conventional sintered cases. On the other hand, Sm ~ 1.0 is showing inferior mechanical properties compared to x= 0 – 0.75 and this could be due to higher porosity. It is well known that the mechanical properties of the materials depend on the microstructure and porosity. These results highlights that the hardness of the SBSmTi ceramic samples increases with deceasing porosity. The Young's modulus of the microwave and conventional sintered samples are ranged from 160 to 180GPa and 135-155GPa respectively. The high Young's modulus values reflect the lower defect density and finer grains of the samples. Moreover it is interesting to observe that the Young's modulus values are depending on the grain size of the samples. The samples which are having less grain size are having higher Young's modulus. Same phenomena are observed by J. Ricote and L. Pardo [53] also. The results obtained implies that the hardness is independent of grain size and Young's modulus seems to decrease with increase of grain size. The improved mechanical strength achieved in microwave processing could be attributed to small grain size and uniform microstructure where crack centers like large pores and defects are few. Density measurements are supporting the mechanical properties of the microwave sintered samples.

For both the conventional and microwave sintered cases, it is quite remarkable that, the highest hardness and Young's modulus values are obtained with samples having x=0.75 and the same composition gave the best dielectric properties as mentioned previously in section 4.3.3 of this chapter. It is true that density, microstructure and composition influences both dielectric and mechanical properties. Yet, this coincidence as observed previously [54] reinforces the suspicion that mechanical and dielectric properties are related at least in these systems, to give best results for both the properties in the same composition, when composition is varied systematically.

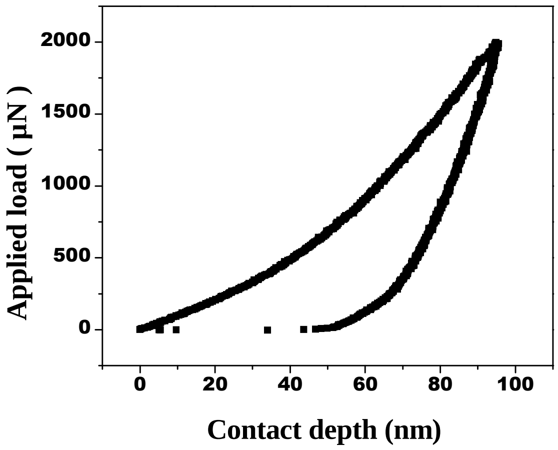

Figure 4.16: Typical measured load-displacement curve.

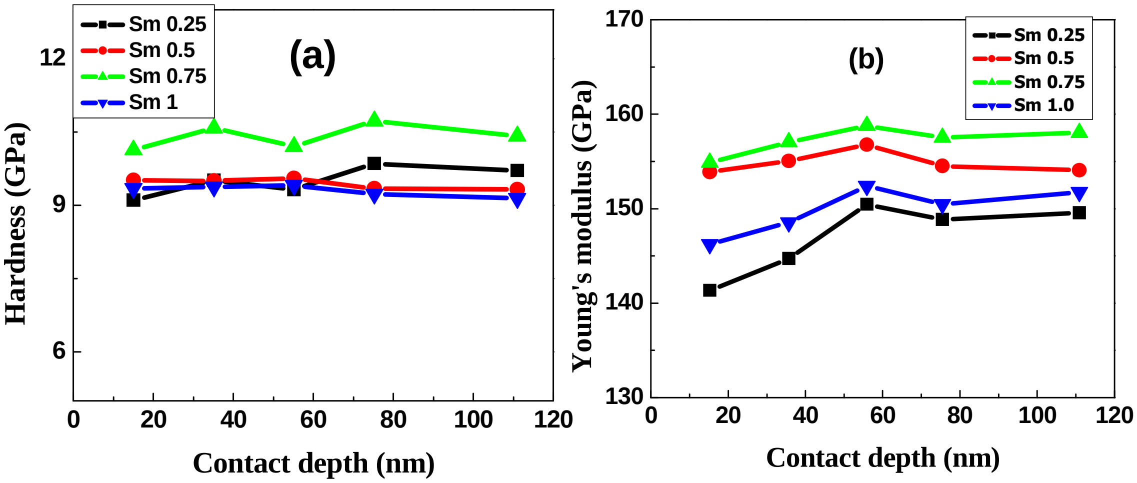

Figure 4.17 (a-b): (a) Hardness (b) Young's modulus of conventional sintered SBSmTi ceramic samples as function of contact depth.

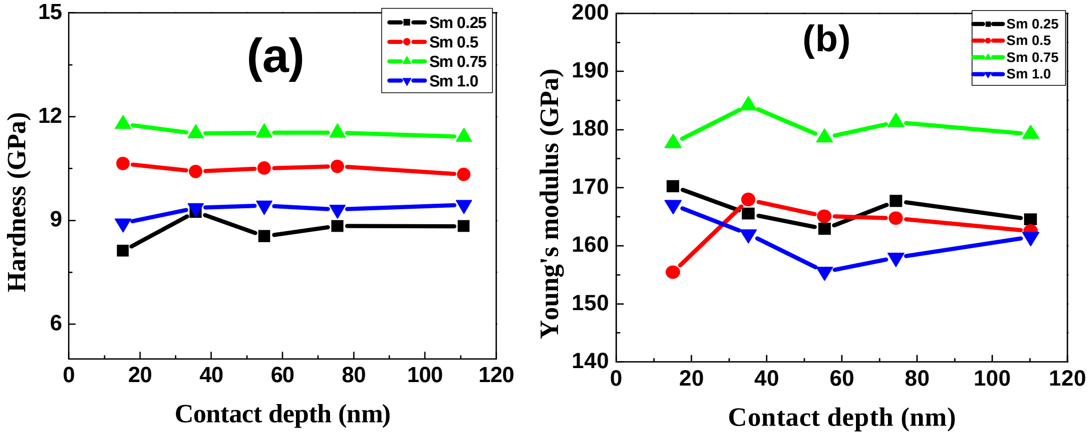

Figure 4.18 (a-b): (a) Hardness (b) Young's modulus of microwave sintered SBSmTi ceramic samples as function of contact depth.

4.4.9 Microwave dielectric properties:

We have used transmission/reflection method to measure complex permittivity. For microwave measurements, the samples were prepared in the form of rectangular disks (10.2 mm x 22.9 mm) to fit snuggly in the X- band waveguide (WR-90). The measurements are carried out by inserting the samples inside the X-band waveguide. The microwave measurements are accomplished for the SBTi sample, obtained in the microwave and conventional sintering process, with substitutions of Sm_2O_3 (0.25, 0.5, 0.75 and 1 wt %). The results were obtained, in terms of dielectric permittivity (ε') and dielectric loss for frequencies in the range of 8.2–12.4 GHz. The microwave dielectric permittivities are related to the structural and bonding characteristics of the material. The relative density, porosity and average grain sizes of sintered bodies are considered to be the key extraneous factors influencing the dielectric properties. Some authors said that the lower dielectric permittivity is due to lower density, because of pore formation [55]. In figure 4.19 (a-b) and 4.20 (a-b), the dielectric permittivity (ε') and dielectric loss (ε'') of SBSmTi ceramic samples are given against the percentage of Sm-substitutions for samples sintered by conventional and microwave methods respectively. In both cases, as the Sm content increases the dielectric constant increases up to x=0.75. There is negligible variation in values of dielectric constant for x= 0.5 and 0.75. The dielectric permittivities of SBTi, regardless of the substitution level, are associated with ionic and atomic polarization. Since the ionic radii of Sm^{3+} are different from the original site ions (Bi^{3+}), increasing the amount of additional ions would lead to a change of both the electronic and ionic polarizations. Ionic polarization is strongly dependent on the crystal structure, including density and lattice constants or unit cell volume [56]. From the observed Raman spectra in section 4.4.3, it is confirmed that Sm^{3+} starts getting into the Bi^{3+} site of Bi_2O_2 layers only at x> 0.5. The observed microwave dielectric properties are strongly dependent on substitution level of the samarium content as observed in low frequency dielectric properties mentioned in section 4.4.4. From Raman analysis, we can explain that the polar distortion got suppressed for x = 0.5 and 0.75 resulting in the observed high dielectric constant values. In addition to that, the observed TiO_6 stretching mode at 866cm^{-1} is rigid even at samarium substitution. The dielectric response of oxygen octahedra based structures are increased when the octahedra are aligned. A stiffening of this mode could mean an alignment of the octahedra resulting in higher values of dielectric constant as it could be seen in the present study. Raman spectra observed for conventional sintered samples gave larger peak width compared to their microwave sintered counterparts. One possible reason for the difference in peak widths could be the difference in Bi volatilization which could lead to structural distortions resulting in line broadening of the Raman spectra as well as a reduction in the microwave dielectric properties. The observed relative densities of the Sm-substituted SBTi samples are shown in table 4.1. It is well known that the dielectric constant increases with density. Also, there would be an increased ionic polarization with an increased Sm^{3+} concentration, due to a combination of an unchanged unit cell volume and a reduced ionic radius. The experimental dielectric constant was corrected for porosity of the ceramic samples. The measured and porosity corrected dielectric constant values are shown in table 4.5. The porosity corrected dielectric constant was calculated using the following equation.

$$\varepsilon_{r,corr} = \varepsilon_{r,\exp}\left[\frac{2+p}{2-2p}\right] \tag{4.3}$$

Where $\varepsilon_{r,exp}$ is the measured permittivity $\varepsilon_{r,corr}$ is the corrected permittivity and P is the porosity.

Frequency (GHz)	Sm 0		Sm 0.25		Sm 0.5		Sm 0.75		Sm 1.0	
	ε_{exp}	ε_{corr}	ε_{exp}	ε_{corr}	ε_{exp}	ε_{corr}	ε_{exp}	ε_{corr}	ε_{exp}	ε_{corr}
8.2	98	105	110.5	121.8	120.4	129.8	122.5	129.8	111.5	114.7
9	92	102	104.2	116.1	116.8	123.3	118	122.8	107	110.1
10	87	95	100.6	111	113.5	120.5	115.6	121.9	103.6	108.8
11	82	91	94.4	107.4	111.2	118.4	114.4	119.5	101	107
12	78	88	90.7	101.5	109.2	117.2	112.7	117.7	100.8	105.7
12.4	75	82	88.8	90.1	105.7	114.4	109.5	115.6	98.2	100.8

Table 4.5: The measured and porosity corrected dielectric constant values of different Sm-substituted SBTi ceramic samples in X band frequencies.

An increase in the dielectric permittivity indicates that the increase in ionic polarization is predominant over the decrease in electronic polarization corresponding to a smaller ionic radius. However, a high concentration of samarium (x=1) caused a reduction in the lattice constants and the unit cell volume. Therefore, both atomic and ionic polarization would decrease with an increasing amount of samarium introduced into the system and lead to reduced dielectric permittivity [57]. The observed dielectric constant values are quite higher than the earlier reported values [58]. Interestingly, the observed dielectric loss is decreased as the Sm-content increases up to x=0.75.

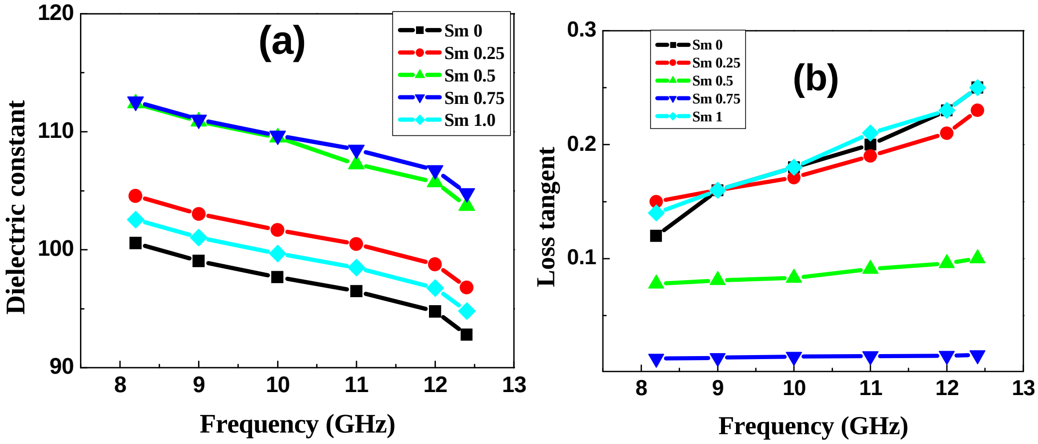

Figure 4.19: (a) X band dielectric constant and (b) loss tangent of the Sm-substituted SBTi ceramic samples sintered in conventional furnace.

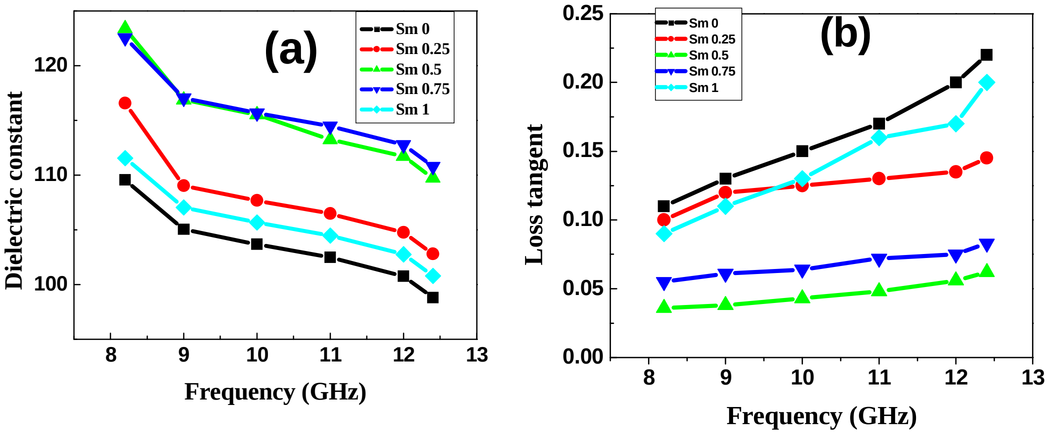

Figure 4.20: (a) X band dielectric constant and (b) loss tangent of the Sm-substituted SBTi ceramic samples sintered in microwave furnace.

4.5. Summary:

- The systematic comparison study for conventional and microwave sintered samples of SBTi ceramics with different amount of Sm-substitution has been studied and their densification dependence on sintering conditions studied.
- There was no observable change in structural properties as the substitution content increases up to x=0.75. With further increase of the Sm content, structural changes are observed due to distortion and grain size is decreased.
- Microwave sintered samples obtained good densities at lower temperature and lesser soaking time compared to conventional sintered samples and smaller grain sizes were obtained in microwave sintering process.
- With substitution of Samarium, there is a clear dielectric permittivity shift towards higher temperature side as the frequency increases and dielectric permittivity of the peak is broadening. These are the typical behavior of relaxor ferroelectrics. This indicates that Sm substitution brings about a strong diffusing of the ferro-paraelectric phase transition. The shift of Tm with measuring frequency suggests the existence of polar regions in Sm-$SrBi_4Ti_4O_{15}$
- For x=1, there is an observable shift in XRD pattern and changes in lattice parameter values which led to the decrease of dielectric constants and Curie temperature. It was found that high concentration of Samarium was likely to promote space charge polarization into the system resulting in a decrease in both dielectric constants and Curie temperature.
- With samarium substitution, both the concentration and coupling of the dipoles are decreased. Consequently, the ferroelectric properties are decreased.

- Mechanical properties of the Sm-substituted SBTi ceramic samples were studied for both microwave and conventional sintered samples. Hardness and Young’s modulus of the microwave sintered samples were higher than the conventional sintered samples which are in agreement with the microstructural and density properties.
- Microwave dielectric measurements were carried out in X-band frequencies by a waveguide based technique. This composition exhibited the high dielectric constant and low loss tangent when x= 0.5 & 0.75 compared to the other layered structured materials. From these results, the Sm-substituted SBTi ceramic samples are seemed to be a good candidate for lead-free ferroelectric applications.
- Over all, the microwave sintered samples have exhibited better properties than the conventional sintered samples, that too with a reduced sintering temperature and soaking time.

References:

1. Cui, L. & Hu, Y, J. Physica B: Cond.Matter., **404**, 150 (2009).
2. Santos, V. B., M'Peko, J. C., Mir, M., Mastelaro, V. R. & Hernandes, A. C, J.Eur.Cer.Soc., **29,** 751 (2009).
3. Simões, A. Z., Stojanovic, B. D., Ramirez, M. A., Cavalheiro, A. A., Longo, E. & Varela, J. A, J.Cer. Inter., **34**, 257 (2008).
4. Park, B. H., Kang, B. S., Bu, S. D., Noh, T. W., Lee, J. & Jo, W, J. Nature., **401,** 682 (1999).
5. Wang, C. M., Lin, S. Y., Kao, K. S., Chen, Y. C. & Weng, S. C., J.Alloys and Comp., **491**, 423 (2010).
6. Wang, X. S., Zhang, Y. J., Zhang, L. Y. & Yao, X., Applied Physics A: Materials Science and Processing, **68,** 547 (1999).
7. Zhi-hui, C., Jun-fu, Q., Cheng, L., Jian-ning, D. & Yuan-yuan, Z., Ceramics International, **36,** 241 (2010).

8. Minglei Zhao, Chunlei Wang, Weilie Zhong, Jinfeng Wang et al., Jpn.J. App Phys **41,** 1455-1458 (2002).
9. Muneyasu Suzuki, Hajime Nagata, Jin Ohara, Hiroshi Funakubo et.al Jpn.J Appl Phys **42,** 6090-6093 (2003).
10. Zheng Liaoying, Li Guorong, Zhang Wangzhong, Chen Daren and Yin Qinrui Mat.Sci and Engg B **99,** 363-365 (2003).
11. Rizwanaa , G.S.Kumar and P.Saraha International Symposium of Research Students on Materials Science and Engineering (ISRS-2004)
12. P.K. Patro, J Ind. Inst. Metals., **59**,229-235 (2006).
13. Morteza Oghbaei, Omid Mirzaee. J. Alloys and comp., **494,**1-2: 175-186 (2010).
14. Chris Y Fang, Clive A Randal, Michael T Lanagan. J. Electro. cer; **22**, 125-130 (2009).
15. S. Kojima, R. Imaizumi, S. Hamazaki et al. J. pn. J. Appl.Phy., Part1; **33**, 5559 (1994).
16. S Kojima, R. Imaizumi, S. Hamazaki et al. J. Mol. Struct. **348**, 37-40 (1995).
17. M. Osada, M. Tada, M. Kakihana, T. Watanabe et al, Jpn. J. App. Phy. *(Par1)* **40**, 5572(2001).
18. R.D Shannon, J. Acta. Crys. A**., 32**,751(1976).

19. N. Sugita, E. Tokumistu, M. Osada et al. Jpn. J. Appl. Phys. (Part2*)* **42**, L944 (2003).
20. N. Sugita, M. Osada, E. Tokumistu et al. Jpn. J. Appl. Phys. (Part1)., **41**, 6810(2002).
21. Jun Zhu, Xiao-Bing Chen, Jun-Hui He et al. J. Solid State. Chem. **178**, 2832-2837 (2005).
22. Y.P Chen, Y.Y Yao, Z.H Bao et al. J. Matt. Lett., **57**, 3623-3628 (2003)
23. Samara, G.A, **56,** 239-458 (2001).
24. Samara, G. A, Phy Rev. B, **71**, 224108 (2005).
25. Dai,X., A.DiGiovanni and D.Viehland, J.Appl.Phy., **74,** 3399-3405(1993).
26. Dai, X., Z.Xu and D.Viehland., Jour Appl.Phy., **79,** 1021-1026 (1996).
27. Priya, S. and D.Viehland., Jour Appl.Phy Lett., **8** ,4217-4219 (2002).
28. Lu.Y ., Jour Appl.Phy.Lett **85**, 979-981 (2004).
29. Gupta, S.M. and Viehland., Jour Appl.Phys., **80**, 5875-5883(1996).
30. Randall, C.A and A.S Bhalla., Jour Mat.Res., **5,** 829-834 (1989).
31. De Mathan, N.,E.Husson, G.Calverin, J.R. Gavarri, et.al., Jour Phys:Condes Matt, **3,** 8159-8171(1991).
32. Conlon, K.H., Luo, D.Veihland, J.F.Li, T.Whan et.at., Jour Phy .Rev.B., **70,** 172204 (2004).
33. Gering,P.M.K. Ohwada and G.shrine., Jour Phy.Rev.B., **70**, 014110 (2004).
34. S.M Pilgrim, A.E Sutherland and S.R Winzer, Jour. Amer. Cer.Soc., **73**,3122 (1990).
35. L.Mitoserius, P.M Vilarinho and A.L Kholkin., Jpn.Jour Appl.Phy.Lett. partI **41,**7015 (2002) .
36. A.Tkach, P.M Vilarinnho and A.L Kholkin., Jour.Appl. Phys.Lett., **86**,172902 (2005) .
37. Y.L Wang, S.S.N Bharadwaja, A.K Tagantsev and N,Setter, Jour.Eur.Cer.Soc., **25,** 2521 (2005).
38. Bell, A.J., jour Phys.Condens.Matter , **5,** 8773-8792 (1993).
39. Cheng, Z.Y., R.S Katiyar, X.Yao and A.Guo., Jour Phy Rev B., **55** 8165-8174 (1997).
40. Samara, G.A and E.L Venturini., jour Phase Transitions., **79,** 21-40 (2006).
41. R.Z Hou, X.M.Chen and Y.W Zeng., J.Ame.Cer.Soc., **89 [9]** , 2839-2844 (2006).
42. R.Macquart, B.J Kennady, T.Vogt., Jpu.Phy.Rev.B., **66,** 212102 (2002).

43. Xiao-Bing Chen, Rong Hui, Jun Zhu, Jour.Appl.Phys., **96,** 5697 (2004).

44. V.V.Kirilov and V.A Isupov, jour.Ferro., **5** ,3 (1973).

45. K.Uchino and S. Nomura., jour ferro.Lett.Sect., **44**, 55 (1982).

46. S.Suresh, A.Ramanand, .Jayaraman,et.al., J.Min & Mat.Charat & Engg, **10**,339-349 (2011).

47. D.A Tenne, A.Soukiassian,M.H.Zhu and A.M Clark, Jour .Phy.Rev.B., **67**,012302 (2003).

48. Wei Wang, Shi-Pu Gu, Xiang-Yu Mao, et.al., J.Appl.Phys., **102**, 024102 (2007).

49. S.K.Kim, M.Miyayama and H.Yanagida, Jour.Matt.Res.Bull., **31**, 121 (1996).

50. C.A.Paz de Araujo, J.D Cuchiaro, L.D.McMIllan., Jour. Nature., **374,** 627 (1995).

51. B.H.Park, B.S Kang,S.D.Bu, T.W Noh, Jour Nature., **40,** 682 (1999) .

52. B.E. Vugmeister and M.D.Glinchuk, Rev.Mod.Phy., **62,** 993 (1990) .

53. J.Ricote, L.Pardo, B.Jimenz . *J Material Science* **29,** 3248-3254 (1994).

54. D Pamu, K C James Raju, G Lakshiminaraya Rao Ceramics. *J Trasa Ind Cer Soc* **67**,1 (2008).

55. Piagai R, Kim I-T, Park J-G and Kim Y *J. Korean Phys.Soc.* **32,** S367 (1998).

56. Yang A-K, Wang C-A, Guo R and Huang Y *Appl. Phys.Lett.* **98,** 152902(2011).

57. Wu Y, Forbess M J, Seraji S, Limmer S J, Chou T P, Nguyen C P and Cao G *J. Appl. Phys.* **90,** 5296 (2001).

58. K Stanly Jacob, R Satheesh, R Ratheesh, Jour Mat Rea Bull., **44,** 2022-2026 (2009).

Chapter 5

Preparation of SBTi thin films and their structural, microstructural, optical and Raman spectroscopic studies

Chapter 5

Preparation of SBTi thin films and their structural, microstructural, optical and Raman spectroscopic studies

---

5.1 Introduction

SBTi is one of the more promising materials among the bismuth layer structured ferroelectrics in view of its high Curie temperature, strong fatigue resistant properties and higher remanent polarization [1]. Among published results, fatigue-free BLT films have been successfully deposited on platinized Si substrates ($Pt/TiO_2/SiO_2/Si$) by various methods, such as sol–gel techniques (a Chemical Solution Deposition technique), MOCVD [2] and more recently by PLD [3]. PLD is known as a technique of choice for congruent deposition of complex materials like BLT. However, until now, PLD suffers from weak uniformity control over large areas, leading to intrinsic difficulties to extrapolate the process towards industrial applications. Among deposition methods, sputtering enables to achieve good uniformity over large areas and is thus widely used for scientific and industrial applications. Published results on reactive sputtering of complex oxides show that, after optimization of experimental conditions, thin films of complex oxides can be obtained with a well-controlled stoichiometry [4, 5] and even improved dielectric properties, while controlling energy of involved species. However, optimization conditions to get single phase films on amorphous substrates and maintaining the oxygen stoichiometry during deposition with rf sputtering is a challenging task.

This chapter describes the structural, microstructural and optical properties of the rf sputtered SBTi thin films. The effect of process parameters such as oxygen pressure during deposition, annealing temperature, etc. on the structural, microstructural and optical characteristics are carefully analyzed. This chapter also presents a detailed study on the influence of process parameters on the local symmetry of thin films using their Raman spectra.

5.2 Target preparation and experimental conditions

The SBTi ceramic target used for rf magnetron sputtering was prepared by solid-state reaction method. For SBTi ceramic target, powders of $SrCO_3$, Bi_2O_3, TiO_2 of 99.9% purities were mixed in deionized water at desired composition. A few wt % of excess Bi_2O_3 were added to the powders to compensate for the Bi loss during the process of sintering and deposition. The mixture was calcined at 750°C for 5 h. To make SBTi target, the calcined powders added with binder were pressed into pellets and then sintered at 1100 °C for 2h. XRD pattern of the SBTi target indicated pure polycrystalline phase with no secondary phases.

The photograph of the RF magnetron sputtering system used in this work is shown in figure 5.1. It consists of a 30 liter stainless steel vacuum chamber which houses 3 cathodes and a substrate holder. Out of 3 cathodes, 2 are RF powered while the other one is dc powered. One of the RF powered cathodes was used for the deposition of SBTi thin films. During the deposition of thin films, the vacuum chamber is continuously cooled by flow of water through the water cooling jackets fitted on the exterior to the vacuum chamber. The vacuum chamber is evacuated through the electro-pneumatic roughing valve from atmospheric pressure to 2×10^{-3} Torr using a rotary vane mechanical pump (RP, DS-102, Varian, Italy). A base pressure of 4×10^{-6} Torr can be achieved in about 2h using turbo molecular pump. Two mass flow controllers which can independently control the flow of argon (99.9%) and molecular oxygen (O_2, 99.99% purity) are connected to the vacuum chamber through a solenoid valve. The use of gas mixture of inert argon and reactive oxygen helps to achieve the same stoichiometry as of the target in the film. The working pressure during the deposition is controlled partly by adjusting the total input gas flow and by reducing the through out of the turbo molecular pump by partially closing the manual gate valve. Once the predetermined working pressure is achieved, the sputter deposition process is started by initiating the plasma using the RF power generator (RF-VII Inc, USA) coupled with matching network.

Figure 5.1. RF magnetron sputtering system used in this study

The experimental conditions such as RF power density, substrate temperature, OMP, working gas pressure, substrate to target distance, type of substrate used and post-deposition annealing treatments influence the properties of the sputtered films. Optimization of all the sputtering conditions for the best material properties in the deposited film can be very difficult and time consuming. Initial studies indicated that the power densities < 2.5 W/cm^2 resulted in very low rates of sputtering where as power densities > 3.5W/cm^2 resulted in target damage. Hence, a power density of 3W/cm^2 was used. The substrate to target distance was fixed at 5cms because larger distances led to lower rate of deposition and lower distances led to damage of vacuum seals.

5.3 Literature survey on thin films of Bi-layer structured materials

Now a days, bismuth-layered perovskite like ferroelectric thin films attract much attention due to their potential application in nonvolatile ferroelectric random-access memory. Bismuth titanate, $SrBi_4Ti_4O_{15}$ and $SrBi_2Ti_2O_9$ are typical bismuth-layered perovskite like material, showing excellent performance like fast switching speed and high fatigue resistance with metal electrodes, suitable for good retention devices [6]. Reports are available on SBT ferroelectric films synthesized by various techniques. **Kazushi Amanuma and Takashi Hase** reported that the $SrBi_2Ta_2O_9$ thin films were synthesized on $Pt/Ti/SiO_2/Si$ substrates using a solution deposition process. A well-crystallized film with dense structure was obtained by firing the films at 700–800°C. A 280nm thick film fired at 800°C showed P_r of 10.0 µC/cm^2 and E_c of 38 kV/cm at 5 V. No fatigue was observed up to 10^9 switching cycles. These properties are very attractive for nonvolatile memory application [7]. **Seshu B. Desu and Tingkai Li** reported that the films deposited by Metal - Organic Decomposition (MOD) technique are found to exhibit excellent ferroelectric properties. Typically, their SBT films (thickness approximately 300 nm), at an applied voltage of 5V, showed $2P_r$ values greater than 20 µC/cm^2, a coercive field E_c less than 60 kV/ cm and a dielectric constant around 300 (at10 kHz). These values are in excellent agreement with earlier reports on laser ablated SBTN films. The films did not show any significant fatigue up to 10^9 cycles. Additionally, a leakage current density of less than 2×10^{-8} A/cm^2 was obtained at an electric field of 167 kV/cm, which is significantly lower (by an order of magnitude) than the corresponding laser ablated films [8]. **Nak-Jin Seong and Soon-Gil Yoon** reported that the films deposited by plasma-enhanced metal organic chemical vapor deposition (PE MOCVD) shows remnant polarization (P_r) and the coercive field (E_c) of 15 µC/cm^2 and 50 kV/cm at an applied voltage of 3 V for 200 nm thick $Sr_{0.9}Bi_{2.3}Ta_{2.0}O_9$ films deposited at 550 °C. The leakage current density was about 5x10^{-8} A/cm^2 at an electric field of 300 kV/cm. The films showed fatigue-free characteristics up to 1x10^{11} switching cycles under a bipolar wave of 6V [9]. **S. T. Tay, X. H. Jiang, and C. H. A. Huan** reported that the rf sputtered SBT thin films, shows a remnant polarization (P_r) and coercive field (E_c) of 4.35 µC/cm^2 and 31.5 kV/cm respectively for the SBT thin films annealed at 750°C. Good insulating properties were obtained for films annealed at 700 and 750°C, but higher leakage currents were observed when the films were annealed at 800 and 850°C. Increase in the leakage current is attributed to degradation of the Pt electrode and diffusion of Ti into the SBT films [10].

5.4 Deposition of SBTi thin films

The SBTi thin films were deposited on fused silica substrates by RF magnetron sputtering at fixed oxygen mixing percentage (OMP). The substrate holder was water cooled to maintain the substrate temperature between 25-27^{0}C in order to prevent the rise in temperature of the substrates due to ion bombardment during sputter deposition process. The temperature of the un-cooled substrate rose up to 100-120^{0}C during deposition. The power density and working pressure was maintained at a constant value of 3W/cm^2 and 20mTorr respectively. The optimized conditions used for the present study are shown in table 5.1

Parameter	Value
Power density	3(W/cm^2)
Substrate to target distance	5cms
Working pressure	20mTorr
Oxygen mixing percentage	Ar: O_2 (50%: 50%)
Substrate type	Fused silica
Post-annealing treatment	Conventional annealing (500-800^{o}C) about 2h. Microwave annealing (500-800^{o}C) about 20min.

Table 5.1: Sputter deposition parameters used in the current study.

Ex-situ annealing of SBTi thin films:

In order to crystallize the films, two ex-situ annealing treatments are adopted. They are

(a) Annealing in a conventional furnace.

(b) Annealing in a microwave furnace.

5.5 Characterization of SBTi thin films annealed by conventional furnace:

5.5.1 Compositional analysis

In order to investigate the compositional deviations if any in the rf processed samples, Energy Dispersive X-ray (EDX) analysis of the deposited films are carried out. Composition of the films was close to the composition of the target. Figure 5.2 present the EDX spectrum of the SBTi thin films deposited on amorphous fused silica substrates. The Bi, Sr, Ti and O peaks appear in the EDX spectrum. The atomic percentage of each element in thin film is almost equal to the corresponding element percentage in the target material as shown in table 5.2.

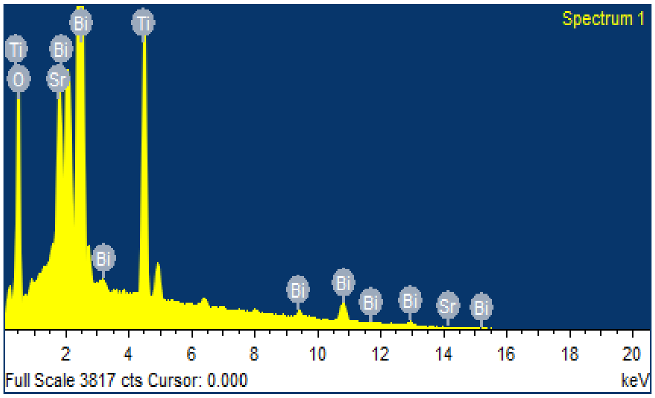

Figure 5.2: EDX spectrum of the SBTi thin films deposited on fused silica substrates.

Element	Weight %	Atomic % of deposited films	Atomic % of Target material
Ti K	**14.51**	**16.96**	**16.04**
Sr L	**6.38**	**4.07**	**4.16**
Bi M	**61.22**	**16.39**	**16.66**
O	**17.89**	**62.58**	**62.31**
Total	**100.00**		

Table 5.2 Atomic percentage of each element in deposited SBTi thin films obtained from EDX analysis.

5.5.2 Structural characterization:

The structural characterization of the deposited films was carried out using X-ray diffraction (XRD) technique with Cu Kα radiation. The XRD pattern of the SBTi thin films deposited on fused silica substrates annealed at different temperatures in the range of 500 – 800^{o}C are shown in figure 5.3. The oxygen mixing percentage was fixed at 50% for the present study. As shown in XRD pattern, films annealed at lower temperatures showed amorphous nature and as the temperature increases films are crystallized into orthorhombic phase with preferred orientation. There is no evidence for secondary phases and the peaks in XRD are well matched with standard JCPDS file [43-0973]. At higher temperatures i.e above 700^{o}C, the diffraction angle showed a shift towards lower angles which indicates the increase of lattice parameters. The increase in lattice parameters could be a result of lattice strain due to volatization of bismuth at higher temperatures [11]. The average crystallite size of the films was estimated from the FWHM values using Scherrer’s formula. The results show an increase of crystallite size from 15 to 25 nm as the annealing temperature increases from 500 to 800^{o}C. The variation of crystallite size with annealing temperature is plotted in figure 5.4.

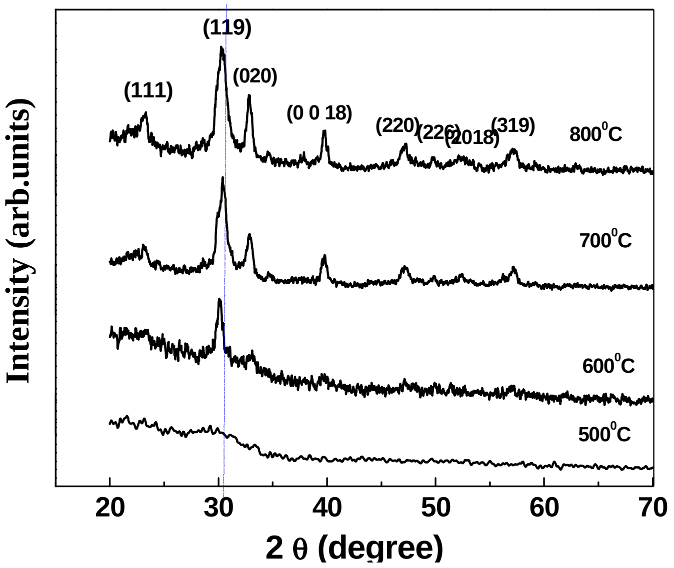

Figure 5.3: XRD pattern of the SBTi thin films annealed at different temperatures in conventional furnace.

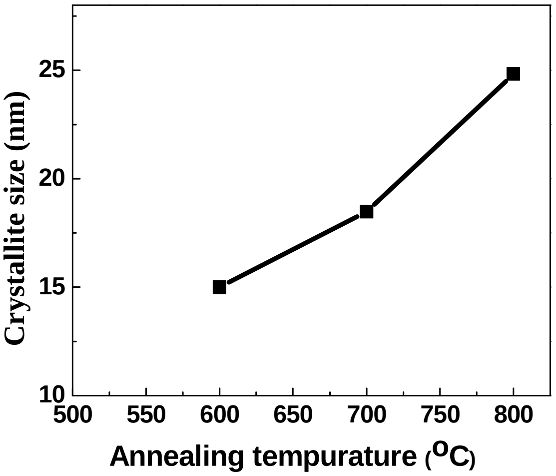

Figure 5.4: Crystallite size as a function of annealing temperature.

5.5.3 Surface morphology

The surface morphology of the SBTi thin films annealed at different temperatures from 500 to 800°C is shown in figure 5.5 (a-d). On annealing, the evolution of grains is evident with pronounced grain boundaries. It is clear that as the temperature increases the grain size is also increasing. The average grain size of the films annealed at 500, 600, 700 and 800^{0}C are 0, 35, 54 and 75nm respectively. The surface roughness of the same films was 6, 5.1, 7.2 and 9 nm.

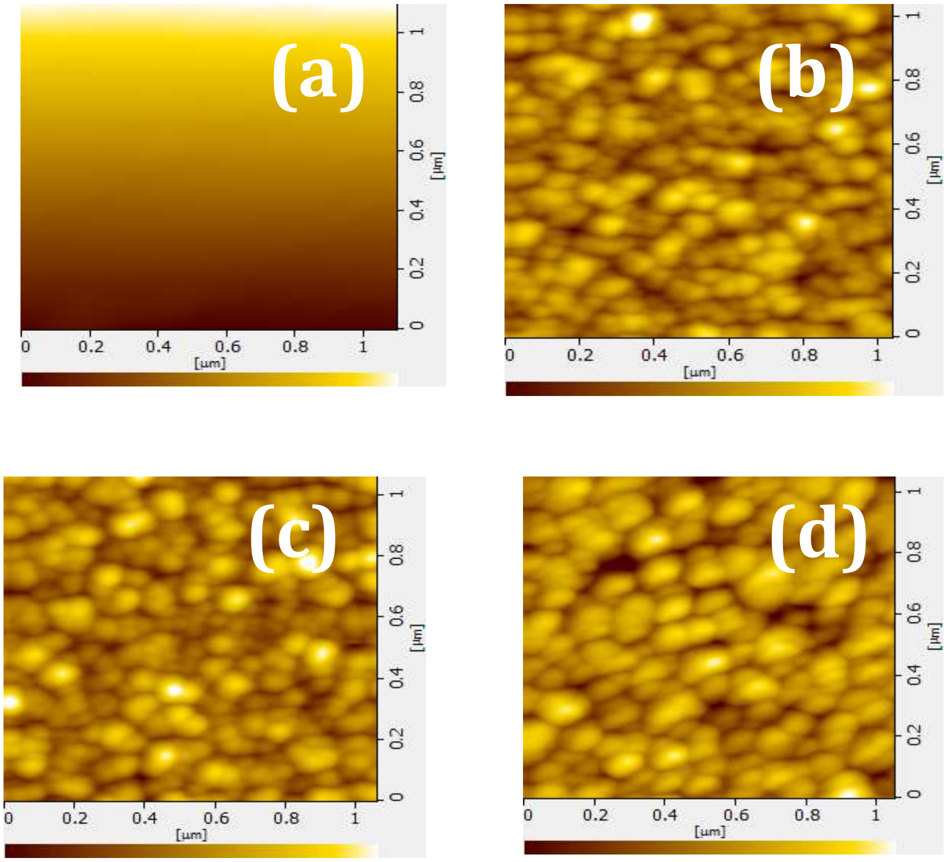

Figure 5.5(a-d): AFM images of SBTi thin films annealed in a conventional furnace at (a) 500 (b) 600 (c) 700 and (d) 800^{0}C.

5.5.4 Optical properties:

The optical properties of the SBTi thin films annealed at different temperatures are investigated from transmittance spectra obtained from JASCO V-570 spectrophotometer. Figure 5.6 shows the transmittance spectra of SBTi thin films annealed at different temperatures. The films annealed above 700°C shows a considerable decrease in optical transmittance. This can be attributed to an increased scattering from films with larger grains.

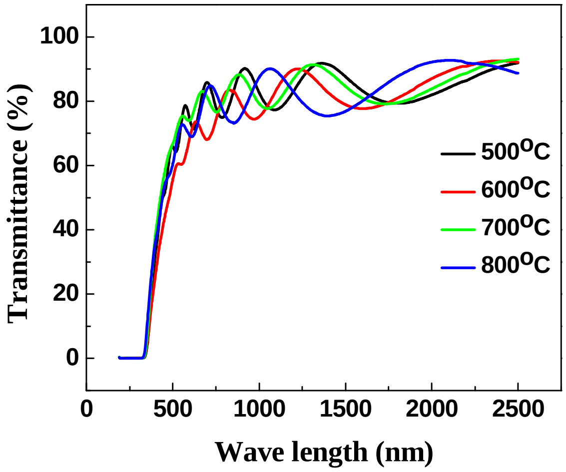

Figure 5.6: Optical transmittance spectra for SBTi thin films annealed at different temperatures.

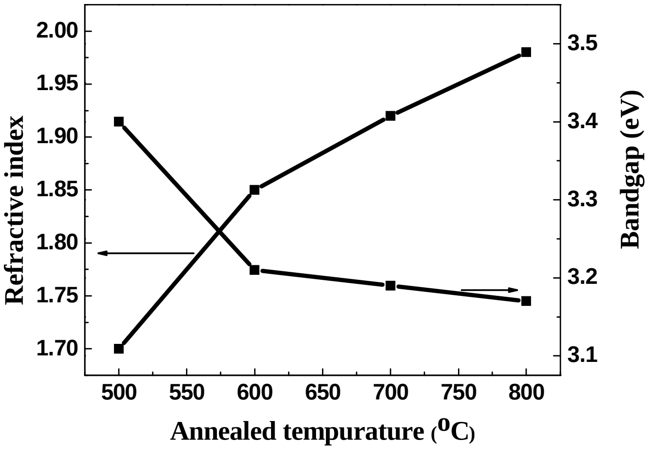

Figure 5.7: Refractive index and band gap as a function of annealing temperature.

The refractive index and band gap of SBTi thin films annealed at different temperatures is calculated and is shown in figure 5.7. As shown in the figure, the refractive index increases with the increase in temperature. The films annealed at low temperatures exhibited lower values of refractive index due to porous microstructure and consequently, with low packing density [12] as well as with onset of crystallization. As the annealing temperature increases, the packing density of the films increases resulting in an increase in refractive index. The decrease in band gap with increasing temperature is a common feature exhibited by many oxide materials [13]. It can be associated with the onset of crystallization. Films annealed at 500^{o}C exhibited the amorphous nature having a higher band edge. On annealing the films at temperatures greater than 500^{o}C, there is a sharp decrease in band edge which correlates with the onset of crystallanity [14] as observed in XRD pattern shown in figure 5.3.

5.5.5 Raman studies:

Raman spectroscopy is a powerful technique for studying vibrational modes in condensed matter, which helps to identify the chemical bonds present in the system. Most of the fundamental vibrational modes in the condensed matter lie in the energy range that corresponds to the middle infrared part of an electromagnetic spectrum with wave numbers from 500 to 4000 cm^{-1}. Raman effect can be interpreted as inelastic scattering of light due to a superposition of skeletal vibrations and dipole oscillations induced by electric field of the incident wave. The vibrational modes are Raman active only if it affects the local polarizability. Since the dielectric properties of ionic solids are primarily dictated by their lattice dynamics, knowledge of the lattice dynamics is important for both bulk and thin film dielectrics. Therefore, Raman spectroscopy is important for dielectrics as it is one of the simple techniques, which gives a good insight into the lattice dynamics of the material. Moreover, it is a nondestructive technique, and it does not require any special treatment of the samples.

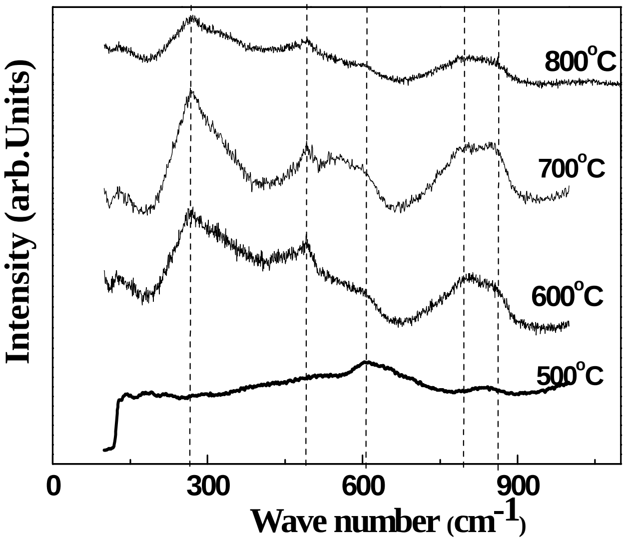

Figure 5.8: Raman spectra of SBTi thin films annealed at different temperatures in a conventional furnace.

The Raman spectra of the SBTi thin films are annealed at different temperatures from 500 to 800°C as shown in figure 5.8. For the BLSFs, the mode between 50 and 60 cm^{-1} is reported to arise from the displacement of Bi^{3+} ions in Bi_2O_2 layers, while those between 90 and 160 cm^{-1} originate from the vibrations of the ions at the A sites of the pseudo-pervoskite blocks [15]. The mode at ~268 cm^{-1} arise from the torsional bending of TiO_6 octahedra and those at ~ 561, 726 and 866 cm^{-1} correspond to the stretching of TiO_6 octahedra [16, 17].

The SBTi thin films were deposited on amorphous substrates, which are Raman inactive due to crystal symmetry, so the substrate should have no effect on the Raman signals. From the figure 5.8, the observed phonon modes are at 128.8, 272.6, 490.6, 598.5, and 860.6 cm^{-1}. No significant shift in the position of these phonon modes has been observed in SBTi thin films and bulk ceramic, which are mentioned in Chapter 3. From a comparison of the observed Raman spectra of thin films and their bulk counterparts, it can be seen that observed Raman modes in thin films are relatively less intense than the corresponding modes in bulk samples. As the annealing temperature increases, the intensity of the phonon modes increases up to 700°C. The films annealed at low temperatures (below and at 600^{o}C) show the amorphous nature. Detailed observation of Raman spectra reveals that as the annealing temperature increases, the intensity of the vibrational modes is enhanced gradually. These results suggest that the films annealed at lower temperatures are amorphous and not fully crystallized. As the annealing temperature increases, grain growth and crystallization takes place. For the films annealed at high temperature (800^{o}C), the intensity of the phonon modes are decreased especially the modes at higher frequency side, which belongs to stretching of TiO_6. Some of these modes are disappearing due to oxygen vacancies and Bi loss at high temperatures which lead to changes in local symmetry of the films. From the above Raman spectra, we can conclude that the films annealed at 700^{o}C exhibited the relatively intense phonon modes compared to other films. These results again show up indirectly through the dielectric properties of these samples which will be discussed in Chapter 7. The peak broadening was more for the thin films than the bulk samples which demonstrate that the stresses endured by the films are more for the films which is understandable as they are constrained by a substrate while undergoing the deposition and annealing processes [18].

5.6 Characterization of SBTi thin films annealed by microwave furnace:

5.6.1 Structural properties:

The XRD pattern of the SBTi thin films deposited on fused silica substrates annealed in a microwave furnace at different temperatures in the range of 500 – 800^{0}C about 20min are shown in figure 5.9. The oxygen mixing percentage was fixed at 50% for the present study. As shown in XRD pattern, films deposited at 500^{o}C films show amorphous nature and as the temperature increases films were crystallized into orthorhombic phase with preferred orientation. There is no evidence for secondary phases and well matched with standard JCPDS file [43-0973]. As the annealing temperature increases, the prominent peak shifted towards the lower angle which indicates the increase of lattice parameters. The increase in lattice parameters could be the result of lattice strain arising from defects in the form of oxygen vacancies [19]. The average crystallite size of the films was estimated from the FWHM values using Scherrer's formula. The results show that the crystallite size increased from 12 to 20 nm as the temperature increases from 500 to 800^{o}C. The variation of crystallite size with the annealing temperature is plotted in figure 5.10.

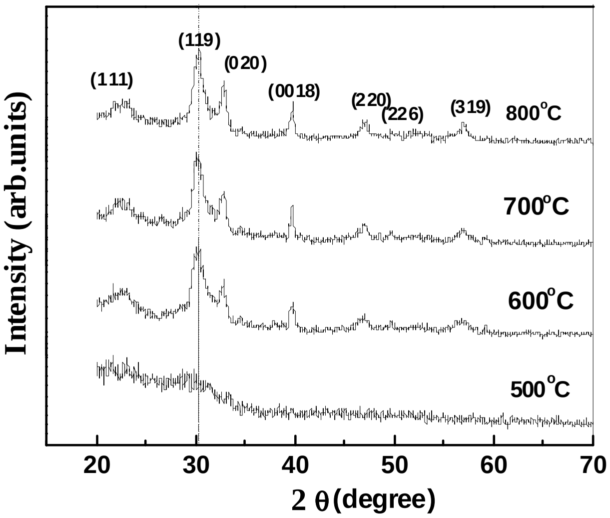

Figure 5.9: XRD pattern of the SBTi thin films annealed in a microwave furnace.

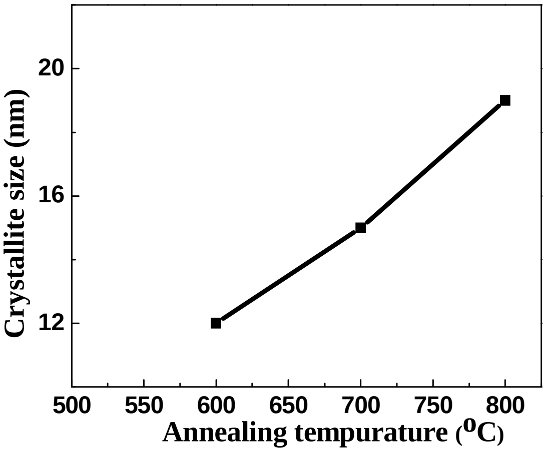

Figure 5.10: Crystallite size of the films annealed at different temperatures.

5.6.2 Atomic force microscopy:

The surface morphology of the SBTi thin films annealed at different temperatures from 500 to 800^{0}C is shown in figure 5.11 (a-d). On annealing, the evolution of grains is evident with pronounced grain boundaries. It is clear that as the temperature increases, the grain size is increasing. The average grain size of the films annealed at 500, 600, 700 and

800^0C are 0, 32, 56 and 82nm respectively. The average roughness of the same films was 4, 5.1, 7.2 and 9 nm.

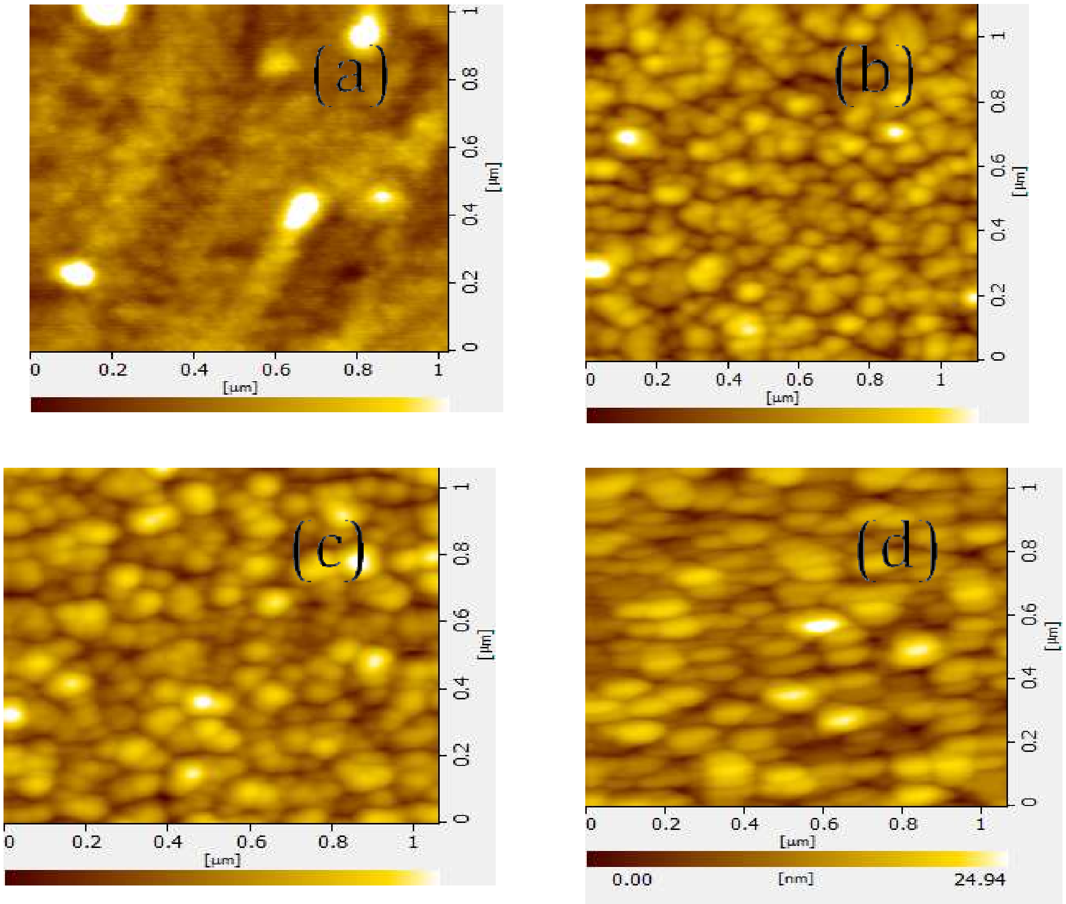

Figure 5.11 (a-d): AFM images of the SBTi thin films annealed in microwave furnace at (a) 500 (b) 600 (c) 700 and (d) 800^0C.

5.6.3 Optical properties:

The optical transmittance spectra of the SBTi thin films annealed in a microwave furnace at different temperatures are as shown in figure 5.12. The films annealed at 800°C shows a considerable decrease in optical transmittance. This can be attributed to an increased scattering in the film with larger grains as well as higher defect density.

The optical band gap E_g for the films was calculated using the envelop method. In the present case, the band gap energy (E_g) has been estimated by assuming as allowed direct transition between the highest occupied state of the valance band and the lowest unoccupied state of the conduction band.

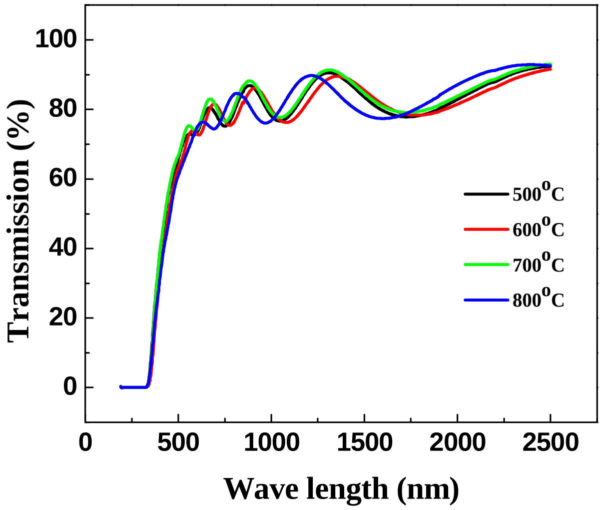

Figure 5.12: Optical transmittance spectra for SBTi thin films annealed in microwave furnace.

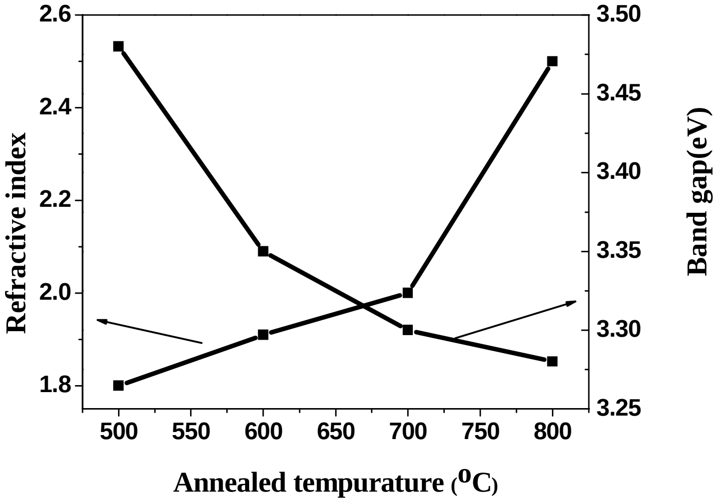

Figure 5.13: Refractive index and band gap of the SBTi films annealed in a microwave furnace.

The variation in the band gap (Eg) and refractive index with the annealing temperature is shown in figure 5.13. The band gap decreases as the annealing temperature increases. The decrease in band gap on annealing is a common feature exhibited by many oxide materials. It is attributed to several reasons such as the grain size effect, stress in the films and the amorphous nature of the material itself. In the present case, grain size difference is observed for the films annealed at different temperatures and stress in the films can be expected due to rapid heating/cooling in the microwave annealed films. But changes in band gap are primarily influenced by the obvious transformation to a crystalline phase.

The refractive index of SBTi thin films annealed at different temperatures in a microwave furnace is calculated and is shown in figure 5.13. The observed refractive index is higher than the conventional annealed films which indicate the advantage of microwave annealing. As shown in the figure, the refractive index increases with the increase in temperature. The refractive index values slowly increase as the films are annealed up to 700^{o}C. At 800^{o}C, the refractive index increased abruptly and it could be the effect of complete transformation to a crystalline phase as well as due to larger grain size. The lower values of refractive index of the films that are annealed at low temperatures can be attributed to their amorphous nature and porous microstructure.

5.6.4 Raman spectroscopy studies:

From figure 5.14, it can be seen that the observed phonon modes are at 128.8, 272.6, 490.6, 598.5 and 860.6cm^{-1}. Raman spectra of the thin films are in almost good agreement with the Raman spectra of bulk samples, which are shown in chapter 3. There is no significant change in conventional annealed and microwave annealed films. As the annealing temperature increases the intensity of the phonon modes increases, and new phonon modes are appearing. Films deposited at 500^{o}C exhibit the amorphous nature as observed in conventional annealed films. For films annealed above 500^{o}C, the intensity of phonon modes increased and new phonon modes are observed. Even at high temperatures (800^{o}C) the phonon modes are existed with the same intensity in the case of microwave annealed films as opposed to the conventionally annealed films described in the previous section. Since in the microwave annealing the bulk Raman spectra is retained, one can conclude that the oxygen and Bi ion loss is under control in the case of microwave annealing resulting in retaining the bulk local symmetry even after 800^{o}C annealing since only short heating, soak and cooling times are required for microwave annealing.

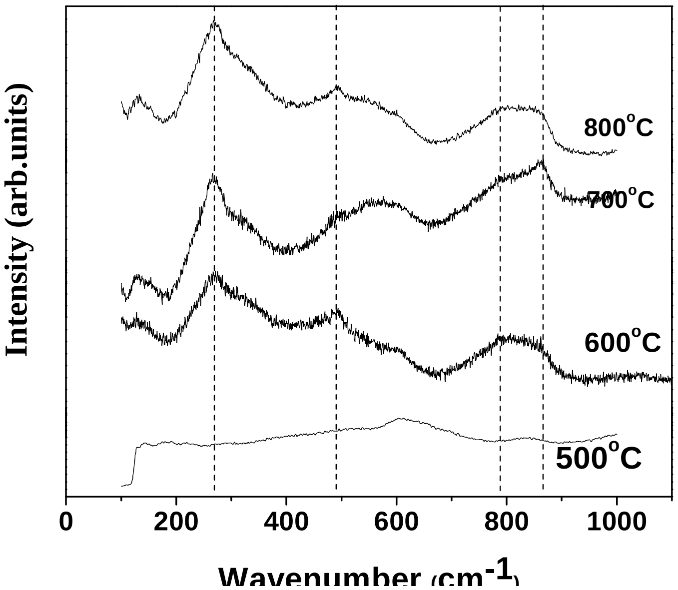

Figure 5.14: Raman spectra of SBTi thin films annealed at different temperatures.

5.7 Deposition of SBTi thin films at different Oxygen mixing percentage (OMP)

The SBTi thin films were deposited on fused silica substrates by RF magnetron sputtering by varying the OMP. The substrate holder was water cooled to maintain the substrate temperature between 25-27^{0}C in order to prevent the rise in temperature of the substrates due to ion bombardment during sputter deposition process. The temperature of the un-cooled substrate rose up to 100-120^{0}C during deposition. The power density and working pressure was maintained at a constant value of 3W/cm^2 and 20mTorr respectively. The different optimized conditions used for the present study are shown in table 5.3.

Parameter	Value
Power density	3(W/cm^2)
Substrate to target distance	5cms
Working pressure	20mTorr
Oxygen mixing percentage	Oxygen mixing percentage varied from 25%- 100% in steps of 25
Substrate type	Fused silica
Post-annealing treatment	Conventional annealing: 750^{o}C for 2h. Microwave annealing:750^{o}C for 20min.

Table 5.3: Sputter deposition parameters used for this study.

5.7.1 Composition analysis for conventional and microwave annealed films:

In order to investigate the compositional difference if any in the conventional and microwave annealed samples, Energy Dispersive X-ray (EDX) analysis is carried out for films deposited at 50%-OMP. The atomic percentage of each element in thin films of conventional and microwave annealed process is shown in table 5.4. EDX spectra of conventional and microwave annealed films is shown in figure 5.15. The atomic percentage of each element of conventional annealed films exhibited lesser values than the microwave annealed films. There is considerable difference observed for Bi and Oxygen between conventional and microwave annealed films. This indicates that the microwave annealing is able to control the Bi-volatization at high temperatures.

Element	Standard values (%)	Atomic % of Conventional annealed Films (750-2h)	Atomic % of Microwave annealed films (750-20min)
Ti K	**16.66**	**16.26**	**16.34**
Sr L	**4.16**	**4.10**	**4.13**
Bi M	**16.66**	**15.91**	**16.46**
O	**62.49**	**62.08**	**62.31**

Table 5.4: Atomic percentage of each element in conventional and microwave annealed films

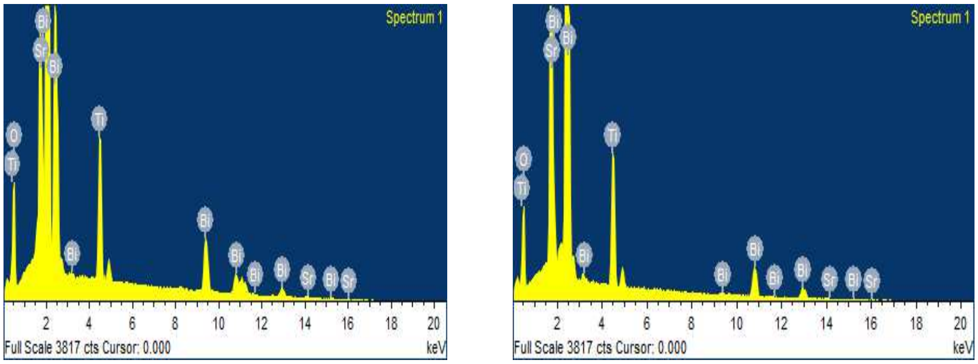

Microwave annealed films

Conventional annealed films

Figure 5.15: EDAX spectra of microwave and conventional annealed films.

5.8 Effect of oxygen pressure on structural properties:

5.8.1 Conventional annealed thin films

The XRD pattern of the SBTi thin films deposited on fused silica substrates as a function of OMP of 25, 50, 75 and 100% at room temperature and annealed at 750^{o}C in oxygen atmosphere using a conventional furnace are shown in figure 5.16. All the SBTi films show orthorhombic structure with no secondary phase formation. The inter-planar spacing corresponding to (119) peak was obtained from the peak position according to the following Bragg formula $d_{119}= \lambda/2 \sin\theta$, where λ is 1.5406 Å, the wavelength of X-rays for CuKα radiation and θ is the position of the (119) diffraction peak. The values of inter-planar spacing and crystallite size are plotted in figure 5.17 as a function of OMP. The slight decrease in the inter-planar distances at lower OMP is the result of lattice strain due to defects in the form of oxygen vacancies [20]. The value of inter-planar distance of the films deposited at 50%-OMP is almost equal to the standard JCPDS value. The intensity of the diffraction peak and crystallite size increased up to 50% of OMP, which indicates improved crystalline quality. The films deposited at 75 & 100% OMP exhibited smaller crystallite size and deteriorating crystalline quality due to low rates of deposition. In addition, films deposited at higher OMP (>50%) have the lower surface roughness as expected due to low rates of deposition [21]. Films deposited at low rates have been shown to have smaller grains than those deposited at high rates. The crystallite size of the films deposited at 25, 50, 75 and 100% OMP are 24, 28, 23.1, and 21nm respectively. The variations in crystallite size are confirmed from the broadening of the XRD pattern.

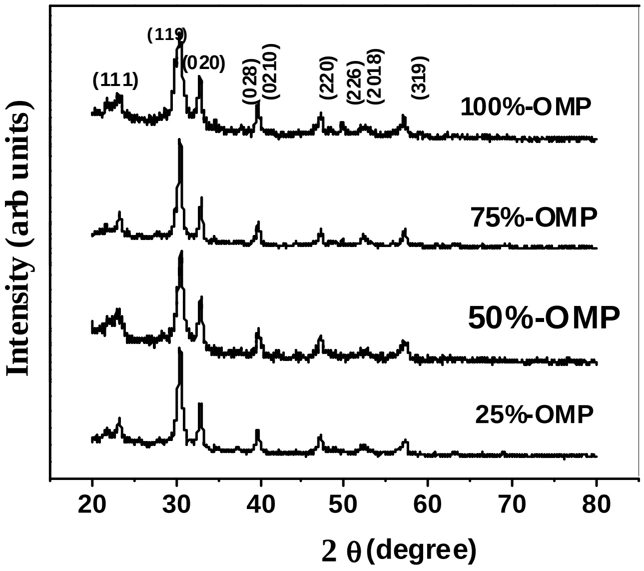

Figure 5.16: XRD pattern of the SBTi films deposited at different OMP.

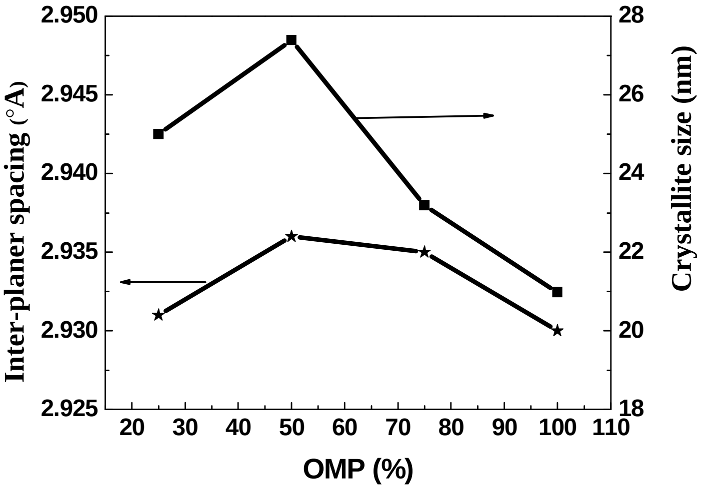

Figure 5.17: Inter-planar spacing and crystallite size as a function of OMP.

5.8.2 Microwave annealed thin films

The XRD pattern of the SBTi thin films deposited on fused silica substrates as a function of OMP of 25, 50, 75 and 100% at room temperature and annealed at 750^{o}C for about 20min in oxygen atmosphere using a microwave furnace are shown in figure 5.18. All the SBTi films show orthorhombic structure with no secondary phase formation. Films deposited at 50% & 75% OMP showed good crystalline quality. In this case also the inter-planar spacing corresponding to the (119) peak was calculated and the values of inter-planar spacing and crystalline size are plotted in figure 5.19 as a function of OMP. The microwave annealed films deposited at an OMP of 50% and 75% gave inter-planar distances that almost matched with the standard d-spacing. The lower values of inter-planar distances at lower OMP are the result of lattice strain due to defects in the form of oxygen vacancies [20]. The oxygen vacancies affect the nearest neighbor distance by reducing the Coulomb attractive force between cations and anions, resulting in increased lattice parameters [22]. The films deposited at 50% OMP shows good quality crystallization. The crystallite size of the films deposited at 25, 50, 75 and 100% OMP are 17.8, 23.8, 20.3 and 18.1nm respectively. The variations in crystallite size are confirmed from the broadening of XRD pattern. The microwave annealed films exhibited more intense XRD peaks than the conventional annealed films in all the cases, which indicate that these films are well crystallized.

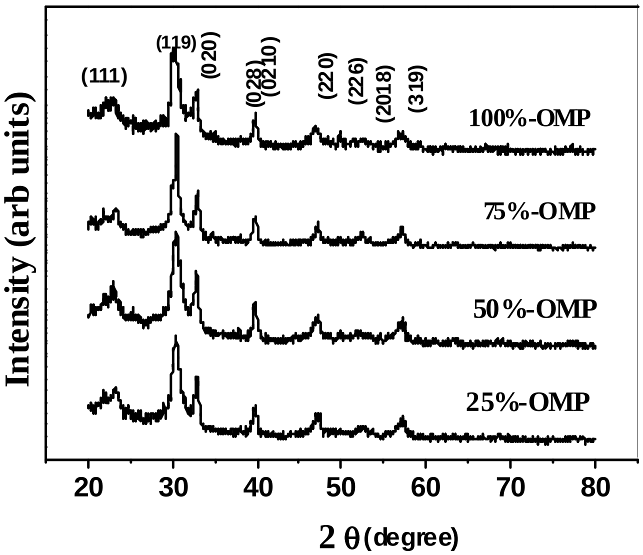

Figure 5.18: XRD pattern of the SBTi thin films deposited at different OMP (after microwave annealing).

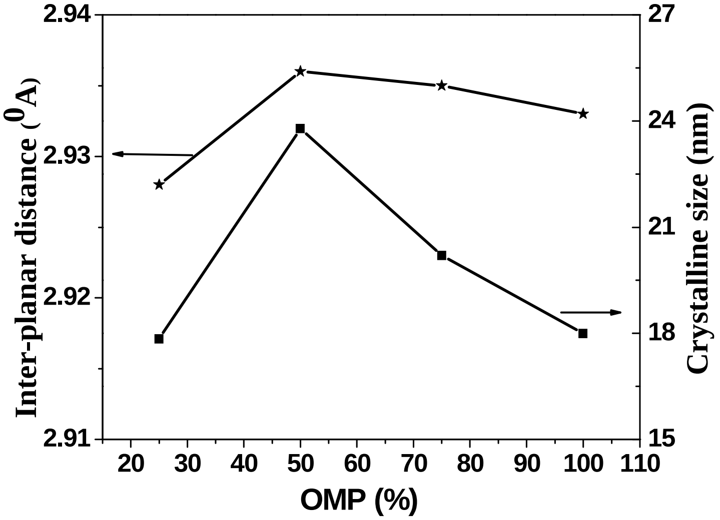

Figure 5.19: Inter-planar spacing and crystallite size of microwave annealed SBTi thin films as a function of OMP.

5.9 Effect of oxygen pressure on morphological properties:

5.9.1 Conventional annealed thin films

The surface morphology of the SBTi thin films deposited at different oxygen mixing percentage and annealed at 750^{o}C in a conventional furnace is shown in figure 5.20 (a-d). As seen in micrographs, the evolution of grains is evident with pronounced grain boundaries by varying the OMP. The average grain size of the films deposited at 25-100% are ranged between 112-88nm. As seen in micrographs, the average grain size is decreasing for the films deposited above 50% -OMP. The surface roughness of the films deposited at 50 and 75%-OMP shows higher value than the films deposited at 25 & 100%-OMP. On other hand, films deposited at high OMP (75 and 100%) have the lowest surface roughness as expected due to low rates of deposition. The surface roughness of the films deposited at 25-100%-OMP is 4.4, 4.9, 3.7 and 3.1nm respectively. These results are supporting the XRD pattern of the same films.

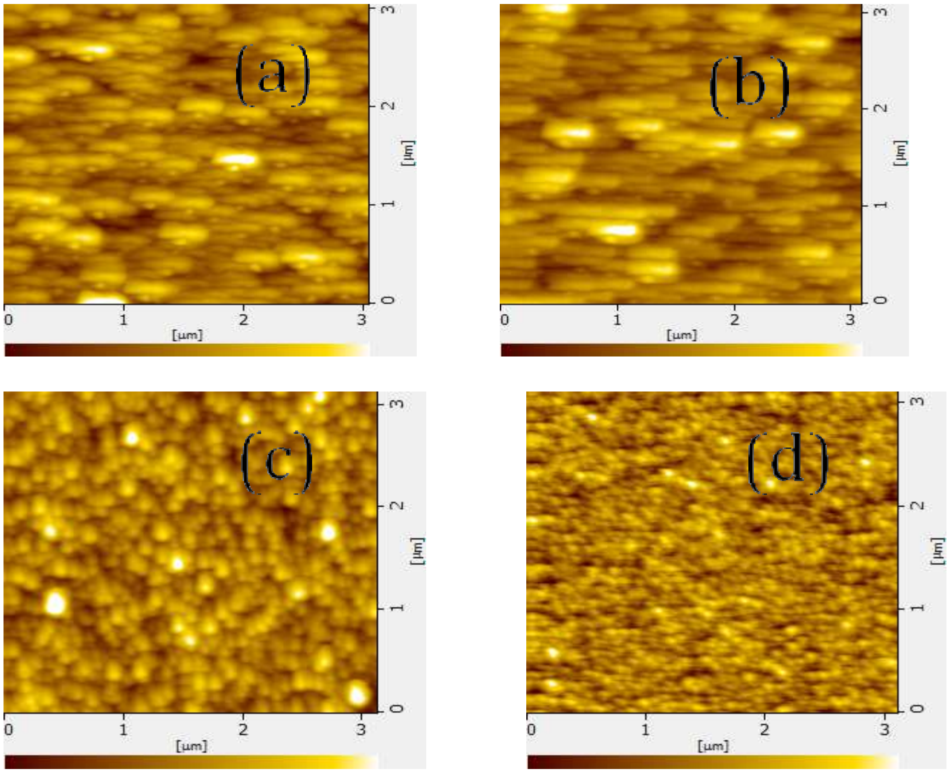

Figure 5.20: AFM images of the SBTi thin films annealed in a conventional furnace at 750^{0}C and deposited at different OMP (a) 25% (b) 50% (c) 75% and (d) 100%.

5.9.2 Microwave annealed films:

Surface morphology of the SBTi thin films deposited at different OMP and annealed in a microwave furnace at 750^0C is shown in figure 5.21 (a-d). It is clearly evident that the microstructures of these films are strongly depending on OMP. The films deposited at 50% OMP shows the larger grain size than the other films. The average grain sizes of the films deposited at 25-100% are ranged between 132-92nm. The average grain size of the films annealed in a microwave furnace exhibited larger grain size than the conventional annealed films. This indicates that the microwave energy is interacting with these films more efficiently to facilitate nucleation and grain growth over short period of time. The average roughness of the films deposited at 50 and 75%-OMP shows higher values than the films deposited at 25 & 100%-OMP. The surface roughness of the films deposited at 25-100%-OMP is 4.4, 9.2, 3.7 and 2.1nm respectively. These values are higher than the corresponding values for the conventionally annealed films, showing that grain growth is more pronounced in the former case. BLSFs are known for their platelet like microstructure as observed in the bulk ceramic samples in chapter 3 figure 3.9. It is remarkable that the films grown at 50% OMP and annealed in the microwave furnace gives the same type of microstructure (fig.5.20(b)). It may be noted that only in this case this type of microstructure got developed in thin film form.

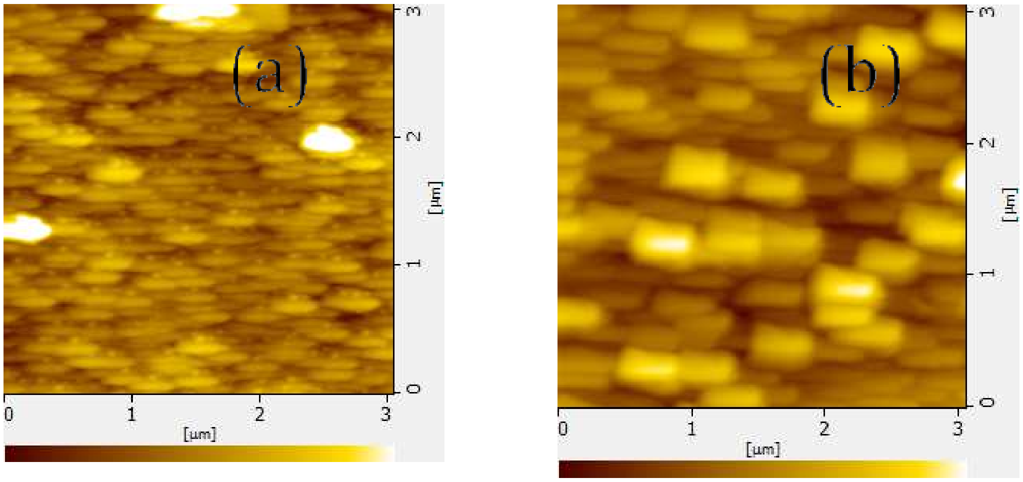

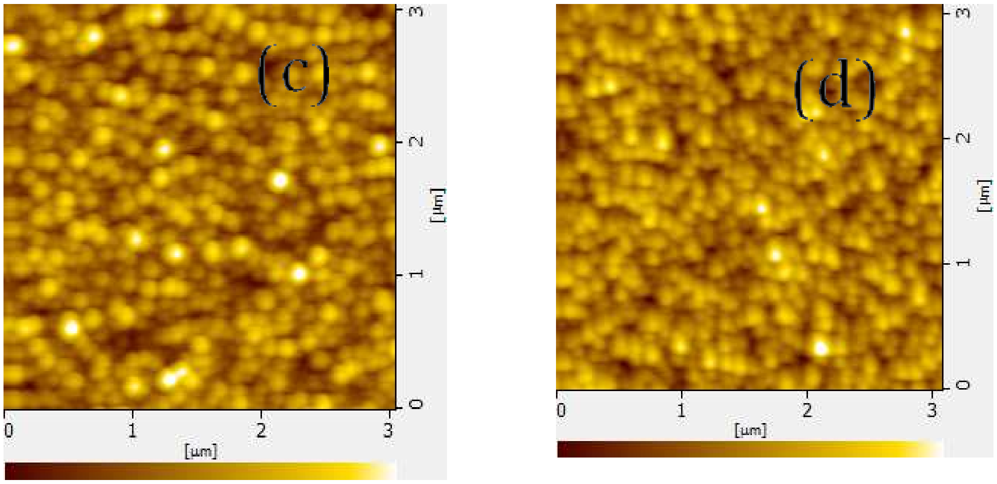

Figure 5.21: AFM images of the microwave annealed SBTi thin films deposited at different OMP at (a) 25% (b) 50% (c) 75% and (d) 100%

5.10 Effect of oxygen pressure on optical properties:

5.10.1 Conventional annealed thin films:

The optical properties of these thin films are interesting for many reasons, including identifying the electronic component of polarizability in these films and monitoring the film growth. Variations in optical parameters such as refractive index and band gap with changes in processing conditions are good indicators of the growth patterns of dielectric films. Moreover, high dielectric constant thin films with high optical transparency have considerable importance in the transparent optoelectronic devices. So a systematic study on the optical properties of these thin films is important for understanding the growth process as well as identifying the suitability of these films in transparent electronic applications.

The **o**ptical transmittance spectra of SBTi thin films deposited at different OMP are shown in figure 5.22. From close observation of transmittance spectra, it can be seen that films deposited at 100% OMP exhibited the least number of interference fringes, indicating that they are least thick compared to other films. The variation in refractive index as a function of wavelength for the films deposited at different OMP on fused silica substrates are as shown in figure 5.23. It is found that refractive index is strongly depending on OMP.

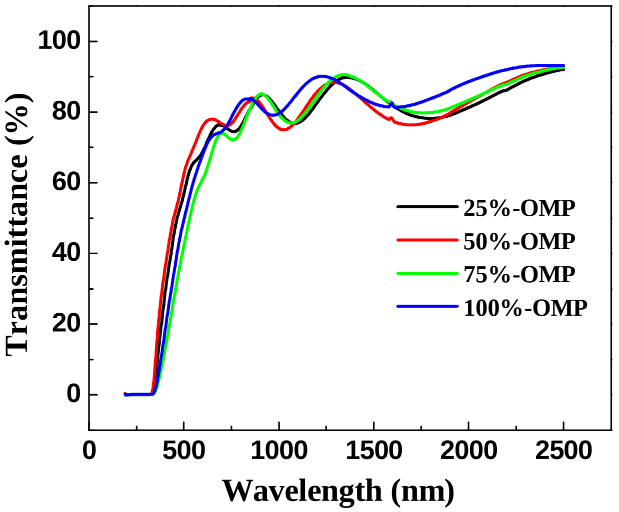

Figure 5.22: Optical transmittance spectra of SBTi films deposited at different OMP.

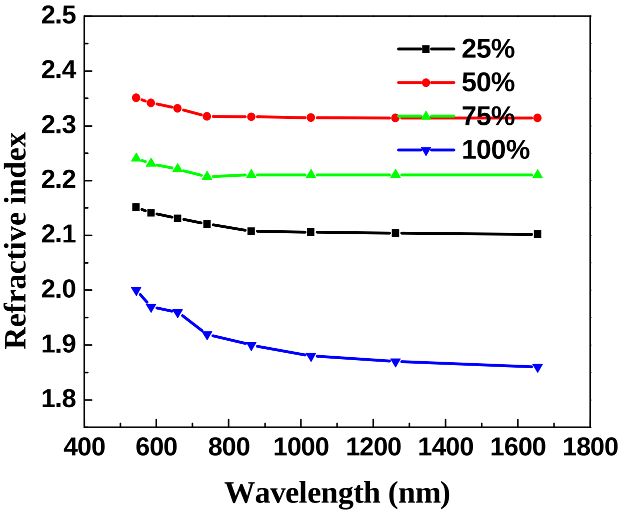

Figure 5.23: Variation of refractive index as a function of wavelength at different OMP.

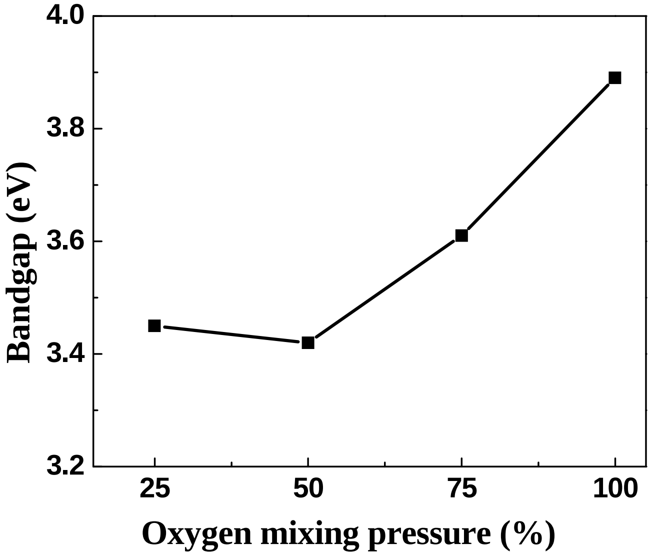

Figure 5.24: Variation of band gap as a function of OMP.

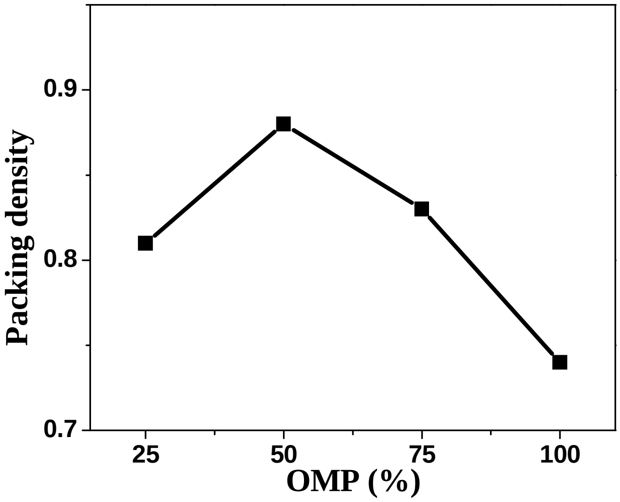

Figure 5.25: Variation of packing density as function of OMP.

The refractive index as a function of wavelength at different OMP is shown in figure 5.23. Highest value of refractive index is about 2.35 (@ 650nm) and was obtained from the films deposited at 50% OMP. The films deposited at 25% and 100% of OMP shows a lower refractive index. The reason could be oxygen vacancies for films deposited at 25%-OMP and less thickness for films deposited at 100%-OMP.

The optical band gap E_g was determined from the absorption coefficient α, calculated as a function of incident photon energy, E, for direct allowed transitions. At shorter wavelengths close to the optical band gap, scattering losses are dominated by fundamental absorption and α at a given wavelength λ, is often expressed as

$$\alpha = -\frac{1}{d}\ln\left(\frac{1}{T}\right) \tag{5.1}$$

Where d is the film thickness and T is the transmittance at that wavelength.

The optical band gap E_g for all the films were calculated using the Tauc relation [23], which is given by

$$\alpha E = B\left(E - E_g\right)^m \tag{5 .2}$$

Where B is the constant that indicates the measure of crystalline order in the deposited films. E is the incident photon energy and m = 0.5, 1.5, 2 or 3 for allowed direct, forbidden direct, allowed indirect and forbidden indirect electronic transitions. Interband optical transitions that can be described by wave functions localized over a distance of the order of lattice constant are relatively unchanged by disorder. Therefore, optical band gap and the constant B estimated from $(\alpha E)^{1/2}$ vs E reflects the local atomic structure which is undetected by XRD.

The refractive index of a transparent thin film is directly proportional to its electronic polarization and the electronic polarization is in turn inversely proportional to the inter-atomic separation [24]. It can be directly correlated to the film packing density, microstructure and crystallanity. It should be noted that in the present case, on annealing there is a reduction in the inter-atomic spacing due to crystallization that leads to higher densification and hence as increase in the refractive index. The relation between refractive index of the film (n_f) and the packing density can be expressed as, [25].

$$P_d = \left[\frac{n_f^2 - 1}{n_f^2 + 2}\right]\left[\frac{n_b^2 + 2}{n_b^2 - 1}\right] \tag{5.3}$$

Where n_b is the bulk refractive index

The values of band gap and packing density of SBTi thin films deposited at different OMP are shown in figure 5.24 and figure 5.25 respectively. The possible reason for the higher values of band gap in the SBTi thin films is the existence of density of states within the gap, as explained by Davis and Mott [26], causing the formation of fundamental absorption edge due to the band tailing rather than an optical band gap. Although, the band gap energy is a constant for a material in the bulk form, it is known to vary in thin films with crystallite size [27]. It can be observed that the films with smaller crystallite sizes exhibited the larger band gap energy than those with larger crystallite sizes. Similar investigations on the dependence of crystallite size on the optical band gap of BaTiO3 [28] and BST [29] thin films have been reported previously.

5.10.2 Microwave annealed thin films:

The spectral transmission curves of the SBTi thin films deposited at different OMP after microwave annealing are shown in the figure 5.26. The transmission spectra show interference fringes, which originate due to interference at the air – film and substrate-film interfaces. The sharp fall in transmission and disappearance of the fringes at the shorter wavelengths is due to the fundamental absorption of the films. There is a clear shift in the interference-free regions suggesting a remarkable change in the optical band edge for films prepared at different oxygen pressures. The spectral transmission behavior shows a strong dependence on thickness of the films as well as oxygen pressure during deposition.

The variation in refractive index as a function of wavelength for the films deposited at different OMP on fused silica substrates is shown in figure 5.27. It is found that the refractive index of microwave annealed films is also strongly depending on oxygen pressure during deposition. The observed refractive index and band gap has followed the same trend for the microwave annealed films also as the OMP is varied. The values of the band gaps of the microwave annealed films deposited at different OMP are shown in figure 5.28. Interestingly, there is no observable difference in refractive index of the conventional and microwave annealed films. However, band gap of the microwave annealed films are less than the conventional annealed thin films due to various factors like heating profile, grain growth and grain size. A shorter band gap means closer packing of the atoms and hence better crystallization. The lowest value (i.e, best crystallization) is obtained for the microwave annealed films prepared at 50% OMP. Indeed the same films gave the platelet like microstructure usually observed in bulk form of the material shown in figure 5.20(b). The refractive index rises rapidly toward the shorter wavelengths, showing the typical shape of a dispersion curve near an electronic inter band transition and becomes dispersion free at higher wavelengths. The strong increase in the refractive index at shorter wavelengths is associated with the fundamental band gap absorption. As mentioned in previous section 5.9.1 of this chapter, the refractive index is directly proportional to the packing density. Packing density as a function of OMP is shown in figure 5.28. In the present case films deposited at 50%-OMP exhibited the high refractive index and high packing density. Refractive index and packing density are going together as observed by many researchers [30-31]. This indicates that OMP plays a key role during the deposition to achieve good optical properties of the films.

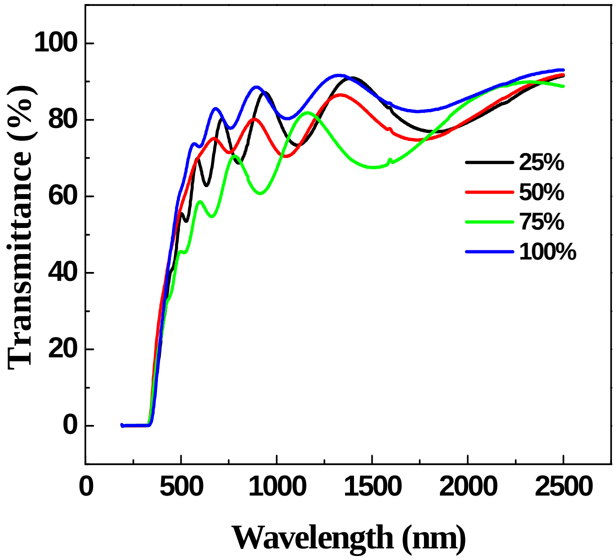

Figure 5.26: Optical transmittance of the microwave annealed SBTi thin films prepared at various OMP.

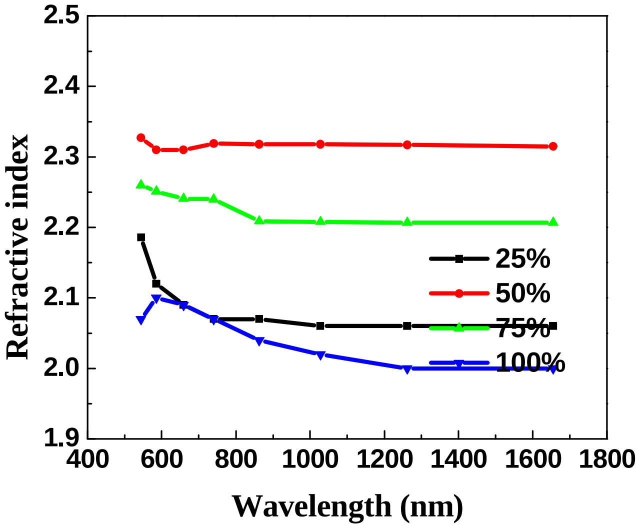

Figure 5.27: Refractive index of the microwave annealed SBTi thin films prepared at various OMP.

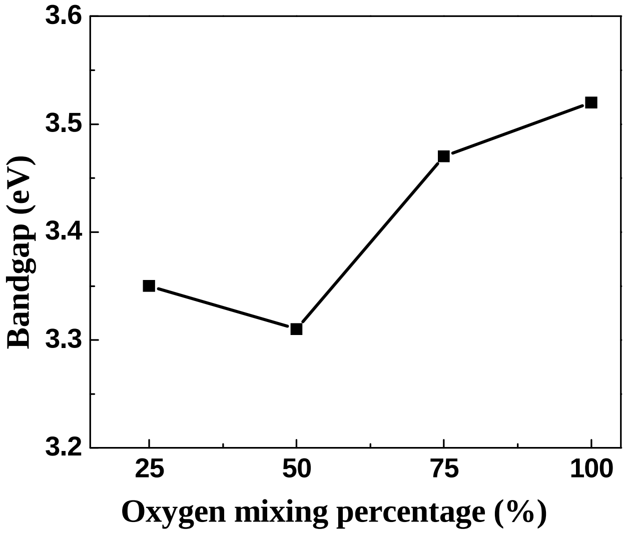

Figure 5.28: Dependence of band gap of the microwave annealed SBTi thin films with OMP during film deposition.

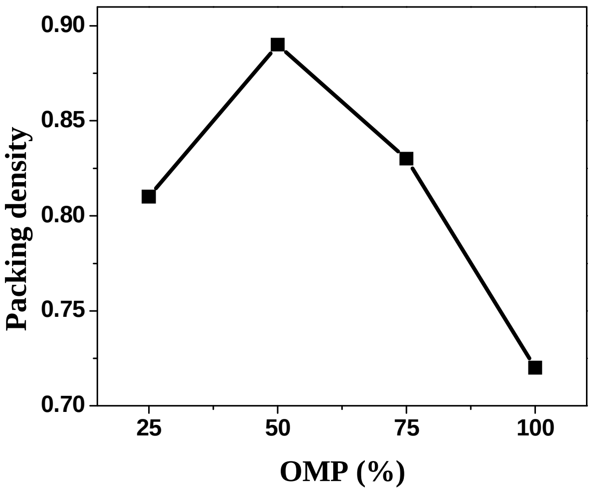

Figure 5.29: Packing density as a function of OMP for microwave annealed films

5.11 Effect of oxygen pressure during film deposition on Raman spectra:

5.11.1 Conventional annealed samples

Raman spectra of the conventionally annealed SBTi thin films deposited at different oxygen mixing percentage are shown in figure 5.30. For the BLSFs, the mode between 50 and 60 cm^{-1} is reported to arise from the displacement of Bi^{3+} ions in Bi_2O_2 layers, while those between 90 and 160 cm^{-1} originate from the vibrations of the ions at the A sites of the pseudo-pervoskite blocks. The mode at ~268 cm^{-1} arise from the torsional bending of TiO_6 octahedra and those at ~ 561, 726 and 866 cm^{-1} correspond to the stretching of TiO_6 octahedra [32, 33].

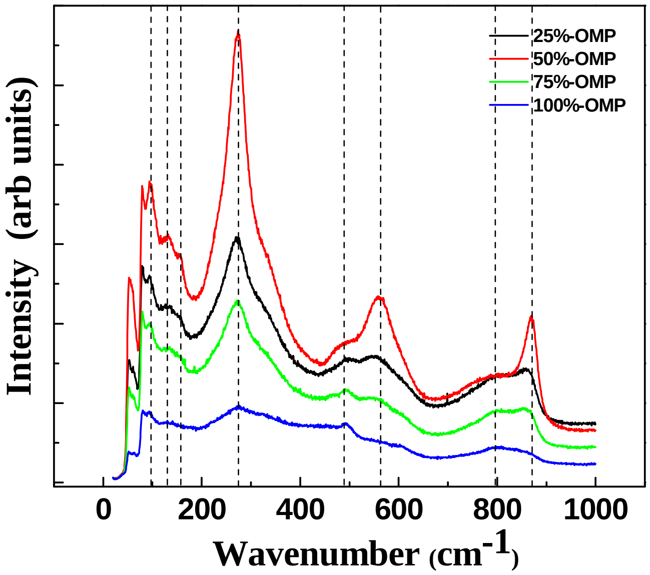

Figure 5.30: Raman spectra of conventionally annealed SBTi thin films deposited at different OMP.

The observed phonon modes are at ~92,129, 154, 270, 489, 555,788 and 865 cm^{-1} from figure 5.30. Raman spectra of the thin films are in good agreement with the Raman spectra of bulk samples, which was shown in Chapter 3 and previously reported results [34-35]. It is interesting to observe the vibrational Raman modes of SBTi thin films on amorphous substrates. It is rare to observe the vibrational modes of SBTi thin films at room temperature. In the present study, the observed Raman spectra exhibited all the vibrational modes of SBTi thin films at room temperature. The modes between 90-160cm^{-1} are arising from the vibrations of the A-site ions of the pseudo-pervoskite blocks. The intensity of these modes decreased and peak broadening is increased for the films deposited at higher OMP (>50%). As the OMP increases, the phonon modes at lower frequency side shifted towards higher-frequency side due to displacement of A-site ions with respect to the TiO_6 octahedra [36]. In addition to that, the shift in the Raman modes to higher-frequency side is an indication of the stiffening of the bonds i.e. it indicates the shorter anion-cation distance which will result in vibration at higher frequencies. The intensity of the mode at 268 cm^{-1} is decreased and became broadened for the films deposited at higher OMP. These results revealed that the rigidity of the TiO_6 octahedra cage in SBTi thin films had changed with oxygen pressure. The observed vibrational modes at 865cm^{-1} show a shift towards lower frequency side as the OMP increases. It is possible that oxygen ions are freed from their defect bonding with increasing oxygen pressure, and thereby free to oscillate more like in single crystals [37]. The observed shift in Raman modes towards the higher-frequency side indicates that these films are under compressive stress. Raman modes in thin films annealed at different temperatures showed in figure 5.14 of this chapter are of relatively less intensity than the films deposited at different oxygen mixing percentage due to oxygen vacancies, which led to non-stoichiometry in thin films. From the above Raman spectra, it can be seen that as the OMP increases, the intensity of the phonon modes increased up to OMP 50%. With further increase of OMP, intensity of the phonon modes decreased and some have disappeared. Films deposited at 50% - OMP showed the more intensity phonon modes and some extra modes, which is in agreement with the corresponding XRD patterns. These results show that OMP is to be carefully controlled to achieve stoichiometric films in these types of oxides.

5.11.2 Microwave annealed samples:

The observed phonon modes are ~92,129, 154, 270, 489, 555, 788, and 865cm^{-1} from the figure 5.31. Raman spectra of the microwave annealed thin films are in good agreement with the Raman spectra of conventional annealed films. As we compare the observed Raman spectra of thin films annealed by both the methods, Raman modes in conventionally annealed thin films are relatively less intense than the microwave annealed films. One major difference we can found in microwave annealed films is that the films deposited at higher OMP (>50%) are able to exhibit the intense phonon modes compared to conventional annealed films. This indicates that microwave annealing is able to control the oxygen vacancies and Bi-volatization (as shown by the EDAX analysis given in section 5.7.1) which has the potential to enhance various material properties [38-40].

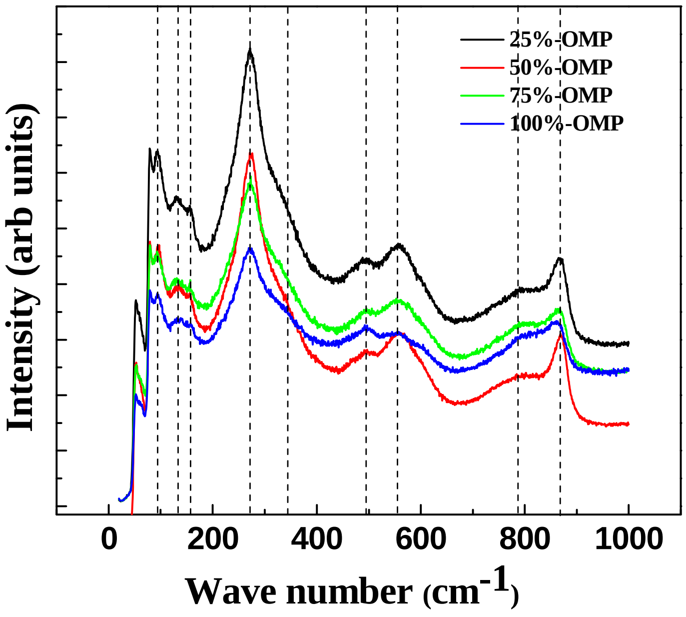

Figure 5.31: Raman spectra of the microwave annealed SBTi thin films deposited at different OMP.

5.12 Summary

In summary, SBTi thin films were grown on fused silica substrates under different deposition conditions. Deposition conditions are optimized to produce SBTi thin films with good crystal structure and microstructural characteristics. The EDX analysis confirmed the stoichiometry of the deposited films. The reflections from the X-ray diffractograms of SBTi thin films showed the formation of an orthorhombic structure with all the major peaks corresponding to the $A2_1am$ Space group. Initially films were deposited at room temperature at fixed OMP and annealed in microwave or conventional furnaces from 500 to 800°C. Films annealed at below 600°C showed the amorphous nature in both microwave and conventional processes. The annealing approach yielded crystalline SBTi films with good structural, microstructural and optical properties. The observed crystallite size is less for microwave annealed thin films. The rms roughness has increased as the annealing temperature increases in both the microwave and conventional annealing. The optical properties of the both conventional and microwave annealed films exhibited the same trend. Whereas the refractive index of the microwave annealed films showed higher values than the conventional annealed films. Even in high temperature (800^{o}C) annealed films, the phonon modes are existing with the same intensity in microwave annealed films. That means, the oxygen vacancies and Bi loss in microwave annealed samples are not high enough to change the local symmetry even after heating at 800^{o}C.

In the second approach, SBTi thin films deposited at room temperature by varying the oxygen mixing percentage and annealed in oxygen atmosphere. The crystallite sizes of the films are found to be varying with the oxygen partial pressure. It is confirmed that these factors can significantly alter the surface morphology of these thin films. The rms roughness was high for films deposited at 50% OMP in both the cases. The films deposited at 50%-OMP and annealed in oxygen atmosphere exhibited the good optical properties compared to films annealed at different temperatures in ambient which is discussed in section 5.6.3. Films deposited at different OMP exhibited well defined Raman spectra as observed for bulk ceramic samples compared to the films annealed at different temperatures. Films deposited at 50%-OMP exhibited more intense and sharp modes compared to other films. Microwave annealed films exhibited better properties compared to conventionally annealed films as observed in first part of this chapter. Stoichiometric SBTi thin films were obtained by successfully optimizing the OMP and controlling oxygen as well as Bi vacancies during the deposition and annealing process.

References.

1. Fan Suhua, Zhang Fengqiung, Wang Peiji, et.al, J.Rare earths., **26**, 575 (2008).
2. Kazumi Kato, Kazuyuki Suzuki, Desheng Fu et.al, Jpn.J.Appl.Phy., **41**, 2110-2114 (2002).
3. S.T.Zhang, Y.F Chen. H.P Sun et.al, J.Phys:Conds.Matter., **15**, 1223 (2003).
4. M.P. Besland, H. Djani-ait Aissa, P.R.J. Barroy, et.al, J.Thin.Solid.films., **495**, 86-91 (2006).
5. C-L, Huang, S.K.Lee, C-H, J.Appl.Phys., **96,** 1186 (2004).
6. Wu Yunyi, Zhang Duanming,Yu Jun, J. Appl. Phy., **105,** 061613 (2009).
7. Kazushi Amanuma, Takashi Hase, and Yoichi Miyasaka, J. Appl. Phys., Lett. **66** 221 (1995).
8. Seshu B. Desu, Tingkai Li., J.Mat. Sci. and Engg. B **34**, L4-L8 (1995).
9. Nak-Jin Seong and Soon-Gil Yoon et al, J.Appl. Phys. Lett., **71**, 81 (1997).
10. S. T. Tay, X. H. Jiang, C. H. A. Huan, A et al, J. Appl. Phys., **88**, 5928 (2000).
11. L A Knauss, J M Pond, J S Horwitz, D B Chrisey, C H Mueller and R Treece, J.App. Phy Lett., **69,** 25 (1996).
12. T.S Moss, J.Phy.Status.Solid., **141**, 119 (1994).
13. S.H Wemple, and M.Didmenico., J. Phys.Rev.B., **3,** 1338 (1971).
14. K.Venkata Sarvanan,K.Sudheendran,K.C.James Raju,et.al, J.Vacuum., **81**, 307-316 (2006).
15. S.C Roy, G.L Sharma, M C Bhatnagar, J.Sol.State. commu. **141**, 243 (2007).
16. K Venkata Saravanan, M Ghanashyam Krishna, K C James Raju et al., Proc 50th Jubliee DAE Solid-state Physics Sym., **50**, 441 (2006).
17. M. Osada, M Tada, M Kakihana et al, Jpn.J. Appl.Phy., (part1) **40,** 5572 (2001).
18. Z.Qu, C.Chen, W.Pan., J.Che.Mater., **19**, 4913 (2007).
19. R.D Shannon, J.Acta.Crys A., **32**, 751 (1976).
20. J. Xu, W.Menesklou and E.Ivers-Tiffee, J.Eur.Cer. Soc., **24**, 1735 (2004).
21. VenkataSarvanan, K.Sudheendran,M.G.Krishna,K.C.J.Raju, J.Phys.D:Appl.Phys., **42**, (045401)
22. L A Knauss, J M Pond, J S Horwitz, D B Chrisey et al, J.Appl. Phys Lett., **69** 25 (1996).
23. J.C.Nino, M.T.Lanagan and C.A.Randall and S.Kamba, J.Appl.Phy.Lett., 81, 4404 (2002).
24. P.Li,J.F.McDonald and T.M.Lu, J.Appl.Phys., **71**, 5596 (1992).

25. G.Bauer, Ann.Phys., **19**, 434 (1934).
26. E.A.Davis, and N.F.Mott, Phil.Mag., **22,** 903 (1970).
27. J.C. Nino, M.T. Lanagan, C.A. Randall and S. Kamba, J.Appl. Phys. Lett., **81,** 4404 (2002).
28. D Pamu, M Ghanashyam Krishna and K C James Raju and A K Bhantnagar, J.Sol. State. Comm., **7**, 135 (2005).
29. X.M Lu, J.S Zhu, W.Y Zhang, G.Q Ma and Y,N Wang, J.Thin. Sol. Films., **274,** 165 (1996).
30. R.Jacobson, Phys.Thin films., **8**, 51 (1975).
31. D.Pamu, et.al., J.Sol. State. Comm, **149**, 1932 (2009).
32. Somnath C, G.L Sharma, M.C Bhatnagar, R.Manchanda et al., J.Appl. Surf. Sci., **236,** 306 (2004).
33. 12. M. Osada, M. Tada, M. Kakihana, T. Watanabe et al. Jpn. J. App. Phy. (Par1)., **40,** 5572 (2001).
34. 14. N. Sugita, E. Tokumistu, M. Osada et al, Jpn. J. Appl. Phys. (Part2)., **42,** L944 (2003).
35. H.Hao, H.X Liu, M.H Cao, X.M Min, S.X Ouyang, J. Appl. Phy. A., **85**, 69-73 (2006).
36. Jun Zhu, Xiao-bing Chen, Zeng-ping Zhang, Jian-cang Shen., J. Act. Mat., **53** 3155-3162 (2005).
37. 15. N. Sugita, M. Osada, E. Tokumistu et al. Jpn. J. Appl. Phys. (Part1)., **41,** 6810 (2002).
38. A.Z. Simoes, M.A. Ramrez, C.S. Riccardi, et.al, J.Alloys and Comps., **455**, 407-412 (2008).
39. A. Z. Simoes and C. S. Riccardi., J.Adv.Mat.Sci. and Engg., 6 pages, doi:10.1155/2009/928545 (2009).
40. D.E. Clark, D.C. Folz, J.K.West, J.Mater. Sci. Eng. A., **287**, 153–158 (2000).

Chapter 6

In-situ deposition of the SBTi and Sm-substituted SBTi thin films and its properties

Chapter 6

In-situ deposition of the SBTi and Sm-substituted SBTi thin films and its properties:

6.1 Introduction:

This chapter deals with the deposition as well as structural, morphological, optical and Raman studies of the SBTi and Sm-substituted SBTi thin films. Films prepared in this study are deposited (in situ) at high temperatures. As mentioned in chapter 1, most of the studies on SBTi thin films for FeRAM and sensor applications have been studied on Pt/Si substrates. In previous chapter, it was shown the crystallization of SBTi thin film on amorphous fused silica substrates is indeed possible. However, post annealing or ex-situ annealing treatment failed to yield desired properties in terms of surface morphology with suitable optical properties. The poor quality of ex-situ crystallized SBTi thin films is mainly due to a difference in thermal expansion and non-stoichiometry at high temperatures and stress developed at the substrate to film interface. To overcome these shortcomings, alternative approach is the deposition of films at particular temperatures. So that crystallization and densification take place together during deposition, which is expected to give better results than ex-situ films.

6.2 Experimental conditions for preparation of SBTi thin films

SBTi thin films are prepared using rf sputtering on amorphous fused silica substrates. Initially, the sputtering chamber was evacuated to a base pressure of $4x10^{-6}$Torr after loading cleaned substrates on to the substrate holder, placed inside the vacuum chamber. All films are deposited at a fixed power density of $3Wcm^{-2}$. A working pressure of 20 mTorr was constantly maintained using a mixture of high pure (99.9%) argon and oxygen. The target to substrate distance was fixed at 5cms. To vary the degree of crystallanity, the deposition temperature (T_d) was varied from 600 to 725^oC. It was observed that without any heating, the un-cooled substrate temperature increased to about 120-130^{o}C during the deposition, presumably due to ion bombardment. The thickness of the thin films was around 450-500nm . Prior to every deposition, the substrates were stabilized at the respective deposition temperature (T_d) for an hour and rate of the increase in temperature was about 10^{o}C/min.

6.3 Results and discussion on SBTi thin films:

6.3.1 Structural properties:

The X-ray diffractograms of the SBTi thin films deposited at different substrate temperatures on amorphous fused silica substrates are shown in figure 6.1. As evident from figure 6.1, films deposited at higher substrate temperatures are crystallized into an obvious pervoskite phase with a standard orthorhombic structure. As the substrate temperature increasing, grain growth orientation changes from (119) to (0010) orientation. In detail, films deposited at 600^{o}C shows polycrystalline nature prominent peak (119) orientation together with its second-order (0010) orientation and films deposited at 650^{o}C showed same nature but intensity of the peak (119) increased along with (0010) peak. Further increasing of substrate temperature i.e at 700^{o}C the intensity of the (0010) peak is almost equal to the intensity of the (119) peak and films deposited at 725^{o}C showed the intensity of the (0010) peak dominated the intensity of (119) peak. Qualitatively these results are proven by calculating the degree of orientation and lattice distortion as shown in figure 6.2. This shows that the deposition temperature plays a pivotal role in preparing the preferred orientational films. As observed in [1] SBTi films are amorphous in nature at substrate temperature below 600^{o}C. From table 6.1, it was clearly shown that the films deposited at 700^{o}C of the lattice parameter values are almost well matched with values of the standard orthorhombic structure compared with the films deposited at other substrate temperatures. The lattice distortion as a function of substrate temperature is shown in figure 6.2. It was calculated as

$$\delta = \frac{d - d_{hkl}}{d_{hkl}} \tag{6.1}$$

Where d is the lattice spacing calculated from measured 2θ value of the XRD peak and d_{hkl} is the ideal lattice spacing of the single crystal [2]. The finite crystallite size (C) for these films was calculated using Scherrer's formula and the micro strain was estimated from the angular line broadening Δ2θ. The calculated micro-strain is shown in table (6.2). The films deposited at 650^{0}C and 700^{o}C are shows less strain than the other films. This is due to the mobility of the adatoms on the growing film.

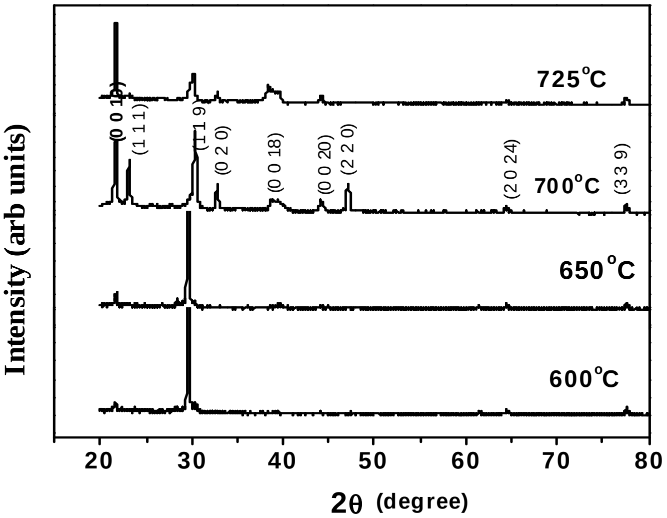

Figure 6.1: XRD pattern of the SBTi thin films deposited at 600-725^{0}C.

Substrate temperature (^oC)	**a (Å)**	**b (Å)**	**C (Å)**	Volume (**Å)^3**
600	5.414	6.0	40.95	1330.21
650	5.408	5.94	40.96	1315.77
700	5.426	5.432	40.94	1206.66
725	5.419	5.610	40.98	1245.81
Standard	5.428	5.438	40.94	1207.11

Table 6.1: Lattice constants for SBTi thin films deposited at 600-725^oC

The micro strain was calculated as

$$\varepsilon = \frac{\beta_{2\theta} Cos\theta}{4} \tag{6.2}$$

The notations have usual meaning

Substrate temperature (^0C)	**Micro strain (ε)**
600	0.0035
650	0.003
700	0.004
725	0.0044

Table 6.2: Micro strain of SBTi films deposited at 600-725^oC

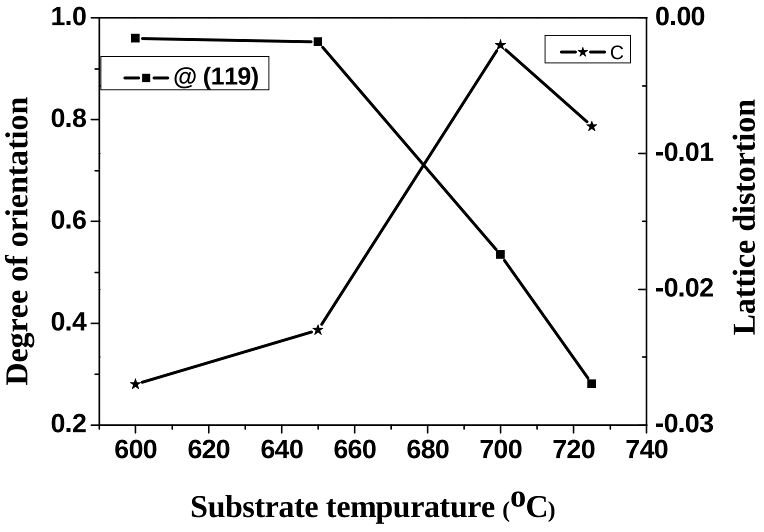

Figure 6.2: Degree of crystallanity and lattice distortion as function of substrate temperature.

6.3.2 Surface morphology:

The microstructure of the SBTi thin films as a function of substrate temperature are examined by atomic force microscopy. The surface morphology of the SBTi films deposited at different substrate temperatures is shown in figure 6.3 (a-d). The average grain size and surface roughness as a function of substrate temperature is shown in table 6.3. It can be observed that the surface morphologies vary with substrate temperature. While deposited at 600^{o}C, the films have smooth and poor crystalline nature. For the films deposited at 650 & 700^{o}C, the grain growth and surface roughness are increased. This is due to the increased mobility of species at higher temperatures and thus induces a higher speed of the coalescence of grain islands as the substrate temperature increases [3]. Further increase in temperature to 725^{o}C, leads to grain growth is in different orientations. These results are in agreement with the XRD pattern of the films.

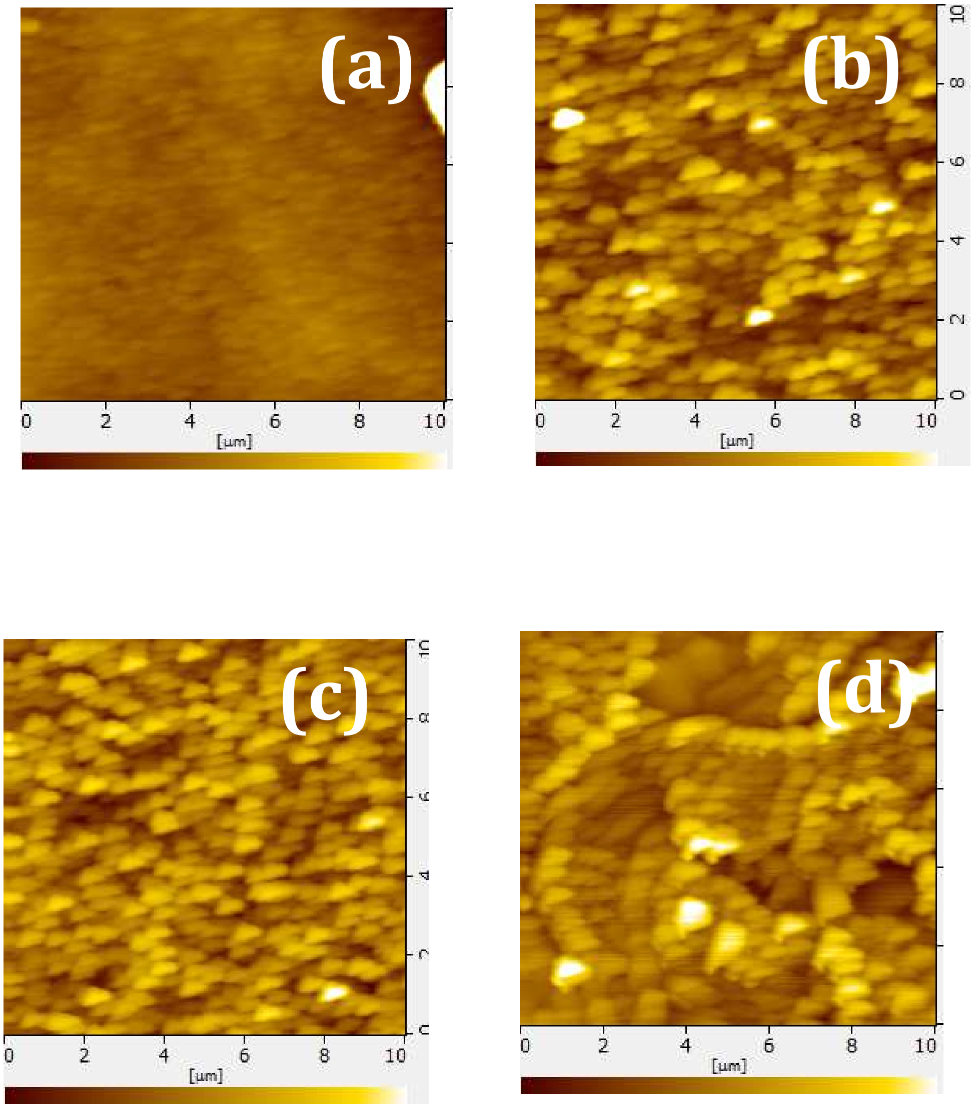

Figure 6.3: AFM images of the SBTi thin films deposited at (a) 600 (b) 650 (c) 700 (d) 725°C

Sub. Temperature (^{o}C)	**600**	**650**	**700**	**725**
Ave. grain size (nm)	**215**	**276**	**311**	**372**
Surface roughness (nm)	**8.5**	**8.2**	**9.6**	**15**

Table 6.3: Average grain size and surface roughness of the SBTi thin films deposited at 600-725^{o}C.

6.3.3 Compositional analysis

In order to investigate the compositional deviations if any in the rf sputtering processed samples. Energy Dispersive X-ray (EDX) analysis for the films deposited at different substrate temperatures were carried out. The atomic percentages of each element in the films are mentioned in the table 6.4. Figure 6.4 presents the EDX spectrum of the SBTi thin film deposited on amorphous fused silica substrates at 700^{o}C substrate temperature. The Bi, Sr, Ti and O peaks appear in the EDX spectrum. Films deposited at 725^{o}C exhibits the lower atomic percentage for each element compared to films grown at other temperatures and standard atomic percentage. These results reveal that the films deposited at higher temperature (725^{o}C) faces problem with evaporation of Bi and oxygen, which lead to decrease in film properties.

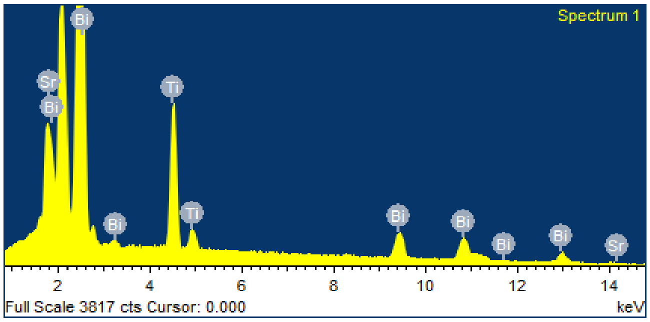

Figure6.4: EDX spectrum of SBTi thin films deposited at 700^{o}C substrate temperature.

Element	Atomic % of each element				
	600°C	650°C	700°C	725°C	Standard
Ti K	17.97	16.97	16.76	16.56	16.66
Sr L	4.18	4.11	4.1	3.98	4.16
Bi M	16.69	16.60	16.30	15.68	16.66
O	63.16	63.11	61.11	58.56	62.49

Table 6.4: Atomic percentage of each in the SBTi films deposited at different temperatures.

6.3.4 Raman spectroscopy:

Figure 6.5 showed the Raman spectra of $SrBi_4Ti_4O_{15}$ thin films deposited at 600-725°C. Raman spectra exhibits the phonon modes at 90, 270, 486, 601 and 863 cm^{-1} in addition to some weak modes. The vibrational modes of Bismuth Layered Structured Ferroelectrics (BLSFs) can be classified as internal modes of TiO_6 octahedra and the lattice translation modes related to the motion of the cations in the pseudo-pervoskite slabs and the Bi_2O_2 layers [4]. For the BLSFs, the mode between 50 and 60 cm^{-1} is reported to arise from the displacement of Bi^{3+} ions in Bi_2O_2 layers, while those between 90 and 160 cm^{-1} originate from the vibrations of the ions at the A sites of the pseudo-pervoskite blocks. The mode at ~268 cm^{-1} arise from the torsional bending of TiO_6 octahedra and those at above 500 cm^{-1} correspond to the stretching of TiO_6 octahedra [5, 6].

In the present study, Raman spectra are observed at room temperature. We can clearly observe the difference between the films deposited at 650 & 700°C and films deposited at 600 & 725°C with respect to phonon modes. Films deposited at 650 & 700°C exhibited more phonon modes than the films deposited at 600 & 725°C. There are no previous reports on Raman spectra of these films on amorphous substrates phonon modes are detected at room temperature and it will be possible by optimizing the experimental processes and conditions [7]. Interestingly, we have observed the phonon modes at room temperature with optimized experimental conditions. All films exhibited the modes between 90 and 160 cm^{-1} that are known to originate from the vibrations of the ions at the A sites of the pseudo-perovskite blocks. Films deposited at 650 & 700^{o}C exhibit the phonon mode at 270 cm^{-1} which arises from the torsional bending of TiO_6 octahedra which are not observed for the films deposited at 600 & 725^{o}C. This might be due to the reason that films deposited at 600^{o}C shows poor crystallanity and films deposited at 725^{o}C exhibited Bismuth loss and oxygen vacancy, which could lead to a decrease in the intensity of phonon modes and even their disappearance as was observed. The phonon modes > 800 cm^{-1} is originated from the O-Ti-O symmetric stretching. As the substrate temperature increases, peak broadening of phonon modes also increases. This indicates that the lattice vibrations of the TiO_6 octahedra are stretched by the inhomogeneous strain in film due to increasing deposition temperature during deposition. Raman studies of these films are in strongly agreement with XRD pattern of the same films.

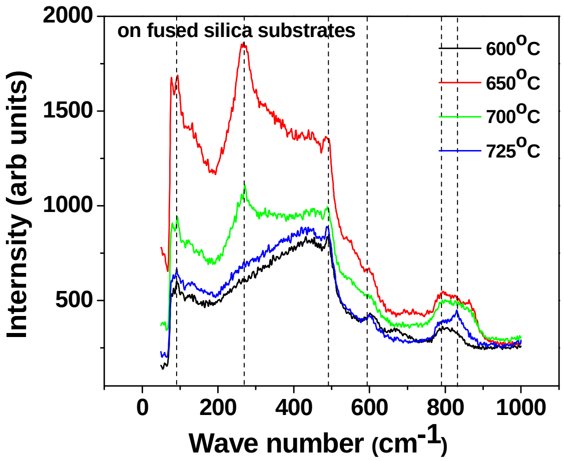

Figure 6.5: Raman spectra of the SBTi thin films deposited at 600-725^{o}C.

6.3.5 Optical properties:

The optical band gap for the films is calculated using the Tauc relation as discussed in Chapter 5. The band gap energy (E_g) has been estimated by assuming an allowed direct transition between the highest occupied state of the valance band and the lowest unoccupied state of conduction band. Optical transmittance spectra of SBTi films deposited at 600-725^{o}C are shown in Figure 6.6. The oscillations in transmittance arise from the interference due to reflection from the top surface of the film and interface between film and the substrate. Variation of the band gap with the deposition temperature is shown in figure 6.7. The band gap has decreased as the deposition temperature increases up to 700^{o}C. With further increase in substrate temperature, the band gap got increased. The band gap of the films deposited at 600^{o}C exhibited higher values due to poor crystallinity of the films as they are deposited at low substrate temperatures. For the films deposited at 700^{o}C the observed band gap has decreased. This indicates that as the substrate temperature increases grain growth increased and crystallization takes place, which led to decrease in the band gap. Further increase substrate temperature (725^{o}C), the band gap is increased due to non-stoichiometry of the films by losing the Bismuth and oxygen at high temperature which acts as defects. These results are supporting with Raman studies and XRD as mentioned in sections 6.3.4 and 6.31 respectively.

On the contrary, refractive index of the films increased as the substrate temperature increases. The refractive index of SBTi thin films deposited at different substrate temperatures is calculated and is shown in figure 6.7. As shown in this figure, the refractive index increases with increase in temperature. The lower values of refractive index for the deposited films compared to films deposited at 650 and 700^{o}C can be attributed to the rf sputtering deposition process that produces films with porous microstructure having low packing density at ambient temperature. However, as the deposition temperature increased up to 700^{o}C, the refractive index increased. The relationship between the packing density and the refractive index has been discussed in detail by many researchers, and they have found that when the film achieves the bulk value of refractive index, its packing density will be the highest [8]. Thus, it is reasonable to assume that one of the causes for an increase in the refractive index with temperature for the films in the present study is the increase in their packing density apart from the obious reason of setting crystallization in the films. Packing density of these films calculated using equation 5.1 mentioned in chapter 5. Optical packing density as a function of annealing temperature is shown in figure 6.8. It can be seen that above 700^{o}C, the refractive index has decreased due to low rates of deposition as well as Bi and oxygen vacancies generated at higher temperatures, which lead to non- stoichiometry along with low packing density.

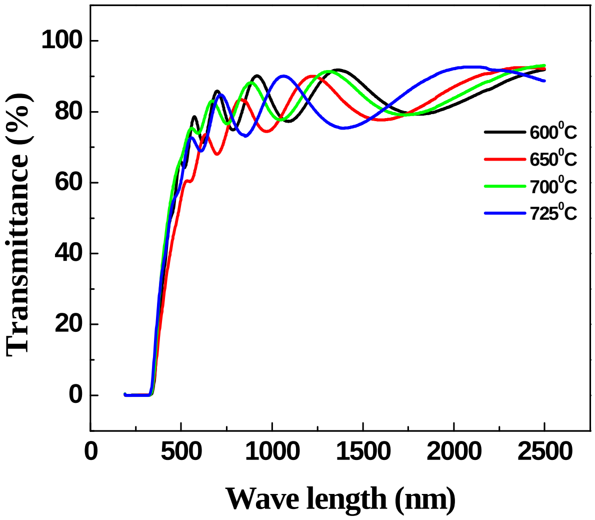

Figure 6.6: Transmittance spectra of SBTi thin films deposited at 600 -725^{o}C.

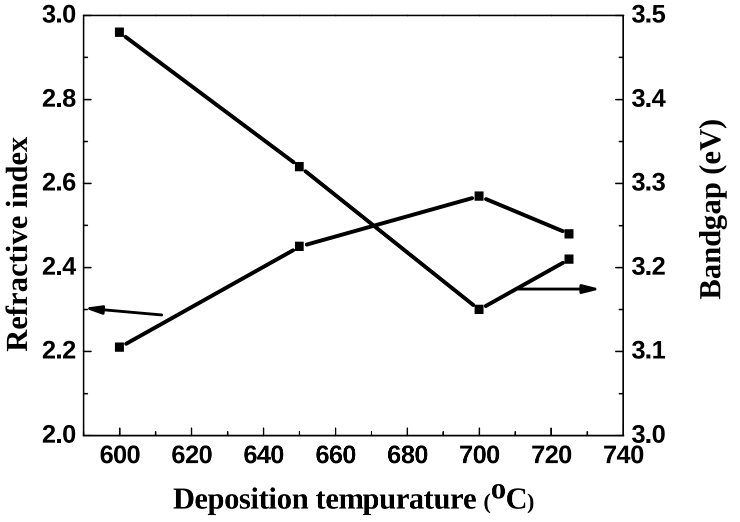

Figure 6.7: Refractive index and band gap of the SBTi thin films deposited at 600-725^{0}C.

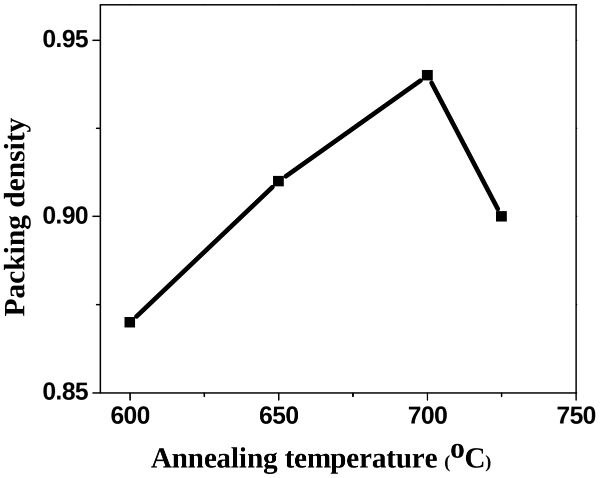

Figure 6.8: Optical packing density as a function of annealing temperature of SBTi films

6.4 Sm-substituted SBTi thin films:

6.4.1 Preparation of Sm-substituted SBTi target and thin films:

The Sm-substituted SBTi (**$SrBi_{3.25}Sm_{0.75}Ti_4O_{15}$**) (SBSmTi) ceramic target used for rf magnetron sputtering were prepared by solid-state reaction method. For SBSmTi ceramic target, powders of $SrCO_3$, Bi_2O_3, Sm_2O_3 and TiO_2 of 99.9% purities were mixed in deionized water at desired composition. A few wt % of excess Bi_2O_3 were added to the powders to compensate for the Bi loss in the process of sintering and deposition. The mixture was calcined at 750°C for five hours to make SBSmTi powder. The calcined powders with binder addition were pressed into target and then sintered at 1190°C for 2h. The detailed procedure is mentioned in Chapter 5. XRD pattern of the SBSmTi target indicated pure polycrystalline phase with no secondary phases. Sm-substituted SBTi (**$SrBi_{3.25}Sm_{0.75}Ti_4O_{15}$**) thin films were deposited using the procedure mentioned in this chapter, section 6.2.

In order to investigate the effect of deposition temperature T_d, on the crystallanity of Sm-substituted SBTi thin films they were deposited at a substrate temperature range of 675-750^{o}C at a constant OMP of 50%. The optimized conditions used for the present study are shown in table 6.5.

Parameter	**Value**
Target type	SBSmTi ($SrBi_{3.25}Sm_{0.75}Ti_4O_{15}$)
Power density	3 (W/cm^2)
Substrate to target distance	5cms
Working pressure	20mTorr
Oxygen mixing percentage	Ar: O_2 (50%: 50%)
Substrate type	Fused silica
Substrate temperature	675 – 750^{o}C

Table 6.5: Sputter deposition parameters used in the present study.

6.4.2 Structural properties:

The X-ray diffractograms of the Sm-substituted SBTi ($SrBi_{3.25}Sm_{0.75}Ti_4O_{15}$) thin films deposited at different substrate temperatures on amorphous fused silica substrates are shown in figure 6.9. The films deposited at temperatures below 700^{o}C showed amorphous nature [1], and films deposited at 700^{o}C shows the beginning of the grain growth which indicates the crystalline nature of the films. With increasing substrate temperature, grain growth increased and films crystallized into orthorhombic structure. Further increase in temperature resulted in, the grain growth orientation changing from (119) to (0010). In detail, films deposited at 725^{o}C showed polycrystalline nature with prominent peak of (119) orientation together with its second-order (0010) reflection and films deposited at 750°C showed the intensity of (0010) peak dominated over the intensity of the (119) peak. This shows that the deposition temperature plays a pivotal role yielding in preferred oriented films. The micro-strain is calculated from equation 6.2 and shown in table 6.6. The films deposited at 725°C shows less strain than the other films. This is due to the increased mobility of the adatoms on the growing film at higher temperatures.

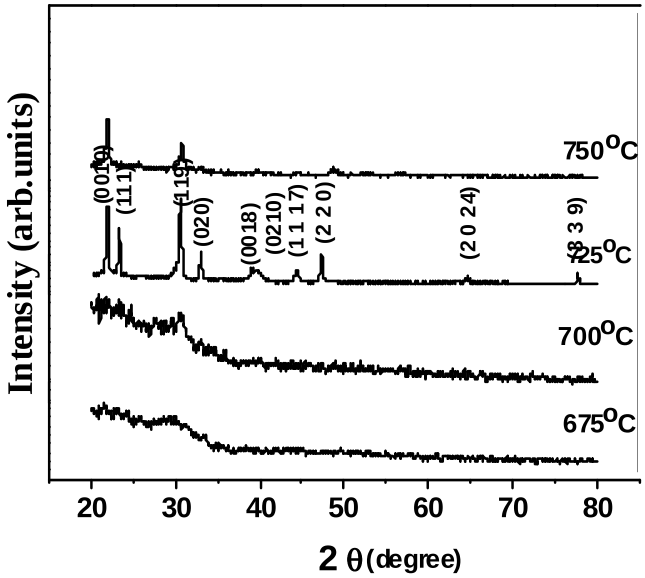

Figure 6.9: XRD pattern of the Sm-doped SBTi thin films deposited at 675-750°C.

Substrate temperature (°C)	**Micro strain (ε)**
675	-----
700	0.0051
725	0.0041
750	0.0067

Table 6.6: Calculated micro strain values of Sm-substituted SBTi films deposited at 675-750°C

6.4.3 Morphological

The microstructures of the Sm-substituted SBTi thin films as a function of substrate temperature were examined by atomic force microscopy. The surface morphology of SBSmTi films deposited at different substrate temperature is shown in figure 6.10 (a-d). The average grain size and surface roughness as a function of substrate temperature is shown in table 6.7. It can be observed that the surface morphology vary with the substrate temperature. Films deposited at 675^{o}C, got smooth surface and with amorphous nature. Films deposited at 700^{o}C showed the beginning of the grain growth. Films deposited at 725^{o}C and 750^{o}C exhibited grains with a platelet microstructure, which is known the microstructure of bulk BLSFs. As the substrate temperature increases, the grain growth and roughness increased simultaneously. This is due to the crystal structure as well as higher mobility of species adsorbed onto the substrate at higher temperatures and thus induces a higher speed of the coalescence of grain islands [9].

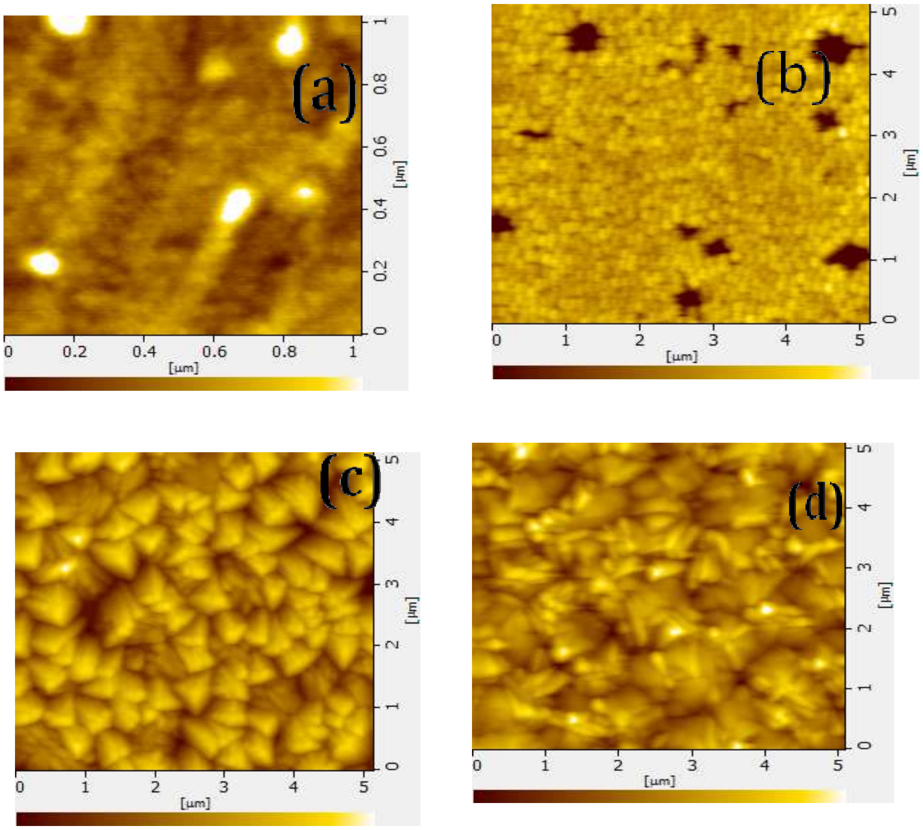

Figure 6.10 (a-d): AFM images of the Sm-substituted SBTi thin films deposited at (a) 675 (b) 700 (c) 725 and (d) 750^{o}C.

Sub. Temperature (^{0}C)	675	700	725	750
Ave. grain size (nm)	0	132	364	372
Surface roughness (nm)	8.5	8.2	9.6	15

Table 6.7: Average grain size and surface roughness of the Sm-substituted SBTi thin films.

6.4.4 Optical properties:

The optical properties of Sm-substituted SBTi films on fused silica substrates are investigated by optical transmittance measurements. Optical transmittance spectra are shown in Figure 6.11. The interference fringes and relatively high transmittance indicate a good homogeneity of the Sm-substituted SBTi films. From figure 6.11, it can be clearly seen that, the transmittance increased for Sm-substitution films compared to pure SBTi thin films. It is useful property for integrated optics applications.

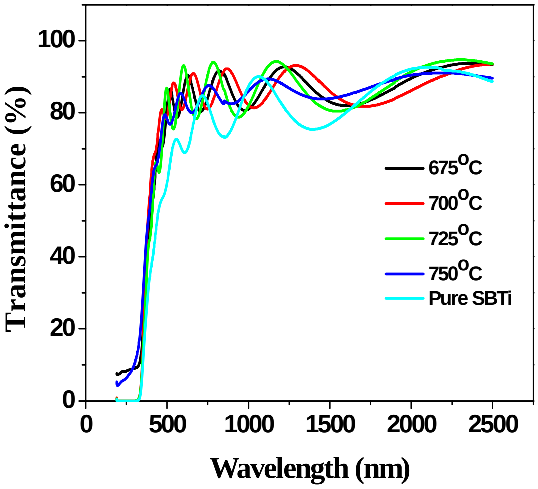

Figure 6.11: Transmittance spectra of Sm-substituted SBTi thin films.

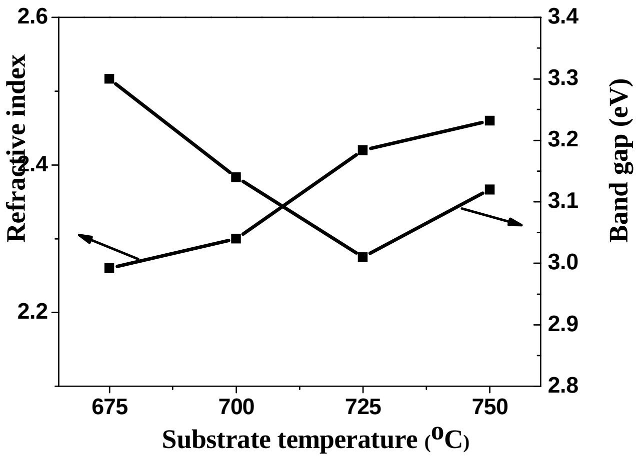

Figure 6.12: Refractive index and band gap of the Sm-substituted SBTi thin films deposited at different temperatures.

The optical band gap E_g for Sm-substituted SBTi thin films was calculated using the Tauc relation [10], which is given by

$$(\alpha h\nu) = C.\,(h\nu - E_g)^r \qquad (6.1)$$

Where C is a constant, α is the absorption coefficient, hν is the incident photon energy and r = 0.5, 1.5, 2 or 3 for allowed direct, forbidden, allowed indirect and forbidden indirect electronic transitions, respectively. In the present case, the band gap energy has been estimated by assuming an allowed direct transition (r = 0.5) between the highest occupied state of the valance band and lowest unoccupied state of the conduction band. The band gap and refractive index of the Sm-substituted SBTi films as a function of deposition temperature are shown in figure 6.12. It is shown that the introduction of Samarium reduced the band gap Eg value from around 3.5 to 3.3 eV compared to un-substituted SBTi. Such a modification of band structure upon the Samarium substitution can be explained on the basis of the high electronegativity of the Samarium ion. It has been well known that the band structure of layered structure materials like $(B_4T_3O_{12})$ is generally defined by the Ti 3d level and O 2p level, which form the conduction band (CB) and valence band (VB), respectively [11]. Considering the fact that the energy of electronic level of an element is inversely proportional to its electronegativity [12] and the substituted Samarium ion is more electronegative than titanium ion, the Samarium 6s state is expected to have lower energy than Ti 3d state, which leads to a lowering of CB and narrowing of band-gap separation. Therefore, it becomes clear that Samarium ion can be a very powerful substituent for the band-gap engineering of strontium bismuth titanate. The observed refractive index of the Sm-substituted SBTi films is higher compared to un-substituted films. This indicates that Samarium substitution increases the packing density of the films.

6.4.5 Raman spectroscopy studies:

Raman spectroscopy studies on layer structure ferroelectrics like SBTi have been reported in ceramic samples and very few reports are available on thin films. In the present study, Sm-substituted SBTi thin films deposited by rf sputtering with different substrate temperatures were studied. Figure 6.13 showed the Raman spectra of $SrBi_{3.25}Sm_{0.75}Ti_4O_{15}$ thin films deposited at 675-750^oC. Raman spectra exhibited the phonon modes at ~ 151, 271, 440, 487, 607, 672 and 796 cm^{-1} in addition to some weak modes. The observed phonon modes at lower frequencies (below 200 cm^{-1}) are shifted towards the lower-frequency side compared to the un-substituted SBTi thin films which are described in section 6.3.4. As in the case of bulk Sm-substituted SBTi samples described in section 4.3.3, vibrational modes are affected by Sm-substitution with a red shift. Such a change in the peak position may be ascribed to the heavier mass of samarium and also to the lowering of bond strength. We can clearly observe the difference between the films deposited at 725 & 750^oC and films deposited at 675 & 700^oC with respect to phonon modes. Films deposited at higher temperatures exhibited more phonon modes with higher intensity compared to films deposited at lower temperatures. As seen in XRD pattern, the films deposited at 675^oC shows amorphous nature, but in Raman spectra we can observe a few modes which indicate that Raman studies are more sensitive to the local symmetry of the films. Films deposited at lower temperatures (675 & 700^oC) exhibited almost the same phonon modes. Films deposited at 725^oC exhibited more phonon modes compared to other films. This would be expected because the XRD pattern of films deposited at 725^oC showed good crystallanity and (119) orientation with maximum intensity. Films deposited at 750^oC shows the same phonon modes even though XRD pattern showed (0010) orientation. This indicates that the local structure of both the films does not change though their orientations differ.

The phonon mode at ~271cm^{-1} has appeared only for the films deposited at higher temperatures (725 & 750^oC) which are a good indication that these films are well crystallized. The mode at 271cm^{-1} from the torsional bending of TiO_6 octahedra does not shift with substitution. The modes in the range of 550 - 830cm^{-1} arises from the stretching of TiO_6 octahedra [13-14]. The Raman mode at 607cm^{-1} has shifted to a higher frequency with Sm-substitution compared to unsubstituted SBTi, which is similar to the behaviour in Ba-substituted SBTi [15]. The mode blue shift implies the reinforcement of the bond strength in comparison with the bonding of TiO_6 octahedra with Bi_2O_2 layers. Since Sm^{3+} substitution into Bi_2O_2 layers induces the bond relaxation in the Bi_2O_2 layers, the neighbouring TiO_6 octahedra might shrink, resulting in the increase in the bond energy and consequent blue shift in the frequency [16-17]. Higher content of Sm-substitution into the (Bi_2O_2) layer resulted in the structural distortion [18]. Sm-O covalent bond is stronger than Bi-O bonding which results in extra phonon modes that appeared at 672cm^{-1} from Sm-O mode. Same trend was observed by H.Hao., et al [19]. The phonon modes at higher frequencies have exhibited the red shift due to the stress involved in the films at high temperatures.

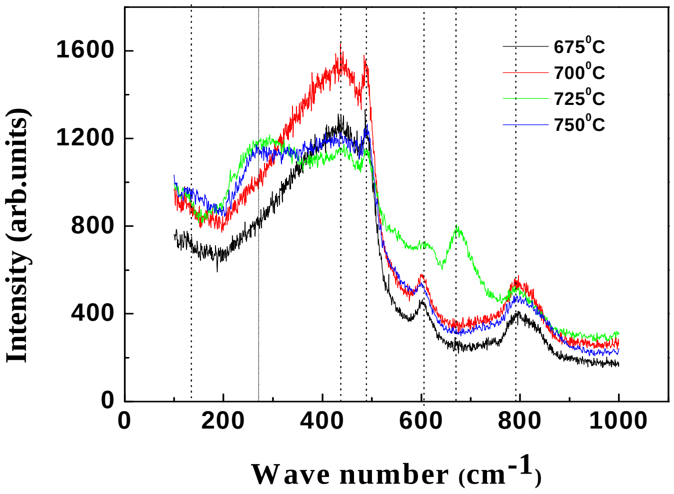

Figure 6.13: Raman spectra of Sm-substituted SBTi thin films

6.5 Summary:

In summary, SBTi thin films are deposited (in situ) at elevated substrate temperatures. Two sets of films were grown and they are (i) SBTi thin films and (ii) Sm-substituted SBTi thin films. In case of SBTi thin films, films are deposited on fused silica substrates at substrate temperatures from 600 to 725°C. The XRD results revealed an increase in degree of orientation with increase in substrate temperature. As the substrate temperature increases, the films changes from non-c-axis orientation (119) to c-axis orientation (0010). This indicates that the orientation of the films can be controlled by optimizing the substrate temperature. The values of the lattice parameters of the films deposited at 700°C are well matched with standard lattice parameter values and have lesser values of micro-stain. It is obvious that the grain size increased as the substrate temperature is increased. As the substrate temperature increased up to 700°C, the observed band gap has decreased. This indicates that, as the substrate temperature increases both grain growth and crystallization takes place, which lead to a decrease in band gap. Further increase in substrate temperature (725°C), lead to the band gap getting increased due to non-stoichometry of the films by losing Bi and oxygen ions at high temperatures which acts as defects.

Sm-substituted SBTi thin films were deposited in-situ at elevated substrate temperatures. The XRD results on SBSmTi thin films deposited on fused silica substrates indicated that the films deposited at lower temperatures (675 & 700°C) showed an amorphous nature and poor crystallanity. As the substrate temperature increases, the grain orientation of the films changes from non-c-axis orientation (119) to c-axis (0010). This change is seen in both SBTi and Sm-substituted SBTi films, which proved that the crystalline orientation can be controlled by optimizing the deposition conditions. Films deposited at 725 and 750°C exhibited the platelet structure which is the hallmark of bulk BLSFs. Sm-substituted SBTi films is more transparent than un-substituted films, which is an important property useful in opto-electronic devices to minimize the transmission losses. It was observed that the introduction of Samarium reduced the band gap E_g value from ~ 3.5 to 3.3 eV compared to un-substituted SBTi films. Such a modification of band structure upon the Samarium substitution can be explained on the basis of the high electronegativity of the Samarium ions. From Raman spectra, shifting of vibrational modes towards a higher-frequency side was observed, which indicates the identification of Samarium substitution.

References:

1. S. T. Tay, X. H. Jiang, C. H. A. Huan, J.App. Phy., **88,** [10] 5928-5934 (2000).
2. Y K Vayunandana Reddy, D Mergel, S Reuter, V Buck and M Sulkowski., J .Phy. D **39,** 1161-1168 (2006).
3. Zhang Bai-shun, Guo Tao, Zhang Tian-jin, Wang Jin., J. Trans. Nonferrous. Met .Soc.China., **16,** s 126-s129 (2006).
4. Jun Zhu, Xiao-Bing Chen, Jun-Hui He, J. Sol. State. Che., **178,** 2832-2837 (2005).
5. N. Sugita, E. Tokumistu, M. Osada et al, Jpn. J. Appl. Phys. (Part2) **42,** L944 (2003).
6. N. Sugita, M. Osada, E. Tokumistu et al, Jpn. J. Appl. Phys. (Part1) **41,** 6810 (2002).
7. C.L Du, S.T Zhang, Z.B Gu, G.X Cheng, J.Wang et.al, J. App. Phy., **99,** 094101 (2006).
8. K Venkata Sarvanan, K Sudheendran, M Ghanashyam Krishna and K C James Raju., J. Mat. Chem. and Phys., **105**, 426-432 (2007).
9. S.Chopra, S.Sharma, T.C Goel, G.G.Mendirata, J.Appl. Surf. Sci., **230**, 207 (2004).
10. K.Venkata Sarvanan, K.Sudheendran, M.Ghanashyam Krishna, K.C James Raju and A.K Bhatnagar, J.Vacuum., **81**, 307 (2006).
11. J.W. Tang, Z.G. Zou, J.H. Ye, J.Chem. Mater., **16,** 1644 (2004).
12. S.G. Hur, T.W. Kim, S.J. Hwang, H. Park,W. Choi, S.J. Kim, J.H. Choy, J. Phys. Chem.B., **109**, 15001 (2005).
13. 12. M. Osada, M. Tada, M. Kakihana, T. Watanabe et al, Jpn. J. App. Phy. (Par1); **40,** 5572 (2001).
14. 14. N. Sugita, E. Tokumistu, M. Osada et al, Jpn. J. Appl. Phys. (Part2; **42**, L944) (2003).
15. Dobal P S and Katiyar R S, J.Raman Spectrosc**., 33,** 405 (2002).
16. Zhu J, Chen X B, Zhang Z P and Shen J C, J.Acta.Mater., **53**, 3155 (2005).
17. Guo Zhen Liu, Can Wang, Hao Shuang Gu and Hui Bin Lu, J.Phy.D:Appl.Phys., **40,** 7817-7820 (2007).
18. Y. P. Chen, Y. Y. Yao, Z. H. Bao, P. Bao, J. S. Zhu and Y. N. Wang. J. Matt. Lett., **57,** 3623 **(**2003).
19. H.Hao, H.X Liu, M.H Cao, X.M.Min et.at, J.Appl. Phy.A ., **85,** 69-73 (2006).

Chapter 7

Mechanical and microwave dielectric properties of SBTi and Sm-substituted SBTi thin films

Chapter 7

Mechanical and microwave dielectric properties of SBTi and Sm-substituted SBTi thin films.

7.1 Introduction

This chapter describes the mechanical and microwave dielectric properties of SBTi and Sm-substituted SBTi thin films deposited at different processing conditions. The results are obtained by a mechanical testing method based on a nanoindentation process leading to the measurement of the depth reached by an indenter as a function of applied load. This study enables us to estimate the capability of nanoindentation method for the determination of some mechanical characteristics of thin films. More precisely, the elastic or Young's modulus of film as well as its hardness (H) which is also an important mechanical parameter and coefficient of friction are obtained. The microwave dielectric properties of these films were determined using an Agilent 8722ES vector network analyzer by employing the Split Post Dielectric Resonator measurement techniques (SPDR). The details of these techniques are mentioned in Chapter 2 and described elsewhere [1].

It is well known that piezoelectric coefficients depend on the mechanical coefficients which are related to the mechanical state of the materials [2]. Moreover, the mechanical behavior plays a crucial role in the delamination, cracking or fracture, and polarization fatigue of the multilayer thin film structures [3-5]. Consequently, the investigation on the mechanical properties of the bismuth layered-structure ferroelectric thin films is of practical importance in various situations and particularly for the design of piezoelectric devices. The importance of such films have now increased with their potential for application in MEMS devices where they can be used not only for sensing and actuation as well as for energy harvesting even at elevated temperatures. These applications require a closer study of the mechanical properties of the deposited thin films. These material properties depend on the substrate, crystallographic orientation, grain size, process conditions and the deposition rate. In a MEMS device, often micromachining converts the deposited films and multi layers into a free standing element and under such situations the device performance critically depends on the mechanical properties of the deposited films or multi layers.

The potential applications of the dielectric thin films in microwave devices have accelerated the research in the development of new materials and thin film processing methods and optimization [6]. The reliable and reproducible measurements of the dielectric properties of these thin films at microwave frequencies have become an essential requirement of these research activities. Microwave characterization techniques for bulk materials are a well developed field, but for thin films it is still challenging. There are few studies on the microwave dielectric properties of thin films even though it is quite important both in terms of application and in academic point of view. There are reports on low frequency dielectric properties for layer structured ferroelectric thin films but there are no reports on their microwave dielectric properties, which again emphasize the relevance of the present study.

7.2 Effect of annealing on mechanical properties of SBTi thin films.

The load-displacement curve obtained by indentation of the rf sputtered films is shown in figure 7.1 and the area of the indent is determined using the known geometry of the indentation tip. While indenting, various parameters such as load and depth of the penetration can be measured. A record of these values can be plotted as a graph to create a load-displacement curve as shown in figure 7.1. These curves can be used to extract mechanical properties of the materials. The presence of discontinuities in the load-displacement response reveals information about cracking, delamination, and plasticity in the film and substrate [7]. In the present case, there is no observable discontinuities in the load-displacement curve which indicates that the films are uniform and crack free.

The SBTi thin films were prepared by rf sputtering technique. Detailed preparation procedure is mentioned in chapter 5. Films are deposited at room temperature and annealed in conventional and microwave furnaces. The hardness and Young's modulus of the films annealed in conventional and microwave furnaces are shown in figure 7.2(a-b) and 7.3 (a-b) respectively. There is no observable difference between conventional and microwave annealed films. It could be because the grain size of films annealed in conventional and microwave furnaces are almost the same. Low temperature annealed films are amorphous as mentioned in chapter 5, and as the annealing temperature increases the degree of crystallanity increased. The hardness of the amorphous films is less than the crystalline films [8]. The Young's modulus increases monotonically from 80 to 103GPa and hardness from 3 to 6GPa with enhancement of grain size from 30 to 75 nm for both microwave and conventional annealed films. As the annealing temperature increases, the value of the hardness and Young's modulus is increased. These results are in accordance with the microstructure of the same films which are mentioned in chapter 5. These results confirm that the mechanical properties of the films are improved after annealing due to grain growth [9]. The increase in grain size leads to a hardening of the material. It may be explained that the main deformation mechanism at these grain sizes is indeed sliding in the grain boundaries and the conventional dislocation-based deformation is not operable in nanocrystalline materials with grain sizes of less than 100nm [10].

In order to have further confirmation, we have done the scratch test for the same films. Scratch test is a versatile tool for analysis of both bulk and thin films [11]. Nanoscratch provides the capability to investigate modes of deformation and fracture which are not possible using standard indentation technique [12]. Nanoscratch is accomplished by applying a normal load in a controlled fashion while measuring the force required for moving the tip laterally across the sample. By selecting the appropriate normal loading profile and lateral displacement pattern, many different types of tests can be performed.

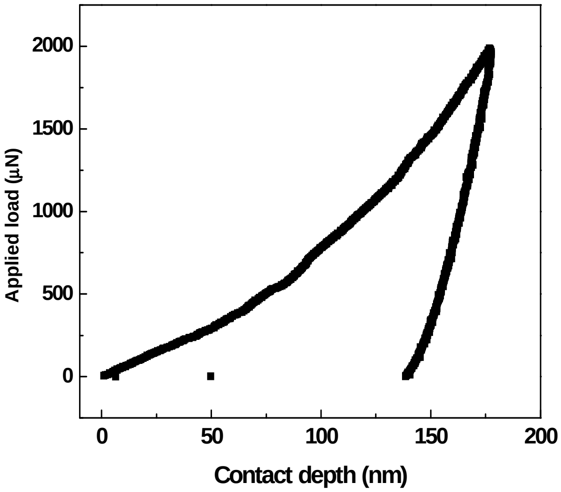

Figure 7.1: Typical load-displacement curve for SBTi thin films.

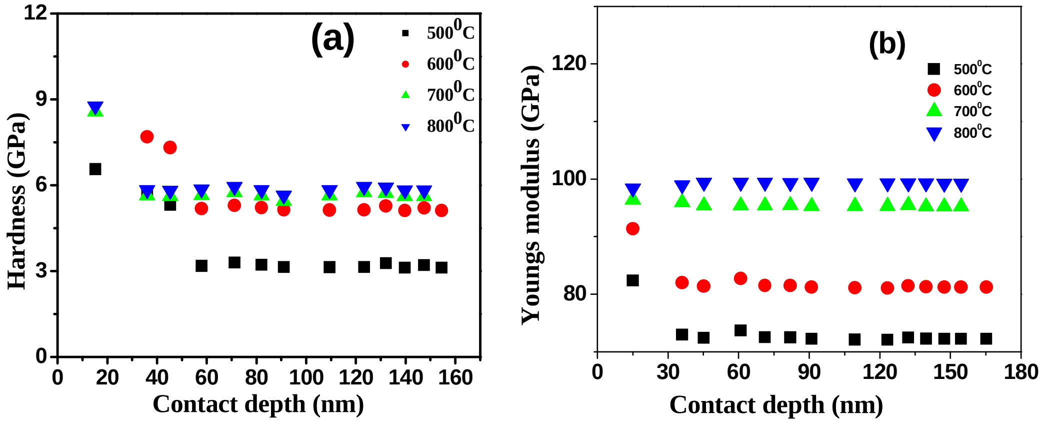

Figure 7.2 (a-b): (a) Hardness (b) Young's modulus of the SBTi thin films annealed in conventional furnace.

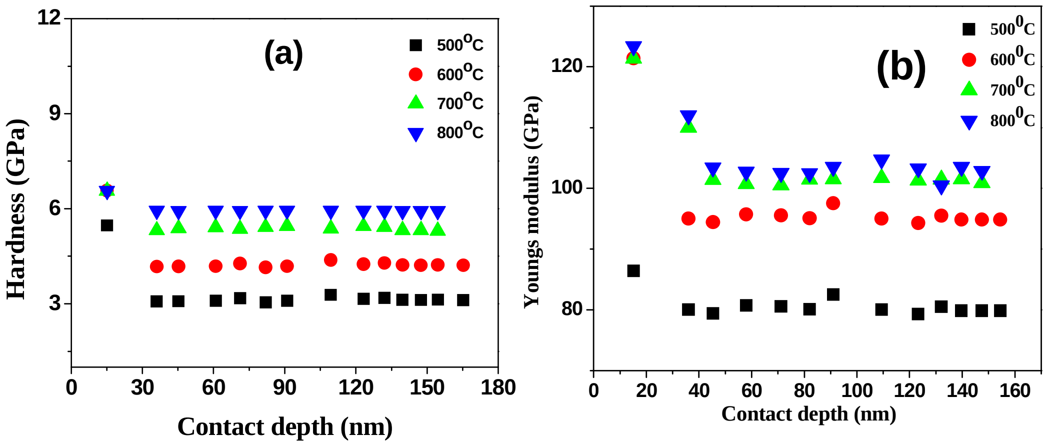

Figure 7.3: (a) Hardness (b) Young's modulus of the SBTi thin films annealed in microwave furnace.

Figure 7.4 and figure 7.5 shows the coefficient of friction of SBTi thin films annealed in microwave and conventional furnace respectively. Coefficient of friction is almost constant as the contact depth increases for both the films. This indicates that the deposited films exhibited the uniform thickness throughout scratch area. Moreover, it also indicates that the adhesion between the films and substrate is good throughout the film. The values of the friction coefficient are higher for films annealed at lower temperatures than the films annealed at high temperatures possibly due to variation in grain size. As the annealing temperature increases, the friction coefficient decreased. This indicates that the grain growth and densification takes place. These results are in support of the hardness and Young's modulus of these films.

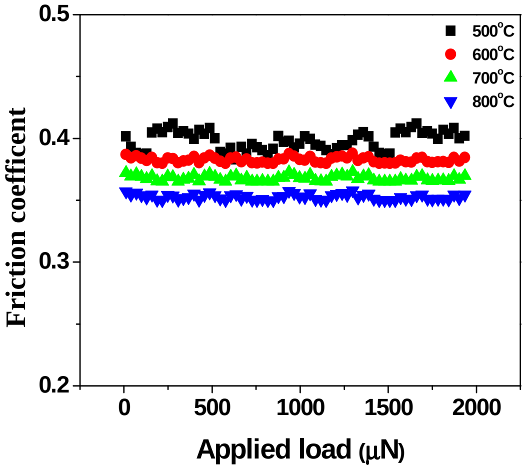

Figure 7.4: Friction coefficient of SBTi films annealed in microwave furnace.

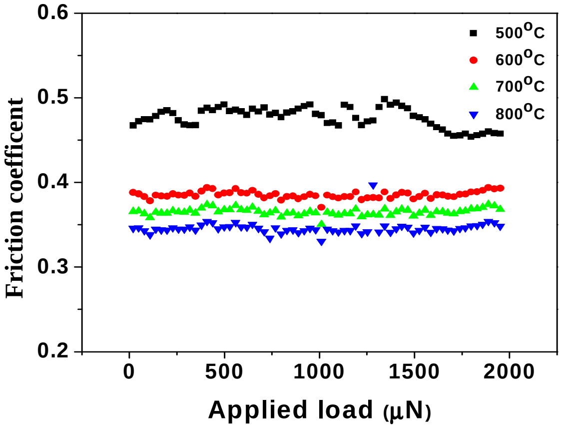

Figure 7.5: Friction coefficient of SBTi films annealed in conventional furnace.

7.3 Effect of OMP on mechanical properties:

Figure 7.6 shows the load-displacement (L-D curve) curve for the films deposited at different oxygen mixing percentage. In the present case, there is no observable discontinues in the load-displacement curves of the films deposited at 25% - 75% of OMP, which indicates that the films are uniform and crack free. Films deposited at 100%-OMP exhibited the discontinuity which indicates that these films are having pores and non-uniform microstructure. For the observed L-D curve, indentation depth is less for the films deposited at 50% and 75% of OMP compared to other films which indicates that these films are more harder than the other films. Films deposited at 100%-OMP shows a higher indentation depth which indicates their lesser hardness.

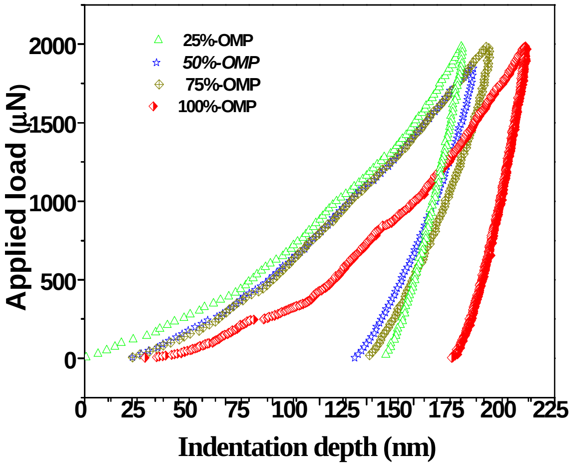

Figure 7.6: Load-Displacement curve of SBTi films deposited at different OMP.

In the present case, SBTi films are deposited at different oxygen mixing percentage (OMP) and annealed in conventional and microwave furnace in oxygen atmosphere. The hardness and Young’s modulus of the films annealed in microwave and conventional furnace are shown in figure 7.7(a-b) and 7.8 (a-b) respectively. The hardness and Young’s modulus values of the microwave annealed films exhibited higher values than the conventional annealed films. Films deposited at 25%-OMP exhibited lower values of hardness and Young's modulus due to oxygen deficiency and smaller grain size than the films deposited at 50%-OMP. The films deposited at 50%-OMP exhibited the higher hardness and Young's modulus compared to other films. Films deposited at 75%-OMP exhibited the hardness and Young's modulus values lesser than the 50%-OMP case and higher than the 25% of OMP case. Films deposited at 100%-OMP exhibited low mechanical properties compared to all other films due to low packing density and smaller grain size, which lead to lesser stiffness. These above results revealed that the mechanical properties of the films are strongly dependent on oxygen mixing percentage as well as grain size. The observed mechanical properties were directly proportional to grain size of the films. As we observed in Chapter 5 section 5.7.2, grain size is primarily dependent on the oxygen mixing percentage (OMP). Films deposited at 50%-OMP exhibited good mechanical properties compared to other films. It may be explained that the 50% of oxygen mixing percentage is influencing the grain growth and reducing the oxygen vacancies which lead to the strengthening of the films and having good optical packing density.

This is confirmed from the friction coefficient values. The friction coefficient as a function of contact depth of the films annealed by microwave and conventional furnace are shown in figure 7.9 and figure 7.10 respectively. The values of the friction coefficient for films deposited at 100%-OMP is the highest, which indicates that these films are having poor adhesion and less stiffness. Films deposited at 50%-OMP exhibited the lowest friction coefficient with higher hardness and Young's modulus indicating that they got better adhesion and are more stiff.

Conventional annealed films also exhibited the same trend as microwave annealed films with varying OMP. Values of the hardness and Young's modulus of the films annealed in conventional furnace are less than the films annealed in microwave furnace. This is due to Bi volatization and oxygen vacancies in the films at higher temperatures and longer soaking time even though oxygen mixing percentage is increased. The values of mechanical properties of the films annealed at different temperatures (mentioned in previous section) are less than the films deposited at different OMP which indicates that oxygen atmosphere during deposition and annealing (and hence oxygen vacancies in the deposited films) plays an important role in yielding densified films which gives improved mechanical properties.

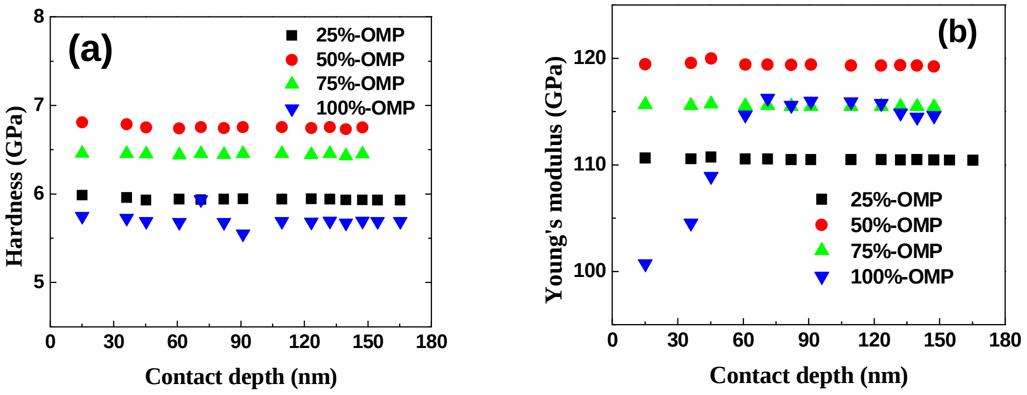

Figure 7.7 (a-b): (a) Hardness and (b) Young's modulus of the films annealed in microwave furnace.

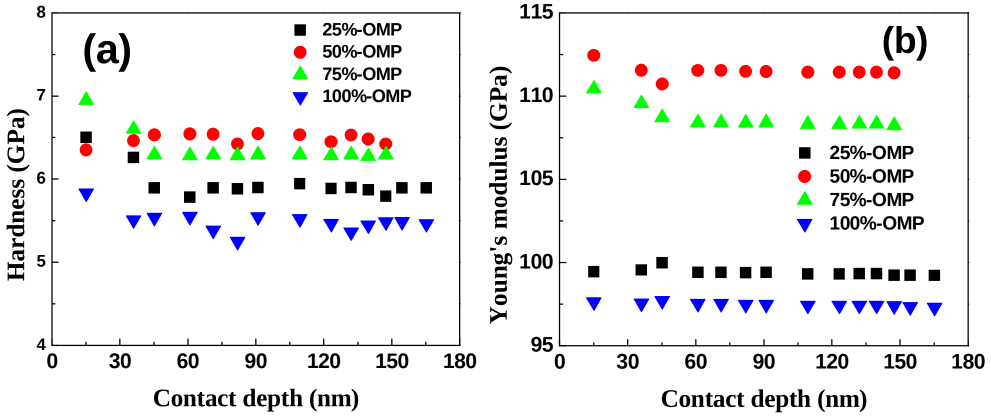

Figure 7.8 (a-b): (a) Hardness and (b) Young's modulus of the films annealed in conventional furnace.

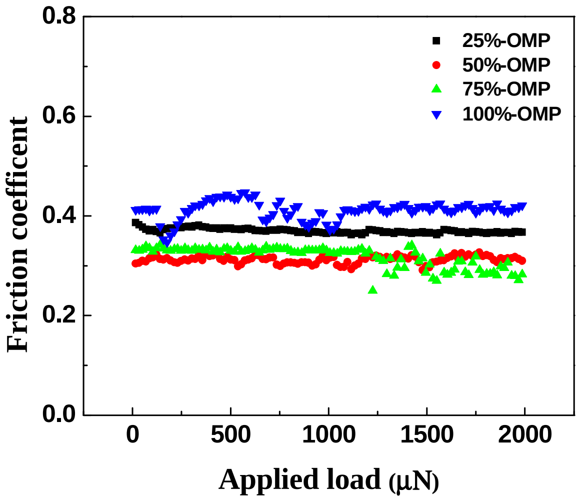

Figure 7.9: Friction coefficient of microwave annealed films

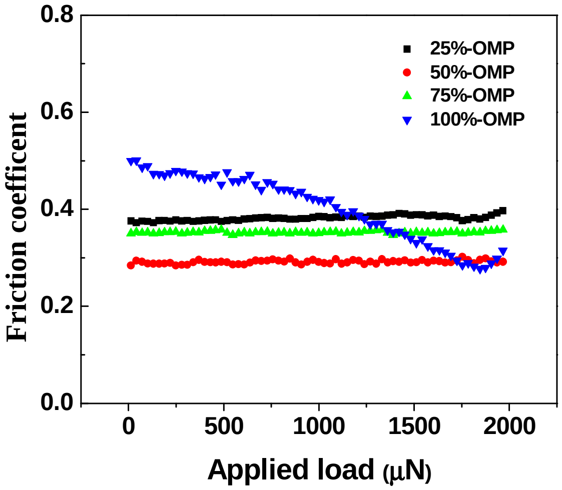

Figure 7.10: Friction coefficient of conventionally annealed films

7.4 Mechanical properties of the *In-situ* deposited thin films of SBTi

In order to investigate the effect of deposition temperature $T_{d,}$ on the mechanical properties of SBTi thin films, these films were deposited *in situ* at substrate temperatures of 600 -725^{o}C at a constant OMP of 50%.

The values of hardness and Young's modulus of the films are shown in figure 7.11(a-b). In this case also the low temperature deposited films exhibits poor crystallization, and as the substrate temperature increases the degree of crystallinity increased as mentioned in Chapter 6, section 6.3.1. The Young's modulus increased from 100 to 123GPa and hardness from 6.3 to 7.8GPa with enhancement of grain size from 210-311 nm as the deposition temperature increases from 600 to 725^{o}C. The values of the hardness and Young's modulus are increased as the substrate temperature increased to 700^{o}C. The films deposited at 725^{o}C showed the least hardness and Young's modulus. This could be the result of porosity in the films by evaporation of Bi at high temperatures which generates non-stoichometry in the films. The above argument is confirmed by compositional analysis of the same films which is discussed in Chapter 6. On the other hand, orientation of the films deposited at 725^{o}C exhibited the (0010) direction which is different from the orientation (119) of films deposited from 600 to 700^{o}C. That shows that the mechanical properties are strongly dependent on porosity and orientation of the films. The same trend was observed also by Huaping Wu [13]. The friction coefficient of the films deposited at 600-725^{o}C is shown in figure 7.12. The values of the friction coefficient decreased as the deposition temperature increased up to 700^{o}C. Films deposited at 725^{o}C shows the high coefficient of friction which indicates that these films are porous with less packing density. Comparison with the two previous section results shows that *in-situ* deposition of the films improved its mechanical properties as expected. *In-situ* deposition plays an important role to attain good microstructure and compact grains which lead to improvement in its mechanical properties. In the other two cases, the mechanical properties decreased due to thermal stress and evaporation of moisture during post annealing process.

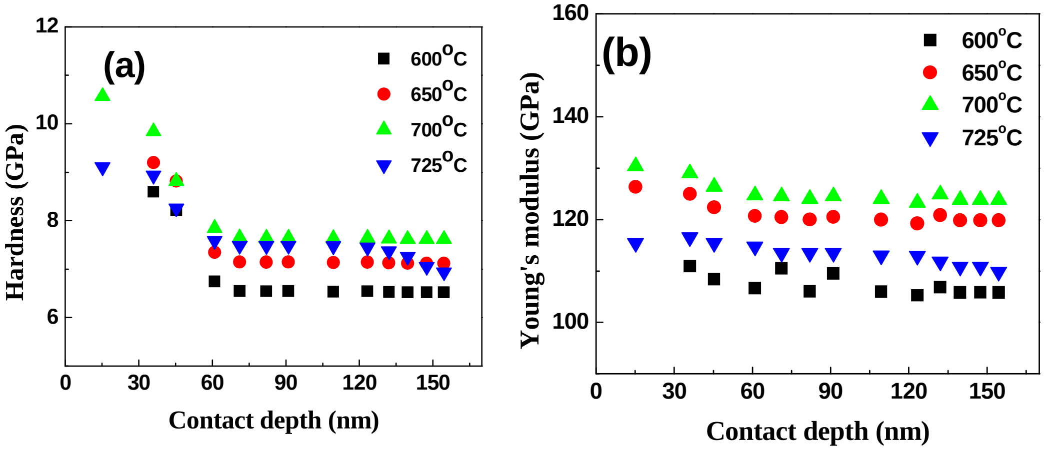

Figure 7.11 (a-b): (a) Hardness, (b) Young's modulus of the films *in situ* deposited at 600-725°C

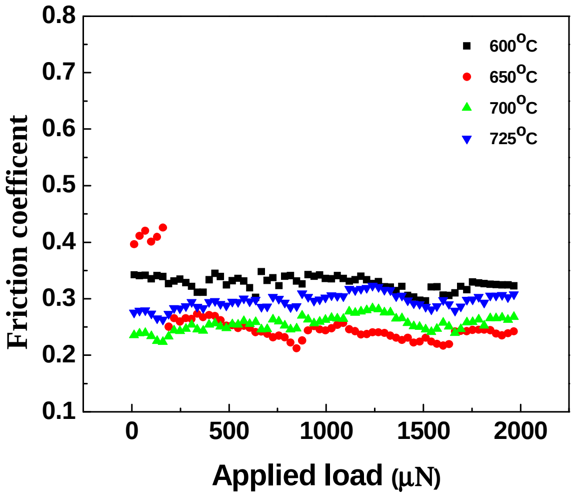

Figure 7.12: Friction coefficient of the films *in situ* deposited at 600-725°C as a function of applied load.

7.5 Mechanical properties of Sm-substituted SBTi thin films

The hardness and Young's modulus of Sm-substituted SBTi films deposited at 675-750°C is shown in figure 7.13(a-b). The details of the film preparation are mentioned in chapter 6, section 6.2. The Young's modulus is increased from 110 to 135GPa and hardness from 4.3 to 8.2GPa with an enhancement of average grain size from 220 to 350nm with respect to increasing substrate temperature during deposition. These results again points out that the mechanical properties of the films are improved while heating to higher temperatures due to grain growth [8]. On the increase in grain size leads to a hardening of the thin film material. It is interesting to observe that the Sm-substituted films got improved mechanical properties compared to the pure-SBTi thin films. The substitution of samarium results in controlling the volatization of Bi- even at higher temperatures which lead to the enhancement observed. We have observed the same trend in bulk ceramic samples which are discussed in chapter 4. One possible reason is that the samarium content suppresses porosity through improved nucleation and grain growth which lead to improving the grain size and packing density without pores and cracks. From these results we can conclude that the mechanical properties are strongly depended on porosity and grain size of the films. The same trend was observed by J.Ricote et.al [14]. The friction coefficient of the films deposited at 675-750°C is shown in figure 7.14. The values of the friction coefficient decreased as the deposition temperature increased. Films deposited at 675°C shows the higher friction coefficient which indicates that the amorphous/less crystalline films are having higher friction coefficient than the crystalline films due to poor adhesion and less packing density. These results are in supporting with the microstructure and mechanical properties (like hardness and Young's modulus) of the Sm-substituted films.

.

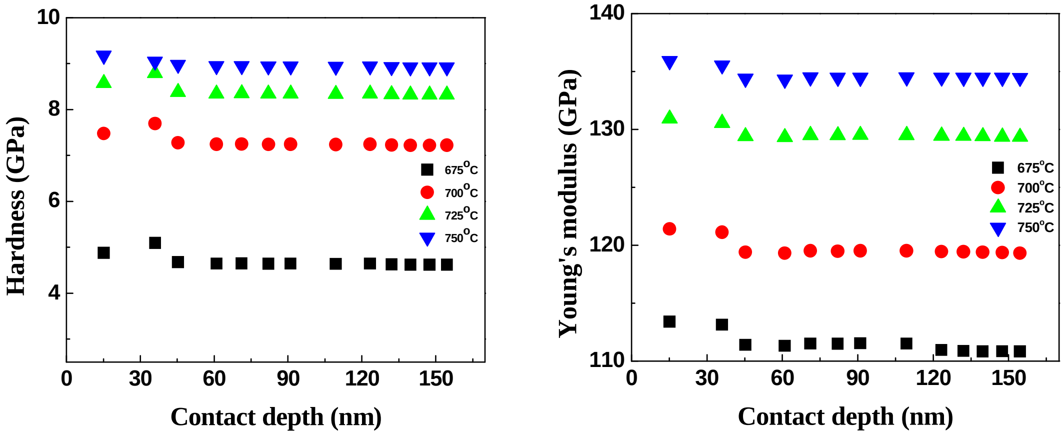

Figure 7.13: (a) Hardness (b) Young's modulus of the Sm-substituted SBTi thin films

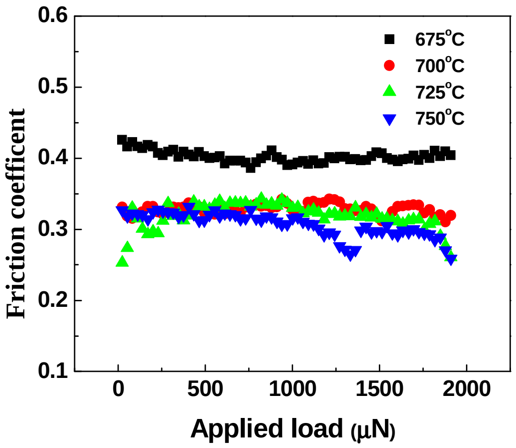

Figure 7.14: Friction coefficient as a function of applied load for Sm-substituted SBTi films

7.6 Effect of annealing on microwave dielectric properties:

The dielectric properties at microwave frequencies are found to strongly get affected by post deposition annealing temperature and duration. In order to study the influence of annealing temperature, the samples are annealed in air at different temperatures from 500 to 800°C. The microwave measurements of permittivity and loss tangent of the annealed SBTi thin films were carried out at the spot frequencies of 10GHz and 20GHz using a split post dielectric resonator (SPDR) technique [15-16]. The details about the measurement techniques are given in chapter 2. This is a non-destructive and accurate technique for measuring the complex permittivity of dielectric substrates and thin films at a spot frequency.

The measured dielectric constant (ε_r) and loss tangent (tanδ) of the conventional and microwave annealed SBTi thin films as a function of annealing temperature are given in figures 7.15 (a-b) and 7.16 (a-b) respectively. It can be observed that the films annealed at 500^{o}C in conventional furnace exhibits low value of dielectric permittivity and loss tangent. There is a sudden increase of dielectric permittivity and loss tangent for the films annealed at 600°C and above. It is clear that the films annealed below 600°C are all amorphous. In the amorphous phase, the observed dielectric constant of these thin films is found to be less than that of the crystalline films predicted using the Clausius-Mosotti theory [17]. On annealing the film, packing density, grain size and the crystallinity starts improving. This results in an increased dielectric constant. The slight decrease in dielectric constant for the films annealed at 800°C may be due to Bi-volatization and formation of oxygen vacancies in the film at those temperatures. Another possible reason for the decrease in dielectric constant at high temperature can be the thermal strain developed in the film due to the difference in thermal expansion coefficients of the substrate and the film. It is observed that the amorphous thin films have a lower dielectric loss when compared to that of the crystalline thin films. This is because the amorphous films will have low intrinsic losses due to the absence of lattice modes. As the film crystallizes, it generates a lattice potential which will allow the phonon- phonon interactions and thereby opening up many loss mechanisms [18].

The microwave dielectric properties of the microwave annealed thin films are shown in figure 7.16(a-b). The values of dielectric constant measured at 10GHz are more than the values measured at 20GHz. As the annealing temperature increases, the values of dielectric constant and loss tangent also increases. These films also followed the same trend as conventionally annealed films up to an annealing temperature 700^{o}C. But, the films annealed at 800^{o}C exhibited a higher value of dielectric constant with lower loss value. This indicates that the Bi-volatization and formation of oxygen vacancies are controlled in microwave annealed films compared to conventionally annealed films. This is a consequence of the shorter heating/cooling and soaking time of microwave annealing compared to conventional method. The values of the dielectric constant for films annealed in microwave furnace are more than the films annealed in conventional furnace indicating better crystallization. In both the cases higher frequency gave a lower value of dielectric constant with higher dielectric loss, showing that the material undergoes a dielectric relaxation process at these frequencies which is expected as the ferroelectric domains relaxes in the microwave frequency range.

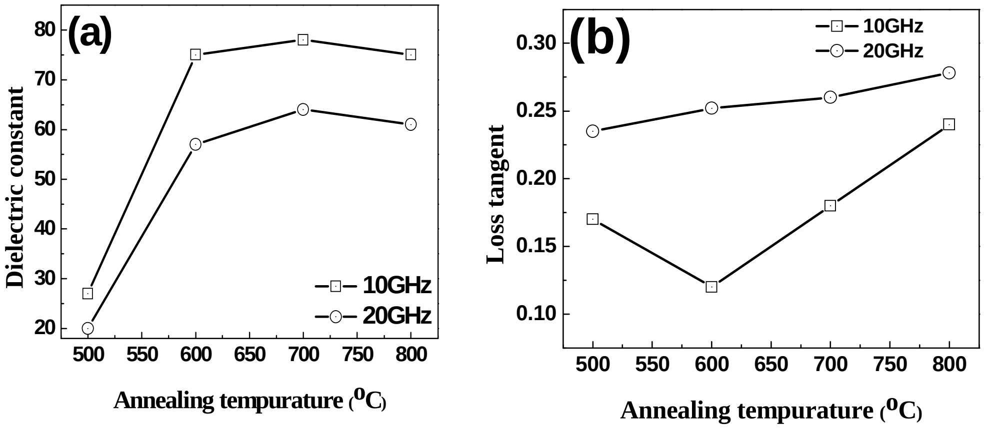

Figure 7.15: (a) Microwave dielectric constant (b) loss tangent of the SBTi films annealed in conventional furnace.

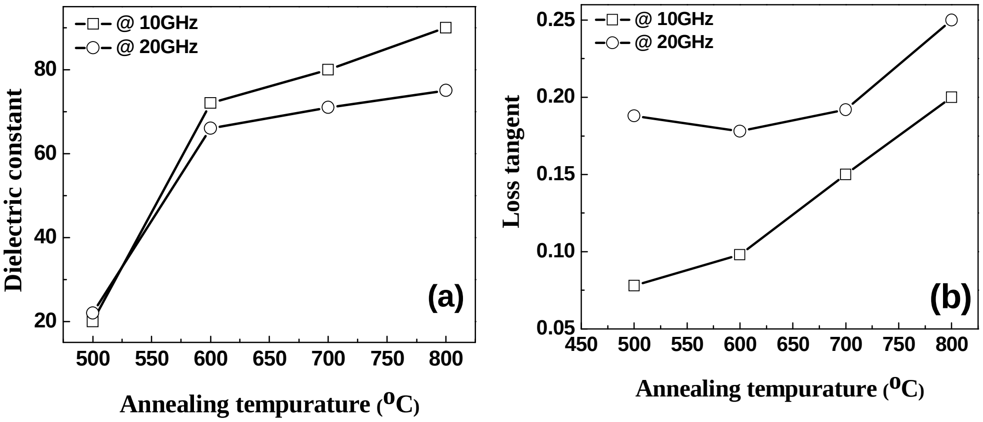

Figure 7.16: (a) Microwave dielectric constant (b) loss tangent of the SBTi thin films annealed in microwave furnace.

7.7 Effect of OMP on microwave dielectric properties:

There are reports about the microwave dielectric properties of SBTi and rare earth-doped SBTi bulk ceramic samples [19-21], but there are no reports on thin films grown on amorphous substrates even though it has technological interest. In the present study, microwave dielectric properties at 10and 20 GHz of SBTi thin films grown on fused silica substrates and deposited at different OMP are discussed. The films are annealed in conventional & microwave furnaces.

In this study, films prepared at different OMP were given a post deposition annealing treatment either in the microwave or in the conventional furnace in presence of a flowing oxygen gas ambient. The annealing treatment in microwave furnace is at 750^{o}C for 20minutes whereas it is at 750^{o}C for 2 hours in the conventional furnace. The microwave dielectric constant and loss tangent of SBTi thin films annealed in microwave and conventional furnace is shown in figure 7.17 (a-b) and 7.18 (a-b) respectively. It is observed that microwave dielectric constant and loss tangent (tanδ) is strongly dependent on the oxygen mixing percentage and the presence of oxygen in the annealing stage. The loss values of the films annealed in the presence of oxygen is 2 orders of magnitude lower compared to the films mentioned in the previous section where the films were annealed in air, indicating the pivotal role played by oxygen vacancies in determining the dielectric properties of these oxide films. While the loss values have decreased, the corresponding dielectric constant values of these films got enhanced compared to films annealed at different temperatures in air. This shows that the films are in a regular crystalline order when prepared in oxygen atmosphere and annealed in oxygen atmosphere. Also it can be noticed that microwave dielectric loss is a very sensitive parameter that responds to even the smallest changes in stoichiometry, composition, structure and microstructure. However it can be controlled by simple techniques like regulating the oxygen content in the processing atmosphere. The observed dielectric constant values are higher for microwave annealed films than conventional annealed films due to difference in grain size and oxygen vacancies occurring in conventional annealed films at high temperatures for longer soaking time. It is observed that, the variation in dielectric constant and loss tangent is due to the process related changes like annealing, structure, deposition pressure and microstructure [22]. From the XRD and AFM analysis which is mentioned in Chapter

5, section 5.7 and 5.8, it is clear that the films deposited at 75% & 100%-OMP is having smaller crystallite size and lesser grain size with less packing density which could lead to a reduction in the dielectric properties in both conventional and microwave annealed films. It is well known that the relative permittivity decreases with increasing material porosity. Thus controlling the porosity can yield a spectrum of dielectric constant from a single material [23]. Improvement of dielectric properties with dense microstructure is reported by Hiroya et.al [24]. Films deposited at 25%-OMP also exhibited a lower dielectric constant compared to 50%-OMP due to generation of oxygen vacancies.

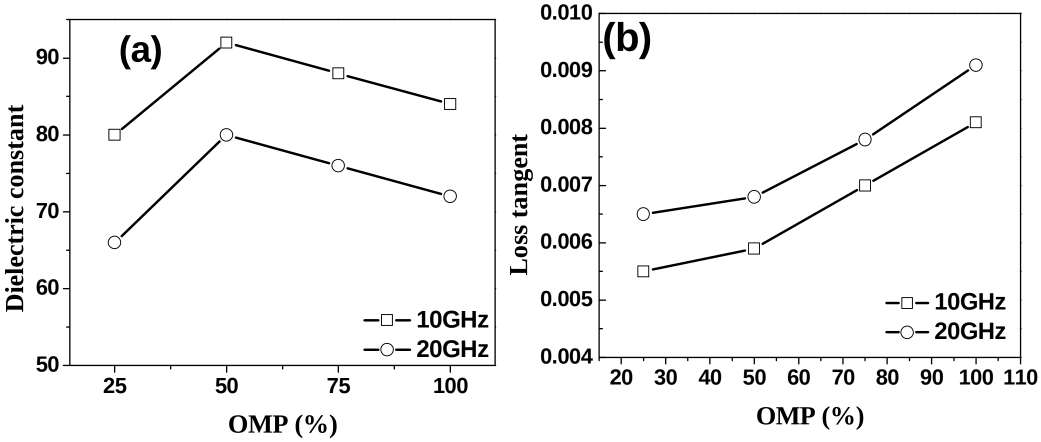

Figure 7.17 (a-b): (a) Microwave dielectric constant and (b) loss tangent of the microwave annealed SBTi thin films, in oxygen atmosphere.

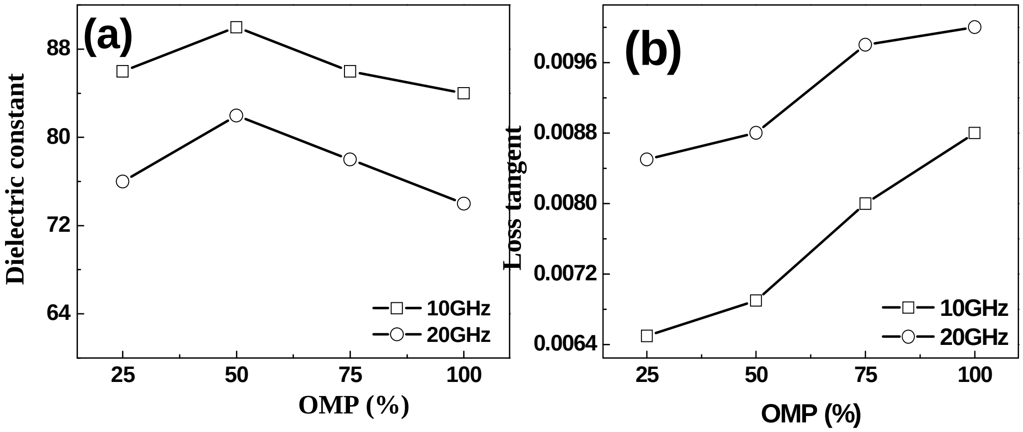

Figure 7.18(a-b): (a) Microwave dielectric constant and (b) loss tangent of conventional annealed SBTi thin films in oxygen atmosphere.

7.8 Microwave dielectric properties of in-situ deposited SBTi thin films:

The measured dielectric properties of the SBTi thin films at 10GHz and 20GHz as a function of substrate temperature for films deposited at higher deposition temperatures is shown in figure 7.19(a-b). From this figure, it is clear that the dielectric loss values are in between the values obtained in the 2 previous cases discussed, i.e, the post deposition annealing in air and deposition in oxygen ambient with annealing in oxygen ambient. In other words, deposition at higher temperatures is good but not as good as growing in an atmosphere where oxygen stoichiometry is ensured. Or in these oxide films, oxygen stoichiometry plays the predominant role even above the deposition temperature which predominantly influence the microstructure. In this case, the dielectric properties showed lesser frequency dispersion indicating a reduction in relaxable diploes present. The dielectric properties are also depending on the substrate temperature. As the substrate temperature increases, the dielectric constant is also found to be increasing and it peaks around 700°C. On further increase of substrate temperature, the dielectric constant starts decreasing. This observed dielectric properties can be explained interms of the crystal orientation as evident from the XRD which is mentioned in Chapter 6, section 6.3.1. It is well known that the spontaneous polarization of these Bi layered oxides is larger along the a-axis as compared to along c-axis. So a film oriented on (100) direction will have naturally more dielectric constant than the films oriented along (001) direction.

In the case of polycrystalline films, the situation will be slightly different since both *a* and the c-axis oriented grains will contribute to the total polarization. The observed dielectric constant will be a resultant of both the contributions and the exact effects of these contributions are not yet well established. As evident from the X-ray diffraction studies which are discussed in Chapter 6, the ratio of the non c-axis orientation (119) to the c-axis orientation (0010) decreases as the substrate temperature increases. As the films become more c-axis oriented, the dielectric constant is found to decrease as expected. But, for the films with more non c-axis orientation, the dielectric constant is found to be improving with increased presence of c-axis orientation. This may be due to the fact that in this region the total polarization shows an additive behavior. It can be found that in poly crystalline SBTi thin films the dielectric constant can be effectively controlled by c-axis oriented grains. A moderate percentage of c-axis oriented grains along with non c-axis oriented grains will result in better dielectric properties. The Raman studies on these films also shows that the films with moderate amount of c-axis oriented grains exhibit an additional Raman mode at 270 cm^{-1} which arises from the torsional bending of TiO_6 octahedra. This may result in higher polarization which could be the reason for the improved dielectric properties. As mentioned in chapter 6, the in-situ deposition of films is expected to improve its properties. Comparing with previous results which are mentioned in 7.5 & 7.6, in-situ deposited films exhibited higher dielectric constant. This indicates that the crystallization and densification takes place together during in-situ deposition which leads to improvement in film properties.

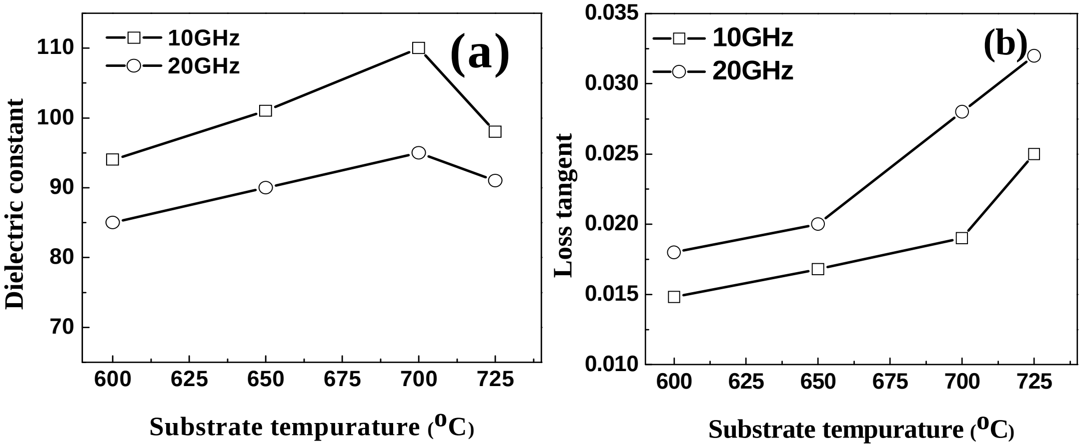

Figure 7.19(a-b): (a) Microwave dielectric constant and (b) loss tangent of the SBTi thin films deposited in the range of 600 to 725°C.

7.9 Microwave dielectric properties of Sm-substituted SBTi thin films:

In order to study the substation effect on SBTi films, the SBSmTi films were deposited at different temperatures from 675°C to 750°C. The microwave dielectric measurements of permittivity and loss tangent of the SBSmTi thin films were carried out at 10GHz and 20GHz using the SPDR technique. The measured dielectric constant (ε_r) and loss tangent (tanδ) of the SBSmTi thin films as a function of substrate temperature is given in figure 7.20 (a-b). The observed results are following the same trend as discussed in the previous section 7.7. This indicates that the substrate temperature plays an important role to grow the films in preferred orientations even after modifying it with substitution.

It is observed from the figure 7.20 that the films deposited at 675°C shows a low value of dielectric permittivity and loss tangent. There is a sudden increase of dielectric permittivity and loss tangent for the films annealed at 700°C and above. The dielectric permittivity has decreasing slightly for the films deposited above 725°C.

From the X-ray diffraction studies presented in Chapter 6, section 6.4.2, it is clear that the films deposited below 675°C are all amorphous. In the amorphous phase, the observed dielectric constant of these thin films is less than that of the crystallized films. On increasing the substrate temperature, packing density, grain size and the crystallinity starts improving and it will result in an improvement in dielectric constant. The slight decrease in dielectric constant for the films deposited above 725°C may be due to the formation of oxygen vacancies in the film. Though the mechanical properties of the films deposited at 750^{o}C exhibited the higher hardness and Young's modulus, the observed microwave dielectric properties of the same films are decreased. This indicates that the high frequency dielectric measurements are sensitive to formation of oxygen vacancies. Another possible reason for the decrease in dielectric constant at high temperature can be the thermal strain developed in the film due to the difference in thermal expansion coefficients of the substrate and the film [25]. It is observed that the amorphous thin films have a lower dielectric loss when compared to that of the crystalline thin films. This is because the amorphous films will have low intrinsic losses due to the absence of lattice modes. As the film crystallizes, it generates a lattice potential which will allow the phonon- phonon interactions and thereby opening up many loss mechanisms [26].

The observed dielectric constant values for the crystalline substituted films are higher than the unsubstituted-SBTi crystalline thin film which is discussed in the previous section 7.7. This indicates that the substitution of Samarium improved its dielectric properties as observed in Chapter 5 for the case of bulk ceramic samples. The enhancement in material properties by substitution of rare-earth element into layered structure materials is observed by many researchers [27-30]. Substitution of Samarium controls the Bi-volatization thereby leading to an improvement in its film properties. With the increased dielectric constant, the loss also showed a corresponding increase while the relaxation trend with frequency is retained indicating that there is no fundamental changes happening to the system with Sm substitution.

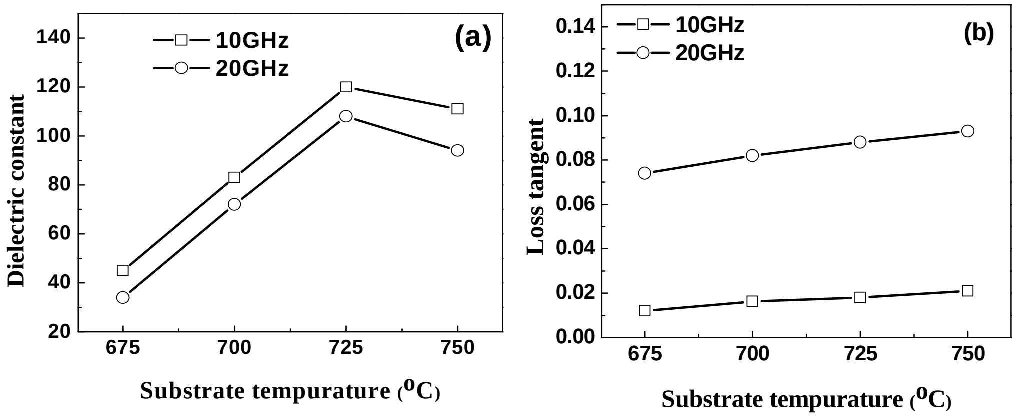

Figure 7.20 (a-b): (a) Microwave dielectric constant and (b) loss tangent of the Sm substituted SBTi thin films deposited at substrate temperatures from 675 to 750°C.

7.10 Summary:

Measurement of mechanical and microwave dielectric properties of SBTi and Sm-substituted SBTi thin films were carried out for different processing conditions such as (i) Annealed at different temperatures (ii) Deposited at different oxygen mixing percentage followed by annealing in oxygen atmosphere (iii) In-situ deposition of SBTi thin films (iv) In-situ deposition of Sm-substituted SBTi thin films.

SBTi thin films were annealed from 500 to 800°C in conventional and microwave furnace. The observed hardness and Young's modulus values are increased along with grain size as the annealing temperatures are increased. There is no observable difference in mechanical properties of conventional and microwave processed films. Films annealed in microwave furnace exhibited the high dielectric constant at microwave frequency range than the films annealed in conventional furnace. These results indicated that the films annealed in microwave furnace exhibited better properties.

Mechanical and microwave dielectric properties of SBTi thin films deposited at different OMP and annealed in oxygen atmosphere are strongly dependent on oxygen atmosphere. Films deposited at 50%-OMP and annealed in oxygen atmosphere have exhibited the highest dielectric constant and good mechanical properties compared to other films which are deposited at 25, 75, 100%-OMP and films annealed at different temperatures in air that are mentioned in section 7.2. These results revealed that controlling the oxygen stoichiometry in oxide thin films during the deposition and annealing process is an important issue to enhance film properties.

In-situ deposition of SBTi thin films exhibited interesting results as expected. As the substrate temperature increases, the film orientation changes from (119) to (0010) direction. Films deposited at 700^{o}C showed that the intensity of the peak (119) and (0010) are almost equal and these films exhibited better dielectric and mechanical properties compared to other films. A moderate percentage of c-axis oriented grains along with non c-axis oriented grains results in better film properties. The in-situ deposited films enhanced its film properties compared to ex-situ annealed films due to the fact that crystallization and grain growth takes place together during in-situ deposition and suppresses the differences in thermal expansion coefficients between the film and substrate.

The Sm-substituted SBTi films are deposited from 675 – 750^{o}C in presence of oxygen atmosphere. Young’s modulus increased monotonically from 110 to 135GPa and hardness from 4.3 to 8.2GPa with enhancement of grain size from 220 to 350nm with respect to substrate temperature. It is interesting to observe that the Sm-substituted films have improved its mechanical properties compared to the pure-SBTi thin films. The substitution of samarium controls Bi-volatization even at high temperatures which lead to an enhancement of its mechanical properties. The friction coefficient results are in agreement with the hardness and Young’s modulus results. The observed microwave dielectric properties of SBSmTi thin films were higher than the pure-SBTi thin films. This indicates that the substitution of Samarium improved its dielectric properties as observed in bulk ceramic samples. It is observed that the amorphous thin films have a lower dielectric loss due to the absence of lattice modes. As the film crystallizes, the excitation of lattice modes and coupling between phonons opens up many loss mechanisms.

References:

1. J Krupa, R.N Clarke, O.C Rochard and A.P Gregory., XII Int. Conf MIKON, Wroclaw, Poland (2000).
2. Huaping Wu, Linzhi Wu, Qiu Sun, Weidong Fei, Shanyi Du., J Appl surf Sci **254**; 5492-5496 (2008).
3. B. Audoly, “Stability of Straight Delamination Blisters” Phy Rev Lett **83**; 4124-4127 (1999).
4. M.H Zhao, R Fu, D.Lu, T.Y Zhang., J Acta Mater **50**; 4241-4127 (2002).
5. A.Lee, Clemensf B.M, W.D.Nic., J Acta Mater **52**; 2081-2093 (2004).
6. K.Sudheendran, K.C James Raju, Manoj K.Singh, Ram S.Katiyar, Jour Appl Phy., **104**, 104104 (2008).
7. Anthony C. Fischer-Cripps, Nanoindentation 3rd edition, Springer science, chapter **2**: page 29-31 (2011).
8. V.Kulikovsky, V.Vorlicek, P.Bohac, M.Stranyanek, et.al., J.Surf.Coat & Tech **202**, 1738-1745 (2008).
9. T.H Fang, S.R Jian, D.S Chuu., J.Phy: Condes.Matter., **15**, 5253 (2003).
10. J.Schiotz, T.Vegge, F.D Di Tolla. K.W Jacobsen., Phy Rev B., **60**, 11971 (1999).
11. Rwei-Cing Chang, Feng-Yuan Chen and Chang-En Sun, J.Key Engg Mat 326-**328,** 357-360 (2006).
12. Hysitron, Inc., Nanoscratch User manual, Minneapolis, MN (2001).
13. Huaping Wu, Linzhi Wu, Qiu Sun, Weidong Fei, Shani Du, J.Appl Sur.Sci., **254** 5492-5496 (2008).
14. J.Ricote, L.Pardo, B.Jimenez., J. Mat Sci., **29,** 3248-3254 (1994).
15. M.A.Subramanian and R.D.Shannon, *Mater.Res.Bull*, **24**, 1477(1989).
16. D.A.Tenne, A.Soukiassian, X.X.Xi, H.Choosciwan and R.Guo and A.S.Bhalla, *Phys.Rev B*, **70**,174302 (2004).
17. Lingling ZHOU, Hongqing ZHOU, Hui SHAO, et al., J.Rare-earth., **30,** 142-145 (2012).
18. N.Santha and M.T Sebastian, J.Mat Res.Bull., **43,** 2278-2284 (2007).
19. P.Sarah, Jour Engg Procedia, **10**, 2684-2689 (2011).
20. J. Krupa, A.P Gregory, O.C Rochard and A.P. Gregory, XIII Int.Conf MIKON.2000, Wroclaw, Poland, **305** (2000).

21. M.A. Rzepecka and M.A.K Hamid., IEEE Trans.Microw.Theory Tech, **20**, 30 (1972).
22. K.Sudheendran, M.Ghanashyam Krishna and K.C James Raju., J.Appl Phys A **95**, 48 (2009).
23. X.Gong, W Han She, Eric E, Hoppenjans, et.al., IEEE Trans.Micro.Theo.Tech, **53,** 3638 (2005).
24. Hiroya Kitahata,Kiyohara Tadanaga, Tsumotu Minami, et.al J. Ame. Cer. Soc **81**, 1357 (1998).
25. Y.M Tao and Y.Z.Yu, J.Appl Phy, **101**, 024111 (2007).
26. D.A.Tenne, A.Soukiassian, X.X.Xi, H.Choosciwan, et.al., J.Eur.Cer.Soc, **10,** 2673 (2001).
27. Hiroyuki Ikawa, Minoru Takemoto., Jour.Mat.Chem & Phys., **79,** 222-225 (2003).
28. Yun Wu, Mike J, Forbess, Seana Seraji, Steven J. et.al., J.Appl. Phy., **90**, 5296 (2001).
29. N.Santha and M.T Sebastian, Jour.Mat Res.Bull. **43**, 2278-2284 (2008).
30. K.Stanly Jacob, R.Satheesh, R.Ratheesh., Jour Mat.Res Bull., **44**, 2022-2026 (2009).

Chapter 8

Conclusions and scope for future work

Chapter 8

Conclusions and scope for future work

8.1 Conclusions

The research presented in this thesis dissertation is centered on the structural, microstructural, Raman, Optical, mechanical and microwave dielectric properties of $SrBi_4Ti_4O_{15}$ (SBTi) and Sm-substituted SBTi bulk ceramics and their thin films. One of the main objectives is to control the grain size and Bi-volatization at elevated temperatures using microwave sintering process to improve its material properties. Secondly, deposition of crystalline SBTi thin films on amorphous substrates and demonstration of mechanical and microwave dielectric properties along with optical and Raman studies. RF magnetron sputtering was chosen as the technique for deposition of these films. Salient conclusions of the thesis work are given below.

Single phase SBTi and Sm-substituted SBTi ceramic samples were prepared through solid-state reaction technique by optimizing the calcination and sintering conditions systematically. The structural, microstructural and dielectric investigations as well as the Raman studies were carried out. The X-ray diffraction study confirms the formation of an orthorhombic structure with all the major peaks corresponding to the $A2_1am$ Space group. Ball mill (reducing the grain size) and microwave sintering are the two alternative approaches that are successfully used to get a finer microstructure, densified ceramics and smaller grain size. It was observed that as the grain size decreases, the dielectric, ferroelectric and mechanical properties of the SBTi ceramics are enhanced. The microwave sintered samples exhibited smaller grain size than conventional sintered samples. It is interesting to observe that microwave sintering is able to control the grain size and Bi volatization at elevated temperatures which leads to better dielectric, mechanical and ferroelectric properties. The results of microwave sintered samples are desirable for microelectronics applications such as capacitors and actuators.

Substitution of samarium into A-site of $SrBi_4Ti_4O_{15}$ system was confirmed from the vibrational modes of the Raman spectra. With substitution of Samarium, SBTi ceramic samples exhibited the relaxor behavior which is useful in relaxor based lead-free ferroelectric applications. Relaxor behavior was confirmed by fitting standard deviation of Curie temperature distribution using inhomogeneous micro region model. It explains the existence of nano polar domains at temperatures higher than T_m. These domains exist as highly polarizable islands which lead to an increase in T_c distribution. 0.75 Sm substituted SBTi ceramics showed good microwave dielectric properties, ferroelectric properties and mechanical properties compared to other substituted compositions and unsubstituted SBTi ceramic samples.

Stoichiometric SBTi thin films were grown on amorphous substrates using rf sputtering and crystallized into orthorhombic structure by optimizing the annealing conditions. Two different ex-situ (post-deposition) annealing approaches were used in order to crystallize SBTi thin films. In the first approach, all the films are deposited at 50% of OMP and annealed in conventional and microwave furnaces. Microwave annealed films are able to exhibit the same results like conventional annealed films though the heating rate and soaking time is much shorter. In the second approach, films are deposited at different OMP and annealed in conventional and microwave furnace in oxygen atmosphere at fixed temperatures. These results show that the film properties are strongly dependent on oxygen mixing percentage. Films deposited at 50%-OMP and annealed in oxygen atmosphere exhibited good microstructure, optical, Raman, mechanical and microwave dielectric properties compared to films deposited at other OMPs and films annealed at different temperatures in air. Stoichiometric SBTi thin films were obtained by successfully optimizing the OMP and controlling oxygen as well as Bi vacancies during the deposition and annealing processes.

In-situ deposition of SBTi thin films has exhibited interesting results. As the substrate temperature increases, the film orientation changes from (119) to (0010) direction. A moderate percentage of c-axis (0010) oriented grains along with non c-axis (119) oriented grains results in better film properties. The in-situ deposited films exhibited enhanced dielectric and mechanical properties compared to ex-situ annealed films due to crystallization and grain growth that takes place together during in-situ deposition process and suppression of the effects of differences in thermal expansion coefficients between the film and substrate. From Raman spectra, it was identified that for the films with increasing percentage of c-axis oriented grains, the torsional bending mode of TiO_6 octahedra is getting loosened which results in an increased dielectric constant and loss factor- the effects of a larger oscillator strength. On correlating the observed microwave dielectric properties to the crystalline orientation, it can be concluded that in poly crystalline SBTi thin films, the microwave dielectric constant follows the population of the c-axis oriented grains. Oriented grain growth in thin films is achieved by optimizing the deposition conditions like substrate temperature and substrate-target distance. This is important for piezoelectric applications as piezoelectric devices require oriented films. It is interesting to observe that the Sm-substituted films exhibited improved film properties compared to the pure-SBTi thin films. Young's modulus increased monotonically from 110 to 135GPa and hardness from 4.3 to 8.2GPa. The highest dielectic constant values observed for films deposited at 725^{o}C are 105 and 120 for 20GHz and 10GHz respectively. Substitution of samarium resulted in suppression of Bi-volatization even at high temperatures which lead to enhancement of its mechanical and microwave dielectric properties.

8.2 Scope for future work

There are many issues that still need to be resolved and could form part of future work.

1. Transport properties of these ceramic materials and films to understand their conduction mechanism and to look for ways to reduce their conductivity so that they can be poled easily.
2. Microwave broadband characterization and study of tunability in these thin films.
3. Non-linear optical properties of these thin films are less studied till now. Knowledge of their optical response is also quite important for practical applications, which could be beneficial in the integration of optoelectronics with microwave electronics in the future.
4. Study of the high temperature piezoelectric properties and piezo force microscopy measurements of these thin films in order to understand the piezoelectric properties in these thin films.
5. Identify the suitable electrode materials and interface materials that will reduce the conductivity in the capacitor structures.
6. Fabrication of device structures like high overtone bulk acoustic resonators (HBAR) and high temperature transducers using these thin films.
7. Correlations between microwave dielectric properties and mechanical properties in these materials can be explored further in both bulk and thin films to understand the commonalities in their origin.

List of Publications

1. Nanomechanical and dielectric properties of microwave annealed Sol-gel derived PZT thin films.

   Rambabu A, Sudheendran K and K C James raju: Jour. Int Ferro, 119 (1):13-21 (2010).
2. Dielectric, ferroelectric and mechanical properties of $SrBi_4Ti_4O_{15}$ ceramics. **Rambabu A** and K C James Raju; Jour Mat science and Engg ,18 (2011): 092028.
3. Effect of Particle Size and Sintering Procedure on Microstructure, Dielectric, Ferroelectric and Mechanical Properties of $SrBi_4Ti_4O_{15}$

   Rambabu A and K C James Raju; Jou.r Ind. Cer Soc., 70 (3) (2011) 135-141.
4. Effect of microwave sintering on structural, microstructural, dielectric and mechanical properties of Sm-substituted SBTi ceramics

   Rambabu A and K C James Raju; Jour. Aus. Cer. Soc., 48 (1) (2012) 102-107.
5. Crystalline $SrBi_4Ti_4O_{15}$ thin films on amorphous substrates sputtered by rf sputtering

   Rambabu A and K C James Raju; Accepted in AIP proceedings - 2012.
6. Crystal orientation dependent microwave dielectric properties of sputtered SBTi thin films on fused silica substrates

   Rambabu A, Sudheendran K and K C James Raju (Accepted in Electronics materials)
7. Effect of substrate temperature on mechanical properties of SBTi thin films deposited by rf sputtering technique

   Rambabu A and K C James Raju (Under review)
8. Mechanical properties sputtered deposited of SBTi thin films sputtered using nanoindentation and nanoscratch test

   Rambabu A and K C James Raju (Under review)
9. Improved dielectric properties of Sm-substituted SBTi ceramic samples at low and high frequencies

   Rambabu A and K C James Raju (to be communicated)

Conference proceedings:

1. Effect of microwave sintering on Bi based High temperature piezoelectric ceramics.
   Rambabu A and K C James Raju, International conference on Electroceramics, New Delhi, Dec-2009
2. Structural, morphological and microwave dielectric properties of BZN ceramics.
   Sudheendran k, **Rambabu A** and K C James Raju, International conference on advanced functional materials, Kerala, Dec-2009
3. Effect of microwave sintering on dielectric, ferroelectric and mechanical properties of SBTi samples.
   Rambabu A and K C James Raju, 3rd International Congress on Ceramics, Osaka-2011
4. Dielectric, ferroelectric and structural properties of La-doped $SrBi_4Ti_4O_{15}$ ceramics, International conference on Material science and engineering, Kerala-Oct-2010.
   Rambabu A and K C James Raju
5. Effect of microwave sintering on SBTi bulk ceramics and thin films
   Rambabu A and K.C.James Raju; Workshop on Frontiers in Physics, University of Hyderabad-2011
6. Microwave assisted synthesis and sintering for achieving nano size structures in materials
   Rambabu A, S. Ramesh, K.C. James Raju; International conference on nanomaterials, MGU- Kottayam-2011
7. Effect of grain size on structural, dielectric and mechanical properties of SBTi thin films.
   Rambabu A and K C James Raju; National conference on Nano Science and technology-IISc, Bangolore-2011
8. Effect of crystallization of $SrBi_4Ti_4O_{15}$ thin films on amorphous substrates obtain by RF magnetron sputtering.
   Rambabu A and K C James Raju, ICWNCN-New Delhi 2012.
9. Effect of microwave annealing on microstructural, optical and Raman studies of SBTi thin films deposited by RF magnetron sputtering
   Rambabu A and K C James Raju, International Conference on Nanoscience and Technology-Hyderabad,2012

10. Effect of increasing Lanthanum substitution and the sintering procedures on the properties of $SrBi_4Ti_4O_{15}$ ceramics

    Rambabu A and K C James Raju, International conference on material science and technology-Palai, 2012
11. Structural, Morphogical and Raman studies of SBTi thin films on amorphous substrates

    Rambabu A and K.C.James Raju, DAE symposium-Bombay 2012

12. Variation in mechanical properties with substrate temperature of SBTi thin films deposited by rf sputtering

    Rambabu A, Anil T and K.C.James Raju, National seminar on ferroelectric and dielectric materials, Bhuwaneswar-2012